

# Properties of Intermittent Transport in the Mega Ampère Spherical Tokamak

Nicholas Ross Walkden

PhD

UNIVERSITY OF YORK

PHYSICS

December 2014

*“But then, science is nothing but a series of questions that lead to more questions, which is just as well, or it wouldn’t be much of a career path, would it?”*

Terry Pratchett

# Abstract

This thesis investigates the properties of intermittent transport on the Mega Amp Spherical Tokamak (MAST) both through dedicated experiment and numerical modelling. A ball pen probe (BPP) diagnostic has been operated on MAST to make a direct measurement of the plasma potential at the plasma boundary. By combining the BPP measurement with the floating potential from a Langmuir probe (LP) a measurement of the electron temperature is obtained, which is compared to the Thomson scattering diagnostic allowing for the accuracy of the BPP measurement of plasma potential to be assessed. From the measurement of the plasma potential the profile of the radial electric field is extracted. Using a third LP on the probe face fluctuation statistics of the ion-saturation current are determined. The skewness of the  $I_{sat}$  fluctuations is shown cross zero at the point where the radial electric field gradient maximizes. This suggests that intermittency in the plasma edge of MAST is produced at the centre of the radial shear layer, with negative skewness inside and positive skewness outside the centre of the shear layer.

The intermittent transport in the scrape-off layer (SOL) can be approximated as the result of successive discrete transport events arising from the motion of individual filaments. The BOUT++ framework has been used to model the motion of individual filaments in a geometry representative of the SOL of MAST. The SOL geometry gives rise to gradients in the filament parallel to the magnetic field through two mechanisms; enhanced diffusion in the divertor region and resistive ballooning. Parallel gradients cause a departure of the filament dynamics from 2D predictions due to the presence of the Boltzmann response in 3D. This provides a mechanism for poloidal motion of the filament alongside a breakdown into resistive drift-wave turbulence with the turbulent scale-length determined by the level of diffusion present in the system. The motion of the filament in the direction normal and bi-normal to the magnetic field line is shown to be approximately decoupled. The velocity of the filament in the normal direction displays a scaling with temperature and filament size congruent with the resistive ballooning or ideal interchange regimes of 2D blob dynamics whilst the bi-normal velocity of the filament adheres to a scaling based on the Boltzmann response. An increase in temperature is shown to provide a slight increase in the net radial transport of particles due to the motion of the filament at the outboard midplane, however an increase in filament width provides a far stronger increase in particle transport. This suggests that for MAST the filament width is the main parameter determining the level of intermittent particle transport in the SOL.



# Contents

<b>Abstract</b>	<b>iii</b>
<b>Contents</b>	<b>iv</b>
<b>List of Figures</b>	<b>ix</b>
<b>List of Tables</b>	<b>xiii</b>
<b>Acknowledgements</b>	<b>xv</b>
<b>Dedicatory</b>	<b>xvii</b>
<b>Declaration of Authorship</b>	<b>xix</b>
<b>Chapters</b>	<b>1</b>
<b>1 Introduction</b>	<b>1</b>
1.1 Energy demand . . . . .	1
1.2 Nuclear Fusion . . . . .	3
1.3 The Tokamak . . . . .	9
1.3.1 Diverted tokamaks . . . . .	12
1.3.2 The scrape-off layer . . . . .	13
1.3.3 The future of the tokamak: ITER and DEMO . . . . .	15
1.3.4 The Mega-Amp Spherical Tokamak (MAST) . . . . .	17
1.4 Plasma Physics . . . . .	19
1.4.1 Definitions of a plasma . . . . .	20
1.4.2 Descriptions of a plasma . . . . .	21
1.4.3 Fluid moments of the kinetic equation . . . . .	24
1.4.4 Plasma drifts . . . . .	28
1.5 Thesis outline . . . . .	30
<b>2 Review of Filament Physics</b>	<b>33</b>
2.1 Introduction . . . . .	33
2.2 Experimental Characterization of Filaments . . . . .	34
2.2.1 Probe Measurements of Filaments . . . . .	34
2.2.2 Imaging of Filaments . . . . .	37
2.2.3 Filament Properties across Machines . . . . .	38

2.3	Models for filament motion . . . . .	39
2.4	Filament Generation . . . . .	44
2.5	Discussion . . . . .	47
2.6	Summary . . . . .	48
<b>3</b>	<b>Ball Pen Probe Measurements on MAST</b>	<b>51</b>
3.1	Introduction . . . . .	51
3.1.1	Langmuir Probe Diagnostics . . . . .	52
3.1.2	The Ball Pen Probe Principle . . . . .	56
3.2	The BPP Collection Mechanism . . . . .	59
3.3	Design and Testing of the MAST BPP . . . . .	63
3.3.1	BPP Design for MAST . . . . .	63
3.3.2	Electronics . . . . .	65
3.3.3	Analysis of Noise . . . . .	66
3.3.4	Comparison of BPP pins . . . . .	69
3.4	Radial Profile Measurements . . . . .	70
3.4.1	Potential Profiles . . . . .	73
3.4.2	Electron Temperature Profiles . . . . .	74
3.4.3	Radial Electric Field . . . . .	84
3.5	Fluctuations in the Radial Shear Layer . . . . .	88
3.6	Improvements to the MAST BPP design . . . . .	96
3.7	Conclusions and Future Work . . . . .	97
<b>4</b>	<b>The BOUT++ Framework</b>	<b>101</b>
4.1	Time Integration . . . . .	103
4.1.1	Explicit and implicit time integration . . . . .	103
4.1.2	Time integration methods in BOUT++ . . . . .	105
4.2	Spatial Differentiation . . . . .	106
4.2.1	Finite Difference Methods in BOUT++ . . . . .	107
4.2.2	Differential operators in BOUT++ . . . . .	110
4.3	BOUT++ code layout . . . . .	113
4.4	Physics module for filament dynamics investigations . . . . .	113
4.4.1	System of Equations . . . . .	114
4.4.2	Boundary Conditions . . . . .	120
4.4.3	Initial Conditions . . . . .	121
4.4.4	Grid Generation . . . . .	121
4.4.4.1	Slab Grids . . . . .	121
4.4.4.2	SOL flux tube grids . . . . .	121
4.5	Summary . . . . .	133
<b>5</b>	<b>3D Filament Dynamics in a MAST SOL Flux Tube Geometry</b>	<b>135</b>
5.1	Introduction . . . . .	135
5.2	The role of parallel electron dynamics . . . . .	137
5.2.1	Symmetry Breaking . . . . .	141
5.3	The role of magnetic geometry . . . . .	143
5.4	The interchange regime . . . . .	151
5.4.1	Cross-field motion . . . . .	151

5.4.2	Parallel profile . . . . .	158
5.5	The Boltzmann Regime . . . . .	162
5.5.1	Cross-field motion . . . . .	163
5.5.2	Parallel profile . . . . .	167
5.6	The Role of Dissipation . . . . .	172
5.7	Discussion . . . . .	175
5.8	Summary . . . . .	178
<b>6</b>	<b>Scaling of the Midplane Filament Velocity in the MAST SOL geometry</b>	<b>181</b>
6.1	Introduction . . . . .	181
6.2	Scaling of the Characteristic velocity . . . . .	183
6.3	Filament velocity in ballooning coordinates . . . . .	186
6.4	Temperature Scan . . . . .	188
6.5	Filament width scan . . . . .	195
6.6	Discussion . . . . .	201
6.7	Summary . . . . .	205
<b>7</b>	<b>Conclusions and Future Work</b>	<b>207</b>
7.1	Conclusions . . . . .	207
7.2	Future Work . . . . .	210
	<b>Appendices</b>	<b>211</b>
<b>A</b>	<b>The BOUT++ Coordinate System</b>	<b>213</b>
A.1	Differential Geometry Primer . . . . .	213
A.2	Field Aligned Coordinates in BOUT++ . . . . .	216
<b>B</b>	<b>Derivation of equations for filament simulations</b>	<b>221</b>
<b>C</b>	<b>Derivation of curvature vector</b>	<b>227</b>
	<b>Bibliography</b>	<b>229</b>



# List of Figures

1.1	Exxon Mobil electricity demand . . . . .	2
1.2	Schematic illustration of the Coulomb barrier . . . . .	4
1.3	Fusion cross-sections of Deuterium and Tritium . . . . .	5
1.4	Schematic of the ICF principle . . . . .	7
1.5	Energy yield from a series of NIF shots showing a yield above the energy deposited into the fuel in 2014. . . . .	7
1.6	Schematic of a tokamak . . . . .	10
1.7	X-point generation . . . . .	13
1.8	Scrape-off layer schematic . . . . .	14
1.9	ITER design . . . . .	16
1.10	Spherical tokamak schematic . . . . .	17
1.11	The MAST vessel . . . . .	19
1.12	Larmor orbit schematic . . . . .	22
1.13	ExB drift schematic . . . . .	28
1.14	Diamagnetic drift schematic . . . . .	29
2.1	Universality of SOL fluctuation PDFs . . . . .	35
2.2	Conditionally averaged filament and hole . . . . .	36
2.3	Examples of 2D probe measurements . . . . .	37
2.4	Filament images from MAST . . . . .	38
2.5	Examples of 2D blob motion . . . . .	42
2.6	Effect of drift-waves on 3D blobs . . . . .	45
3.1	Schematic example of a Langmuir probe I-V characteristic . . . . .	55
3.2	BPP schematic . . . . .	57
3.3	CASTOR BPP measurements . . . . .	58
3.4	BPP collection schematic . . . . .	61
3.5	$\alpha$ from ion filtering model . . . . .	62
3.6	3D rendering of the MAST BPP . . . . .	64
3.7	Dimensions on the BPP head . . . . .	64
3.8	Langmuir and BPP probe tip redesign . . . . .	65
3.9	Structure of PF noise . . . . .	66
3.10	PF pick-up noise during plasma-probe interaction . . . . .	67
3.11	Effect of PF noise on fluctuation measurements . . . . .	67
3.12	Comparison of BPP, Isat and floating potential fluctuation spectra . . . . .	68
3.13	Comparison of fluctuation spectra between BPP pins . . . . .	70
3.14	RP on MAST . . . . .	71
3.15	RP waveforms for shots 28819, 28830 and 28834 . . . . .	72

3.16	Plasma current in shots 28819, 28830 and 28834	72
3.17	BPP potential vs major radius	73
3.18	BPP potential vs $R - R_{LCFS}$	74
3.19	BPP TS comparison of $T_e$	76
3.20	Secondary electron yield	78
3.21	Secondary electron yield as a function of energy and temperature	79
3.22	$\alpha_{LP}$ including secondary electron emission	80
3.23	BPP-TS comparison including secondary electron emission	80
3.24	Effect of enhancement to $\bar{\delta}(T_e)$	81
3.25	SOL $T_e$ from the BPP	81
3.26	Temperature decay lengths	82
3.27	Corrected plasma potential profiles	85
3.28	17 <sup>th</sup> degree polynomial fits to the BPP potential profile	86
3.29	Radial electric field profiles	86
3.30	Magnetic fields for velocity calculation	87
3.31	Toroidal and poloidal $\mathbf{E} \times \mathbf{B}$ velocity components	87
3.32	PDF schematic	88
3.33	$I_{sat}$ moments Vs time	91
3.34	Skewness Vs Kurtosis in shot 30250	91
3.35	$T_e$ comparison in shot 30250	92
3.36	Comparison of $I_{sat}$ skewness, potential	93
3.37	Comparison of radial electric field with $I_{sat}$ skewness	94
3.38	$I_{sat}$ Skewness vs $dE_R/dR$	94
3.39	PDFs of $I_{sat}$	95
4.1	Meshes schematic	107
4.2	Schematics of upwind differencing	109
4.3	Schematic of the layout of the BOUT++ code	114
4.4	Test of the drift ordering in MAST	117
4.5	Schematic example of the time-history of a filament	119
4.6	Visualisation of the $\psi_N = 1.15$ flux surface in the poloidal plane	123
4.7	Schematic of the curvature vector	125
4.8	$R, Z$ and $B_\zeta, B_\theta$ comparison with Hypnotoad	128
4.9	Comparison of curvature calculations in the flux-tube and in Hypnotoad	128
4.10	Effect of smoothing on curvature comparison	129
4.11	Perpendicular metric coefficients from flux-tube and Hypnotoad calculations	130
4.12	3D visualisation of typical computational domain	131
4.13	Grid spacing in flux-tube grid	132
4.14	Perpendicular resolution in MAST flux-tube	133
5.1	Schematic example of symmetry components	141
5.2	Schematic of flux-tube transformation	146
5.3	Transformation matrix components in MAST SOL fluxtube	146
5.4	Transformation of a flux-tube in the divertor	147
5.5	Transformation of filament widths	148
5.6	Curvature in the perpendicular plane	149
5.7	Filament velocity along magnetic field line	150

5.8	Filament evolution at the midplane in the interchange regime . . . . .	152
5.9	Resistive drift-waves on the filament front . . . . .	153
5.10	Dipole formation away from the midplane . . . . .	153
5.11	Potential, vorticity and current at the midplane in the interchange regime	154
5.12	Even and odd components of potential in the interchange regime . . . . .	155
5.13	Growth of the even and odd components of potential . . . . .	156
5.14	Filament evolution in the divertor region . . . . .	157
5.15	Spatial morphology in the divertor . . . . .	157
5.16	Evolution of filament peak density . . . . .	158
5.17	Parallel profile of a filament in the interchange regime . . . . .	159
5.18	Comparison of ballooning mechanisms . . . . .	160
5.19	Density and potential correlation at $66\mu s$ . . . . .	161
5.20	Evolution of filament correlation in the interchange regime . . . . .	162
5.21	Evolution of midplane cross-section in the Boltzmann regime . . . . .	163
5.22	Evolution of the filament cross-section during the transition into drift- wave turbulence . . . . .	164
5.23	Filament evolution with the Boltzmann source removed . . . . .	165
5.24	Spatial morphology of potential, vorticity and $J_{\parallel}$ in the Boltzmann regime	166
5.25	$\nabla_{\parallel} \ln(n)$ and $\nabla_{\parallel} \phi$ during the pole rotation phase . . . . .	167
5.26	Odd and even components of potential in the Boltzmann regime . . . . .	168
5.27	Growth of the even and odd components of potential in the Boltzmann regime . . . . .	169
5.28	Parallel profile in the Boltzmann regime . . . . .	169
5.29	Parallel profiles with Boltzmann source removed . . . . .	170
5.30	Filament parallel correlation in the Boltzmann regime . . . . .	170
5.31	Correlation between midplane and divertor in the Boltzmann regime . . .	171
5.32	Midplane filament cross-sections over $Ra$ scan . . . . .	174
5.33	Divertor filament cross-sections over $Ra$ scan . . . . .	175
6.1	Normal and bi-normal filament velocity at the midplane . . . . .	188
6.2	Averaged normal and bi-normal velocities at the midplane over $T_e$ scan .	189
6.3	Peak filament velocity over temperature scan . . . . .	190
6.4	RB / $C_I$ scaling of peak filament velocity . . . . .	191
6.5	Centre of mass displacement over temperature scan . . . . .	191
6.6	Instantaneous particle flux profiles over $T_e$ scan . . . . .	193
6.7	Integrated particle flux profile across the temperature scan . . . . .	194
6.8	Integrated particle flux with and without Boltzmann source . . . . .	194
6.9	Midplane filament cross-sections over $\delta_{\perp}$ scan . . . . .	196
6.10	Symmetry components over $\delta_{\perp}$ scan . . . . .	197
6.11	Velocity evolution over $\delta_{\perp}$ scan . . . . .	197
6.12	Filament displacement over $\delta_{\perp}$ scan . . . . .	198
6.13	Scaling of normal displacement with $\delta_{\perp}$ . . . . .	199
6.14	Instantaneous particle flux evolution over $\delta_{\perp}$ scan . . . . .	200
6.15	Integrated particle flux over $\delta_{\perp}$ scan . . . . .	200
6.16	$\Lambda, \Omega$ trajectories of $T_e$ and $\delta_{\perp}$ scan . . . . .	202
6.17	Corrected $\Omega, \Lambda$ trajectories . . . . .	204

A.1	Illustration of curvilinear coordinates . . . . .	214
A.2	Schematic of BOUT++ coordinates . . . . .	219

# List of Tables

1.1	ITER parameters . . . . .	16
1.2	MAST parameters . . . . .	18
2.1	Table of cross-machine filament parameters . . . . .	39
3.1	Table of BPP pin parameters . . . . .	63
3.2	BPP shot parameters . . . . .	71
4.1	Table of coordinate independent differential operators in BOUT++. . . . .	111
4.2	Differential operators implemented in BOUT++ which depend on the equilibrium magnetic field. . . . .	112
4.3	Characteristic parameters in a MAST L-mode plasma . . . . .	115
4.4	Table of parameters used to set up slab grid simulations . . . . .	122
4.5	Output parameters from the SOL flux tube grid generator . . . . .	124
5.1	Normalizations . . . . .	138
5.2	Parameters for <i>Ra</i> scan . . . . .	173



# Acknowledgements

There are a great many people who deserve my thanks for their generous help and support during the course of my PhD. In particular I extend my sincerest gratitude to my supervisors, Dr Geoff Fishpool and Dr Ben Dudson, who have been patient and supportive during the many trials and tribulations that I have presented them with over the last three years. I would also like to thank Dr Ian Chapman who gave me my first experience in research, and the many collaborators who have worked alongside me in the last few years.

As a PhD student in the Fusion Doctoral Training Network I have been able to benefit from the excellent training and support made available to me by the FTDN and the University of York for which I am grateful. I also thank CCFE for providing me with the facilities to carry out my research and for making me feel so welcome during my PhD. I thank also the EPSRC for funding this PhD.

The CCFE student community have been an endless supply of assistance, laughs and welcome distractions during my time there. Developing a good group of friends makes so much more of a PhD than simply scientific research and, among the many brilliant people at CCFE, I would like to thank Stuart Henderson, Matt Leyland, Sarah Elmore and Richard Lake for making my PhD such an enjoyable time. You have managed to provide the perfect blend of procrastination and encouragement; an outlet for frustrations and a willingness to laugh at my (usually awful) jokes. Work of any variety is always more enjoyable when you can share it with people you care about.

I have always received unwavering support from my mother Val, father Dave and brother Tim. They have acted (not always entirely willingly) as sounding boards and advice givers and they have my deepest thanks for helping me to reach the end and keeping me on track when I needed it.

These last three years have contained many ups and downs and throughout it all my wonderful, amazing wife Tanith has been by my side. It is no understatement to say that I couldn't have done it without her. Not only did she experience first-hand the 'Mr Hyde'-like transformation that has occurred in me during the write-up of this thesis, but she actually decided to marry me! Tan, you have my eternal thanks and now that I've reached the end I promise to stress less, shave more and take care of you as well as you have taken care of me.



*This thesis is dedicated to the memory of Dr Colin Williams, a loving father and husband whose passion for knowledge and education will forever be an inspiration.*



# Declaration of Authorship

I, N. R. WALKDEN, declare that this thesis titled, 'Properties of Intermittent Transport in the Mega Ampère Spherical Tokamak' and the work presented in it are my own. I confirm that:

- This work was done wholly while in candidature for a research degree at this University.
- Where any part of this thesis has previously been submitted for a degree or any other qualification at this University or any other institution, this has been clearly stated.
- Where I have consulted the published work of others, this is always clearly attributed.
- Where I have quoted from the work of others, the source is always given. With the exception of such quotations, this thesis is entirely my own work.
- I have acknowledged all main sources of help.
- Where the thesis is based on work done by myself jointly with others, I have made clear exactly what was done by others and what I have contributed myself.

Parts of chapter 3 have been submitted for publication in *Review of Scientific Instruments*.

Parts of chapter 5 are based on work published in Walkden *et.al* [1].



# Chapter 1

## Introduction

### 1.1 Energy demand

Global energy demand is evolving at a quickening rate. At present OECD (**O**rganization for **E**conomic **C**o-operation and **D**evelopment) countries are responsible for 41% of global energy consumption [2]. By 2040 total global energy demand is projected to grow by up to 30% [3] however the energy demand of OECD countries will remain relatively constant, despite their continued economic growth. The large growth in energy demand will be primarily due to rising populations and economic development in Asia and Africa. China in particular will contribute > 30% of this growth in energy demand whilst energy usage in India, Indonesia, Brazil and the Middle East will grow even faster than that of China [4]. The rise in electricity demand is even more drastic. Figure 1.1, taken from [3], shows a projected 80% increase in electricity demand by the year 2040. Fossil fuels will provide the primary fuel source for electricity production particularly through coal and gas, with oil taking a secondary position as reserves begin to dwindle and expense increases. Fossil fuel reserves are limited and in the long term this presents the problem of excessively high cost for electricity production driven by excessively low fuel supplies. A more immediate problem is the impact of fossil fuels on the environment via greenhouse gas emission; the increasing global dependence on fossil fuels is in striking contrast to the global goal of reduced CO<sub>2</sub> emissions. Consequently electricity production via fossil fuels must be replaced with sustainable, safe and environmentally responsible options. This problem can only be addressed through a portfolio of options including renewables (solar, wind and hydro power), nuclear fission and carbon capture and sequestration (the process of capture and long-term storage of CO<sub>2</sub> from the atmosphere). Renewable sources for electricity production suffer from high levels of inefficiency which limit their impact on the global scale. Nuclear fission has the potential to play a key role in electricity

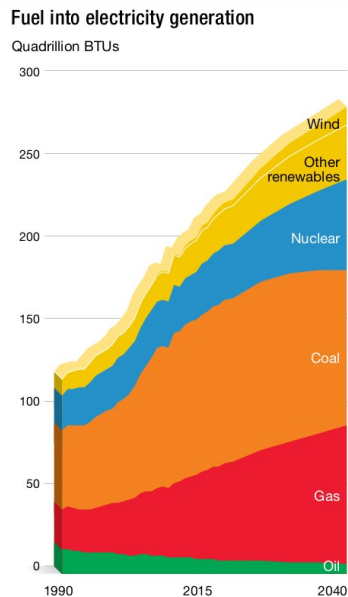


FIGURE 1.1: Exxon Mobil projection of electricity demand categorized by the consumption of various fuels for electricity production in BTUs (Billion Tons of Oil), taken from [3]

production yet it remains a politically undesirable option due to the inherent risks which have been evidenced by a number of large scale disasters in the past few decades. With fast-breeder technology yet to reach maturity the fuel reserves for nuclear fission are not vastly more abundant than fossil fuels themselves [5], yet the development of breeder technology will greatly aid in the proliferation of nuclear material, making fission an even less desirable energy source. Nuclear fusion offers the prospect of a safe, environmentally friendly energy source with practically limitless fuel resources. The waste product from the nuclear fusion process is Helium which is not harmful to the environment. Given that future energy policy is being driven by the need for reductions in  $\text{CO}_2$  this makes fusion a desirable source of energy. The fuel for nuclear fusion consists of two isotopes of Hydrogen, Deuterium and Tritium. Approximately 1 in every 6400 Hydrogen atoms in naturally occurring water is actually Deuterium, which can be readily extracted and stored. Tritium, on the other hand, is not a naturally occurring isotope. With a half-life of approximately 12 years Tritium is difficult to create and store. Instead nuclear fusion reactors will breed Tritium through nuclear reactions with Lithium. Once again Lithium can be harnessed from naturally occurring sea water making it a practically limitless fuel. The main chemical reaction occurring during the combustion of fossil fuels is the oxidization of hydrocarbons where the bonds between hydrogen and carbon atoms in a hydrocarbon are broken and the atoms rebond with oxygen to form water and carbon dioxide. These reactions are exothermic (the bonds formed with oxygen atoms require less energy than the hydro-carbon bonds, thus the reaction produces excess energy).

Taking methane in natural gas as an example the chemical reaction is



The approximate energy content in the constituents of the reaction are [6] 1640kJ/mole +988kJ/mole  $\rightarrow$  1598kJ/mole +1840kJ/mole which gives a total energy released in the reaction of 810kJ/mole or 50.6kJ/g. By contrast the energy output in the neutron from a single D-T fusion reaction is [7] 14.1MeV or  $2.26 \times 10^{-12}$ J. Thus if the entirety of 1g of D-T fuel can be forced to fuse the energy output would be  $\approx 2.7 \times 10^8$ kJ/g. Consequently for the energy produced in fusing 1g of D-T fuel, approximately 5 tonnes of natural gas must be burnt. This monumental potential drives interest in nuclear fusion and underpins the global investment in its research.

## 1.2 Nuclear Fusion

Nuclear fusion is the process by which two light nuclei combine to form a heavier nucleus and by-products. The deficit in rest-mass energy between the reactants and the products is converted into kinetic energy in the products which can be harnessed to produce usable energy output. Fusion occurs when the reactants can become sufficiently close that the mutual Coulombic repulsion between them is overcome by the attractive strong nuclear force. Quantum tunnelling of the nuclei through the Coulomb barrier can facilitate a small percentage of reactions occurring with separations greater than required to overcome the Coulomb barrier. This is illustrated in figure 1.2. Given the huge energy yield available from nuclear fusion, this small percentage is enough to allow for significant energy gain under controlled conditions.

The reaction rate of the fusion reaction can be calculated from the distribution functions of the reactant species by [7]

$$\mathcal{R} = \int \int \sigma(v') v' f_1(v_1) f_2(v_2) d^3v_1 d^3v_2 \quad (1.2)$$

where  $v' = v_1 - v_2$  and  $\sigma$  is the reaction cross-section. The cross-section parametrizes the likelihood of a reaction to occur by an effective area over which the reaction occurs. The larger the cross-section, the more likely the reaction to occur. Physically this describes the number of reactants with a high enough velocity to overcome the Coulomb barrier per unit time per unit volume. For Maxwellian distributions the reaction rate is often written in a simpler form given by

$$\mathcal{R} = n_1 n_2 \langle \sigma v \rangle \quad (1.3)$$

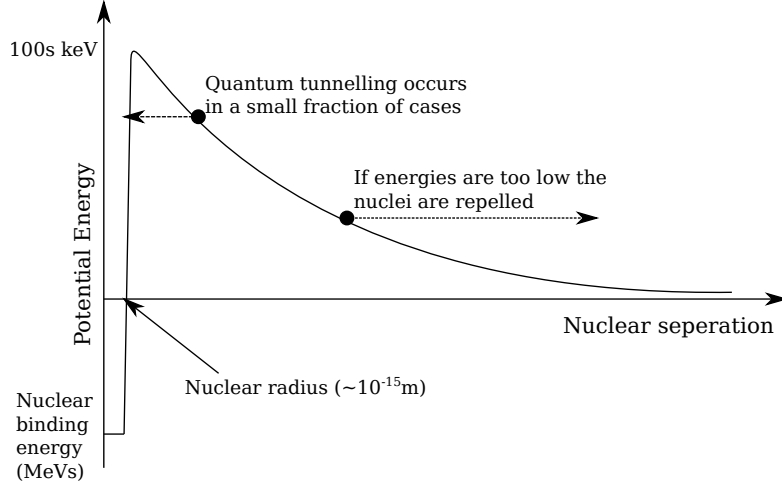


FIGURE 1.2: Schematic illustration of the Coulomb barrier. Only nuclear with kinetic energies surpassing the Coulomb barrier are subject to fusion. A small fraction of nuclei can fuse with energies smaller than the barrier with the assistance of quantum tunnelling. All other nuclei are repelled.

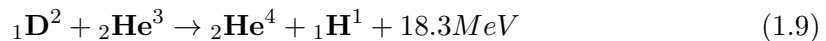
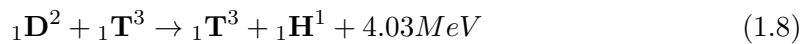
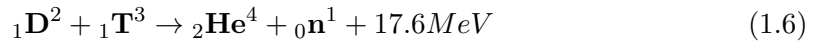
where  $n_{1,2}$  is the number density of reactant nuclei of species 1 and 2.  $\langle\sigma v\rangle$  is given by

$$\langle\sigma v\rangle = 4\pi \left(\frac{\mu}{2\pi T}\right)^{\frac{3}{2}} \int \sigma(v') v'^3 \exp\left(-\frac{\mu v'^2}{2T}\right) d^3v' \quad (1.4)$$

where  $\mu = m_1 m_2 / (m_1 + m_2)$  is the reduced mass of the two nuclei and  $T$  is the temperature of the nuclei (assuming they are strongly thermally coupled). For reactions that occur at energies below the Coulomb barrier the quantum tunnelling effect is the only means by which fusion can occur and the reaction cross-section is proportional to the tunnelling probability[8];

$$\sigma \sim \exp\left(-\frac{2\pi Z_1 Z_2 e^2}{\hbar v'}\right) \quad (1.5)$$

More generally the fusion cross-sections are calculated by parametrizations of existing experimental data. Figure 1.3, taken from [7], shows  $\langle\sigma v\rangle$  for the most promising fusion reactions. The fusion reactions with the highest probability of occurrence at sustainable temperatures are the D-T, D-D and D-He<sup>3</sup> reactions shown below:



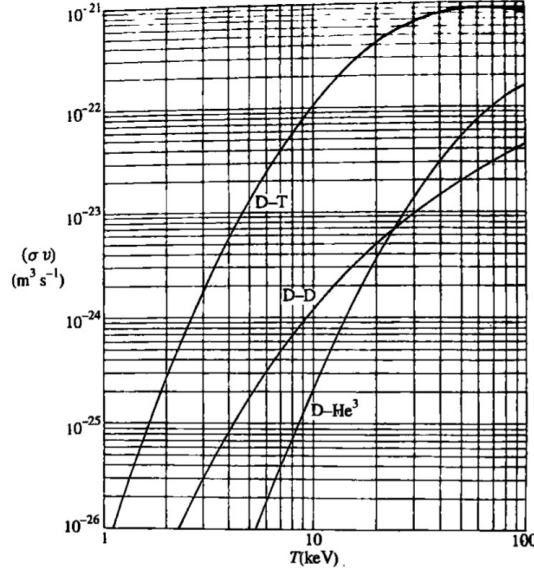


FIGURE 1.3: Fusion cross-sections taken from [7] showing that the reaction of Deuterium and Tritium is the most promising for significant amounts of fusion.

where D represents a Deuterium nucleus, T represents a Tritium nucleus and  $\text{He}^{3,4}$  are isotopes of the Helium nucleus. n represents a lone neutron and H represents a Hydrogen nucleus (i.e. a lone proton). It is clear from figure 1.3 that the D-T reaction is orders of magnitude more likely to occur at attainable energies. Interestingly the cross-section for H-H fusion, which is responsible for the nucleation of the stellar fusion cycle, is approximately  $10^{26}$  times smaller than D-T fusion. The energy that arises from the fusion reaction is calculated from the deficit in mass across the reaction. For D-T fusion this is given by

$$\begin{aligned}
 \Delta m &= m_D + m_T - m_{\text{He}} - m_n & (1.10) \\
 &= (2 - 0.000994) m_p + (3 - 0.006284) m_p - (4 - 0.0027404) m_p - (1 + 0.001378) m_p \\
 &= 0.01875 m_p
 \end{aligned}$$

where  $m_p = 1.6726 \times 10^{-27} \text{kg}$  is the proton mass. From mass-energy equivalence this mass deficit results in an energy gain of

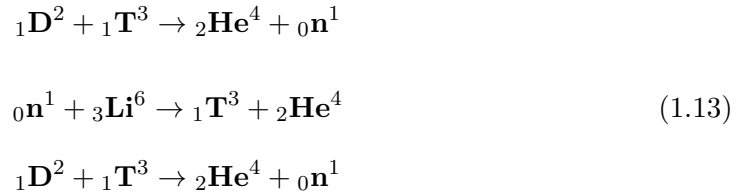
$$\Delta E = \Delta m c^2 = 2.819 \times 10^{-12} \text{J} = 17.6 \text{MeV} \quad (1.11)$$

To ensure that both energy and momentum are conserved through the reaction the neutron carries approximately 4/5 of the energy as kinetic energy, at 14.1MeV, whilst the alpha particle carries away 3.5MeV. The energy in the neutron is the practically usable energy. In fusion reactors this neutron will heat a water blanket surrounding the fuel which will then drive a steam turbine to generate electricity.

To maintain the fusion process Tritium will be bred from Lithium. One prominent reaction allowing for Tritium breeding is



which leads to a cyclic fusion reaction



and so on. A balance must then be struck between the use of neutrons for Tritium breeding and the harvesting of energy from neutrons.

In the sun intense gravitational pressure at its core provides the conditions required to achieve fusion. Controlling this process on earth requires the confinement of the fuel. With temperatures exceeding 100 million K required for fusion to occur, clearly this confinement cannot be attained simply by placing the fuel inside a material container. As such other methods of confinement are required. There is a variety of methods for controlled nuclear fusion. The two most prominent and promising methods are *inertial confinement fusion* (ICF) and *magnetic confinement fusion* (MCF). In ICF a small capsule of fuel is compressed on *ns* time-scales to extreme temperatures and densities [9, 10]. To achieve the compression the fuel is irradiated by very high energy lasers or X-rays. The radiation causes an ablation surface on the exterior of the capsule to expand explosively outwards. Conservation of momentum then causes the interior fuel of the capsule to implode, behaving like a spherical, ablation driven rocket. This process is highlighted in figure 1.4. A fuel capsule consists of a high density ablation surface surrounding a low density fuel, usually composed of a frozen D-T mix. Both the capsule and the radiation deposition must be extremely symmetric to minimize the impact of fluid instabilities and ensure a uniform heating of the central fuel. ICF is a promising approach to fusion which is evidenced by the development of the National Ignition Facility (NIF)[11]. The NIF, housed at Lawrence Livermore National Laboratory, is a 1.8 MJ laser facility which focusses 192 laser beams onto a gold cylindrical container housing the fuel capsule. The irradiated gold then bathes the fuel in high energy X-rays which provide the drive for ablation. This approach is known as indirect drive [9, 10]. The goal of any fusion method is to achieve ignition; a state where the heating of the fuel is self-sustained by energetic  $\alpha$  particles born out of the fusion reaction itself. In early 2014 the NIF took an important step towards ignition by demonstrating energy yield above the level of energy deposited into the fuel [12]. This is shown in figure 1.5 taken

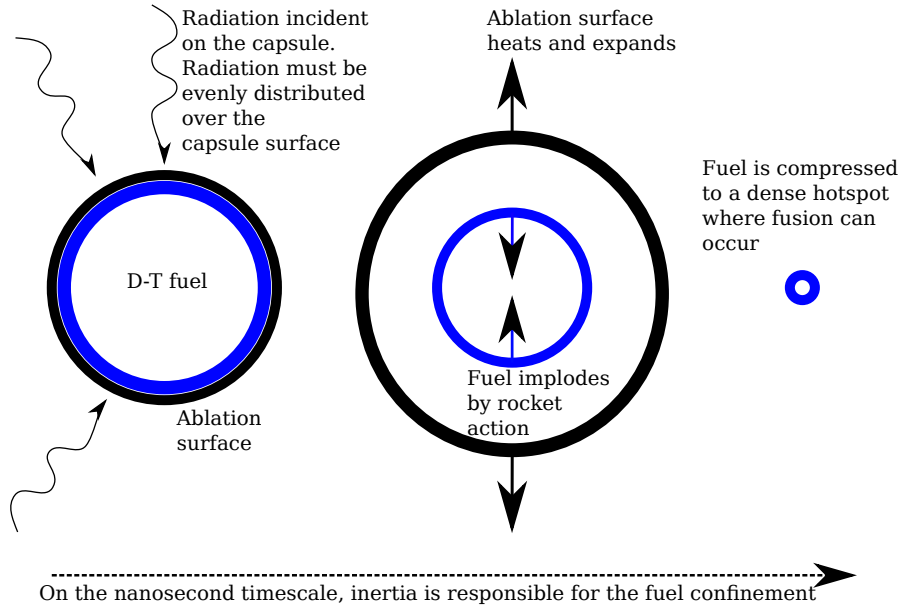


FIGURE 1.4: Schematic of the ICF principle. Inertia confines the fuel whilst radiation causes an implosion of the fuel by rocket action. A dense hotspot of fuel forms where nuclear fusion can occur.

from [12]. This result demonstrates the occurrence of self-heating in the fuel capsule,

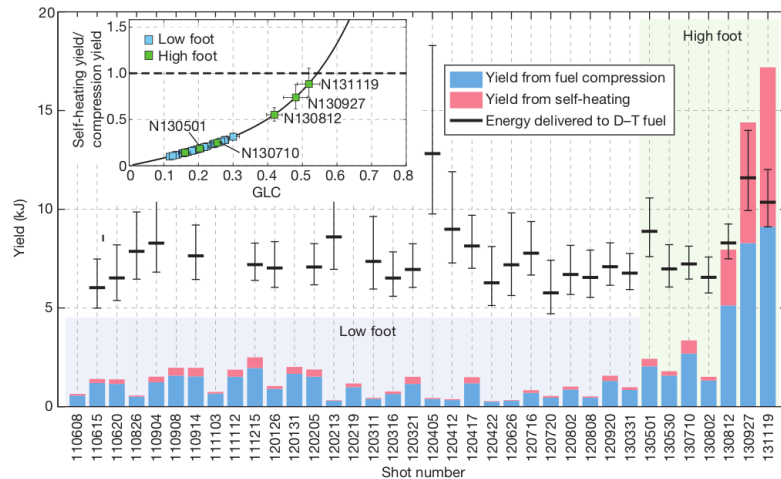


FIGURE 1.5: Energy yield from a series of NIF shots showing a yield above the energy deposited into the fuel in 2014.

however it does not represent energy gain. The energy gain shown is in reference to the energy deposited into the central hotspot of the fuel and does not account for the

energy contained in the ablator,  $\sim 150\text{kJ}$ , or the energy deposited from the laser to the capsule initially,  $\sim 1.8\text{MJ}$ . To achieve net energy gain the NIF needs to achieve at least two orders of magnitude increase in its energy yield. Furthermore the complexity of operating a machine such as the NIF makes any sort of reactor concept based on ICF difficult. Each fuel capsule must be fabricated by hand, however in a reactor individual capsules need to be provided to the machine every second. Therefore, whilst the ICF concept has demonstrated promising features, it is worth pursuing other avenues of fusion in parallel.

The MCF principle exploits the charged nature of the fusion fuel under extreme temperature and pressure. In these conditions electrons are liberated from their atoms and the fuel consists of freely moving electrons and ions. This state of matter is called a *plasma* and will be described later in this chapter. In a magnetic field charged particles are subject to a Lorentz force;

$$\mathbf{F} = Ze \left( \mathbf{E} + \frac{1}{c} \mathbf{v} \times \mathbf{B} \right) \quad (1.14)$$

In the absence of electric fields, projecting equation 1.14 onto  $\mathbf{B}$  shows that charged particles may move freely along magnetic field lines but are restricted in the plane perpendicular to the magnetic field. This means that, through careful design of the magnetic field, the plasma can be confined in a vacuum permeated by magnetic fields. The structure of the confining magnetic field is constrained on a fundamental level by two well known theorems: The 'hairy ball' theorem by Brouwer [13], and the Virial theorem [14] first proposed by Clausius in 1870. The hairy ball theorem states that any tangent vector on a sphere must contain at least one null point. This is often paraphrased with the problem of combing a 'hairy ball'. It is impossible to comb the hair such that every strand lies flat to the surface and a cow-lick will always appear. The hair is analogous to a tangent vector field on the surface of the ball. Plasma confined in a magnetic sphere can escape through the magnetic null created at the cow-lick. The problem does not arise for toroidal configurations (it is easy to comb the hair of a 'hairy donut') which can therefore confine a plasma indefinitely in the absence of internal processes transporting the plasma across the magnetic field. The Virial theorem provides a calculation for average kinetic energy of a system governed by potential forces. In the case of an electromagnetic thermodynamic system, such as a plasma in a magnetic field, it shows that in the case with no bounding walls of pressure (either thermodynamic or magnetic) the system will expand indefinitely and fail to reach equilibrium. Consequently the confinement of a plasma requires externally applied pressure, through the application of external magnetic fields.

There are many magnetic confinement approaches which satisfy the hairy ball and Virial theorems. The most notable of these are the reversed field pinch [15], the spheromak

[16], the stellerator [17] and the tokamak[7]. In each case a toroidal configuration provides closed magnetic field lines with no magnetic null points. Of these approaches the tokamak is the most mature and widely studied.

### 1.3 The Tokamak

The tokamak (from the Russian “**T**Oroidal’naya **K**Amera v **M**Agnitnykh **K**atushkakh” meaning “Toroidal chamber in magnetic coils”) was originally conceived by Igor Tamm and Andrei Sakharov in the early 1950s with the first tokamak, T-1, built at the Kurchatov institute in Moscow and starting operation in 1958<sup>1</sup>. That year also marked the first open conference on fusion (The 2nd International Conference on the Peaceful use of Atomic Energy, often referred to as the ‘Atoms for Energy’ conference, Geneva, 1958) and is often regarded as the birth year of the tokamak. 10 years later, in 1968 at the IAEA conference in Novosibirsk, results from the T-3 tokamak, an upscaled version of T-1, from the Kurchatov institute showed internal temperatures far outperforming anything achieved in the rest of the world. This prompted a team from the UK, led by Dr Nick Peacock, to travel to the Kurchatov institute in Russia to independently verify these claims. This was the first international collaboration in fusion research and confirmed the tokamak as the leading candidate towards achieving temperatures suitable for magnetically confined fusion. Since the early days of tokamak research a number of machines have been built in a number of different countries. The next stage in tokamak research, ITER, is currently under construction in Cadarache, France, and is hoped to provide the stepping stone needed to bring the tokamak to reactor scale.

The principle components of the tokamak are an externally applied toroidal magnetic field, produced through coils wrapped around a toroidal vacuum chamber, and an inductively driven poloidal magnetic field. To produce the poloidal magnetic field a solenoid is placed at the centre of the torus. By ramping the current in the solenoid a time-varying magnetic flux is produced. This cuts through the plasma and induces a toroidal current in the plasma. This current then produces a poloidal magnetic field encircling it. When the externally applied toroidal magnetic field and the induced poloidal magnetic field are superposed a helical magnetic field is produced. This process is illustrated in figure 1.6. If the plasma is solely confined by the toroidal field and the induced poloidal field it is vertically unstable; any small vertical push to the plasma will result in its vertical acceleration, eventually leading to the plasma hitting the floor or ceiling of the vacuum vessel. To prevent this extra poloidal field components are produced by the poloidal field coils shown in figure 1.6. The induced current in the plasma has a secondary function as a source of heating. The finite resistivity of the plasma results in Ohmic heating as

---

<sup>1</sup><https://www.efda.org/newsletter/50-years-of-tokamaks>

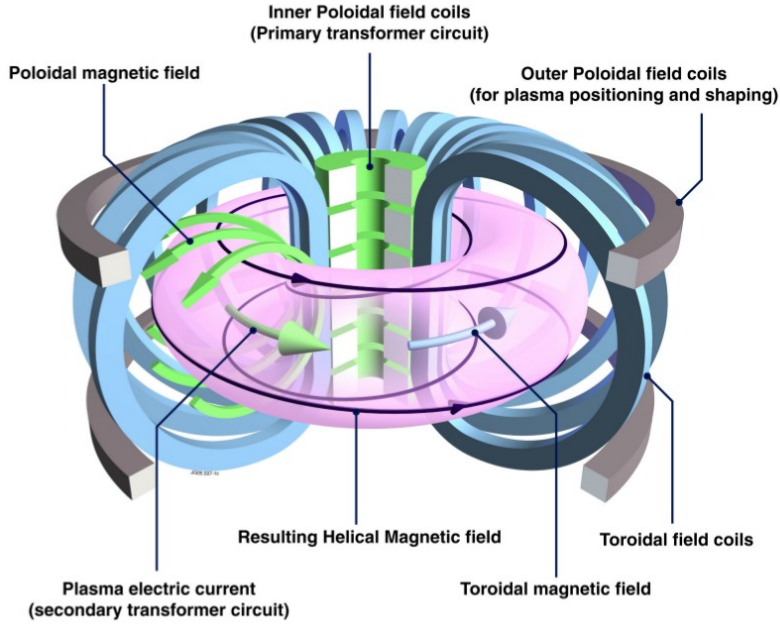


FIGURE 1.6: Schematic diagram of a tokamak showing the formation of the helical magnetic field from an externally applied toroidal field and an inductively produced poloidal magnetic field. Image courtesy of the JET image database.

the current is driven. As the plasma heats collisions among the plasma constituents become rarer and its resistivity drops, limiting the effect of Ohmic heating. To further heat the plasma other methods are required such as neutral beam heating, where high energy neutral particles exchange energy with the plasma through collisions [18, 19], and I/ECRH where the plasma is heated through a resonant interaction with an externally driven electromagnetic wave fired into the plasma [20, 21]. The requirement of current induction presents a further limit for future reactor scale tokamaks. A reactor will have to run in steady state to make electricity economically. The inductive current drive requires a ramped current in the central solenoid. The current ramping can only continue to the limits of the power supplies used to perform the ramp and consequently cannot be operated as a steady state [22].

The goal of the tokamak is to reach a state of 'ignition' where the fusion reactions are sustained solely by heating provided by fusion born  $\alpha$  particles. The criteria for reaching ignition conditions in a tokamak is often quantified by the fusion triple product [7],  $nT\tau_E$ , where  $n$  is the characteristic plasma density,  $T$  is the characteristic plasma temperature and  $\tau_E$  is the energy confinement time (the characteristic time taken for energy from the plasma core to leave the plasma). In a tokamak reactor the power loss from the plasma must be compensated by either external heating or heating by  $\alpha$  particles;

$$P_L = P_H + P_\alpha \quad (1.15)$$

Power is continuously lost by the plasma at a rate of  $P_L = W/\tau_E$  where  $W$  is the total internal energy of the plasma. The total internal energy of a plasma with three degrees of freedom and equal densities of ions and electrons is

$$W = \int 3nTdV = 3nTV \quad (1.16)$$

where  $nT$  represents volume averaged quantities now. The heating power due to  $\alpha$  particle heating is given by the fusion rate, equation 1.3, times the energy in each  $\alpha$  particle,  $E_\alpha = 3.5\text{MeV}$ . Taking  $n_D = n_T = n/2$  gives

$$P_\alpha = \int \frac{1}{4}n^2\langle\sigma v\rangle E_\alpha dV = \frac{1}{4}n^2\langle\sigma v\rangle E_\alpha V \quad (1.17)$$

At ignition the plasma will be self-sustained by  $\alpha$  heating meaning that external heating power,  $P_H = 0$ . Furthermore at temperatures of significance for fusion, i.e. the range  $10 - 20\text{keV}$ ,  $\langle\sigma v\rangle$  can be parametrized approximately as [7]

$$\langle\sigma v\rangle \approx 1.1 \times 10^{-24}T^2(m^3s^{-1}) \quad (1.18)$$

Now evaluating equation 1.15 gives a condition on the fusion triple product required for ignition in a tokamak of

$$nT\tau_E \geq 5 \times 10^{21}(keVsm^{-3}) \quad (1.19)$$

The most direct route to achieving ignition is to increase the confinement time of energy in the tokamak,  $\tau_E$ . The transport of heat and particles out of the plasma is set by internal physics and is hard to affect directly. By increasing the volume of the plasma the distance of travel required for energy to reach the plasma edge increases thereby increasing the confinement time of energy. This is the approach taken in the tokamak community and is reflected in the increase in plasma major radius over time from the first diverted tokamak, ASDEX [23], with  $R = 1.62m$ , through the JET tokamak with  $R = 3m$  [7] to the future tokamak ITER [24] with  $R = 6.2m$ . On ITER  $\alpha$  particle heating will provide a consistently strong heating source for the first time in a tokamak. Particles in a tokamak are confined on the helical magnetic field lines produced in the vacuum vessel. The magnetic field lines wind around the torus and form closed surfaces. On these closed surfaces the flux of the poloidal magnetic field is constant, giving the surfaces the name of 'flux surfaces'. The surfaces form concentric toroids which encircle the central solenoid. The helicity of the magnetic field on a given surface is characterised by the safety factor,  $q = n/m$  where  $m$  is the number of times a magnetic field line wraps around the poloidal direction whilst  $n$  is the number of times it wraps around the toroidal direction. Perfect confinement would be achieved if the plasma remained on these surfaces, unfortunately in reality this is not the case. Collisions, turbulence

and particle drifts all act to move plasma from surface to surface. If this is uncontrolled then the plasma will eventually hit the vessel walls potentially damaging important components of the tokamak. To prevent this unwanted interaction the plasma-material interface must be controlled

### 1.3.1 Diverted tokamaks

The control of the interface between the plasma and material surfaces in early tokamaks was through the use of a 'limiter'. A limiter is simply a piece of material protruding from the wall of the machine designed specifically for the plasma to interact with. When large fluxes of plasma are incident on material surfaces a significant number of the surface atoms can become liberated from the surface and enter the plasma as impurities [25]. Electronic transitions in partially ionized impurities radiate energy as electromagnetic waves which then act to cool and degrade the plasma. This is an unfavourable situation and as a result an alternative to the limiter, the divertor was developed. The notable feature of a divertor tokamak is a null point in the poloidal magnetic field, which forms an 'X' in the poloidal plane. This X-point is induced by running a current parallel to the plasma current below the plasma itself. The superposition of the two poloidal fields includes a null point between the two currents. This is shown schematically in figure 1.7. By placing a material surface intersecting the poloidal magnetic field lines below the X-point the material interface with the plasma can be moved away from the core plasma. The benefit of this approach was immediately apparent to the tokamak community. The first tokamak to adopt the divertor was the ASDEX tokamak [23] which demonstrated that a regime of enhanced energy confinement can be accessed with a large amount of plasma heating [26]. This is called H-mode and is characterised as a state of reduced transport allowing access to higher core pressures. This is contrasted by L-mode, where radial transport is large and plasma pressures are reduced. Importantly H-mode was only detected in diverted plasmas, and never in limited plasmas.

With a well defined plasma-material interface, either through the use of a limiter or a divertor, the plasma is split into two regions depending on whether magnetic field lines close in on themselves, or intersect the material surface. The closed region is the tokamak core. The open region is called the scrape-off layer (SOL) because it is the region where particles and energy from the plasma are 'scraped off' onto the divertor or limiter target. These two regions are separated by a single magnetic surface called the separatrix. The separatrix is the surface that contains the X-point and is the only magnetic surface that contains a magnetic null point.



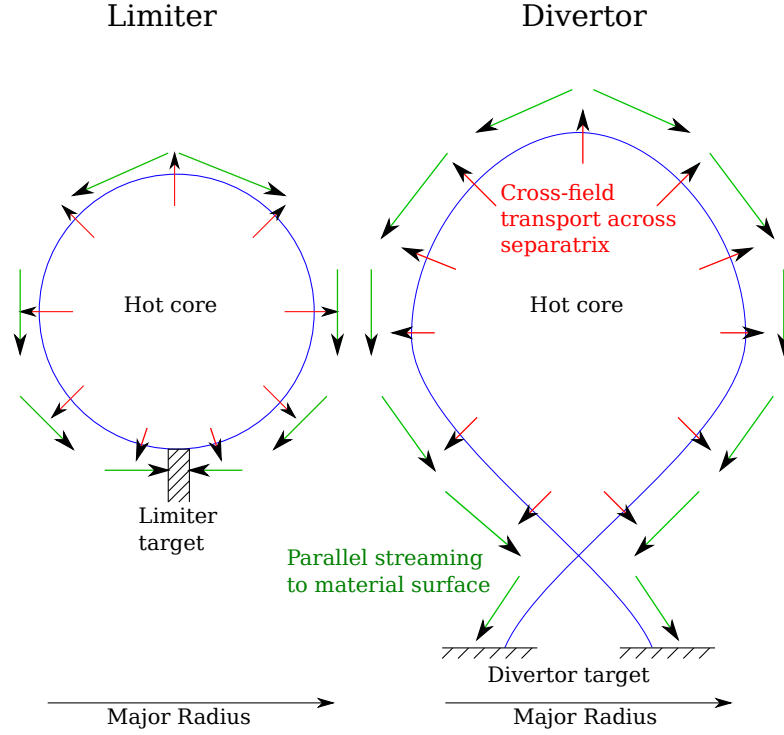


FIGURE 1.8: Schematic diagram of SOL formation. Cross-field processes transport heat and particles from the core plasma onto open magnetic field lines, where parallel streaming motion efficiently transports them to material surfaces.

field line is taken as the sound speed,  $c_s$ . The radial coordinate  $r$  has its origin at the separatrix. This equation is solved by a density profile of the form

$$n(r) = n_S \exp\left(-\frac{r}{\lambda_{SOL}}\right) \quad (1.21)$$

where  $n_S$  is the density at the separatrix and the SOL width is given by

$$\lambda_{SOL} = \sqrt{\frac{D_{\perp} L_{\parallel}}{c_s}} \quad (1.22)$$

Taking typical SOL parameters of  $D_{\perp} \sim 1\text{m}^2\text{s}^{-1}$ ,  $c_s \sim 50\text{kms}^{-1}$  and  $L_{\parallel} \sim 50\text{m}$  gives a typical SOL width of  $\lambda_{SOL} \sim 3\text{cm}$ . Compared to the radius of the core plasma, typically on the order of 1m, the SOL is a very thin region. This is fortuitous as it allows walls to be very close to the plasma without contacting it. Given that cost of magnetic real-estate inside the vacuum vessel, primarily associated with the cost of building the toroidal magnetic field coils, will be on the order of millions to billions of dollars per  $\text{m}^3$  in reactor scale tokamaks a close fitting wall is highly desirable. The thinness of the SOL also presents a major issue however. All power lost from the core plasma is transported into the SOL and to material surfaces in a thin radial band. The consequential power

flux density to the material surface is extremely high. Predictions for ITER H-mode plasmas, based on experimental scalings from current tokamaks, suggest that the SOL width has no dependence on machine size [27]. If this proves to be the case then the enormous heating power expected in ITER will be deposited in a very thin SOL. Material surfaces will be unable to handle such high heat fluxes and this is an open issue for the operation of ITER and future devices.

In reality cross-field transport across the separatrix is rarely diffusive and usually dominated by anomalous transport associated with turbulence. A review of these processes will be given in chapter 2. Furthermore interactions with the material surface can play a significant role in the SOL behaviour. When plasma is incident on the divertor target ions can become weakly bound to the surface. As other ions bombard the surface the weakly bound ions can once again become dissociated, entering the plasma as a neutral particle and subsequently re-ionizing [25]. The steady state that results from this process is called recycling. If the mean-free-path of neutral-plasma collision is long then the recycled neutrals are re-ionized in the plasma core and the SOL is unaffected, however if the collisional mean free path is short re-ionization can occur within the SOL, affecting the density distribution of the SOL itself. If the SOL is sufficiently cold then ions and electrons in the plasma can recombine without the need for material surface interaction. Such recombination can produce a 'detached' divertor where a region of partially ionized plasma directly precedes the target surface [28]. Detachment can be a favourable situation since fluxes to targets are strongly reduced [29], yet it significantly complicates the physics of the SOL.

The SOL represents the boundary between the core plasma and the outside world. Furthermore it determines the exhaust of heat and particles from the plasma. The exhaust of heat from the plasma presents a problem for future fusion reactors, the significance of which is reflected in the EFDA roadmap to fusion which concludes that<sup>2</sup>.

*A reliable solution to the problem of heat exhaust is probably the main challenge towards the realisation of magnetic confinement fusion*

### 1.3.3 The future of the tokamak: ITER and DEMO

In 1987 an agreement was made between the European Union, Japan, the Russian Federation and the USA to initiate the conceptual design of ITER (originally an acronym of International Thermonuclear Experimental Reactor, now recognised as a proper noun), the goal of which is to demonstrate the scientific and technological feasibility of fusion energy for peaceful purposes [30]. The ITER design was originally completed in 1992,

---

<sup>2</sup>Page 8, paragraph 2. Accessible at <https://www.efda.org>

though has since been scaled down [24]. The present parameters of the ITER design are given in table 1.1, taken from [24]. The parameters have been compared to those on JET [7], the worlds largest tokamak at present. ITER represents a major step forwards

Parameter	ITER attribute	JET attribute
Major Radius	6.2m	3m
Minor Radius	2.0m	1.25m
Plasma volume	$\sim 800\text{m}^3$	$\sim 80\text{m}^3$
Plasma current	15MA	3MA
Toroidal magnetic field	5.3T	3.5T
Fusion power	500MW	–
Fusion gain	10	–

TABLE 1.1: Table of ITER parameters compared to those of JET.

in size, capability and technological complexity. The design of ITER, taken from [24] is shown in figure 1.9. ITER will use superconducting material in its magnetic field coils

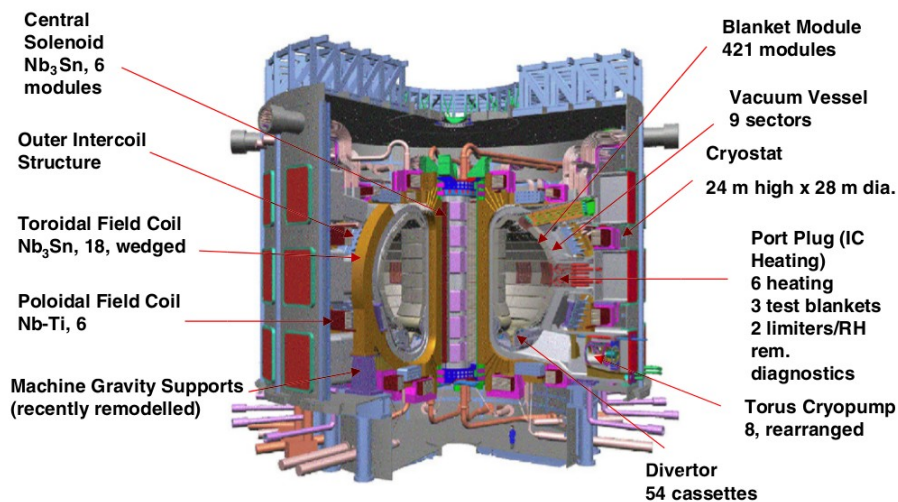


FIGURE 1.9: The design of the ITER tokamak [24]

made from Niobium-Tin ( $\text{Nb}_3\text{Sn}$ ) for the solenoid and toroidal field coils, and Niobium-Titanium ( $\text{Nb-Ti}$ ) for the poloidal field coils. It will act as a test of Lithium breeding technology housed in breeder blanket modules around the vacuum vessel. The proof of Lithium breeding technology on ITER is a key milestone on the path to fusion energy. ITER will provide a key stepping stone towards a demonstration fusion reactor (DEMO) which will act as a proof-of-principle by demonstrating the feasibility of fusion providing

electricity for commercial use. The design of DEMO is not yet determined and will certainly depend on the results from ITER, as well as other supporting tokamaks such as JET.

### 1.3.4 The Mega-Amp Spherical Tokamak (MAST)

MAST is an example of a spherical tokamak; a tokamak design, based initially on the spheromak concept, which confines the plasma tightly to the central solenoid to minimize the magnetic field strength required to achieve significant core pressures. The spherical tokamak concept was first proposed in 1986 [31] and was shown theoretically to engender the prospects of a compact nuclear fusion device at moderate cost. Figure 1.10 shows schematically the geometrical difference in the design of the spherical and conventional tokamak plasma. The first spherical tokamak, the Small Tight Aspect Ratio Tokamak

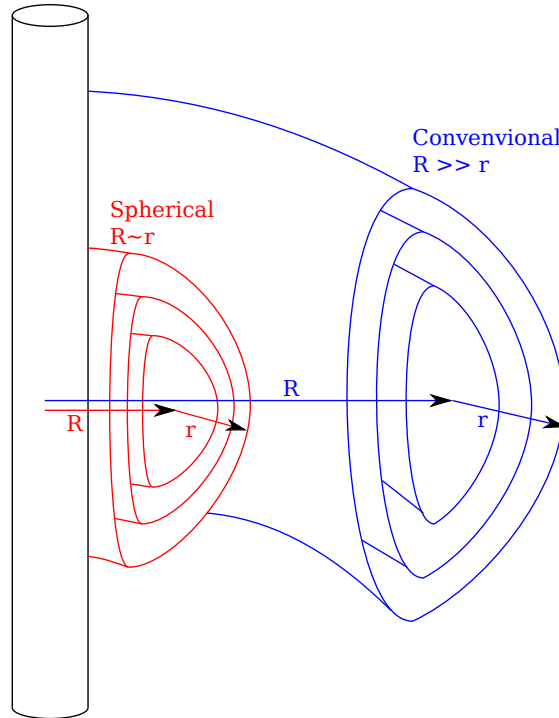


FIGURE 1.10: A schematic comparison between the spherical tokamak geometry, where  $R \sim r$ , and the conventional (large-aspect-ratio) geometry where  $R \gg r$ .  $R$  is the machine major radius and  $r$  is the plasma minor radius.

(START) was built at Culham Centre for Fusion Energy (CCFE) beginning operation in 1991 [32, 33]. It was designed as a proof of principle of spherical tokamak confinement of a hot plasma but quickly proved more successful. It showed extremely good confinement, quantified by the measure

$$\beta_T = \frac{2\mu_0}{VB_0^2} \int pdV \quad (1.23)$$

where  $V$  is the plasma volume,  $B_0$  is the toroidal magnetic field at the magnetic axis and  $p$  is the plasma pressure.  $\beta_T$  shows how much pressure can be confined in a plasma for a given magnetic pressure. Higher  $\beta_T$  means higher confinement. In general the  $\beta_T$  accessible to a tokamak is limited by the presence of violent plasma instabilities[34]. The limited value of  $\beta_T$  is increased as the aspect-ratio of the tokamak is decreased. START broke the record for  $\beta_T$ , set at 12% by the DIII-D conventional tokamak, by achieving a  $\beta_T \geq 30\%$  [35]. Furthermore START was shown to achieve H-mode [36] providing it with all the attributes of the much larger conventional tokamaks in operation at the time. The successor of START was MAST. MAST was designed as an enlarged version of START [37] ran its first physics campaign between January and June 2000 [38]. Table 1.2 gives the parameters of a typical MAST discharge [39]. The MAST

Parameter	MAST	START
R (Major radius)	0.85m	0.32m
r (Minor radius)	0.65m	0.25m
V (plasma volume)	10m <sup>3</sup>	1m <sup>3</sup>
$B_T$ (Toroidal field)	0.51T	0.31T
$I_p$ (Plasma current)	1MA	0.31MA

TABLE 1.2: Table of operational parameters for MAST and START

tokamak is a very open design with poloidal magnetic field coils suspending from the wall of the vacuum vessel. This design has two major advantages: It allows for a greater diagnostic coverage of the plasma and it allows for flexible shaping of the plasma itself. Figure 1.11 shows an engineering design of the MAST vacuum vessel, as well as the three major plasma configurations available. These are the Upper/Lower Single Null and the Connected Double Null configurations. Toroidal magnetic field coils encompass the vessel. The P1 coil is the central solenoid which is responsible for driving the plasma current and initiating the plasma itself [40]. Coil P3 aids in this process to reduce the flux requirement on P1. The P4, P5 and P6 coils are responsible for plasma shaping and motional stability. Coil P2 generates the X-point which creates the divertor region of the plasma.

The spherical tokamak concept has been suggested as a complimentary pathway to a fusion reactor[41]. The smaller size and higher operating efficiency of the ST design makes it an economical option for a fusion reactor. Other applications of the ST design for future machines are:

- A volumetric neutron source in support of ITER and DEMO [42]. This is a high powered ST machine used to test the effect of extreme neutron irradiation on wall materials.

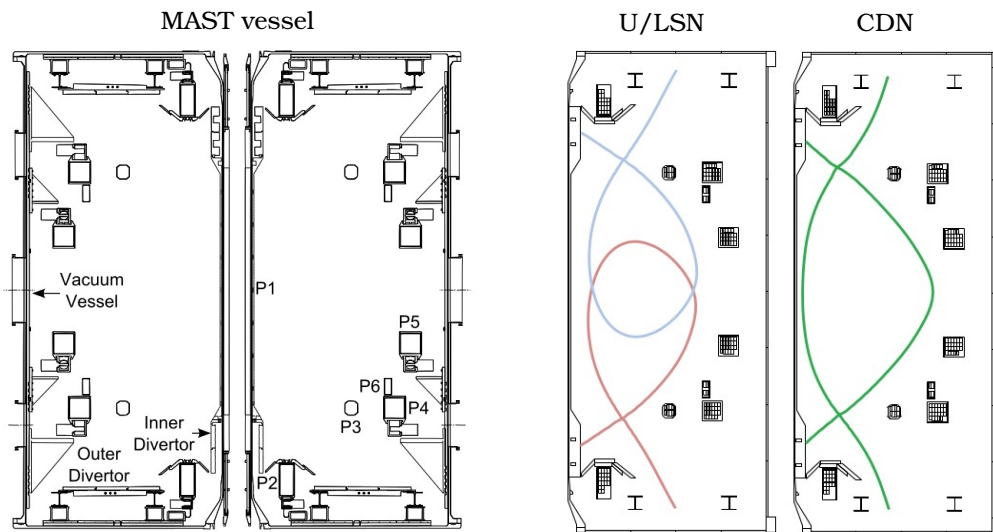


FIGURE 1.11: The MAST vacuum vessel (left) and the major plasma configurations available to MAST; the Upper/Lower Single Null and Connected Double Null configurations. Images taken from [40].

- A components test facility[43]. This has a wider reaching aim and is designed to expose modules for testing in a fusion reactor relevant plasma environment.

## 1.4 Plasma Physics

The word plasma, derived from the Greek meaning 'formed or moulded', was first used to describe the clear liquid in blood left after the removal of all corpuscular material. In 1922 the same word was adopted by Irving Langmuir to describe the state of electrons, ions and neutrals in an ionized gas[44]. Langmuir originally postulated that the charged particles were the equivalent of blood cells suspended in a fluid solution. In fact the ions and electrons themselves *are* the fluid and no plasma, in the original sense exists. The term '*plasma*' has since been adopted to describe the state of matter created in Langmuir's experiments consisting of ions, electrons and neutrals with behaviour determined through collective interactions as opposed to interactions between individual constituents. In fact the term plasma can be extended to describe any abstract system of many constituents dominated by collective behaviour rather than binary interactions

including, for example, neural networks in the brain and stock-markets [45].

A large proportion of the matter in the known universe (estimates ranging from 97 = 99%) is thought to exist as in the plasma state [46]. This is not apparent on earth because the conditions proficient for supporting life are not proficient for matter to adopt the plasma state. This can be seen by examining the Saha equation[46]:

$$\frac{n_i}{n_n} \approx 2.4 \times 10^{21} \frac{T^{3/2}}{n_i} \exp \left[ -\frac{\epsilon_i}{k_B T} \right] \quad (1.24)$$

where  $n_{i,n}$  is the number density of ions and neutrals,  $T$  is the temperature in K and  $\epsilon_i$  is the ionization energy. The Saha equation describes approximately how much ionization can be expected in a gas at thermal equilibrium with temperature  $T$  due to ionizing collisions. For conditions on Earth,  $T \sim 300\text{K}$ , and Nitrogen in air has a density roughly  $3 \times 10^{25}\text{m}^{-3}$  with an ionization energy 14.5eV. The fraction of ionized Nitrogen atoms is then

$$\frac{n_i}{n_n} \sim 10^{-122} \quad (1.25)$$

By contrast in many astrophysical environments temperatures are high and gasses become easily ionized. This is also the case in a tokamak, where temperatures routinely exceed 10,000,000 – 100,000,000K and therefore the plasma state is adopted by the fuel in a tokamak.

### 1.4.1 Definitions of a plasma

Chen [46] defines a plasma as

*A quasineutral gas of charged and neutral particles which exhibits collective behaviour.*

Quasineutrality is the requirement that, despite the charges of the individual constituents of the plasma, the plasma as a whole remains approximately neutral. Globally this arises because the number of electrons arising in plasma formation is exactly equal to the number of electrons lost by the ions, hence the charge due to electrons is exactly opposite to the charge from ions. On smaller length scales though the plasma remains quasineutral. Within a plasma a net imbalance of ions over electrons may occur, due to random thermal fluctuations, producing a net charge excess in the form of a potential well. Electrons react extremely efficiently to this charge imbalance and are attracted into the well (or repelled if the charge imbalance is negative) and neutralize the charge imbalance. In a thermal plasma some of the electrons will have sufficient energy to escape the well allowing the charge imbalance to leak into the plasma slightly. The natural

length scale over which such a charge imbalance can exist is the *Debye length*,  $\lambda_D$ , given by

$$\lambda_D = \frac{\epsilon_0 k_B T}{n_0 e^2} \quad (1.26)$$

The Debye length is used to define a quantity known as the *plasma parameter*, given by

$$N_D = \frac{4\pi\lambda_D^3 n}{3} \quad (1.27)$$

which is the number of electrons that inhabit a sphere of radius the Debye length. If  $N_D$  is too small then there will not be enough electrons in close enough proximity to a potential well to efficiently neutralize it and the plasma can not be quasi-neutral. The conditions for a quasineutral plasma then become:

$$\lambda_D \ll 1 \quad (1.28)$$

$$N_D \gg 1 \quad (1.29)$$

Given that bare charges in a plasma can only exist on length scales below  $\lambda_D$ , if the latter condition is violated the charge density can no longer be viewed as a continuous function and instead the discrete nature of the charges takes precedence. The population of the Debye sphere then ensures that the charge density of the plasma has a statistically significant meaning. Charged particles in a plasma must also remain charged for a statistically significant period of time. If this is violated then the plasma is a transient event in an otherwise neutral gas and the motion of the gas is hydrodynamic. For a typical frequency in a plasma,  $\omega$ , and a typical collision time between the plasma and the neutrals,  $\tau$ , this condition can be expressed as

$$\omega\tau > 1 \quad (1.30)$$

such that processes occur fast enough that the dynamics are associated with the plasma itself and are not simply hydrodynamic. The conditions 1.28, 1.29 and 1.30 are used to define a plasma.

## 1.4.2 Descriptions of a plasma

The most fundamental description of a plasma is on the scale of individual plasma particles. In a magnetic field charged particles feel a Lorentz force,  $\mathbf{F}_L$ , and obey a Newtonian equation of motion of the form

$$m_j \frac{d\mathbf{v}_j}{dt} = \mathbf{F}_L = q_j (\mathbf{E} + \mathbf{v}_j \times \mathbf{B}) \quad (1.31)$$

where  $\mathbf{v}_j$ ,  $m_j$  and  $q_j$  are the particle velocity, mass and charge respectively with  $\mathbf{E}$  and  $\mathbf{B}$  the electric and magnetic fields that the particle experiences. In the simplest magnetized case with no electric field and constant magnetic field in the  $z$  direction, projecting equation 1.31 onto the magnetic field  $\mathbf{B}$  shows that the particle freely streams along the magnetic field line with a velocity  $v_{\parallel}$ . The perpendicular components of equation 1.31 give

$$v_x = v_{\perp} \sin(\Omega t) \quad v_y = v_{\perp} \cos(\Omega t) \quad (1.32)$$

which describes a gyration of the particle around the magnetic field line with a gyro-frequency

$$\Omega = \frac{ZeB}{m} \quad (1.33)$$

where the charge  $q_j = Ze$  and subscripts have been dropped. Integrating the equations for  $v_x$ ,  $v_y$  and  $v_z = v_{\parallel} = \text{const}$  in time then gives the trajectory of the particle:

$$\begin{aligned} x &= x_0 - r_L \cos(\Omega t) \\ y &= y_0 + r_L \sin(\Omega t) \\ z &= z_0 + v_{\parallel} t \end{aligned} \quad (1.34)$$

This orbital motion is a Larmor orbit and has a radius

$$r_L = \frac{v_{\perp}}{\Omega} = \frac{v_{\perp} m}{ZeB} \quad (1.35)$$

This motion is illustrated schematically in figure 1.12. Larmor orbital motion underpins

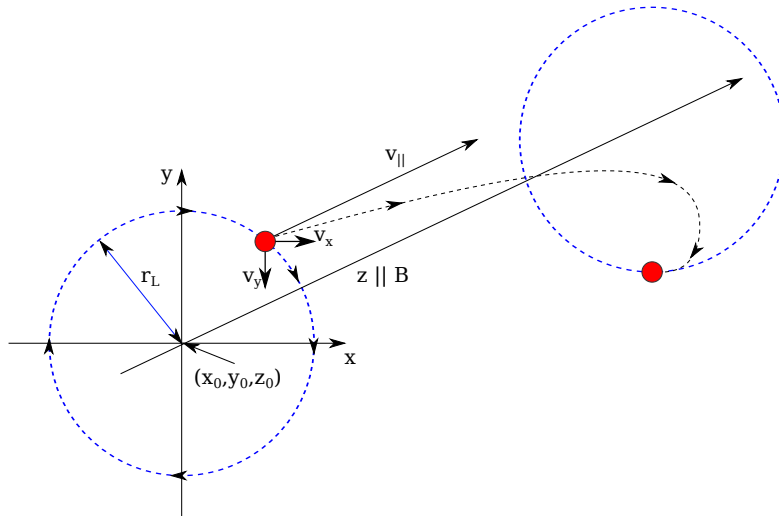


FIGURE 1.12: Schematic illustration of charged particle motion in a constant magnetic field with no external electric field. The particle experiences a gyration in the plane perpendicular to the magnetic field, but is free to stream along the magnetic field.

all motion of charged particles in a magnetized plasma. In principle if the motion of

every particle could be treated with this level of detail, and the interactions between all plasma particles could be accounted for a complete description of the plasma would emerge. Even for very sparse plasmas, with densities  $\sim 10^{15}\text{m}^{-3}$  for example, this kind of computation requires accounting for many more particles than is feasible. As a consequence a statistical formulation of the problem is often necessary.

The distribution function,  $f(\mathbf{x}, \mathbf{v}, t)$ , measures the probability density for a particle to exist at time  $t$  having a position  $\mathbf{x}$  and velocity  $\mathbf{v}$  [7]. The measure  $f d^3\mathbf{x} d^3\mathbf{v}$  is the number of particles that inhabit the 6D phase space volume spanned by  $\mathbf{x}, \mathbf{x} + d\mathbf{x}$  and  $\mathbf{v}, \mathbf{v} + d\mathbf{v}$ . To ensure conservation of particle number the distribution function is a conserved quantity such that, in the absence of any external sources, it obeys a continuity equation

$$\frac{\partial f}{\partial t} = -\nabla \cdot (\dot{\mathbf{x}}f) - \nabla_v \cdot (\dot{\mathbf{v}}f) \quad (1.36)$$

Using Hamilton's equations

$$\dot{\mathbf{q}} = \partial_{\mathbf{p}}H, \quad \dot{\mathbf{p}} = -\partial_{\mathbf{q}}H \quad (1.37)$$

where  $\mathbf{q} = \mathbf{x}$  is position and  $\mathbf{p} = m\mathbf{v}$  is momentum and  $H$  is the Hamiltonian, to expand the divergence terms allows the conservation equation to be written in advective form as

$$\frac{\partial f}{\partial t} + \mathbf{v} \cdot \nabla f + \frac{\mathbf{F}}{m} \cdot \nabla_v f = 0 \quad (1.38)$$

This is the *collisionless Boltzmann equation* [46]. Substituting the Lorentz force gives the *Vlasov equation*:

$$\frac{\partial f}{\partial t} + \mathbf{v} \cdot \nabla f + \frac{Ze}{m} (\mathbf{E} + \mathbf{v} \times \mathbf{B}) \cdot \nabla_v f = 0 \quad (1.39)$$

If collisions play a significant role in the redistribution of  $f$  then an extra term is added, called the collision operator, which depends on the exact type of collision present. This then results in the more general *Vlasov-Fokker-Planck equation*:

$$\frac{\partial f_j}{\partial t} + \mathbf{v}_j \cdot \nabla f_j + \frac{Z_j e}{m_j} (\mathbf{E} + \mathbf{v}_j \times \mathbf{B}) \cdot \nabla_v f_j = \mathcal{C}[f_j, f_i] \quad (1.40)$$

This equation describes the evolution of the distribution function for a particle species  $j$  under the influence of the electromagnetic fields  $\mathbf{E}$  and  $\mathbf{B}$  and under collisions with partial species  $i$ . This equation represents the starting point for many theoretical studies of plasmas. The drift-kinetic equation is generated from equation 1.40 under conditions where  $f$  evolves slowly in comparison with the gyro-motion of the particles, and gradually in space compared to the gyro-radius of the particles[45]. The gyro-kinetic equation is similar but allows for electromagnetic fields to vary on and below the gyro-orbit length scale [45]. In each case the fast motion of the Larmor gyration makes the dynamics of

the system approximately independent of the phase of the gyro-motion, which constrains one degree of freedom in the system and reduces the problem to 5 dimensions [7].

Typical applications of the VFP equation are too complicated to solve analytically and numerical techniques are often used. Numerical solutions require some form of spatial discretization to represent the spatial continuum on a computer. In the VFP equation there are 6 dimensions requiring discretization. Thus if  $N$  nodes per dimension are used, the total number of nodes required to solve the problem is  $N^6$ . Hence for even moderately sized grids,  $N = 1024$  for example, the computational cost of working in 6D quickly becomes prohibitive. Reducing this to 5D, in the case of the drift-kinetic and gyro-kinetic equations, represents a major reduction in computational cost, but  $N^5$  is still limiting in most cases of interest.

### 1.4.3 Fluid moments of the kinetic equation

The electromagnetic fields that influence the plasma distribution function in 1.40 are determined by Gauss's law

$$\nabla \cdot \mathbf{E} = \rho / \epsilon_0 \quad (1.41)$$

and Amperes law

$$\nabla \times \mathbf{B} = \mu_0 \mathbf{J} \quad (1.42)$$

where  $\mathbf{E}$  and  $\mathbf{B}$  are the electric and magnetic fields and  $\rho$  and  $\mathbf{J}$  are the charge and current densities respectively. The electromagnetic fields are dependant only on the lowest order moments of the distribution, namely the density and flow velocity of each plasma species, therefore it is enticing to approach the problem by taking moments of equation 1.40.

The particles within a confined plasma are characterized to lowest order by the Maxwell-Boltzmann velocity distribution,  $f_m$  [47]:

$$f_m \equiv n \left( \frac{m}{2\pi T} \right)^{3/2} \exp \left[ -\frac{m}{2T} v^2 \right] \quad (1.43)$$

where  $n$  is the density,  $T$  is the temperature and  $\mathbf{u}$  is the flow velocity of the plasma. To derive the properties of the density,  $n$ , velocity,  $\mathbf{u}$ , and temperature  $T$ , the distribution function can be averaged over velocity space yielding the definitions

$$n_j \equiv \int f_j(t, \mathbf{x}, \mathbf{v}_j) d^3 \mathbf{v}_j \quad (1.44)$$

$$\mathbf{u}_j \equiv \frac{1}{n_j} \int \mathbf{v}_j f_j(t, \mathbf{x}, \mathbf{v}_j) d^3 \mathbf{v}_j \quad (1.45)$$

$$T_j \equiv \frac{1}{n_j} \int \frac{m_j}{3} (v_j - \mathbf{u}_j)^2 f_j(t, \mathbf{x}, \mathbf{v}_j) d^3 \mathbf{v}_j \quad (1.46)$$

To derive evolution equations for these quantities moments are taken of the VFP equation, 1.40. The  $n^{\text{th}}$  moment of the VFP equation is taken by evaluating

$$\begin{aligned} \int \mathbf{v}_j^n \frac{\partial f_j}{\partial t} d^3 \mathbf{v}_j + \int \mathbf{v}_j^{n+1} \cdot \nabla f_j d^3 \mathbf{v}_j + \int \mathbf{v}_j^n \frac{Z_j e}{m_j} (\mathbf{E} + \mathbf{v}_j \times \mathbf{B}) \cdot \nabla_v f_j d^3 \mathbf{v}_j \\ = \int \mathbf{v}_j^n \sum_i \mathcal{C}[f_j, f_i] d^3 \mathbf{v}_j \end{aligned} \quad (1.47)$$

Evaluating equation 1.47 for the  $N^{\text{th}}$  moment gives a moment hierarchy [48]

$$\frac{\partial \mathbf{M}^N}{\partial t} + \nabla \cdot \mathbf{M}^{N+1} + \frac{Ze}{m} [\mathbf{E} \mathbf{M}^{N-1} + \mathbf{M}^N \times \mathbf{B}]^* = \mathbf{C}^N \quad (1.48)$$

where the  $N^{\text{th}}$  moment,  $\mathbf{M}^N$  is an order  $N$  tensor constructed by

$$\mathbf{M}^N = \frac{1}{n} \int \mathbf{v}^N f d^3 \mathbf{v} = \frac{1}{n} \int \mathbf{v} \mathbf{v} \mathbf{v} \dots f d^3 \mathbf{v} \quad (1.49)$$

and the  $N^{\text{th}}$  moment of the collision operator is similarly defined by

$$\mathbf{C}^N = \frac{1}{n} \int \mathbf{v}^N \sum_i \mathcal{C} d^3 \mathbf{v} \quad (1.50)$$

In equation 1.48 the starred bracket  $[]^*$  indicates symmetrization of the tensor(s) within the bracket. For  $N = 1$  this has no effect on the bracket contents and for  $N = 2$  this is just an addition of the bracket contents by its transpose. The moment hierarchy illustrates the fundamental issue with fluid theory; the evolution equation for the  $N^{\text{th}}$  moment of the distribution function will always contain a dependence on the  $(N + 1)^{\text{th}}$  moment; hence the system of equations derived by this approach is only closed as  $n \rightarrow \infty$ . The moment hierarchy is valid for  $N > 0$  whilst the zeroth moment of the VFP equation is evaluated term by term below:

- First term:

$$\int \frac{\partial f_j}{\partial t} d^3 \mathbf{v}_j = \frac{\partial}{\partial t} \int f_j d^3 \mathbf{v}_j = \frac{\partial n_j}{\partial t}$$

- Second term:

$$\int \mathbf{v}_j \cdot \nabla f_j d^3 \mathbf{v}_j = \int \nabla \cdot (\mathbf{v}_j f_j) d^3 \mathbf{v}_j = \nabla \cdot \int \mathbf{v}_j f_j d^3 \mathbf{v}_j = \nabla \cdot (n_j \mathbf{u}_j)$$

where the fact that  $\mathbf{v} \neq \mathbf{v}(\mathbf{x})$  has been exploited.

- Third term:

$$\int (\mathbf{E} + \mathbf{v}_j \times \mathbf{B}) \cdot \nabla_v f_j d^3 \mathbf{v}_j = \int f_j (\mathbf{E} + \mathbf{v}_j \times \mathbf{B}) \cdot d\mathbf{S}_v - \int f \nabla_v \cdot (\mathbf{E} + \mathbf{v}_j \times \mathbf{B}) d^3 \mathbf{v}_j$$

where an integration by parts followed by an application of Gauss' theorem in  $\mathbf{v}$  space has been performed. Assuming that  $f_j \rightarrow 0$  faster than  $\mathbf{v} \rightarrow \infty$  the first term here is 0.  $\mathbf{E}$  is assumed independent of  $\mathbf{v}$ , and writing the second part of the volume integral in component form

$$\frac{\partial}{\partial v_\alpha} v_\beta B_\gamma = 0$$

shows that the entire term results in 0

- Fourth term: Assuming that no ionization or recombination of the plasma occurs collisions preserve the particle number and only shift the velocity distribution. Consequently

$$\int \sum_i \mathcal{C}[f_j, f_i] d^3 \mathbf{v}_j = 0$$

Thus the zeroth moment equation is the density continuity equation and is given by

$$\frac{\partial n_j}{\partial t} + \nabla \cdot (n_j \mathbf{u}_j) = S_{n,j} \quad (1.51)$$

where  $S_{n,j}$  is an external particle source. The first and second moments are evaluated from the moment hierarchy and result in the momentum and energy conservation equations (the energy conservation resulting from a contraction of the  $N = 2$  moment equation):

$$n_j m_j \frac{\partial \mathbf{u}_j}{\partial t} + n_j m_j \mathbf{u}_j \cdot \nabla \mathbf{u}_j + \nabla p_j + \nabla \cdot \overleftrightarrow{\Pi}_j = Z_j e n_j (\mathbf{E} + \mathbf{u}_j \times \mathbf{B}) + \mathbf{R}_j + \mathbf{S}_{m,j} \quad (1.52)$$

$$\frac{3}{2} n_j \left( \frac{\partial}{\partial t} + \mathbf{u}_j \cdot \nabla \right) T_j + n_j T_j \nabla \cdot \mathbf{u}_j + \nabla \cdot \mathbf{q}_j + \overleftrightarrow{\Pi}_j : \nabla \mathbf{u}_j = W_j + S_{T,j} \quad (1.53)$$

$\mathbf{S}_m$  and  $S_T$  represent external momentum and energy sources. The pressure tensor is given by

$$\overleftrightarrow{P}_j \equiv \int m_j \mathbf{v}_j \mathbf{v}_j f_j d^3 \mathbf{v}_j = p_j \overleftrightarrow{\mathbf{I}} + \overleftrightarrow{\Pi}_j \quad (1.54)$$

where

$$p = \frac{1}{3} \text{Tr} \left( \overleftrightarrow{P} \right) = \int m \frac{v^2}{3} f d^3 \mathbf{v} = nT \quad (1.55)$$

is the scalar pressure and

$$\overleftrightarrow{\Pi} = \overleftrightarrow{P} - p \overleftrightarrow{\mathbf{I}} = \int \left( \mathbf{v} \mathbf{v} - \frac{v^2}{3} \overleftrightarrow{\mathbf{I}} \right) f d^3 \mathbf{v} \quad (1.56)$$

is the anisotropic viscosity tensor with  $\overleftrightarrow{\mathbf{I}}$  the identity tensor. The collisional terms are the ion-electron friction given by

$$\mathbf{R}_i = -\mathbf{R}_e = \int m_i \mathbf{v}_i \mathcal{C}[f_i, f_e] d^3 \mathbf{v}_i \quad (1.57)$$

and the frictional heating term

$$W_j = \int \frac{m_j v_j^2}{2} \mathcal{C}[f_j, f_i] d^3 \mathbf{v}_j \quad (1.58)$$

Finally the vector  $\mathbf{q}$  is the flux density of heat and is the next moment of the distribution function

$$\mathbf{q} = \int \frac{m}{2} (v - u)^2 (\mathbf{v} - \mathbf{u}) f d^3 \mathbf{v} \quad (1.59)$$

These equations are exact; approximations are introduced when the series of equations is closed to make the system tractable. The closure is achieved either through physically motivated truncation of the moment hierarchy or by an asymptotic calculation of higher order moments. As an example of the truncation method the plasma can be considered as a single fluid consisting of a density composed of both the ions and electrons, and a centre of mass momentum between the ions and electrons [49]. The plasma is considered adiabatic and the isotropic pressure is given by an equation of state of the form

$$\left( \frac{\partial}{\partial t} + \mathbf{u} \cdot \nabla \right) p n^{-\gamma} = 0 \quad (1.60)$$

where  $\gamma$  is the adiabatic index, typically taken as 5/3. This closure approximation leads to *magnetohydrodynamics* (MHD).

An asymptotic closure approach can be obtained by evaluating the heat flux density vector,  $\mathbf{q}$  to lowest order in a small ordering parameter. This is the approach taken by Braginskii [47] and Grad [50] for the case where the lowest order cross-field flow is comparable to the sound speed, and by Mikhailovskii and Tsypin [51], and Simakov and Catto [52, 53] for the case where flows are much slower than the sound speed. This closure scheme assumes that the distribution function is at most only a small deviation from a Maxwellian such that

$$f_j \approx f_{M,j} + f_{1,j} \quad (1.61)$$

where  $f_1/f_M \ll 1$ . The VFP equation can then be expanded asymptotically in orders of  $f_1/f_M$  and used to provide approximate solutions for the heat flux, viscosity tensor and collision friction terms. The Braginskii heat flux is given for electrons by [47]

$$\mathbf{q}_e = -\kappa_{\parallel} \nabla_{\parallel} T_e + \kappa_{\perp} \nabla_{\perp} T_e - \frac{0.71 T_e J_{\parallel}}{e} + \frac{5 n T_e}{2 m_e \Omega_e} \mathbf{b} \times \nabla T_e + \frac{3 \nu_e T_e}{2 e \Omega_e} \mathbf{b} \times \mathbf{J} \quad (1.62)$$

where  $\kappa_{\parallel,\perp}$  is the parallel/perpendicular thermal conductivity,  $J_{\parallel} = e\mathbf{b} \cdot (n_i\mathbf{u}_i - Zn_e\mathbf{u}_e)$  is the parallel current and  $\nu_e$  is the electron-ion collision frequency.

#### 1.4.4 Plasma drifts

The motion of a plasma is composed of the larmor orbits of individual particles, free streaming motion parallel to the magnetic field, and drift motion across the magnetic field [46]. The drift motion of the plasma is responsible for many of the global dynamics observed in tokamaks. There are three principle mechanisms by which particle drifts can occur:

1. Expansion/contraction of the particle Larmor orbit: This mechanism is responsible for the  $\mathbf{E} \times \mathbf{B}$  drift, the curvature drift and the  $\nabla B$  drift.
2. Polarization of the Larmor orbit: This is responsible for the polarization drift.
3. Fluid flows due to Larmor motion: This is responsible for the diamagnetic drift.

The first of these drift mechanisms is illustrated in figure 1.13. Forces directed per-

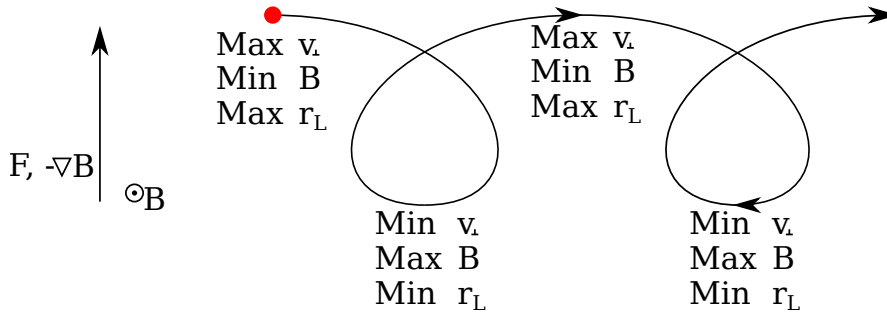


FIGURE 1.13: Drift motion due to expansion and contraction of the Larmor orbit. Expansion can occur either due to acceleration by a force perpendicular to the magnetic field, or by a variation in magnetic field strength,  $\nabla B$ , perpendicular to the field.

pendicular to the magnetic field accelerate the charged particle on the upward swing of its orbit. The increased particle velocity expands the Larmor radius with the particle velocity and radius at maximum at the top of the orbit. On the downward swing the force decelerates the particle and the opposite effect occurs with the velocity reducing and the Larmor radius contracting. This expansion/contraction leads to a net motion perpendicular to both the magnetic field,  $\mathbf{B}$  and the perpendicular force,  $\mathbf{F}$ . The same effect occurs if a gradient in the magnetic field exists perpendicular to the field itself. The velocity of a drift due to a perpendicular force,  $\mathbf{F}$ , is given by [46]

$$\mathbf{u}_d = \frac{1}{ZeB^2} \mathbf{F} \times \mathbf{B} \quad (1.63)$$

The curvature drift is an example of such a drift, where the bending of magnetic field lines produces a centripetal force felt by particles as they stream along magnetic field lines. The force is given by

$$\mathbf{F}_c = \frac{mv_{\parallel}^2}{R_c^2} \mathbf{R}_c \quad (1.64)$$

where  $R_c$  is the radius of curvature. The drift motion in this case reverses if the charge of the particle changes sign, meaning that charge separation can be driven and such drifts give rise to currents in the plasma. An exception is the  $\mathbf{E} \times \mathbf{B}$  drift, which arises due to perpendicular electric fields. In this case the force on the particle is  $\mathbf{F}_E = Ze\mathbf{E}$ . Now if the charge reverse, the Larmor orbit reverses as does the perpendicular force, leading to an invariance of the drift motion. Consequently ions and electrons drift in the same direction and no current is produced.

The diamagnetic drift does not depend on the motion of individual particles and fits into the third category outlined above. Taking a simplified form of equation 1.52 (retaining only pressure, Lorentz terms and Lagrangian derivative terms) and applying  $\mathbf{B} \times$  leads to an expression for the perpendicular fluid velocity of a plasma:

$$\mathbf{u}_{\perp} = \frac{\mathbf{E} \times \mathbf{B}}{B^2} + \frac{\mathbf{B} \times \nabla p}{ZeB^2} + \frac{1}{B\Omega} \mathbf{B} \times \frac{d\mathbf{u}}{dt} \quad (1.65)$$

The second term represents the diamagnetic drift. Figure 1.14 illustrates the processes leading to the diamagnetic drift. If a density gradient exists perpendicular to the mag-

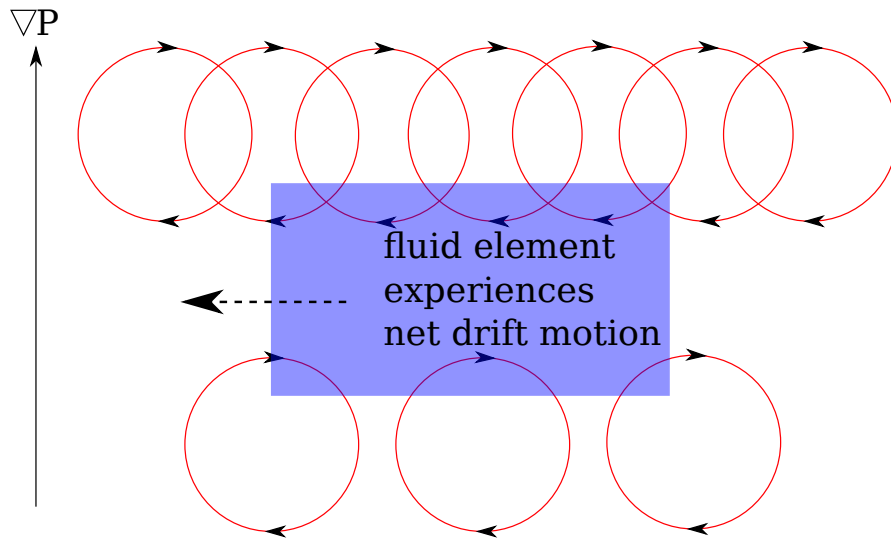


FIGURE 1.14: Schematic illustration of the origin of the diamagnetic drift from Larmor orbit motion across a pressure gradient.

netic field a net flow occurs where more particles exist on the downward swing of their Larmor orbit than the upper. The same effect occurs if a temperature gradient exists, in which case the difference in speed of the Larmor orbits leads to a net fluid flow. This

drift does not occur on a single particle level but requires a distribution of particles to occur. The diamagnetic drift is charge dependant allowing it to drive cross-field currents in the plasma.

The final drift of importance is the polarization drift. This is the third term in the equation above. Taking the velocity in this term as being primarily due to the  $\mathbf{E} \times \mathbf{B}$  velocity, and assuming a steady magnetic field results in

$$\mathbf{u}_p = \frac{1}{B^2 \Omega} \frac{d\mathbf{E}_\perp}{dt} \quad (1.66)$$

where the time derivative is  $d/dt = \partial/\partial t + \mathbf{u} \cdot \nabla$ . As  $\mathbf{E}$  varies the centre of gyration of the Larmor orbit shifts and the orbit becomes polarized. Once again the polarization drift is charge dependant and can lead to current formation. The polarization drift is smaller than the former drifts however the current arising from the polarization drift can be important in plasma dynamics.

## 1.5 Thesis outline

In chapter 2 a review of the physics of the filaments and intermittent transport in the plasma edge is given. This includes aspects of the plasma material interface, turbulence in the plasma edge and the emergence of intermittency. The physics of the plasma edge is strongly non-linear and a significant body of work exists dedicated to its experimental characterization, as well modelling this transport. The chapter will outline the relevance of this thesis within the field.

Chapter 3 presents the design and operation of a ball pen probe on MAST. The ball pen probe is a novel probing technique allowing for direct measurements of the plasma potential in the plasma edge. The plasma potential is an important quantity in determining the dynamics of the plasma edge. Gradients in the averaged profile give rise to radial electric fields, in turn leading to radial velocity shear layers. On the fluctuation scale the potential is a determining factor in the turbulence at the plasma edge. The operation of the probe is assessed by a direct comparison with the Thomson scattering diagnostic on MAST. Fluctuation characteristics in the edge are analysed and the interaction between the radial electric field and the production of intermittency is commented on.

Chapter 4 gives an overview of the BOUT++ code. The BOUT++ code is used in this thesis to model intermittent events which dominate transport in the edge of tokamaks. Developments in mesh generation for BOUT++ have been made to facilitate these studies and these are described here. A description of the physics module implemented in BOUT++ to carry out the work detailed later in this thesis is given.

Chapter 5 presents results of filament dynamics simulations in BOUT++ using a geometry representative of the SOL magnetic geometry in MAST. Simple scaling arguments are used to show that the dynamics of filaments vary as the resistivity of the plasma is varied. This is investigated by conducting simulations with a range of resistivity, varied using the electron temperature. The impact of the magnetic geometry on plasma filament dynamics is assessed and shown to play a key role when resistivity is high. When resistivity is low the Boltzmann response is shown to cause a drastic departure from conventional 2D dynamics.

Chapter 6 extends the investigations in chapter 5 by conducting a scan in both electron temperature and filament cross-sectional width. This is compared to the Two-region model of Myra *et.al* [54].

Chapter 7 presents conclusions drawn from the work presented in this thesis. It also outlines possible extensions to the work, and areas where the work is being continued for future study.

Appendices A, B and C present an introduction to the geometry used in BOUT++, a derivation of the equations underlying the simulations in chapters 5 and 6 and a derivation of the curvature vector respectively.



## Chapter 2

# Review of Filament Physics

### 2.1 Introduction

Filaments are coherent field aligned plasma structures found in the edge and scrape-off layer (SOL) regions of many magnetically confined plasma devices, not least the tokamak. Filaments are defined by D'Ippolito *et.al* [55] through three criteria:

1. A monopole density distribution with a density peak significantly higher than the RMS profile of the background plasma (typically  $\geq 2$  times)
2. Alignment to the background magnetic field such that variation in filament features along the magnetic field is significantly weaker than their perpendicular variation
3. A dominantly dipole potential in the perpendicular plane resulting in a strong component of  $\mathbf{E} \times \mathbf{B}$  motion radially away from the core plasma

Filaments have been referred to in literature by a number of names including avaloids, intermittent plasma objects (IPOs), streamers and blobs but all are used synonymously to describe these filamentary objects. In the last thirteen years research into the nature, motion and transport induced by filaments has increased rapidly. This was strongly motivated by experiments on ALCATOR C-mod which demonstrated a regime of operation where the particle balance in the SOL was dominated by recycling at the vessel wall mediated by anomalously high levels of cross-field advective transport [56]. This excess in cross-field transport is now thought to be, at least in part, due to filament motion [57–59] which motivates the study of filaments both experimentally and theoretically. In future high power devices such as ITER and DEMO interaction with the vessel walls will need to be tightly controlled to avoid violation of the Tritium inventory or damage to first wall components [60]. Consequently the study of filaments and the transport

they may provide is of prime importance to the tokamak community.

In this chapter the body of work concerning filaments is reviewed to lay the foundations for much of the work carried out within this thesis. This is not intended as an exhaustive review but rather as an overview to precede the work undertaken herein. A full review of the subject has recently been conducted by D'Ippolito *et.al* [55].

## 2.2 Experimental Characterization of Filaments

Filaments have been observed experimentally in many different plasma devices including the MAST [61], NSTX [62], TCV [63], ALCATOR-Cmod [64], DIII-D [65], ASDEX [66], QUEST [67], JET [68] and TEXTOR [69] tokamaks as well as stellerators such as TJ-K [70] and simpler magnetic configurations such as the toroidal TORPEX device [71] and the linear PISCES device [72]. Filaments were first observed as excessive fluctuations in the periphery of the ALCATOR tokamak [73] though the measurements were integrated in time and space which limited the conclusions that were drawn. The development of fast imaging techniques, alongside statistical analysis of signals generated from Langmuir probes allowed these fluctuations to be studied in greater detail in terms of both their temporal and spatial characteristics.

### 2.2.1 Probe Measurements of Filaments

Langmuir probes operating in ion-saturation mode and/or floating potential mode (see Chapter 3 for a description of probe diagnostics) are typically used to measure fluctuations in the SOL and edge regions of tokamak plasmas. The characteristics of the fluctuations can provide a multitude of information concerning the underlying processes occurring in the plasma. In particular measurement of the probability distribution function  $\mathcal{P}(x)$  (PDF) of a time series  $x(t)$ , which describes the probability of finding the value of a fluctuating quantity between  $x$  and  $x + dx$ , can give insight into the nature of fluctuations. Random fluctuations have a Gaussian PDF centred on the average of the time-series with a width given by twice the standard deviation. This is in response to the equal likelihood of finding a positive or negative fluctuation about the mean. By contrast the presence of filaments in the SOL provides a source of large, intermittent fluctuations which are always positive and cause a departure of the PDF from a Gaussian. This behaviour is found to be universal to magnetically confined plasmas [74] as shown in figure 2.1 taken from Antar *et.al* [74]. The presence of filaments causes the positive leg of the PDF to be extended outwards and describes the tendency of the signal towards large intermittent events. Importantly, as can be seen in figure 2.1, this structure of the PDF is universal among tokamaks, and other machines. The structure

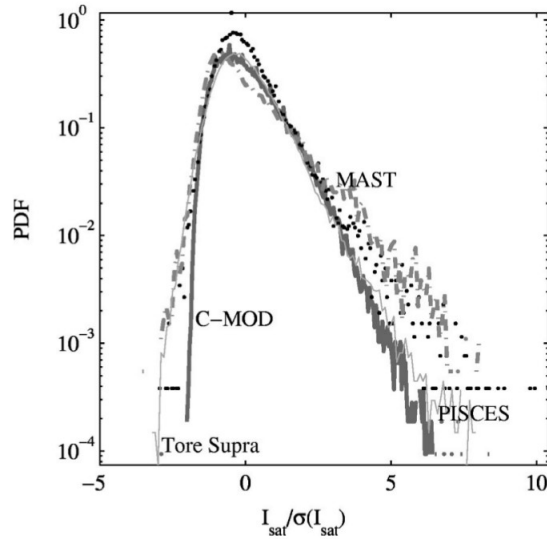


FIGURE 2.1: Fluctuations in ion saturation current measurements on several magnetically confined devices showing universality of the structure of the PDF. In particular in all cases, even the linear machine PISCES, a strong tendency towards large intermittent events is observed.

of the PDF can be quantified by the skewness,  $S$ , which measures how much the PDF is biased towards positive or negative events, and can be calculated by taking the third moment of the PDF (see section 3.5 of chapter 3). A positive skewness implies the presence of filaments whilst a negative skewness implies the presence of holes of density. These holes are often observed just inside the separatrix whilst filaments are present outside [68, 75, 76]. This will be investigated in detail in chapter 3.

The temporal nature of SOL fluctuations can also be inferred from the PDF by constructing PDFs over differing time windows and applying analysis techniques described in detail by Dudson *et.al* [77]. In particular fluctuations in the SOL are self-similar [63, 77, 78] indicating that long time correlations exist. This self-similarity begins to break down in MAST beyond a correlation time of  $\tau \approx 40\mu\text{s}$  [78] which is in agreement with the observed lifetime of filaments on MAST [79]. The properties of the PDFs and of the fluctuations in general are insensitive to modest changes in magnetic geometry [78] further highlighting the universal nature of these fluctuations.

Aside from the statistics of fluctuations, probes can also be used to investigate the individual properties of fluctuations. The process of conditional averaging [75] involves the identification of individual filament events in the probe time series through a pre-set detection threshold. The time series data is then binned according to its proximity to the filament event. This is repeated for many different filament events and an average profile of the fluctuation is produced. Figure 2.2 shows such a conditional averaging procedure on the DIII-D tokamak used to produce profiles of fluctuations of density due

to both filaments and holes [75]. Also shown in figure 2.2 is the conditionally averaged

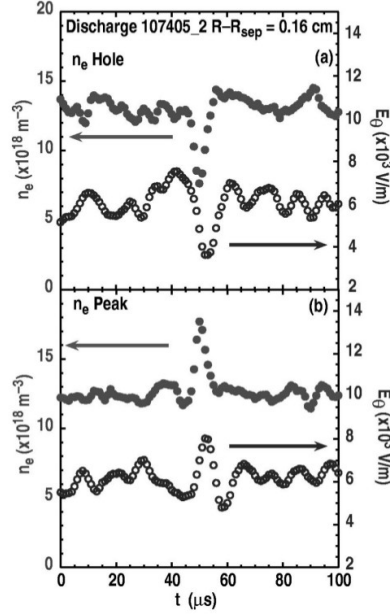


FIGURE 2.2: Conditional averaging of probe data on DIII-D providing profiles of both filament and hole events. Also shown is the conditionally averaged electric field across the event. This confirms the inward motion of holes and the outward motion of filaments.

electric field across the filament measured by the difference in the floating potential between two poloidally separated probe pins either side of the central measurement of ion saturation current. If the plasma temperature can be suitably measured or approximated the floating potential can be used to infer the plasma potential and as such an approximation for the electric field across the filament can be produced. Importantly in figure 2.2 the measurement of the electric field suggests that  $\mathbf{E} \times \mathbf{B}$  motion is responsible for the propagation of the filament and hole. Using such measurements of the electric field and filament density, filaments with a fluctuation magnitude greater than 2.5 times the RMS level were shown to contribute  $\approx 50\%$  of the total particle flux in the SOL plasma in DIII-D [65].

Conditional sampling can provide unique insight into the nature of filaments and can be achieved with a relatively simple probe set-up, however by complicating the design of the probe system significantly more information can be attained. Either through instantaneous measurement [80] or through an optimized conditional averaging measurement [81, 82] the 2D shape of profiles across the filament can be measured. Two examples are shown in figure 2.3. These measurements provide highly resolved 2D profiles and demonstrate the presence of a polarization of potential across the filament cross-section which provides the mechanism for  $\mathbf{E} \times \mathbf{B}$  motion. Since the probe arrays typically

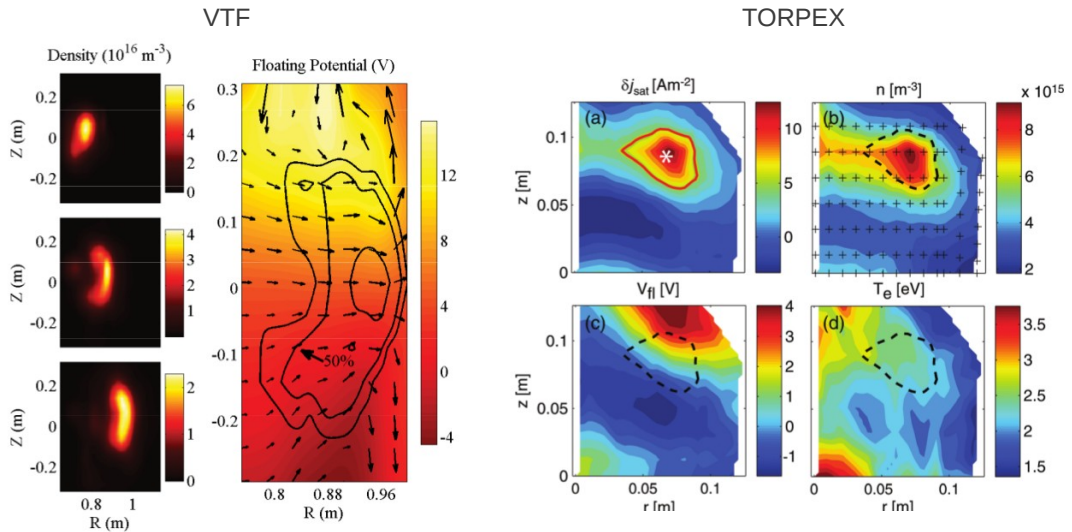


FIGURE 2.3: 2D profile measurements using probe arrays in the simple toroidal plasma devices VTF, taken from [80], and TORPEX, taken from [82]. The VTF measurement is an instantaneous measurement whilst the TORPEX measurement is a conditional average over 600 filament events centred on the starred position in the  $J_{\text{sat}}$  plot.

used are supported by thin frames to avoid excessive perturbations to the plasma, these highly resolved 2D probe measurements are usually limited to simple magnetic devices where space inside the vacuum vessel is not an issue, and where excessive heat and particle fluxes cannot damage the diagnostic. To make similar measurements on tokamaks requires the use of other diagnostics. Principle among these are visible imaging diagnostics.

### 2.2.2 Imaging of Filaments

Visible imaging has provided strong evidence of the existence of filaments. The advantages of imaging measurements is that they are inherently 2D by nature and provide at most a negligible perturbation to the plasma, allowing accurate measurements of the geometry of filaments. The disadvantage is that it is often very hard to achieve absolutely calibrated measurements of quantities such as density since the intensity of emission measured by the camera is often a complex function of local plasma conditions [40]. As such a combination of imaging and probe measurements is usually optimal.

Imaging of filaments has been obtained experimentally in two fashions: 1) through imaging of passive light emission arising from the interaction between the plasma and the naturally occurring neutral gas within the vacuum vessel and 2) through gas-puff imaging (GPI) [62, 83] where a localised puff of gas (usually consisting of neutralized

Helium or Deuterium) is used to enhance the emission around a local area of the plasma boundary. The first of these methods can be used to provide global imaging of filaments whilst the latter is used to provide detailed local imaging of the filament cross-section. On MAST [79, 84, 85], NSTX [62] and ALCATOR C-mod [86, 87] imaging of fluctuations in light emission proved that filaments are field aligned objects with a significant extent along the magnetic field line. Furthermore measurements on MAST were carried out in L-mode, inter-ELM H-mode and in H-mode during ELMs and showed that this field aligned filamentary structure is ubiquitous to SOL fluctuations in all confinement regimes [84]. Images taken on MAST [84], shown in figure 2.4, show these filamentary structures.

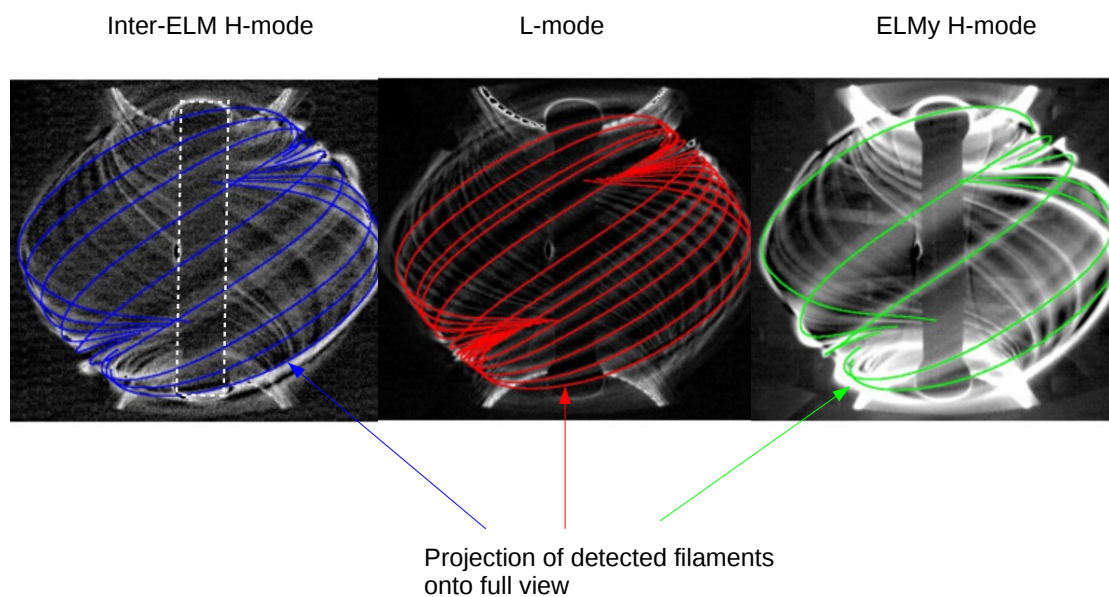


FIGURE 2.4: Visible imaging from MAST of filament structures in L-mode, inter-ELM H-mode and ELMy H-mode taken from [84].

Using GPI the perpendicular structure of filaments on ALCATOR C-mod has also been shown to translate along the magnetic field line [87] in response to the expansion and shearing of magnetic flux tubes of the magnetic field. The fluctuation characteristics from imaging observations have been compared to probe measurements in linear devices [88] and on tokamaks [83, 85] proving that filaments, as imaged by cameras, are responsible for the fluctuations observed in probe data.

### 2.2.3 Filament Properties across Machines

Using imaging diagnostics, probes or a combination of the two a number of studies have been carried out on a variety of machines to characterize key aspects of filaments. In

table 2.1 the size, lifetime and radial velocity of filaments in L-mode conditions in a number of different devices is given, with data taken from [68, 71, 72, 75, 79, 89, 90]. Table 2.1 highlights the universal nature of filament properties. The range of machines

Device	Perpendicular Diameter (cm)	Lifetime ( $\mu\text{s}$ )	Radial Velocity ( $\text{km s}^{-1}$ )
MAST	5 - 10	40 - 60	0.5 - 1.5
NSTX	3 - 5	N/A	0.2 - 1.4
ALCATOR C-mod	0.55 - 0.85	10 - 20	0.1 - 0.6
DIII-D	0.5 - 4	15 - 20	0.33 - 2.6
JET	0.5 - 2	20 - 40	0.2 - 0.6
TORPEX	3 - 5	N/A	1 - 1.75
PISCES	N/A	N/A	0.5 - 1.5

TABLE 2.1: Comparison of quoted filament parameters across a range of tokamaks and other machines. Data is quoted from [68, 71, 72, 75, 79, 89, 90]

included in the comparison contains spherical and conventional tokamaks of varying size and magnetic field strength, a simple toroidal plasma and a linear plasma, yet the properties of the filaments produced are remarkably similar. Filaments are always produced on the cm scale, with a lifetime of 10s of  $\mu\text{s}$  and velocities on the km/s scale. Some variation can be noted between machines. Particularly a tendency towards smaller filaments, slower filaments is observed as the magnetic field of the machine increases. The upper limit of the results from DIII-D are outliers to this trend however as described by Boedo *et.al* [75] these upper limits occur at the separatrix, whilst data from other machines mainly concerns far SOL properties. The lower bound values in the DIII-D data are more comparable to other machines, and do adhere to the trend.

## 2.3 Models for filament motion

The previous section has shown that, not only is the existence of filaments ubiquitous in magnetically confined plasmas but aspects of the filaments and their motion is highly universal. As a consequence significant efforts have been made to understand filaments theoretically. This can be broadly split into efforts in understanding the production of filaments and efforts into understanding the isolated motion of filaments. The modelling within this thesis is concerned with the latter of these two areas.

The first model of isolated filament motion was proposed in 2001 by Krashenninikov [91]. The model, as well as all major models since, is based on the fact that in a quasineutral filament there can be no net generation of current, otherwise a source of charge occurs and quasineutrality is broken. This can be expressed by the condition of a divergence free current density

$$\nabla \cdot \mathbf{J} = \nabla \cdot \mathbf{J}_{\perp} + \nabla \cdot (\mathbf{b}J_{\parallel}) = 0 \quad (2.1)$$

where  $\mathbf{J}$  is the total plasma current density and  $\mathbf{J}_\perp$  and  $J_\parallel \mathbf{b}$  are its components perpendicular and parallel to the magnetic field line which has a tangency vector  $\mathbf{b}$ . The motion of density in the model is advective due to  $\mathbf{E} \times \mathbf{B}$  advection such that

$$\frac{\partial n}{\partial t} = -\mathbf{v}_E \cdot \nabla n \quad (2.2)$$

where  $n$  is the density of the filament and  $\mathbf{v}_E$  is the  $\mathbf{E} \times \mathbf{B}$  velocity. The potential difference across the filament is determined by the current balance in equation 2.1. In the Krashenninikov model the only source of perpendicular current in the filament is due to charge dependant curvature and  $\nabla B$  drifts which cause electrons and ions to drift in opposite directions. When this occurs across the density monopole of the filament a net excess of positive charge accumulates on one side of the filament and negative charge accumulates on the other forming a potential dipole which gives rise to the  $\mathbf{E} \times \mathbf{B}$  motion observed in experiment. The current balance equation in this case then gives [91]

$$\nabla \cdot \mathbf{J}_\perp = \left( \nabla \times \frac{\mathbf{b}}{B} \right) \cdot \nabla P \approx \frac{1}{BR} \frac{\partial P}{\partial z} = \nabla_\parallel J_\parallel \quad (2.3)$$

where the vector  $\nabla \times \frac{\mathbf{b}}{B} = \frac{2}{B} \mathbf{b} \times \kappa + \frac{2}{B^2} \mathbf{b} \times \nabla B$  points in the  $z$  direction perpendicular to both the radial and parallel directions. In the Krashenninikov model the current induced by curvature and  $\nabla B$  drifts is closed by currents flowing into the sheath at the divertor target. Assuming minimal variation in the density, temperature or potential along the magnetic field line integration parallel to the magnetic field line from divertor plate to divertor plate leads to

$$\int_0^{L_\parallel} \frac{1}{BR} \frac{\partial P}{\partial z} dl \approx \frac{L_\parallel}{BR} \frac{\partial P}{\partial z} = J_\parallel|_{sh}^u - J_\parallel|_{sh}^d \quad (2.4)$$

where  $J_\parallel|_{sh}^u, J_\parallel|_{sh}^d$  are the sheath currents at the upper and lower divertors respectively and  $L_\parallel$  is the connection length between the two divertor boundaries. The sheath currents are given by [92]

$$J_\parallel|_{sh}^{u,d} = \pm en_{u,d} c_s \left( 1 - \exp \left( \frac{e\phi_W - e\phi^{u,d}}{T_e} \right) \right) \quad (2.5)$$

where the upper divertor expression (sub/superscript u) is positive and the lower (sub/superscript d) divertor expression is negative. The wall potential,  $\phi_W$ , which is negatively biased by the formation of a sheath (see chapter 3 for a description of sheath formation), can be considered a constant reference potential in an isothermal plasma and can therefore be cast as a reference potential and set to zero. For relatively small potentials expression 2.5 can be linearised. Assuming that density and potential respectively are symmetric about the midplane, substitution of the above equation into

equation 2.4 gives the expression derived by Krasheninnikov for the potential difference across the filament.

$$\frac{e\phi}{T_e} = \frac{L_{\parallel} T_e}{BRen_t c_s} \frac{\partial n_b}{\partial z} \quad (2.6)$$

where  $c_s = \sqrt{T_e/m_i}$  is the sound speed,  $n_t$  is the density at the divertor target and  $n_b$  is the blob density. This expression relates the potential difference across the bi-normal radius of the filament explicitly to the filament density. Using this expression an  $\mathbf{E} \times \mathbf{B}$  velocity can be derived in terms of the filament density which can then be substituted into the continuity equation 2.2. By making the assumption that the target density,  $n_t = \epsilon n_b$  where  $\epsilon$  is a constant and  $n_b$  is the midplane blob density, the resulting equation for the filament density can be written as a ballistic equation if the density can be written in a separable form  $n_b(x, z, t) = n_b^x(x, t) n_b^z(z)$  where  $n_b^z \propto \exp(-z^2/\delta^2)$ . This describes a filament moving radially with a velocity

$$v = c_s \left( \frac{\rho_s}{\delta} \right)^2 \frac{L_{\parallel}}{R} \frac{n_b}{n_t} \quad (2.7)$$

where  $\rho_s = c_s/\Omega_i$  is the gyro-radius with  $\Omega_i = eB/m_i$  the gyro-frequency. This model of filament motion is commonly termed the sheath-limited model since sheath currents are responsible for closing the filament circuit.

An additional source of current closure can be included through cross-field polarization currents, where the polarization drift of the ions opposes the curvature driven current and grows in strength as the potential dipole grows. This modifies the 2D circuit equation, equation 2.6 to

$$\frac{T_e n_b}{B^2 \Omega_i} \left( \frac{\partial}{\partial t} + \mathbf{v}_E \cdot \nabla \right) \nabla_{\perp}^2 \phi = \frac{T_e}{BR_e} \frac{\partial n_b}{\partial z} - \frac{n_t c_s}{L_{\parallel}} \phi \quad (2.8)$$

where  $\phi$  is now normalized to  $T_e$  in eV. The LHS of equation 2.8 is the divergence of the polarization current. When this term is dominant over the sheath current the filament velocity obtains an alternative scaling to the sheath limited regime. The filament velocity scales with the filament size,  $\delta$ , as  $v \propto \delta^{1/2}$  [93] compared to the  $v \propto \delta^{-2}$  scaling in the sheath limited regime showing that the motion of a filament is highly sensitive to the filament size. A particular filament size exists where the strength of the two current dissipation channels is balanced [94], often termed the 'fundamental blob size', and is given by

$$\delta^* = 2\rho_s \left( \frac{L_{\parallel}^2}{\rho_s R} \right)^{1/5} \quad (2.9)$$

Generally for full solutions of equation 2.8 numerical methods are used. Such simulations have been investigated widely in literature [54, 94–103]. These simulations show that below the fundamental blob size,  $\delta \ll \delta^*$ , blobs form a mushroom like shape as a result of interchange motion with the surrounding cold plasma and a subsequent roll up

of the filament front due to secondary Kelvin-Helmholtz instabilities [98, 99]. Above the fundamental blob size,  $\delta \gg \delta^*$  the blobs form finger-like structures as the dipole vortex structure across the blob becomes entirely internalized. When  $\delta \sim \delta^*$  the two current channels balance and the filament remains highly coherent, propagating a distance many times its own diameter. These three types of behaviour are shown in figure 2.5 which were obtained using the `blob2D` module of the `BOUT++` code [104] (see chapter 4 for details of `BOUT++` and a more general blob modelling module). Numerical simulations

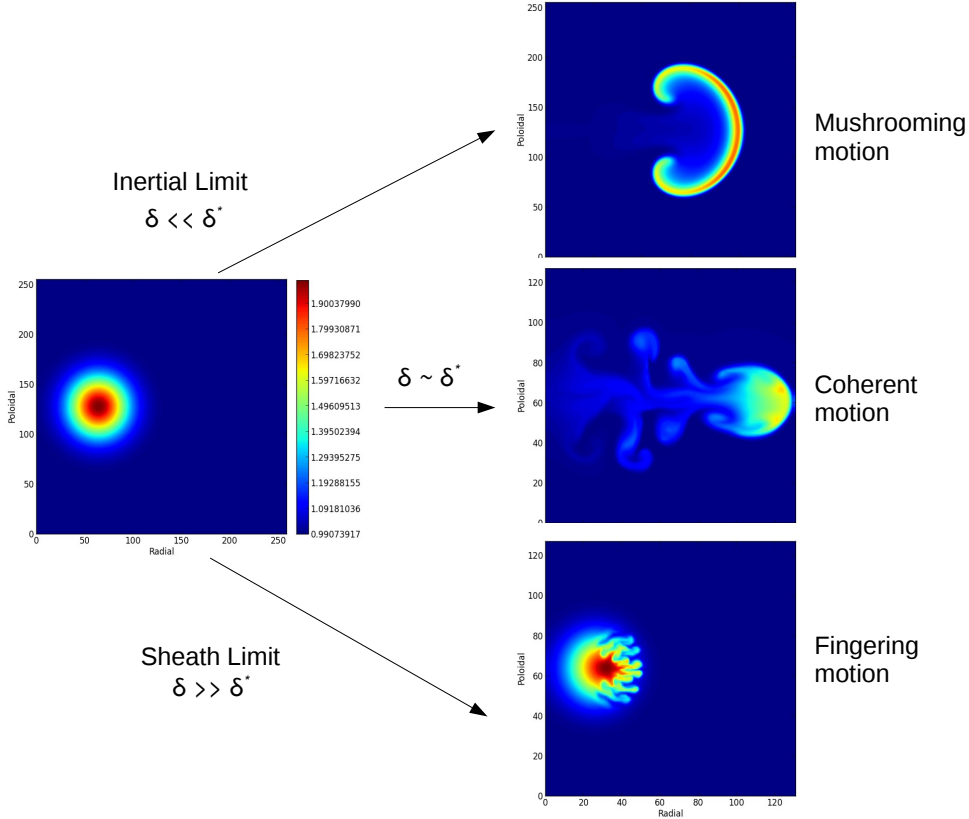


FIGURE 2.5: Examples of the three limits of 2D blob motion. Simulations were run in the `BOUT++` `Blob_2D` module. Chapter 4 describes `BOUT++`, as well as an extended version of the `Blob_2D` module.

show that not only is the blob velocity strongly dependant on blob size, but the general dynamics of blobs can differ significantly too.

Extensions of the basic model resulting in equation 2.8 have been made in a number of ways. Firstly alternative mechanisms for driving the polarization of potential have been investigated including thermal gradients [105, 106] and frictional forces induced by interaction with a 'wind' of neutral particles [107]. The latter of these two developments provides a source of drive for filament motion in linear plasma devices, such as PISCES, where forces associated with curved or varying magnetic fields are absent. Other extensions include alternative closures for the parallel current. These include accounting

for Alfvén wave generation in electromagnetic filaments [95] and enhanced resistivity induced by plasma shaping at the X-point [54, 108–110]. Electromagnetic effects tend to stabilize the structure of the filament as  $\delta > \delta^*$  which provides greater parameter ranges over which coherent motion of filaments may be observed. This may be particularly applicable to ELMs which also have a strongly filamentary structure [111] and are likely to be electromagnetic by nature [112].

Of particular interest for tokamak related applications is the inclusion of X-point shaping effects on the filament. Perhaps the most complete model of these effects to date is the two-region model [54, 113]. This model separates the filament into two coupled regions. In the first region, which encompasses the midplane to the X-point, curvature drive is present and produces the potential dipole. This current can be closed locally in the first region by cross-field polarization currents, or can be coupled into region two through parallel currents which depend on the parallel resistivity of the plasma. In the second region, which connects the X-point to the sheath, curvature drive is assumed to be negligible, so the potential dipole is a result of a coupling with region one. The second region contains current closure through sheath currents and through cross-field polarization currents. In region two the shaping of the filament, induced by the magnetic geometry, which causes the filament to become elliptically stretched and sheared [114], is included by a transformation of the perpendicular differential operators. These shaping effects strongly enhance cross-field polarization currents by increasing perpendicular gradients in the filament. In this model four regimes of blob dynamics are present:

1. *The Resistive Ballooning Regime:* In the RB regime parallel resistivity is strong and effectively decouples region one from region two. As such the dynamics of the filament are determined locally to the source of curvature drive, causing the filament to balloon at the midplane and become disconnected from the sheath. This regime is accessed at small filament sizes and/or high collisionalities.
2. *The Resistive X-point Regime:* In the RX regime the parallel resistivity is high, but still allows some coupling into the divertor region. The high resistivity however prevents the current from connecting to the sheath with the enhanced polarization in region two closing the current circuit long before any sheath connection can be established. This regime is accessed at intermediate collisionalities.
3. *The Ideal Interchange Regime:* In the  $C_I$  regime resistivity is sufficiently low that significant coupling into the divertor region can occur and the filament is connected to the sheath. The filament size is small however, so the effects of sheath current closure are sub-dominant to closure by polarization currents. This is analogous to the inertial limit in the simple 2D theory outlined previously in this chapter. This regime is accessible at low collisionality and small blob size.

4. *The Sheath Interchange Regime:* In the  $C_s$  regime the filament is once again able to connect fully to the sheath. The filament is large and the sheath current closure dominates over polarization currents. This is analogous to the sheath limited regime in simple 2D models. This regime is accessible at low collisionality and large blob size.

Other more heuristic models for X-point current closure exist [108, 110] where an enhanced cross-field electron conductivity is also included.

In recent years models for filament dynamics have been increased from 2D to 3D by including the full  $\nabla_{\parallel} J_{\parallel}$  term into the filament circuit equation and treating the sheath current closure as a boundary condition [115, 116]. The parallel current is then taken from the electron parallel momentum equation, neglecting electron inertia, electromagnetic effects and parallel ion streaming to give

$$J_{\parallel} = \frac{\sigma_{\parallel} T_e}{e} (\nabla_{\parallel} \ln(n) - \nabla_{\parallel} \phi) \quad (2.10)$$

The inclusion of parallel electron dynamics introduces the resistive drift-wave instability into the system. This is an inherently 3D instability [117] with a finite wave-number parallel to the magnetic field line. If the cross-sectional size of the filament is small then these drift-waves can have a profound impact on the filament, causing it to break up and rapidly disperse. This is shown in figure 2.6 from Angus *et.al* [115] which compares a 2D and a 3D filament simulation in a simple curved slab geometry highlighting the effect of resistive drift-waves. Angus *et.al* [116] give a condition on the filament size at which point drift-wave effects may become prominent of  $0.15\sqrt{R/2\delta_{\perp}} \geq 1$  which implies that smaller filaments will be more susceptible to breakup due to resistive drift-waves. If this is the case then this may set a lower limit on the range of filament sizes observed in the far SOL of tokamaks. It should be noted though, as will be shown in chapter 5 of this thesis, drift-wave effects are sensitive to collisional dissipation and can be readily stabilized in the SOL.

## 2.4 Filament Generation

The modelling of filament motion is an idealized situation in that it is not concerned with processes that generate the filament, but solely focusses on the isolated motion of the filament. By contrast the problem of understanding filament generation depends on a multitude of aspects and often requires the simulation of saturated turbulence; a difficult problem in any context.

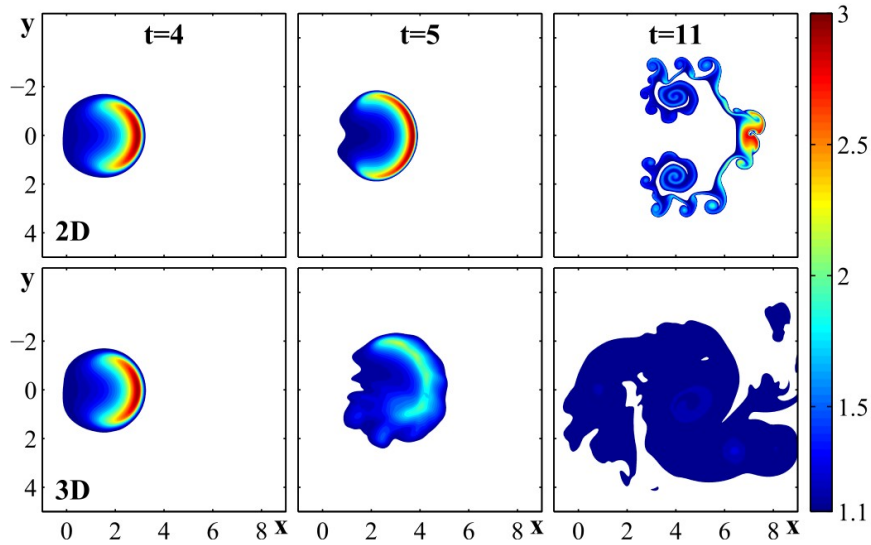


FIGURE 2.6: Results from [115] comparing 2D and 3D simulations of filament dynamics. In 3D resistive drift-wave instabilities form on the filament front and cause it to break up and disperse.

To reduce the complexity of the problem of filament generation through turbulence simulations models are often reduced to 2D. This is achieved by focussing the simulation domain on the plane perpendicular to the magnetic field at the outboard midplane region of the tokamak. Physics parallel to the magnetic field line is accounted for either by averaging along the magnetic field line or by making assumptions for the form of dissipative terms which remove plasma by convection or conduction along the magnetic field line [118]. Highly non-linear problems such as plasma turbulence are often limited by computational feasibility, usually either through an under-resolved simulation domain or insufficient computational time to reach statistical saturation. Reducing the dimensionality of the problem can therefore allow for highly resolved simulations and/or reduction in computational time. There is a large body of work conducted using models of this variety [93, 119–126]. Two particularly prominent models of this sort are the ESEL model [93, 119] and the SOLT model [122]. The ESEL model includes the effects of curvature drive and contains physically motivated models for dissipative processes and parallel losses [118]. Turbulence in the ESEL model is driven solely by interchange motion [93, 99]. The SOLT model on the other hand is able to capture drift-waves by assuming an adiabatic response for the electrostatic potential in the core region, motivated by the Hasegawa-Wakatani equations [127]. In SOLT therefore turbulence can be driven through both the interchange mechanism and by drift-waves. Both models have similar geometrical approaches where the domain is broken down into a core region and

a SOL region. In the core region an artificial source is present which provides drive for the turbulence, whilst the SOL region contains heuristic dissipation terms associated with losses to the sheaths. Being reduced to 2D, these codes cannot recover dynamic interactions in the direction parallel to the magnetic field, however they can fully resolve the perpendicular dynamics of filament generation and motion.

Filament generation in 2D codes has been compared against experiment in a number of tokamaks including TCV [128], MAST [129], NSTX and ALCATOR C-mod [130]. In the case of TCV [128] and MAST [129] comparisons are made between fluctuation data captured with probes in experiment and with synthetic probe diagnostics applied to the simulation output. Statistical moments of the fluctuation PDFs as well as characteristics of individual fluctuations agree well between simulations and experiment. The simulations contain few to no free parameters, with heuristic terms calculated from plasma parameters, rather than included in an ad-hoc manner. In the case of NSTX and ALCATOR-Cmod [130] a detailed comparison is made between experiment and a synthetic GPI diagnostic applied to the 2D plane of the simulation output. In this way trajectories of individual blob events are tracked and compared directly between experiment and simulation. Good agreement of both the poloidal velocity of blobs and the resulting Reynolds stress between the simulation and experiments in the separatrix and SOL regions of the domain is observed. The agreement between experiment and modelling is encouraging and suggests that suitably reduced 2D models can capture the leading order dynamics of edge plasma transport. This is further supported by 3D simulations of MAST conducted in BOUT [85] which suggest that the dominant processes in the SOL region are 2D by nature, however in the tokamak edge 3D effects were shown to play a role also.

Whilst 2D models can reproduce experimental measurements of blobs in the SOL, it appears that 3D effects are required to fully describe the method of blob birth; that is to say the processes that provide the perturbation that will eventually grow and become ejected as a blob. Models of these processes have shown that inverse cascade dynamics in electromagnetic drift-Alfvén turbulence may provide such an initial perturbation by transferring energy from small scale electrostatic fluctuations to meso-scale electromagnetic structures [131–134]. This transfer can either be the result of kinetic effects [131, 132] or four-wave coupling leading to a modulational instability [133, 134]. The large scale structure is driven in part by Reynolds stresses and can then be ejected by the interchange mechanism. Since drift-waves are inherently 3D and the inverse cascade requires coupling between drift-waves of differing wave-number, 2D codes are unlikely to be able to capture fully the mechanisms leading to blob generation.

## 2.5 Discussion

Particle transport due to filament ejection is complex by nature; however significant progress has been made in this area by decoupling the problem into two parts: the modelling of filament generation and the modelling of filament motion. The main aspects affecting the flux of particles from the plasma due to filaments can be listed as:

1. The number of filaments emitted from the plasma per unit time
2. The distribution of sizes of emitted filaments
3. The distribution of amplitudes of emitted filaments
4. The radial propagation velocities of the emitted filaments
5. The loss of particles from the emitted filaments

Aspects 1 - 3 are all properties of the underlying generation of the filaments, whilst aspects 4 and 5 are properties of the filaments themselves. Whilst full turbulence simulations can in principle contain all aspects 1 - 5, it is equally possible to use reduced turbulence simulations to investigate aspects 1 to 3, whilst isolated filament simulations can be used to investigate in detail aspects 4 and 5. It is this effective separation between the dynamics of filaments and the dynamics of filament production that may account for the excellent agreement often observed between edge turbulence modelling in 2D and experiment, despite the knowledge that these simulations cannot replicate properly the features of filament production. The exact comparisons made are usually encompassed by aspects 4 and 5, properties of the filaments themselves, which are known to be well approximated in 2D models.

Naturally there are many factors which complicate this simplistic splitting of filament dynamics and filament production. For example the process of filament disconnection from closed to open field lines during their production will likely set the parallel length scale of filaments which can in turn directly impact their radial motion. Furthermore given the level of approximation used in both models for filament motion and production it is likely that there are unknown aspects connecting the two.

Looking to the future there are a number of areas where continued research focus is strongly motivated. In terms of isolated filament simulations the inclusion of non-isothermal effects is of prime importance with a view to understanding not only density but thermal transport generated by intermittency. This is particularly important in the framework of next stage high-powered fusion devices where present experimental scalings for the power deposition fall-off length onto divertor targets is unfavourable [27]. Thus a fuller understanding of the detailed processes determining such transport is a

necessary step towards controlling this excess power deposition.

Including the role of electromagnetic effects is another area of importance for future modelling research. This will begin to bridge the gap between modelling of turbulence and filaments with the modelling of ELMS. During an L-H transition it is well established that turbulence is suppressed, however filaments are still observed in the SOL between ELMS [84] so to properly understand this physics an electromagnetic model will likely be required.

Models of isolated filament dynamics are currently conducted in either 2D or simplified 3D geometries. This is useful for understanding purposes and indeed, as has been demonstrated in this chapter, can yield favourable agreement with experiment. The reality of the tokamak SOL is somewhat more complicated than a slab however and it is likely that the topology of the magnetic field line may play a role in the dynamics of filaments. This will be the subject of chapters 5 and 6 where the effect of the magnetic geometry on isothermal 3D filament motion is characterized using a geometry representative of the MAST SOL.

Diagnostic development is continually increasing and this has made visual observations of filaments increasingly attainable. This type of measurement has even reached the point of complexity now where, through an advanced GPI diagnostic, the complex relationship between turbulent fluctuations and flow-shear can be observed [135]. Such a relationship has yet to be quantifiably determined by probes since probes commonly cannot measure flow-shear to the required accuracy. Properties of filament production can be inferred from the statistical moments of probability distribution functions, however to then relate these moments to profiles of, for example, poloidal velocity requires a mapping between diagnostics. This typically results in error through the accuracy of the mapping and therefore the results can only be compared qualitatively as in [68, 76]. This will be addressed in chapter 3.

## 2.6 Summary

This chapter has presented a brief review of the physics of filaments including an overview of both experimental observations and attempts at modelling filaments. The understanding of intermittent transport is of clear importance to the understanding, prediction and operation of current and future fusion devices given the universal nature of the observed processes. Experimentally filaments have been observed in a wide variety of magnetic confinement fusion devices and, as demonstrated by a brief cross-machine comparison through a literature search, the parameters of these filaments are remarkably comparable. The approach of modelling the motion of these filaments has been presented in terms of a balancing of currents, as well as the role played by turbulence simulations in

modelling filament production. It is hoped that this chapter places the work contained in the following chapters of this thesis in context and motivates the work carried out herein.



## Chapter 3

# Ball Pen Probe Measurements on MAST

### 3.1 Introduction

In this chapter the development, implementation of and results from a ball-pen probe (BPP) on MAST are presented. The BPP is a probe technique developed with the aim of directly measuring the plasma potential [136, 137]. The plasma potential is an important quantity in determining convective transport at the plasma edge, as illustrated in chapter 2. In the standard ordering of drifts in the tokamak plasma edge the  $\mathbf{E} \times \mathbf{B}$  drift, where  $\mathbf{E} = -\nabla\phi$  is a leading order contribution to advective cross-field flows (see appendix B). The equilibrium plasma potential can drive flows in the plasma edge which appear to play a role in the generation of filaments [68] in L-mode and the suppression of turbulence in H-mode [138], whilst the plasma potential on the fluctuation scale can determine non-linear turbulent interactions and the motion of filaments [55]. The plasma potential is a desirable quantity to measure however direct measurements are inherently difficult. A probe placed in a plasma does not naturally measure the plasma potential alone, but floats below the plasma potential [139]. The level of this deviation is dependant on the electron temperature of the plasma, therefore measurement of the plasma potential by conventional methods requires knowledge of the electron temperature which can tend to limit the availability of measurements. Recent forward modelling on MAST has shown that, on the scale of fluctuations, inference of the plasma potential from the floating potential can lead to significantly erroneous results [129]. This motivates the development of alternative (often more complicated) probe configurations such as the BPP.

This chapter begins with an overview of the principles of probe diagnostics in general

and in particular the BPP. The collection mechanism of the BPP is then discussed before the specific BPP design for MAST is presented. Results are then presented from measurements in three MAST shots comprising a two-point plasma current scan and a two-point density scan in Ohmic L-mode connected double null plasmas. These measurements are used to determine the validity of the BPP by comparison with complementary diagnostics. The role of the radial electric field on fluctuations is investigated, before a discussion on improvements to the probe design and concluding remarks.

### 3.1.1 Langmuir Probe Diagnostics

The Langmuir probe has been a workhorse diagnostic in laboratory plasmas since its development by Irving Langmuir in the 1920s [140, 141]. Quantities that are measurable by Langmuir probes include [142] the electron temperature, the electron density, the plasma potential and plasma flows, as well as more detailed measurements of the distribution function of ions and electrons [143]. In tokamaks probe measurements are limited to the boundary region of the plasma where power and neutron fluxes to the probe are tolerable and do not damage the apparatus. As such they are regularly used to diagnose properties of the SOL and edge plasma. The act of placing a probe in the plasma naturally has a perturbative effect and the perturbation on the plasma must be accounted for when interpreting any measurements made by the probe.

The large disparity in mass between ions and electrons in a plasma gives the electrons a much higher mobility. As a result of quasineutrality, any volume in a plasma contains approximately equal numbers of ions and electrons at any instant in time, however electrons can travel through the volume much more rapidly than ions. If a surface, such as a probe, is placed within the volume of plasma then electrons and ions will impact the surface and begin to accumulate. Since more electrons impact the surface per unit time than ions a negative charge builds up on the surface until electrons are sufficiently repelled that their flux to the surface is equal to the ion flux. The plasma response to the presence of a charge is governed by Poisson's equation [139]

$$\nabla^2 V = \frac{-e}{\epsilon_0} (n_i - n_e) \quad (3.1)$$

where  $e$  is the electron charge,  $n_e$  is the electron density,  $n_i$  is the ion density assuming singly charged ions and  $V$  is the potential in the plasma. On sufficiently fast time-scales the ions can be regarded as stationary, and the electrons adopt a Boltzmann relation such that

$$n_e = n_\infty \exp \left[ \frac{eV}{T_e} \right] \quad (3.2)$$

where  $n_\infty$  is the ion and electron density far from the source of potential. Substituting this expression into Poisson's equation gives

$$\nabla^2 V = \frac{-en_i}{\epsilon_0} \left( 1 - \exp \left[ \frac{eV}{T_e} \right] \right) \approx \frac{1}{\lambda_D^2} V \quad (3.3)$$

where the second equality results from an expansion of the exponential, assuming  $T_e \gg eV$ . The potential profile in the plasma as a result of the bare charge is an exponential  $V = V_0 \exp[-x/\lambda_D]$  where  $\lambda_D = \epsilon_0 T_e / e^2 n_\infty$  is the Debye length and characterizes the distance that the potential produced by the charge can penetrate into the plasma. Within a length scale  $\lambda_D$  quasineutrality breaks down and this region is termed the sheath. The solution of Poisson's equation can be split into separate solutions in the plasma, where quasineutrality must be satisfied, and in the sheath, where the full form of Poisson's equation applies. On time-scales where the ions appear stationary and their thermal motion can be neglected (ie they can be considered as cold), any kinetic energy obtained by ions must be a result of the electrostatic energy in the sheath such that

$$\frac{1}{2} m_i v_i^2 = -eV \Rightarrow |v_i| = \left( \frac{-2eV}{m_i} \right)^{1/2} \quad (3.4)$$

This gives an ion current density to the probe of

$$J_i = A n_i v_i \Rightarrow n_i = \frac{J_i}{A} \left( \frac{-m_i}{2eV} \right)^{1/2} = \text{const} \quad (3.5)$$

where  $A$  is the collection area of the probe. The interface between the plasma and the sheath is characterised by a sheath potential,  $V_s$ . This may be different to both the plasma and/or the probe potential (if the probe is externally biased). Poisson's equation takes the form

$$\nabla^2 V = \frac{-e}{\epsilon_0} \left( n_i - n_\infty \exp \left[ \frac{e(V - V_s)}{T_e} \right] \right) = \frac{-e}{\epsilon_0} \left( \frac{J_i}{A} \left( \frac{-m_i}{2e(V - V_s)} \right)^{1/2} - \exp \left[ \frac{e(V - V_s)}{T_e} \right] \right) \quad (3.6)$$

This equation can now be solved on both the plasma and probe side of the sheath entrance. Solving this within the sheath, by exploiting the expression for  $J_i$  to give  $n_i = n_s (V_s/V)^{1/2}$ , yields the inequality

$$V_s \leq -\frac{T_e}{2e} \quad (3.7)$$

Solving equation 3.6 in the plasma, far from the probe where  $V = 0$  and  $\nabla^2 V = 0$ , by differentiating the resultant expression for  $J_i$ , yields the inequality

$$V_s \geq -\frac{T_e}{2e} \quad (3.8)$$

Since both solutions must match at the sheath entrance, the only possible solution for  $V_s$  is

$$V_s = -\frac{T_e}{2e} \quad (3.9)$$

which gives an ion velocity at the sheath entrance of

$$v_i = \left(\frac{T_e}{m_i}\right)^{1/2} = c_s \quad (3.10)$$

This is the Bohm criterion [25] which shows that ions are accelerated to the local sound speed at the sheath entrance. If the probe is now externally biased negatively such that all electrons are repelled, the current to the probe is approximately the ion current crossing the sheath entrance [139], given by

$$I_i = A_s n_\infty \left(-\frac{2eV_s}{m_i}\right)^{1/2} \exp\left[\frac{eV_s}{T_e}\right] = A_s n_\infty \left(\frac{T_e}{m_i}\right)^{1/2} \exp\left[-\frac{1}{2}\right] \approx A_s n_\infty \left(\frac{T_e}{m_i}\right)^{1/2} \quad (3.11)$$

where  $A_s$  is the effective sheath area. This is termed the ion saturation current and represents the maximum possible ion current to the probe. In general the total current to the probe is a combination of the ion and electron currents,  $I = I_i + I_e$ . The ion current to the probe is given by the value above. The electron current to the probe can be taken as a random thermal current, reduced by a Boltzmann factor due to the probe bias,  $V$ , such that

$$I_e = -\frac{1}{4} n_\infty e v_e A_p \exp\left[\frac{eV}{T_e}\right] = -\frac{1}{2} e n_\infty A_p \left(\frac{2T_e}{\pi m_e}\right)^{1/2} \exp\left[\frac{eV}{T_e}\right] \quad (3.12)$$

The total current measured by the probe is then given by

$$I = A_p \left( J_{e,s} \exp\left[\frac{eV}{T_e}\right] + J_{i,s} \right) \quad (3.13)$$

where the transmission area across the sheath is assumed equal to the probe collection area such that  $A_s \approx A_p$  and the electron and ion saturation currents are given by

$$J_{s,e} \equiv -n_\infty e \left(\frac{T_e}{2\pi m_e}\right)^{1/2} \quad (3.14)$$

and

$$J_{s,i} \equiv n_\infty e \left(\frac{T_e}{m_i}\right)^{1/2} \quad (3.15)$$

The voltage here is taken with respect to the local plasma potential. These expressions describe the I-V characteristic of the Langmuir probe and can be used to make a number of measurements in the plasma local to the vicinity of the probe. The bulk electron/ion

density can be given by a measure of the ion saturation current, if the electron temperature is known. The electron temperature itself can be measured from the slope of the I-V characteristic by the expression[25, 139]

$$T_e = e(I - A_p J_{s,i}) \left( \frac{dI}{dV} \right)^{-1} \quad (3.16)$$

The plasma potential can be taken as the potential at which the electron current saturates, as this represents the point at which electrons are no longer repelled by the sheath. These features of the I-V characteristic are illustrated in figure 3.1.

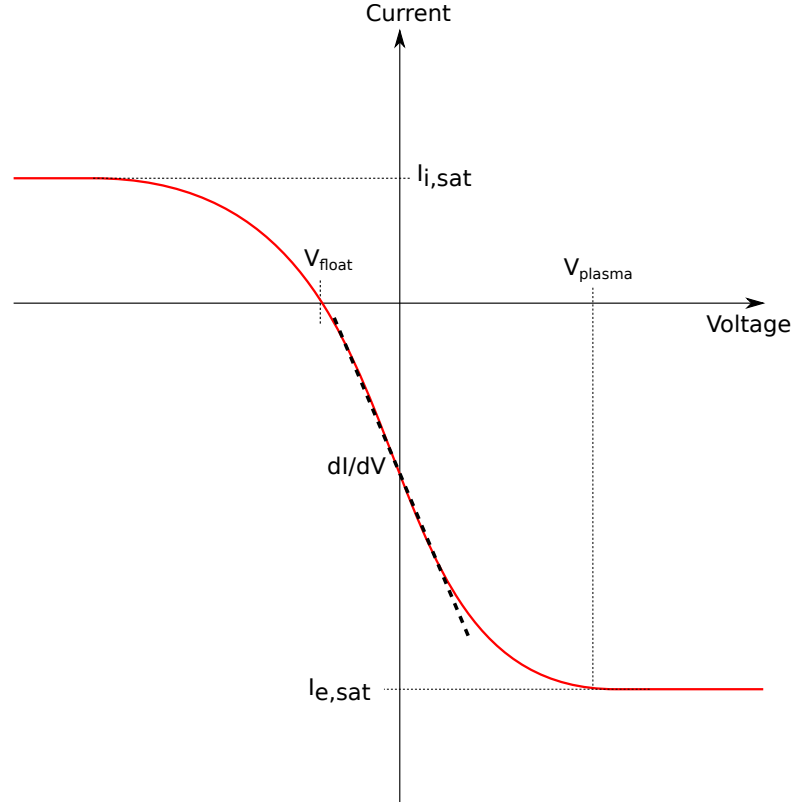


FIGURE 3.1: Schematic illustration of an I-V characteristic indicating the properties usually exploited to measure local plasma quantities.

The voltage at which the probe draws no current from the plasma does not equate to the plasma potential but instead represents the potential that the probe floats at within the plasma. Taking  $I = 0$  in equation 3.13 gives

$$V_{fl} - V_{pl} \equiv -T_e \ln \left( \frac{|J_{s,e}|}{J_{s,i}} \right) = -\frac{1}{2} T_e \ln \left( 2\pi \frac{m_i}{m_e} \right) \quad (3.17)$$

where  $V_{pl}$  is the reference plasma potential and  $T_e$  is given in eV. Relaxing the assumption of cold ions gives a finite ion temperature correction to the Bohm criterion of [25]

$$v_i = \left( \frac{T_i + T_e}{m_i} \right)^{1/2} \quad (3.18)$$

which then modifies the floating potential to

$$V_{fl} - V_{pl} = \frac{1}{2} T_e \ln \left( 2\pi \frac{m_e}{m_i} \left( 1 + \frac{T_i}{T_e} \right) \right) \quad (3.19)$$

If  $T_e \gg V_{pl}$  then the floating potential can be used to measure the local electron temperature. On the other hand when  $T_e \ll V_{pl}$  the floating potential can be used directly as a measurement of the plasma potential [142]. Unfortunately in many fusion relevant scenarios  $T_e \sim V_{pl}$  which then requires a complementary measurement of the electron temperature profile before  $V_{pl}$  can be extracted. Alternatively  $V_{pl}$  can be derived from the LP I-V characteristic, however in reality the electron current rarely saturates and the voltage corresponding to  $V_{pl}$  is difficult to accurately infer.

Many advanced probe techniques exist which draw and expand on the basic theory of the Langmuir probe. On MAST an array of Langmuir probes is situated in the divertor to measure radial profiles of electron density and temperature at the target plates. MAST also has a number of probes which are interchangeably used on a reciprocating system [144] allowing fast plunges into the plasma edge near to the midplane. These include a retarding field energy analyser [145] which measures the ion energy distribution function by systematically sampling ion energies through a series of potential grids which reflect low energy ions and electrons [145]. The Mach probe [146] and the Gundestropp probe [147, 148] exploit differences between the I-V characteristics of the plasma in a region of high and low flow to infer flow velocities.

Despite the multitude of probe measurements available in modern day experiments, the plasma potential remains a difficult quantity to accurately measure. To determine the plasma potential from an I-V characteristic requires an entire voltage sweep to obtain one measurement, limiting temporal resolution. Furthermore fluctuations in local plasma conditions can introduce significant error into the I-V characteristic. The purpose of this chapter is to investigate an alternative probe principle, named the ball pen probe, designed to directly measure the plasma potential.

### 3.1.2 The Ball Pen Probe Principle

The principle of the ball pen probe is illustrated by equation 3.17; a probe may be made to float at the plasma potential if the ion and electron saturation currents are equalized

such that

$$\ln(R) = \ln\left(\frac{I_{s,e}}{I_{s,i}}\right) = 0 \Rightarrow V_{fl} = V_{pl} \quad (3.20)$$

This principle is already exploited by the emissive probe [142]. In an emissive probe a wire, usually made of Tungsten or a Tungsten composite material, is heated externally. As the wire heats it emits electrons from its surface with the rate of emission proportional to the level of heating applied. When inserted into a plasma the negative current arising from the net emission of electrons enhances the ion saturation current. This is then varied to achieve the ratio  $R = 1$  which allows the emissive probe to float at the plasma potential. The drawback of the emissive probe is weak structural design since it requires the exposure of a thin wire to the high power fluxes in a fusion plasma. This limits the use of emissive probes in tokamaks to the far SOL.

The ball pen probe was originally developed by Adamek *et.al* [136] and exploits the difference in the Larmor radii between ions and electrons in a magnetized plasma. The original design aim of the BPP was to shield a portion of the electron current to the collector in order to equalize the total ion and electron currents to the probe. The total ion and electron currents incident on the collection surface are given by  $I_i = A_i J_i$  and  $I_e = A_e J_e$  where  $A_i$  and  $A_e$  are the collection area for ions and electrons respectively which have a current density  $J_i$  and  $J_e$ . The emissive probe increases  $J_i$  to achieve  $R = I_i/I_e = 1$ . By contrast the BPP aims to decrease  $A_e$  again with the aim of achieving  $R = 1$ . Figure 3.2 describes schematically the BPP principle originally proposed by Adamek *et.al* [136].

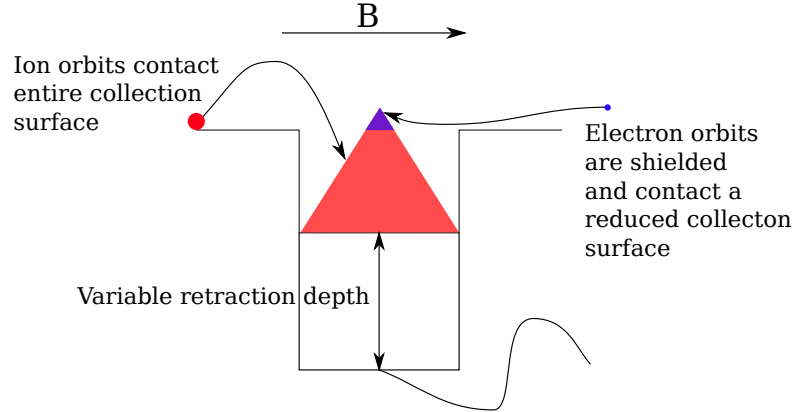


FIGURE 3.2: Schematic of the BPP principle originally proposed by Adamek *et.al*. The reduction in the electron collection area compensates the higher electron current density. By adjusting the retraction depth of the collector the ion and electron current ratio,  $R$ , is reduced to 1.

The BPP is closely related to the Katsumata probe[149], also known as the Ion-sensitive probe (ISP), where the collector is flat, rather than conical and the walls are independently biased from the collection surface. This acts to filter the electron current out of

the measurement to the collector. By independently biasing the collector the ion energy distribution can be obtained and the ion temperature can be measured. In contrast to the ISP the walls of the collection tube in the BPP are made of an insulating material, usually Boron Nitride. The conical collector can then be retracted into the shielding tube until the ion-electron current ratio equalises. Figure 3.3 shows the original BPP designed by Adamek *et.al*, alongside measurements of  $R$  as the retraction depth of the collector,  $h$ , is increased, taken from [136].

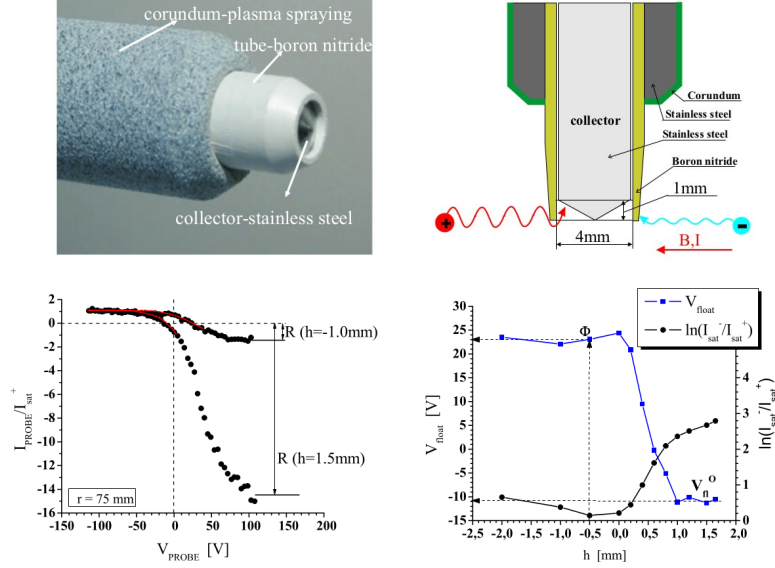


FIGURE 3.3: Top: The original BPP design for the CASTOR tokamak by Adamek. Bottom: Measurements on CASTOR showing the systematic decrease of  $\ln(I_i/I_e)$  as the BPP is retracted. At  $h < -0.5\text{mm}$  the BPP measures the plasma potential. Images taken from [136].

Figure 3.3 demonstrates that the ratio  $R$  is reduced in a BPP by retraction of the collector inside the shielding tube. The BPP measurement of  $V_{pl}$  has been compared favourably to measurements made by an emissive probe on CASTOR [137] and a self-emitting Langmuir probe on COMPASS [150]. The BPP has also been implemented on the ASDEX-Upgrade tokamak to make measurements of the plasma potential during L-mode [151, 152] and H-mode [151, 153]. The BPP principle has also been implemented in low temperature plasma devices [154, 155] where the electrons remain strongly magnetized, but unlike a tokamak the ions are demagnetized. In these plasmas the BPP was again shown to measure the plasma potential effectively, though the shielding of the electron current to the collector becomes highly dependant on the probe geometry [155]. The empirical success of the BPP is encouraging and motivates continued study. Furthermore the BPP is a robust diagnostic capable of surviving the harsh environment at the tokamak plasma edge. Steep gradients at the edge of tokamak plasmas are important features of tokamak operation, therefore the capability of the BPP to diagnose this

region is desirable. This gives the BPP a unique capability among probe diagnostics for well resolved plasma potential measurements across the separatrix. The BPP is hindered however by a lack of a first principles model in support of its operation.

### 3.2 The BPP Collection Mechanism

The simple model for BPP collection proposed originally by Adamek is appealing and shows some qualitative agreement with experiments, however a review of BPP results in literature reveals a number of empirical features which suggest that the physics of BPP collection is more complex than the simple model proposed by Adamek *et.al.* Firstly, as acknowledged by Adamek in [136, 137], the BPP on CASTOR was never observed to reduce the electron current to exactly the level of the ion current. This suggests that a net excess of electrons over ions always occurs at the BPP collection surface, even when the collector is retracted well below the ion Larmor radius,  $\rho_i$ . This also illustrates a second discrepancy; the ratio  $R = I_e/I_i$  remains close to unity even when the entire collector is retracted well below the shielding tube entrance[136]. The simple model based on geometrical shadowing predicts  $I_e \rightarrow 0$  as the collector retracts below the shielding tube entrance. These two observations indicate that electron transport to the collector occurs by a different means, and in the case of a deep collector retraction this transport must occur across the magnetic field. This is further evidenced in [156] where an alternative BPP design was implemented where the conical collector was replaced by a flat collector, removing the possibility of geometrical shadowing. A current in both the ion and electron channels was observed at the probe surface, even when the collector is retracted below  $\rho_i$ . This shows that the conical shape of the collector is not necessary for the BPP measurement and again suggests that cross-field transport processes must play a role in BPP collection.

Dedicated modelling of the BPP [157], as well as modelling of ISPs [158, 159] has shown that the BPP perturbs the local Maxwellian distribution of particles due to the shadowing of electron and ion trajectories into the collection tube. A potential forms within the shielding tube which can transport electrons to the collection surface by  $\mathbf{E} \times \mathbf{B}$  motion. This has been cited as an explanation for the anomalously high electron currents often observed in ISPs [159], and also plays a role in related problems such as heat fluxes to tile gaps [160]. Dedicated ISP experiments using a split collection surface have shown that the electron and ion current to the collection surface is asymmetric [161], suggesting experimentally that  $\mathbf{E} \times \mathbf{B}$  motion plays a role in ISP collection. The question of BPP collection however has received significantly less attention in literature. Since the BPP shielding walls are insulating, they cannot be externally biased, but can sustain a potential due to charge accumulation. Any potential distribution within the shielding

tube will likely be complex and will consist of at least two parts: 1. Sheath formation on the walls of the tube where electrons may impact along the field line. 2. An ion space charge in the centre of the tube where ions can initially penetrate beyond the reach of electrons. The resulting motion of ions and electron in response to this potential structure will likely perturb the potential further until a steady state is reached.

As discussed, the collection process to the collector in a BPP appears to occur perpendicular to the field line and is likely, in part at least, to be the result of  $\mathbf{E} \times \mathbf{B}$  motion. To avoid specific details of the collection mechanism for now a simple model is assumed where both ions and electrons are transported down the shielding tube to the collector at a constant collection velocity  $v_c$ . The physics behind  $v_c$  will be discussed shortly, however first an argument based on a filtering of the ion distribution function will be laid out which can be used to bound possible values of  $v_c$ . Electron impact on the shielding tube walls will lead to formation of a sheath. The sheath, formed on the shielding tube walls is assumed to form homogeneously on all walls. In reality the biasing of the shielding walls will likely vary with depth, since the electron distribution function has a progressive loss of high energy electrons through the sheaths. For the purpose of simplicity however this is not accounted for here. The presence of the sheath repels electrons with energies below the energy required to cross the sheath and impact the wall. This corresponds to a parallel velocity  $v_{||} > v_{sh}$  where  $v_{sh}$  is the velocity required to penetrate the sheath, given by

$$\frac{1}{2}m_e v_{sh}^2 = eV_{sh} \Rightarrow v_{sh} \equiv \left( \frac{2eV_{sh}}{m_e} \right)^{1/2} \quad (3.21)$$

Only a small fraction of the electron distribution function satisfies  $v_{||} > v_{sh}$  and the distribution function is approximately unfiltered, but is reflected by the sheath. Consequently all electrons entering the tube are repeatedly reflected whilst undergoing cross-field transport to the collection surface, and the electron current to the collection surface is approximately

$$J_e \approx -n_{0,e} e v_c \quad (3.22)$$

By contrast ions are not reflected by the sheath but can freely impact the walls of the collection tube. Assuming the collection surface is retracted deeper than the ion Larmor radius,  $h > \rho_i$ , where  $h$  is the retraction depth, for the collection of ions to occur their time spent in crossing the diameter of the collection tube must be longer than their time spent travelling down the tube to the collection surface. If this is not the case then ions will impact the walls before they can be collected. This results in a condition on the ion parallel velocity of

$$\frac{d}{v_{||,i}} > \frac{h}{v_c} \Rightarrow v_{||,i} < v_c \frac{d}{h} \quad (3.23)$$

This then limits the collection of ions to the portion of the velocity distribution function that satisfies the above condition such that the ion current to the collector is given by

$$J_i = ev_c \int_{-\infty}^{\infty} dv_{\perp} \int_{-v_c \frac{d}{h}}^{v_c \frac{d}{h}} dv_{\parallel} f_i(\mathbf{v}_{\perp}, v_{\parallel}) \quad (3.24)$$

where  $f_i$  is the ion distribution function. Taking  $f_i$  as a Maxwellian this can be reduced to

$$J_i = ev_c n_{0,i} \int_{-v_c \frac{d}{h}}^{v_c \frac{d}{h}} dv_{\parallel} \bar{f}_i(v_{\parallel}) \quad (3.25)$$

where  $\bar{f}_i(v_{\parallel})$  is the normalized 1D Maxwellian distribution in  $v_{\parallel}$ . In a more advanced version of this model the perpendicular velocity distribution may also affect collection, however this is not included here and only the parallel velocity distribution is considered. The filtering of the ion distribution function acts to reduce the ion current to the collector. The transport of ions and electrons to the collector is described schematically in figure 3.4.

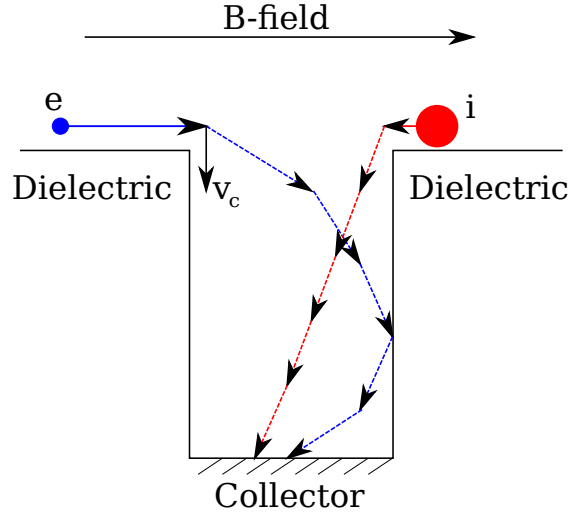


FIGURE 3.4: Schematic illustration of the motion of ions and electrons to the collection surface in the simple model of ion kinetic filtering.

It is now possible to estimate the value  $\alpha = \ln(I_e/I_i)$  using

$$\frac{I_e}{I_i} = \frac{A_e n_{0,e}}{A_i n_{0,i}} \left( \int_{-v_c \frac{d}{h}}^{v_c \frac{d}{h}} dv_{\parallel} \bar{f}_i(v_{\parallel}) \right)^{-1} \quad (3.26)$$

where  $n_{0,e}$  and  $n_{0,i}$  are the electron and ion densities entering the collection tube and  $A_e$  and  $A_i$  are the collection areas for electrons and ions respectively.  $A_e = A_i$  is assumed here. It is likely that the exterior surfaces of the BPP will play a role in determining the incoming densities however this requires advanced modelling and is not accounted

for here and  $n_{0,i} = n_{0,e}$  is assumed. The current ratio is estimated as

$$\frac{I_e}{I_i} = \left( \int_{-v_c \frac{d}{h}}^{v_c \frac{d}{h}} dv_{\parallel} \bar{f}_i(v_{\parallel}) \right)^{-1} \quad (3.27)$$

Figure 3.5 shows a calculation of  $\alpha = \ln(I_e/I_i)$  based on the model presented here for a typical ion temperature of  $10eV$  with  $d = 4mm$  and  $h = 5mm$ . Figure 3.5 shows

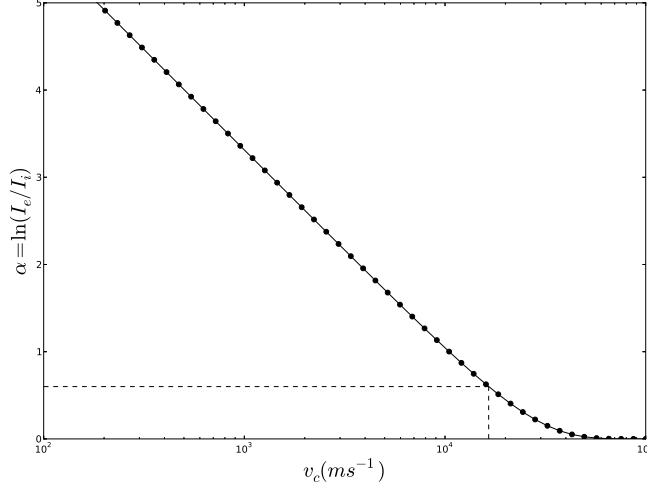


FIGURE 3.5: Predicted  $\alpha$  from the ion filtering model as a function of collection velocity. Indicated is the velocity required for  $\alpha = 0.6$ .

that a collection velocity on the order of  $10 - 50km/s$ , which is on the order of the sound speed,  $c_s \approx 20km/s$  at  $T_e = 10eV$ , is required in this geometry for experimentally relevant values of  $\alpha$ . This simple model can now be used to assess possible mechanisms of collection. A trivial example is to test whether the motion of the reciprocating probe alone can affect the collection. The RP moves with a velocity of  $v \approx 1m/s$ , which is well below the order required for  $\alpha_{BPP} < 0.6$  and can therefore not contribute to BPP collection. It is likely that  $\mathbf{E} \times \mathbf{B}$  motion is, at least partly, responsible for this collection and two possible scenarios can be considered:

1.  $\mathbf{E} \times \mathbf{B}$  motion due to sheath formation on the shielding walls. Taking an order of magnitude electric field as  $E \sim 2T_e/d$  where  $d$  is the probe diameter and  $\phi \sim T_e$  is taken for the potential on the shielding walls gives a collection velocity due to  $\mathbf{E} \times \mathbf{B}$  motion of

$$v_c \sim \frac{E}{B} \sim \frac{2T_e}{dB} \sim 10km/s \quad (3.28)$$

2.  $\mathbf{E} \times \mathbf{B}$  motion due to ion space charge. This was investigated in [159] where the approximate collection velocity was estimated as

$$v_c \sim \frac{en_id}{4\epsilon_0 B} \sim 1000 km/s \quad (3.29)$$

The analysis of [159] predicts very large  $\mathbf{E} \times \mathbf{B}$  velocities due to ion space charge which is likely to be a result of a large overestimate of the electric field strength. Nevertheless it is plausible that both mechanisms may provide a means for collection in a BPP. A deeper analysis is hindered by the complexity of the probe geometry and it is likely that a full understanding of the BPP collection mechanism will require full 3D3V particle-in-cell modelling which is beyond the scope of this thesis.

### 3.3 Design and Testing of the MAST BPP

#### 3.3.1 BPP Design for MAST

The BPP for MAST has been designed as a modification to an existing probe head with Gundestropp probe capabilities [147, 148] rather than as a bespoke design. This is motivated by the reduced cost of modification compared to full fabrication, combined with the as yet unproven nature of the BPP. Figure 3.6 shows the design of the BPP. The normal vector to the face of the probe lies anti-parallel to the major radius of the plasma. Probe tips are held in place by a two-part retainer which sits inside the body of the probe (shown in the cutaway in figure 3.6) held in place by a strut (not shown). Probe tips on the axial surface are inherited from the Gundestropp probe (see [148] for a description) and are not used in this study. The layout of the probe face is shown in figure 3.7.

The positions of pins BPP2, Vf1 and P1 were inherited from an existing triple probe configuration on the face of this Gundestropp probe. The geometry of the probe face was designed to eliminate the shadowing of any probe tip by any other along a magnetic field line. Table 3.1 shows the BPP pin diameters and retractions.

Pin	Retraction (mm)	Diameter
BPP1	2	1.5
BPP2	5	4
BPP3	8	1.5

TABLE 3.1: Parameters of the BPP pins designed for maximum flexibility.

Significant variability was designed into both the retraction and diameter of the probe tips. Since this work was the first implementation of a BPP on MAST there was little

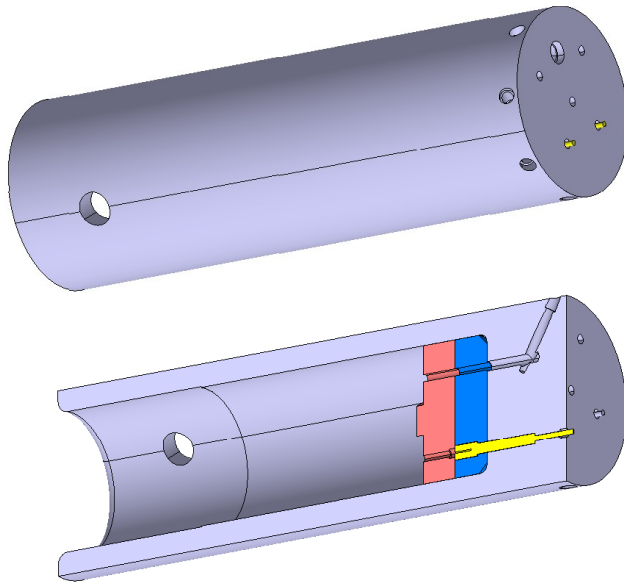


FIGURE 3.6: 3D rendering of the MAST BPP showing the design of the BPP. Also shown is the internal structure developed to hold the Langmuir and BPP pins in place. Shown is the particular case of a Langmuir probe, though the design is identical for all pins on the probe face.

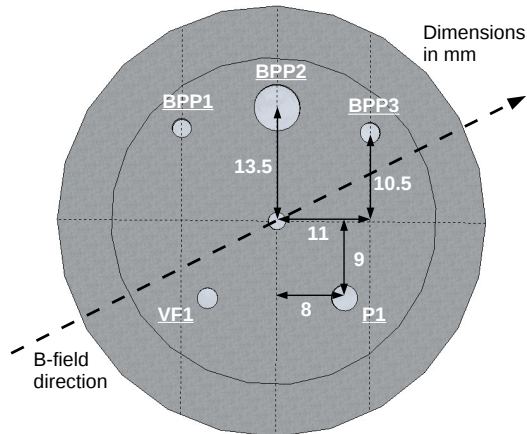


FIGURE 3.7: Dimensions between probe tips on the BPP probe face. BPP2, P1 and VF1 were inherited from the Gundestropp design. The head is mirror symmetric about the vertical axis. The layout of probe tips is designed to minimize shadowing between probes, however this results in probe tip distances  $\sim 2$ cm, which may be too large for detailed analysis of correlations of fluctuations between pins.

guidance on the specific design of pin geometries. To mitigate the risk of choosing an inappropriate pin geometry a range of parameters was chosen, guided by previous experiments. As will be shown later BPP2 proved to be the best combination of retraction and diameter. Other than the addition of extra probe pins to the probe face, the other significant modification from the Gundestropp probe design was the detailed design of the probe tips, shown in figure 3.8. The original design of the probe tips on the face of

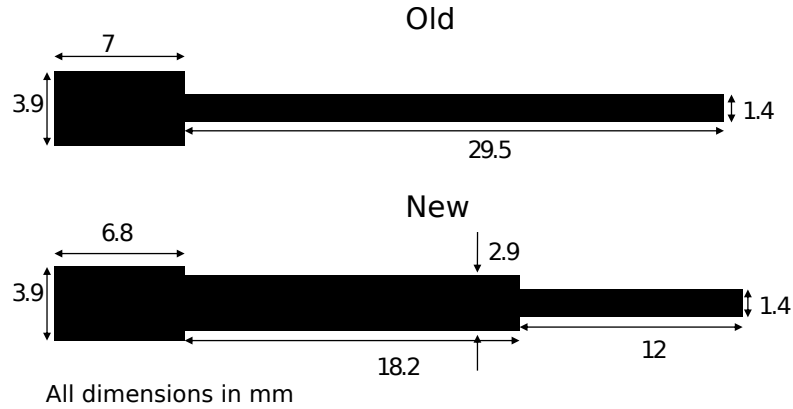


FIGURE 3.8: Redesign of the probe tip structure for the BPP. The specific case illustrated is for a Langmuir probe, however the BPP tips are identical with dimensions scaled accordingly. The redesign provides far greater structural stability during assembly.

the probe, shown in the upper section of figure 3.8, were found to be structurally fragile. This presented a significant challenge in assembly where multiple probe tips were shattered. This called into question the durability of the probe tip during installation onto MAST and as a result the tip was re-designed with the aim of added structural stability. To achieve this a pedestal structure of the probe tip was added, with 0.5mm gradient added to each right-angle. These features significantly increased the durability of the probe tips. The design was similar in the case of BPP probe tips with dimensions scaled accordingly.

### 3.3.2 Electronics

The BPP pins were operated as floating measurements throughout the experimental time on MAST. The BPP potential, as well as the floating potential measurements are made with respect to a diagnostic earth. The pins are connected to a set of optical isolation amplifiers with an impedance of  $300k\Omega$  and a bandwidth of 50kHz. This bandwidth is sufficient for fluctuation measurements in the SOL which typically occur with frequencies  $\leq 30\text{kHz}$ . The signals were digitized with a sampling frequency of 500kHz.

### 3.3.3 Analysis of Noise

Noise on the BPP signals occurs from two principle sources: High frequency, low amplitude noise which occurs within the electronics of the system, and narrowband bursting noise which occurs due to electrical pick-up from poloidal magnetic field coils. The mid-plane reciprocating probe, upon which the BPP is mounted, lies in close proximity to the P5 coils and to a lesser degree the P4 and P6 coils. The electronic noise is random, and generally does not affect the measurements with the BPP. The PF pick-up noise has a distinct response in the BPP signals. Figure 3.9 shows the structure of the PF noise during shot 28815, where the probe was positioned far from the plasma edge such that no interaction between the probe and the plasma occurred. Note that this is a worst case scenario with the amplitude of PF noise decreasing as the probe moves towards the plasma, away from the PF coils.

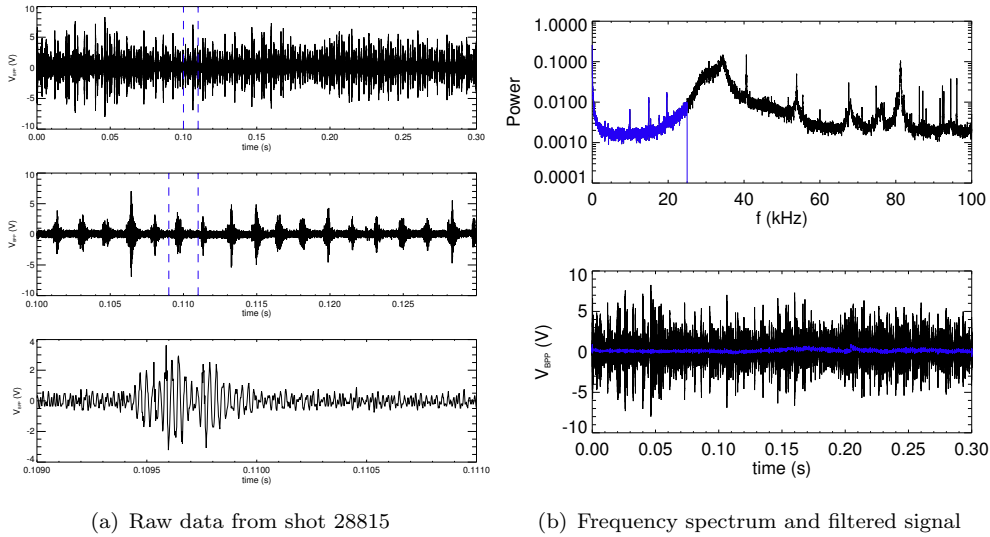


FIGURE 3.9: Structure of PF pick-up induced noise from shot 28815, alongside its power spectrum. The power spectrum is normalized to the total power within the signal. Filtering below the primary noise peak effectively removes the noise. Filtered signals are shown in blue.

The PF noise has a characteristic frequency peak at approximately 30kHz with higher frequency harmonic peaks present towards the upper end of the spectrum. The power in the primary frequency peak dominates the spectrum and is nearly 100 times greater than the baseline power. Filtering the frequency spectrum below the primary peak (blue profiles in figure 3.9) reduces the noise source by an order of magnitude from  $\pm \sim 5V$  to  $< \pm 0.5V$ . Figure 3.10 shows the effect of the PF noise during two shots where significant interaction with the plasma was observed.

In each shot the PF noise is identifiable in the frequency spectrum. Filtering the signal

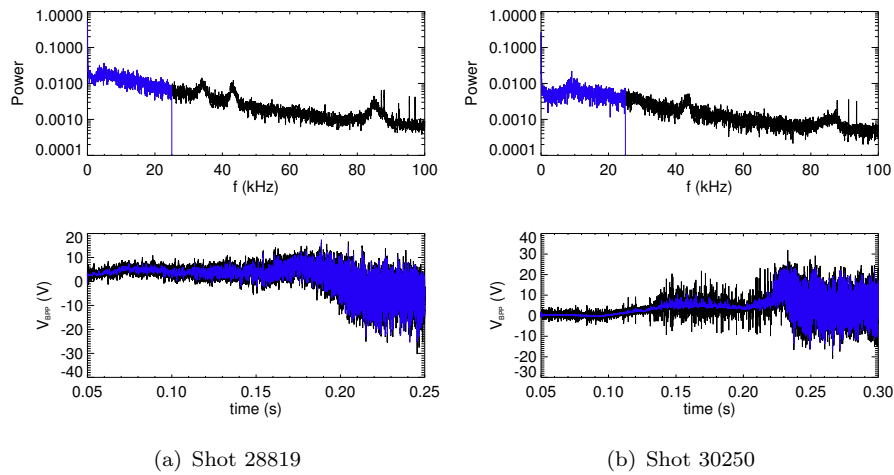


FIGURE 3.10: Examples of PF pick-up noise during a reciprocation of the probe into the plasma in shots 28819 and 30250 (described later in the chapter). In each case the PF noise is identifiable in the frequency spectrum, normalized to the total power within the signal. Filtering below the primary frequency peak removes the noise, but retains the fluctuation characteristics during the probe-plasma interaction phase.

below the primary frequency peak removes the PF noise, but retains the shape of the underlying signal during strong interaction with the plasma. In figure 3.11 the form of individual fluctuations in both the BPP and  $I_{\text{sat}}$  time series are compared in shot 30250 with and without the filtering of the PF noise.

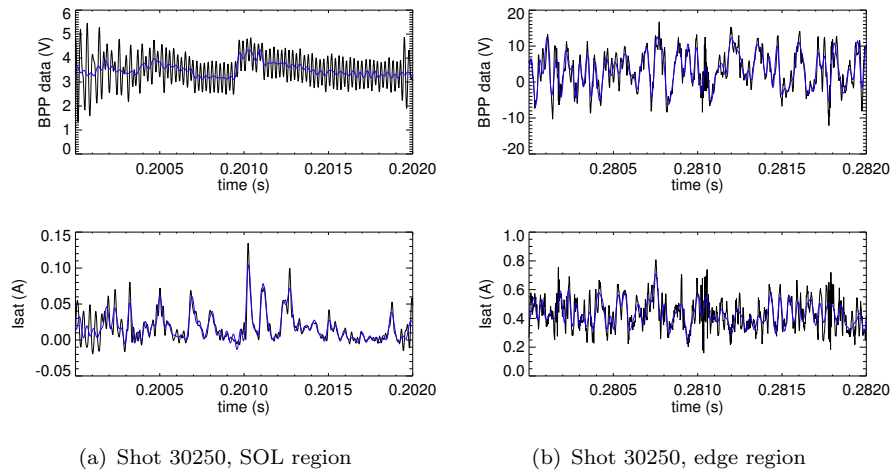
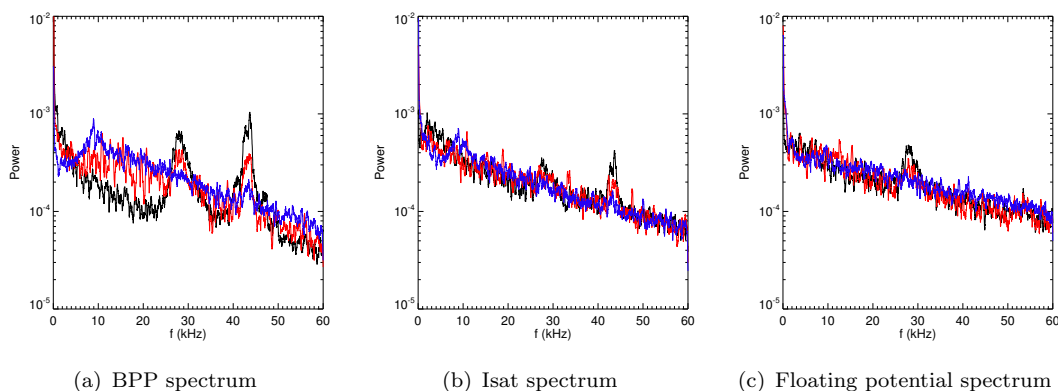


FIGURE 3.11: Fluctuation data from the BPP and an LP in  $I_{\text{sat}}$  mode in shot 30250 sampled in the SOL region and the edge region. In the SOL the BPP signal lies well below the noise level, though in the edge region where the interaction of the plasma is strong the BPP signal dominates over the noise. Overlaid are the filtered signals with the PF noise removed.

The structure of fluctuations in the  $I_{\text{sat}}$  signal and in the edge region of the BPP signal

show minimal variation between the filtered and unfiltered cases suggesting that PF noise does not affect the signal in these cases. In the SOL region of the BPP signal however the noise is on a similar level to the underlying signal. In this region fluctuations occur primarily due to large intermittent events which can be identified as filaments. The Isat signal in the SOL shows multiple blobs passing the probe, whilst the BPP signal in the same time frame only shows one significant event. The initial impulse in the BPP signal is followed by a long falloff time which encompasses many blob events in the Isat signal. The example given in figure 3.11 is representative of the BPP signal in the SOL in all shots analysed. Figure 3.12 shows the frequency power spectrum, normalized to the total power in the spectrum, sampled in the SOL, in the region where the probe crosses the separatrix and within the plasma edge, of the BPP signal and the Isat signal.




---

FIGURE 3.12: Power spectra, normalized to the total, from the BPP (a), Isat (b) and floating potential (c) signals in shot 30250. The spectra are sampled in the SOL (black), separatrix region (red) and edge region (blue). The BPP shows a significant suppression of the frequency spectra in the SOL.

Figure 3.12 shows a systematic suppression of fluctuations in the BPP signal in the SOL region. This suppression is not present in the Isat or floating potential signals, though in all three cases the PF noise contributes a larger portion of the power in the signal than the near separatrix and edge regions. Whilst it is possible that fluctuations in the plasma potential, which should dominate the BPP signal, are strongly suppressed in the SOL the frequency suppression is more likely associated with an excessively high probe impedance. The probe and amplifier form an RC circuit where the resistance is provided by the coupling of the probe with the plasma, and the capacitance is provided by interaction between cables in the probe head. A typical RC circuit acts as a low pass filter since the capacitor requires a finite amount of time to charge up. Before the capacitor is charged current can flow through it to ground. This filters the high frequency component of the signal. If the resistance of the probe is large, then the current drawn

by the probe is weak and the capacitor takes longer to charge, thereby filtering a larger amount of the frequency spectrum. This behaviour has recently been observed in BPPs used in low temperature plasmas, where very high impedance amplifiers were required to accurately measure the frequency range of the BPP signal [154, 155]. Whilst the capacitance of the cabling to the amplifier is not known, it will remain constant across all BPP measurements. Consequently the increase in high frequency power in the BPP spectrum as the probe nears the plasma edge shows that the probe impedance varies as the local plasma conditions vary. By the time the probe enters the plasma edge the BPP frequency spectrum no longer exhibits significant filtering compared to the Isat and floating potential signals.

From the analysis presented in this section the following conclusions are drawn:

- The primary source of noise in BPP measurements, as well as floating potential and Isat signals, arises from poloidal field coil pick-up and has a distinctive frequency spectrum.
- This noise does not affect the measurement of average profiles.
- The noise can strongly affect BPP fluctuation measurements in the SOL region, but can be removed by filtering the signal in frequency spectrum below the primary noise peak.
- Strong suppression of the high frequency components of the BPP signal occurs in the SOL as a consequence of an increased probe impedance in the cold, low density SOL plasma. The suppression of BPP fluctuations in the SOL makes the analysis of blob fluctuations in the BPP signal infeasible. The SOL frequency suppression could be avoided in future implementations of the BPP by the use of a high impedance amplifier [154].

### 3.3.4 Comparison of BPP pins

This section briefly compares the response of the three BPP pins built into the probe. The comparison is conducted in shots 28819, 28830 and 28834. In shot 30250, which occurred much later in the MAST M9 experimental campaign, a failure in pin 3 prevented further comparison. Figure 3.13 compares the frequency spectra of the three BPP pins.

From figure 3.13 it is clear that the signal in the highly recessed pin, BPP3, is strongly suppressed across the entire spectrum and the PF noise, analysed at the beginning of this section, dominates the signal. Pin BPP1 follows a similar trend though to a lesser extent. In particular in shot 28819 pin BPP1 matches the low frequency part of the spectrum

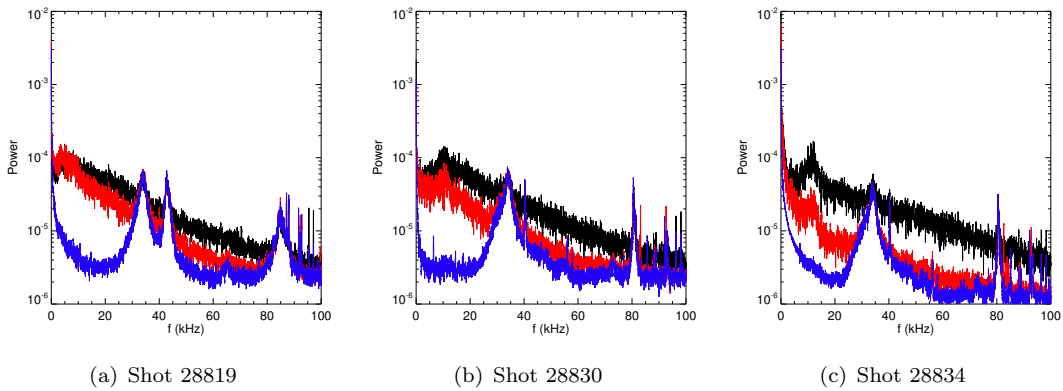


FIGURE 3.13: Comparison of the fluctuation spectra between pins BPP1 (red) BPP2 (black) and BPP3 (blue) in shots 28819, 28830 and 28834. A systematic suppression of the frequency spectra is observed in BPP3 and lesser so in BPP1 with respect to BPP2. The signal from BPP3 is dominated by PF noise.

of pin BPP2, however the two then deviate, and the PF noise certainly plays a stronger role in the BPP1 power spectrum than pin BPP2. The deviation between the two pin spectra is greater in shot 28830 and greater still in shot 28834. The strong frequency suppression in pins BPP1 and BPP3 makes them unsuitable for use in experimental profile measurement, as such the BPP2 pin will be used in this chapter as the principal BPP measurement.

### 3.4 Radial Profile Measurements

During the MAST M9 campaign (April - October 2013) the BPP was placed on the reciprocating probe (RP) system [144] on MAST. The RP is located at the outboard midplane in a connected double-null (CDN) MAST plasma, supported by a flange at the equatorial plane. The placement of the RP in relation to a standard MAST CDN plasma is shown in figure 3.14.

There are two drive mechanisms for the reciprocation of the probe. A motorized drive is used to set the initial placement of the probe head. This can move the probe head by up to 1m from outside to inside the vessel through a high vacuum valve. Once in place a pneumatic drive is used to quickly plunge the probe head into the plasma and subsequently retract it. The probe can reciprocate a maximum of 10cm over 0.2s inwards and 0.4s outwards, attaining a maximum velocity  $\sim 1\text{ms}^{-1}$ .

The reciprocation of the probe head allows for the measurement of radial profiles of plasma parameters with the BPP. Radial profile measurements have been made in three Ohmic L-mode CDN plasmas in MAST. These are shots 28819, 28830 and 28834. The details of these shots are summarized in table 3.2. Shots 28819 and 28830 can act as

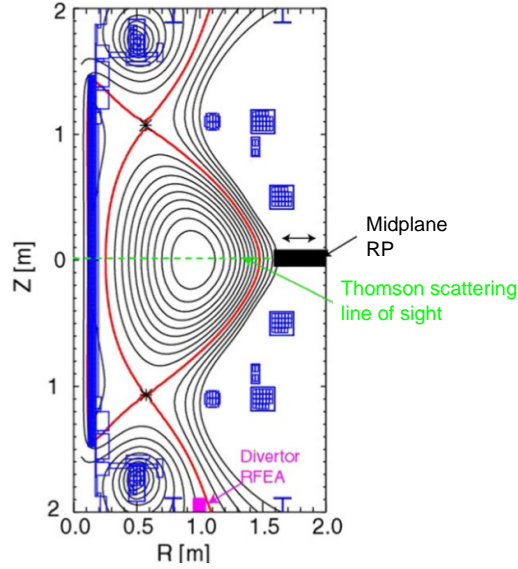


FIGURE 3.14: Position of the reciprocating probe system on MAST in a CDN plasma. The probe is located at the outboard midplane and samples the plasma over the same line of sight as the Thomson scattering diagnostic. Image adapted from [145]

Shot	$I_p$ (kA)	$B_T$ (T)	$n_{e,sep}$ ( $10^{19}$ ) $m^{-3}$	$\bar{n}_e$ ( $10^{18}$ ) $m^{-2}$
28819	400	0.585	0.7 - 0.9	120
28830	600	0.585	0.7 - 0.9	110
28834	600	0.585	0.2 - 0.4	70

TABLE 3.2: Relevant parameters for MAST shots 28819, 28830 and 28834, in which the BPP was reciprocated into the plasma edge.  $I_p$  is the plasma current,  $B_T$  is the toroidal field on the magnetic axis,  $n_{e,sep}$  is the electron density at separatrix and  $\bar{n}_e$  is the line integrated electron density.

a two-point plasma current scan, whilst shots 28830 and 28834 can act as a two-point electron density scan. The reciprocation profile of the RP is identical in each shot, however the motion of the plasma edge varies and leads to varying reciprocation depths (with respect to the plasma edge). The plasma edge radius is measured by EFIT[162] constrained by the peak in  $D\alpha$  light emission at the plasma edge. This measurement is subject to systematic uncertainty of  $\approx 2$ cm, however since the error is systematic it does not affect comparisons between datasets containing the error, and therefore will not affect any conclusions in this chapter. The uncertainty has the effect only of shifting the  $x$  axis of radial measurements. In figure 3.15 the position of the end of the BPP is compared to the position of the plasma edge. Shot 28819 exhibits a deeper reciprocation than shots 28830 and 28834. The motion of the plasma edge can be accounted for by constructing profiles as a function of  $R - R_{LCFS}$ , allowing for a direct comparison between the three shots.

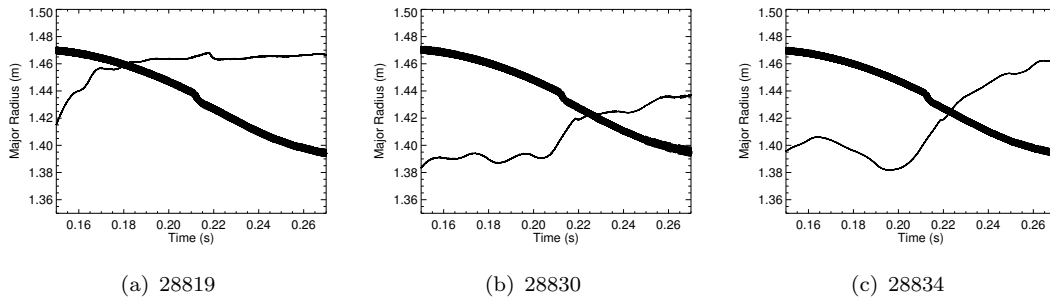


FIGURE 3.15: Position of the BPP head (thick) compared to the position of the plasma edge (thin) during the reciprocation of the BPP for shots 28819, 28830 and 28834.

BPP data is sampled in the time interval  $t = [0.15, 0.27]$ s in each shot. To construct profile measurements the data is separated into 50 discrete temporal windows with a width  $\approx 2.4$ ms. On this time-scale the motion of the RP can be neglected and the profile can be constructed from averages within each window. Each window contains  $> 1200$  data points which is sufficient to make a mean measurement with insignificant error. The standard error on the mean of a data set of  $N$  samples is

$$\sigma_m \approx \frac{\sigma}{\sqrt{N}} \quad (3.30)$$

where  $\sigma$  is the standard error of the data sample,  $x_i$ , given by

$$\sigma \approx \left( \frac{\sum_i x_i^2 - \frac{1}{N} (\sum_i x_i)^2}{N - 1} \right)^{1/2} \quad (3.31)$$

Thus by making a large number of samples the error on the mean is greatly reduced (provided the samples are independent).

Figure 3.16 shows the plasma current evolution in the three shots analysed.

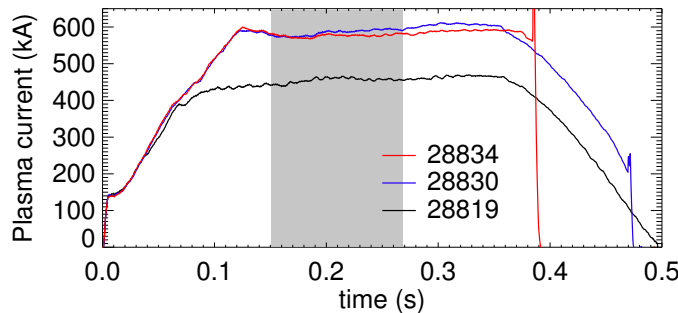


FIGURE 3.16: The plasma current evolution during shots 28819, 28830 and 28834. Highlighted is the region in which BPP data is sampled. The plasma current remains relatively constant within this region, allowing the plasma to be treated as steady.

The plasma current remains steady during the reciprocation of the RP so the plasma

conditions can be considered approximately constant during the reciprocation of the BPP.

### 3.4.1 Potential Profiles

Figure 3.17 shows the mean potential profile measured by the BPP compared with the floating potential during the time window  $[0.15, 0.27]$ s in shots 28819, 28830 and 28834.

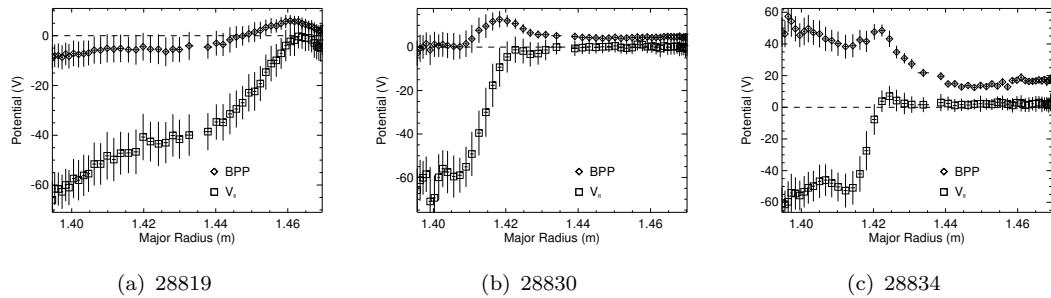


FIGURE 3.17: Potential measured by the BPP, compared to the floating potential as a function of the major radius  $R$  for shots 28819, 28830 and 28834. Error bars represent one standard deviation of the data within each window. The error on the mean is  $\approx 35$  times smaller than the standard deviation.

The signal measured by the BPP differs significantly from the floating potential during the reciprocation of the probe. Before associating the BPP measurement with the plasma potential, some features of the measurement and its comparison to the floating potential can be made. Firstly the polarity of the BPP signal is opposite to the floating potential in a significant portion of each shot. This indicates that the BPP signal cannot simply be a scaled measurement of the floating potential. Secondly the shape of the BPP profile contains significant qualitative differences to the shape of the  $V_{fl}$  profile. This is particularly prevalent in shot 28830 where the BPP signal exhibits a change in sign of its gradient, where the  $V_{fl}$  profile has a continuously decreasing profile. Finally the difference between the two profiles grows during the probe reciprocation, suggesting that a change in plasma parameters may be responsible for the deviation between the two profiles. These features are all in agreement with the qualitative features expected from expression 3.17. The floating potential is always more negative than the BPP potential due to the strong electron temperature contribution. The deviation between the two profiles increases during the reciprocation as the probe enters regions of hotter electrons.

Figure 3.18 shows the mean potential measured by the BPP, compared to the mean floating potential, as a function of distance from the LCFS,  $R - R_{LCFS}$ . In each shot

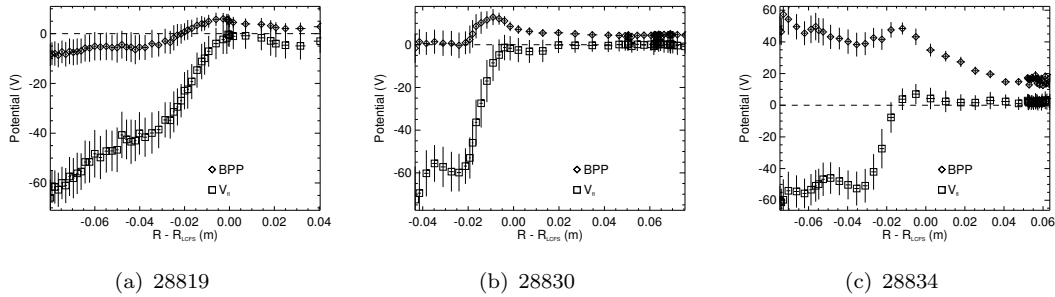


FIGURE 3.18: Potential measured by the BPP as a function of distance from the LCFS. This accounts for both the motion of the RP and the motion of the plasma edge.

there is a region in the BPP potential measurement where the gradient of the potential changes sign. This region is always in the vicinity of the separatrix, though precise identification of the separatrix is hindered by the error on the EFIT calculation. The peak in the potential profile is consistent with the presence of a radial velocity shear layer in the vicinity of the separatrix [70]. The velocity, being dominantly due to  $\mathbf{E} \times \mathbf{B}$  motion, can be related to an electric field  $E_R = -d\phi/dR$  where  $\phi$  is the plasma potential. The radial electric field will be calculated from the BPP potential in a later section.

### 3.4.2 Electron Temperature Profiles

The ball pen probe potential and the floating potential measured by a Langmuir probe can be written in the general forms

$$V_{BPP} = \phi - \alpha_{BPP} T_e \quad (3.32)$$

and

$$V_{fl} = \phi - \alpha_{LP} T_e \quad (3.33)$$

where  $\alpha = \ln(I_e/I_i)$  is the logarithmic ratio of electron and ion saturation currents in each probe type. From these expressions the electron temperature can be extracted as

$$T_e \text{ (eV)} = \frac{V_{BPP} - V_{fl}}{\alpha_{LP} - \alpha_{BPP}} \quad (3.34)$$

The calculation of  $T_e$  depends critically on the parameters  $\alpha_{LP}$  and  $\alpha_{BPP}$ .  $\alpha_{LP}$ , is given by [25] (neglecting secondary electron emission for now)

$$\alpha_{LP} = \frac{1}{2} \ln \left( 2\pi \frac{m_i}{m_e} \left( 1 + \frac{T_i}{T_e} \right) \right) = \frac{1}{2} \left[ \ln \left( 2\pi \frac{m_i}{m_e} \right) + \ln \left( 1 + \frac{T_i}{T_e} \right) \right] \quad (3.35)$$

where  $m_{i,e}$  is the ion/electron mass, evaluated in this section for Deuterium ions, and  $T_{i,e}$  is the ion/electron temperature. The ratio of  $T_i/T_e$  cannot readily be measured during shots 28819, 28830 and 28834 and requires the replacement of the probe head on the RP system. As a consequence this ratio introduces a source of error into the calculation of  $\alpha_{LP}$ . Previous measurements on MAST [145] indicate that the ratio  $T_i/T_e$  is commonly in the range of 1 to 2 in the SOL and edge plasma. Taking these as bounding values,  $\alpha_{LP}$  can be evaluated for MAST as

$$\alpha_{LP} \approx 2.7 \pm 0.1 \quad (3.36)$$

where the error in  $\alpha_{LP}$  arises from the uncertainty in  $T_i/T_e$ . At present no first principles model exists to evaluate  $\alpha_{BPP}$ . The arguments laid out in section 3.2 suggest that collection due to  $\mathbf{E} \times \mathbf{B}$  motion within the collection tube may provide  $\alpha_{BPP}$  values within the ranges found in experiment, however this is far from a predictive model. The quantity

$$\alpha_{BPP} = \ln \left( \frac{I_e}{I_i} \right) \quad (3.37)$$

has been measured empirically in the past by sweeping the probe tip bias and measuring the current drawn [136]. The BPP used in MAST cannot be swept and as a consequence  $\alpha_{BPP}$  cannot be measured directly. In a following section a procedure for evaluating  $\alpha_{BPP}$  by calibration with the Thomson scattering system will be presented, however for an initial investigation  $\alpha_{BPP}$  is taken as

$$\alpha_{BPP} \approx 0.6 \pm 0.3 \quad (3.38)$$

which is an empirical value motivated by previous experiments [136]. In measurements of  $T_e$  the quantity  $\alpha_{LP} - \alpha_{BPP}$  is important which, from the values stated above, takes the value

$$\alpha_{LP} - \alpha_{BPP} \approx 2.1 \pm 0.4 \quad (3.39)$$

The electron temperature can now be measured with uncertainty determined by  $\alpha_{LP} - \alpha_{BPP}$ .

To assess the validity of the BPP measurement it will be directly compared to the Thomson scattering system on MAST [163]. To make this comparison the TS data is sampled over a radial range encompassing the reciprocation of the RP. The TS data is sampled in a time window during which the plasma edge is stationary. This allows the measurement to be expressed in terms of distance from the LCFS, rather than major radius, by subtracting the position of the plasma edge again taken from EFIT. As already stated the EFIT measurement of the LCFS position is subject to unknown systematic error. Using the EFIT value in both the BPP and TS measurements removes any effect of this

error from the comparison between the two diagnostics. During the sampling window the mean of the data is taken. Data points with a random error greater than 50% of the mean are rejected from the sample (although in practice this is not a significant portion). Furthermore radial windows with less than three data points in them are rejected as too small a sample to construct a mean measurement. This occurs in the SOL region, where low temperatures and densities lead to large amounts of random error on the data. Furthermore the TS system has a floor measurement of 5eV, making it unsuitable for SOL measurements.

Figure 3.19 shows the electron temperature,  $T_e$ , calculated from the BPP using equation 3.34, compared with the TS measurement of  $T_e$  during the three analysed MAST shots. The two diagnostics compare favourably, with the TS measurement of electron

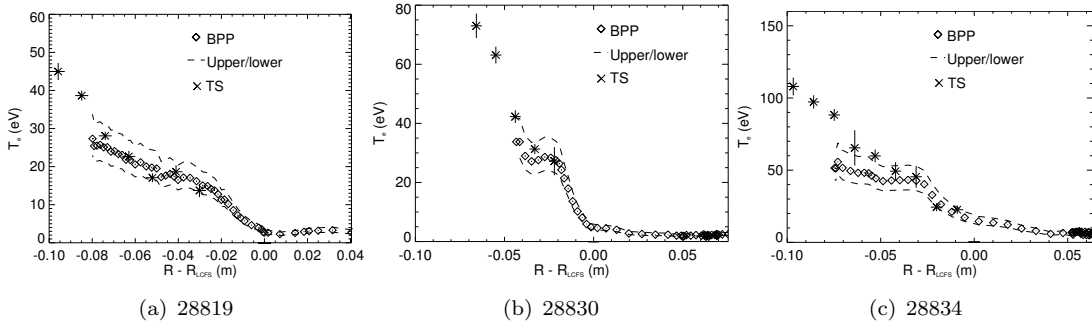


FIGURE 3.19: Comparison of the electron temperature,  $T_e$ , measured by the BPP and the TS system during MAST shots 28819, 28830 and 28834. The dotted lines show the upper and lower bounded values of the BPP temperature due to the uncertainty in  $\alpha_{LP} - \alpha_{BPP}$ . The error bars on the TS data are the standard error on the mean within each radial window. The error arises from a combination of the data variance within each window and random error on the measurements.

temperature falling within error bars of the BPP measurement over much of the radial range where the two data sets overlap. In particular shot 28819, which has the deepest probe reciprocation, shows excellent agreement with the TS system in both the magnitude and gradient of the  $T_e$  profile. The BPP profiles show a rapid decrease of the electron temperature at  $-2$ cm. This is consistent with the efficient transport of heat to the divertor target in the SOL and suggests that the EFIT calculation of  $R_{LCFS}$  is offset by 2cm. There is a gradual relaxing of the gradient as the probe penetrates deeper into the plasma. This is particularly pronounced in shots 28830 and 28834. This relaxation is expected, however the BPP profile appears to underestimate the gradient of the profile as the temperature increases. This has the result of a growth in the disagreement between the BPP and TS measurements as the magnitude of  $T_e$  increases. The TS system is a well established diagnostic therefore the source of disagreement is assumed to lie in the BPP measurement. The increase in disagreement between the BPP and TS measurements suggests that a temperature dependant process may be present in the

BPP measurement which is not accounted for in the present analysis. Given the lack of a robust model for BPP collection it is not possible to identify such a process which may affect the ball pen probe contribution to the measurement. The measurement of  $T_e$  also depends on the Langmuir probe potential measurement however which may also be responsible for the observed disagreement. In particular the neglect of secondary electron emission is an approximation which may affect the measurement of  $V_{fl}$ . Secondary electron emission is the emission of electrons from a surface as a result of an incident flux of electrons in a plasma [25]. In principle the yield of electrons has a component due to electrons released from the surface and a component due to backscattered electrons [164], though in temperature regimes of relevance to the edge plasma in MAST the backscattered component is negligible [25]. The emission of electrons from a surface enhances the ion current to the surface and can therefore reduce the floating potential of the surface. The floating potential including the effects of secondary electron emission (SEE) is given by [25]

$$\alpha_{LP} = -\frac{1}{2} \ln \left( 2\pi \frac{m_e}{m_i} \left( 1 + \frac{T_i}{T_e} \right) (1 - \delta)^{-2} \right) \quad (3.40)$$

where  $\delta$  is the secondary electron yield and measures the average number of electrons emitted from the surface per incident electron. The secondary electron yield can be well described over a wide range of material surfaces by the empirical formula [25, 165]

$$\delta = 2.72^2 \delta_{max} \frac{E}{E_{max}} \exp \left[ -2 \left( \frac{E}{E_{max}} \right)^{1/2} \right] \quad (3.41)$$

where  $\delta$  is the SEE yield,  $E$  is the incident electron energy and  $\delta_{max}$  and  $E_{max}$  are material dependant parameters. For graphite (the material used for the probe tips in the BPP constructed for MAST)  $\delta_{max} = 1$  and  $E_{max} = 300\text{eV}$  [25, 165]. This formula is derived from an experimental fit over multiple data sets shown in figure 3.20

SEE is conventionally neglected in Langmuir probe measurements at divertor targets. Since the magnetic field is highly oblique to the collection surface electrons emitted normal to the probe surface will be recaptured as they complete their first Larmor orbit. The case of the LP on the midplane RP system is in contrast to the divertor. In the case of the RP the magnetic field has a close to normal angle of incidence on the probe. In this case the sheath that forms on the probe acts to accelerate the emitted electrons away from the probe along the magnetic field line. The electrons are not then recaptured by the probe and so the effect of SEE can be significant.

Generally expressions for the secondary electron yield,  $\delta$ , are given in terms of incident electron energy, as in equation 3.41 for example. To factor  $\delta$  into the floating potential expression in terms of electron temperature rather than electron energy, the distribution of electron energies must be accounted for to provide an average  $\delta$  as a function of

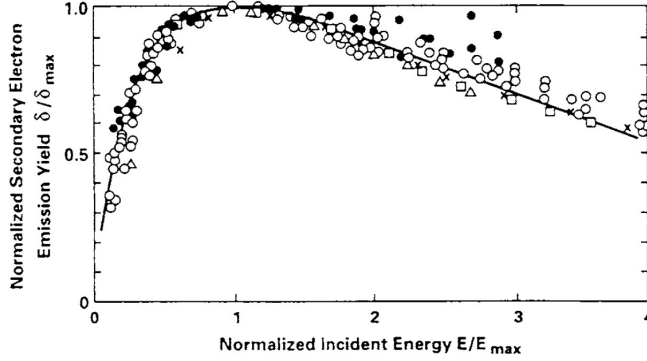


FIGURE 3.20: Normalized secondary electron emission as a function of normalized incident energy. The line is the semi-empirical curve given in equation 3.41. Figure taken from [25], originally from [165]

$T_e$ ,  $\bar{\delta}(T_e)$ . To calculate  $\bar{\delta}$  the electrons are assumed to have a Maxwellian distribution function. The experiments carried out to derive the expression for  $\delta(E)$ , equation 3.41, were carried out with an electron beam at normal incidence to the surface [165]. As a result the expression does not account for any variation in the angle of incidence of the electrons. For this reason in the calculation of  $\bar{\delta}(T_e)$  the angle of incidence on the surface is assumed to have no effect on  $\delta$ . This translates to the assumption that the pitch angle part of the Maxwellian distribution of the electrons has no effect on  $\bar{\delta}$ . It should be noted however that in [166] electrons incident on a variety of surfaces at below normal incidence were shown to enhance secondary electron emission. As such the neglect of pitch angle here is likely lead to an underestimate in the calculation of  $\bar{\delta}$ . With these approximations in mind,  $\bar{\delta}$  can be obtained by averaging the mono-energetic  $\delta(E)$  over a Maxwellian energy distribution so that

$$\bar{\delta}(T_e) = \frac{\int_0^\infty \delta(E) \exp[-E/T_e] dE}{\int_0^\infty \exp[-E/T_e] dE} \quad (3.42)$$

Figure 3.21 shows  $\delta(E)$  and  $\bar{\delta}(T_e)$  as a function of incident electron energy and electron temperature respectively.

The SEE yield calculated as a function of  $T_e$ ,  $\bar{\delta}(T_e)$  is reduced compared to the mono-energetic case. This is a result of the Maxwellian distribution being biased towards  $E = 0$ , where  $\delta(E)$  is lowest. Woods has shown [166] that including the effect of pitch angle in the calculation of  $\bar{\delta}(T_e)$  can lead to a strong enhancement of the SEE yield. An enhancement by up to  $\approx 50\%$  was noted in graphite, however no parametrization exists for this enhancement, so it must be neglected here. It should also be noted that the

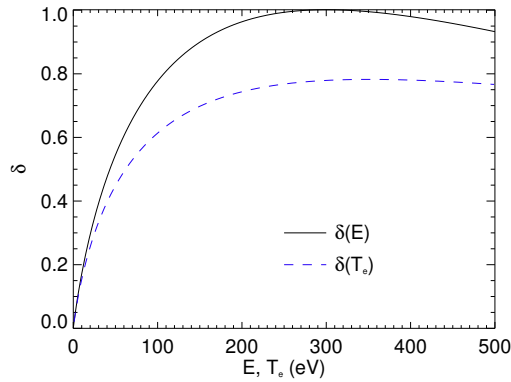


FIGURE 3.21: Secondary electron yield as a function of incident electron energy,  $\delta(E)$  calculated from 3.41, and as a function of electron temperature calculated from 3.42 by integration over a Maxwellian.

deviation between the mono-energetic and Maxwellian calculations begins to become significant within the experimentally relevant range of  $T_e$ , showing that the Maxwellian calculation must be accounted for in order to consistently include the effects of SEE on  $V_{fl}$ .

With the calculation of  $\bar{\delta}(T_e)$  established the effects of SEE can now be included in the calculation of  $\alpha_{LP}$  through equation 3.40. The experimental temperature is approximated by taking a linear fit of the Thomson scattering measurement to the point where  $T_e = 1\text{eV}$ , beyond which the temperature is fixed at 1eV. Higher order fitting functions were tested but were found to have a negligible effect on results presented.  $\alpha_{LP}$  can be calculated as a function of electron temperature, which can then be mapped onto  $R - R_{LCFS}$ . Figure 3.22 shows the approximated temperature profiles and resulting radial profiles of  $\alpha_{LP}$  for each shot analysed. Using these profiles of  $\alpha_{LP}$  the electron temperature can be recalculated from the BPP data this time accounting for the presence of secondary electron emission. Three cases are presented which take  $\alpha_{BPP} = 0$ ,  $\alpha_{BPP} = 0.15$  and  $\alpha_{BPP} = 0.30$  respectively. This new comparison with the TS system is presented in figure 3.23.

The inclusion of secondary electron emission in the measurement of the floating potential improves the agreement between the BPP and TS measurements of  $T_e$ . This comparison also allows the parameter  $\alpha_{BPP}$  to be approximately constrained to  $0 \geq \alpha_{BPP} \leq 0.3$  which is below the empirical values found by Adamek *et.al* [136]. The validity of the BPP measurement of the plasma potential is further strengthened by considering that the influence of pitch angle on SEE has been neglected here. As shown in [166] including the effects of pitch angle on SEE can enhance  $\bar{\delta}(T_e)$  by up to 50%. This is exemplified in figure 3.24 where a 30% enhancement to  $\bar{\delta}(T_e)$  has been applied to the BPP measurement in shot 28834 and is compared to the case with no enhancement. A 30%

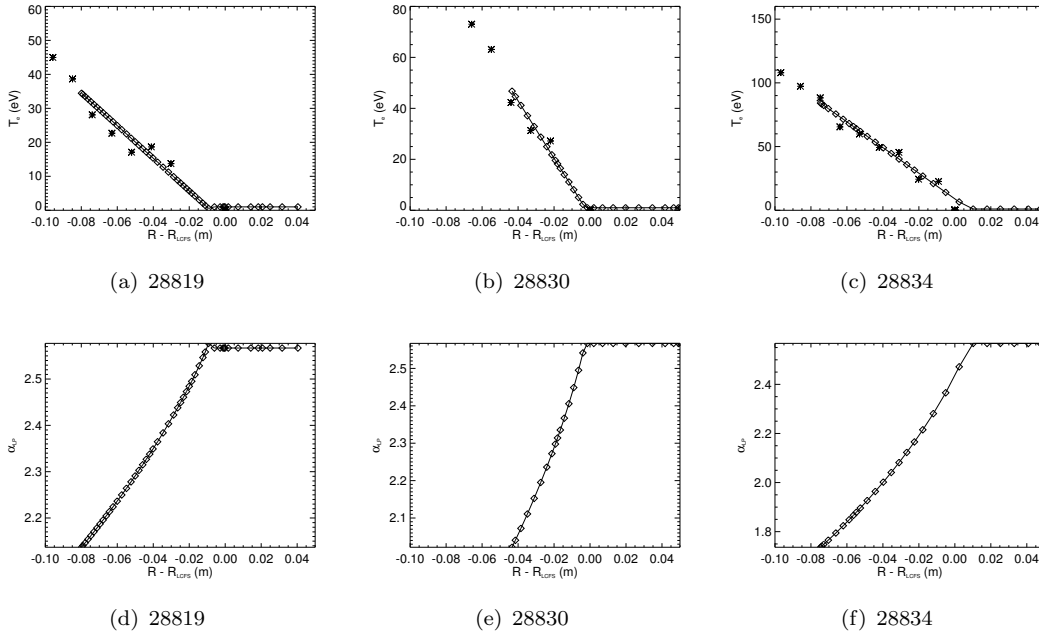


FIGURE 3.22: Upper: Linear fits to Thomson scattering measurement of electron temperature. Lower: Calculated radial profiles of  $\alpha_{LP}$  including self-consistently the effects of secondary electron emission.

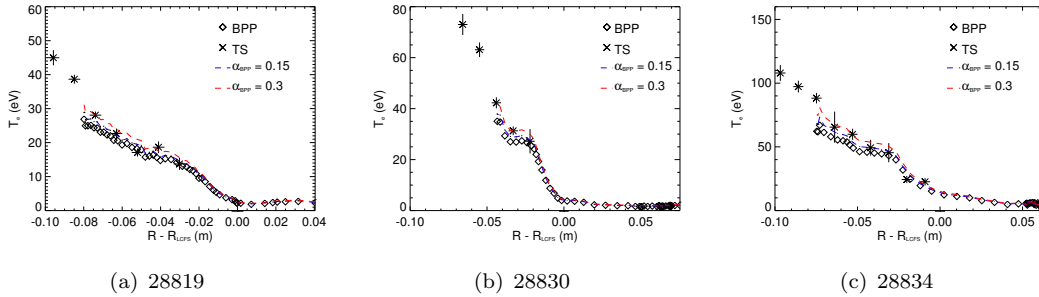


FIGURE 3.23: Comparison of the electron temperature measured by the TS system with the BPP measurement including the effects of secondary electron emission. A range of  $\alpha_{BPP}$  are tested.

enhancement to  $\bar{\delta}(T_e)$  can bring the BPP measurement with  $\alpha_{BPP} = 0$  into very close agreement with the TS measurement of  $T_e$ . This suggests that within the uncertainty induced from the neglect of pitch angle effects in the calculation of  $\bar{\delta}(T_e)$ , the BPP potential can be considered to be a good estimate of the true plasma potential. In the following sections the effect of finite  $\alpha_{BPP}$  will be retained as a source of uncertainty, although ultimately it will be shown that  $\alpha_{BPP}$  has little impact on the most significant measurements made by the probe.

The BPP electron temperature profile resolves the temperature gradient in the SOL. Figure 3.25 shows the temperature profile in the near separatrix region for the three

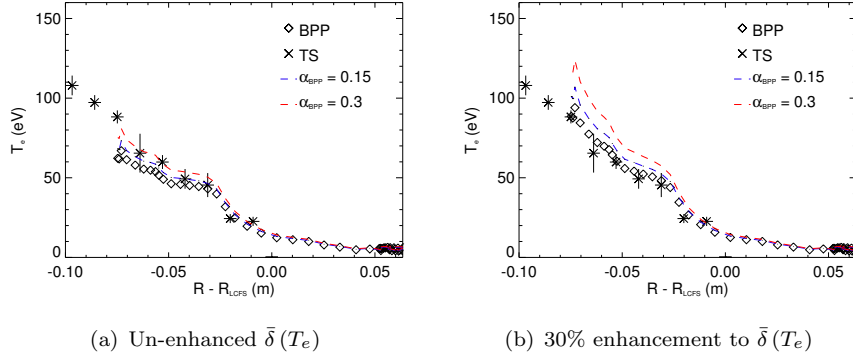


FIGURE 3.24: Comparison of the BPP  $T_e$  measurement with 30% enhancement to the SEE yield,  $\bar{\delta}(T_e)$  compared to the un-enhanced case for shot 28834.

analysed shots. The electron temperature decay length in the near separatrix region is a

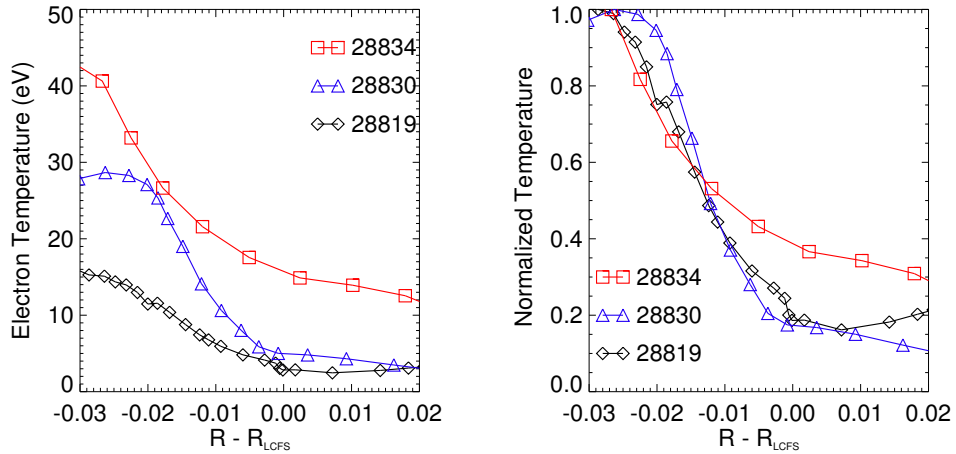


FIGURE 3.25: Left: Electron temperature profile in the near separatrix region showing the sharp falloff. Right: Electron temperature normalized to the maximum value for scale length comparisons between the three shots.

critical quantity since it determines the radial extent over which the majority of power is deposited on the divertor. Figure 3.25 suggests that the temperature decay length in shot 28834 significantly exceeds the other two. Despite the lower temperature in shot 28819, due to a reduced Ohmic heating power by virtue of a reduced plasma current, the decay length remains close to that of shot 28830. The temperature decay length,  $\lambda_T$  is defined as

$$\lambda_T = \frac{T_e}{dT_e/dR} \quad (3.43)$$

where  $T_e$  here refers to the time and flux surface averaged electron temperature. In the two-point model of the conduction limited SOL [25] the heat flux decay length,  $\lambda_q$  can be

related directly to the temperature decay length by  $\lambda_q \approx \frac{7}{2} \lambda_{Te}$ .  $\lambda_T$  has been calculated in shots 28819, 28830 and 28834 in figure 3.26.

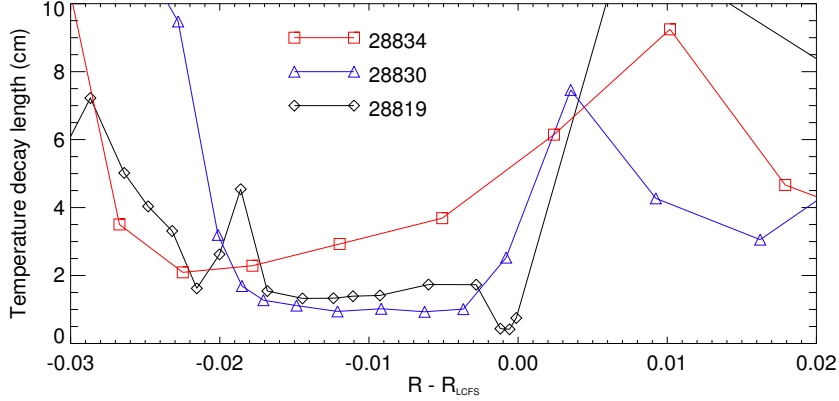


FIGURE 3.26: Temperature decay length,  $\lambda_T$  calculated as a function of  $R - R_{LCFS}$  for shots 28819, 28830 and 28834. Similar profiles are observed in shots 28819 and 28830, whilst 28834 exhibits extended decay lengths.

Shot 28834 exhibits larger  $\lambda_T$  than shots 28819 and 28830. Shot 28834 has a lower density than both 28819 and 28830 and has a plasma current of 600kA making it comparable to 28830 but greater than 28819. Since the change in decay length between shots 28819 and 28830, which represent a current scan, is minimal this suggests that the reduced plasma density causes the increased temperature decay length. It should be noted that the minimum in  $\lambda_T$  may be expected to occur in the near SOL where efficient parallel transport of heat to the divertor targets reduces the electron temperature radially. In figure 3.26 this appears not to be the case when accounting for the 2cm systematic offset of the EFIT calculation of  $R_{LCFS}$ . The presence of this offset however prevents exact determination of the proximity of the profiles to the separatrix, only that they occur in the near separatrix region.

Millitello *et.al* [167] have derived numerically a scaling for the temperature decay length using the 2D ESEL model [93, 118, 119] for MAST-like parameters. The ESEL model, reviewed in chapter 2, is based on 2D interchange turbulence in the plane perpendicular to the magnetic field with local sources and sinks accounting for motion parallel to the field line. The scaling derived in this model for the temperature decay length is [167]

$$\lambda_T \propto q^a n_e^b T_e^c \quad (3.44)$$

where the indices  $a, b, c$  depend on the dimensionless collisionality  $\nu^*$  [167], where

$$\nu^* = L_{||} / \lambda_c \quad (3.45)$$

and are

- For  $\nu^* \ll 4$

$$a = 1.52 \quad b = 0.45 \quad c = -0.55$$

- For  $4 \ll \nu^* \ll 12$

$$a = 1.63 \quad b = 0.59 \quad c = -0.73$$

- For  $12 < \nu^* < 63$

$$a = 2.18 \quad b = 1.11 \quad c = -1.77$$

In each case the general trends are the same with an increase in  $\lambda_T$  with the safety factor,  $q$  and the density  $n_e$  at the separatrix and a rapid decrease with separatrix temperature,  $T_e$ . Comparing this scaling behaviour with the BPP measurements of  $T_e$  there are two notable points:

- An increase in  $\lambda_T$  is observed between shots 28830 and 28834. These two shots represent a two-point density scan with 28830 higher in density and 28834. On the other hand the magnitude of the temperature, shown in figure 3.25, is greater in shot 28834 than in 28830. The increase in  $\lambda_T$  is therefore in contrast to the expectations from the numerical scaling predictions. This could suggest that as temperature increases the scalings based on 2D turbulence breaks down, potentially due to the impact of 3D features of the turbulence.
- A reduction in  $\lambda_T$  is observed between shots 28819 and 28830. Shots 28819 and 28830 represent a two-point plasma current scan. Increasing plasma current simultaneously reduces  $q$  and increases  $T_e$  so the observed reduction in  $\lambda_T$  is in qualitative agreement with the numerical scaling

This is not a complete parametric study of  $\lambda_T$  and a much larger parameter scan is required to assess the agreement between numerical and experimental measurements of the temperature decay length. Nevertheless the above analysis shows that the BPP measurements contain qualitatively similar features to numerical modelling and, more importantly, demonstrates the capability of the BPP at measuring the electron temperature profile. A full scan of  $q, T_e$  and  $n_e$  would be an excellent avenue of future work to experimentally characterize the scaling of  $\lambda_T$  with the BPP.

### 3.4.3 Radial Electric Field

The radial electric field can be calculated from the plasma potential by

$$E_R = -\frac{\partial\phi}{\partial R} \quad (3.46)$$

and is an important quantity in the plasma edge. By  $\mathbf{E} \times \mathbf{B}$  motion the radial electric field induces flows of the plasma within the flux surface. This can be decomposed into a poloidal and a toroidal flow,  $v_\theta$  and  $v_\zeta$ , by

$$v_\theta = \frac{\mathbf{E} \times \mathbf{B}}{B^2} \cdot \frac{\mathbf{B}_\theta}{|\mathbf{B}_\theta|} = -\frac{B_\zeta E_R}{B^2} = \frac{B_\zeta}{B^2} \frac{\partial\phi}{\partial R} \quad (3.47)$$

$$v_\zeta = \frac{\mathbf{E} \times \mathbf{B}}{B^2} \cdot \frac{\mathbf{B}_\zeta}{|\mathbf{B}_\zeta|} = \frac{B_\theta E_R}{B^2} = -\frac{B_\theta}{B^2} \frac{\partial\phi}{\partial R} \quad (3.48)$$

where  $B_\theta = |\mathbf{B}_\theta|$  is the poloidal magnetic field strength and  $B_\zeta = |\mathbf{B}_\zeta|$  is the toroidal magnetic field strength and  $B = \sqrt{B_\theta^2 + B_\zeta^2}$  is the total magnetic field strength. In deriving equations 3.47 and 3.48 quantities have been taken at the outboard midplane such that  $\nabla\psi/|\nabla\psi| = \mathbf{R}/R$  and  $\mathbf{B}_\theta/|\mathbf{B}_\theta| = \mathbf{Z}/Z$  where  $\mathbf{R}$  and  $\mathbf{Z}$  are the major radius and vertical position of the plasma in cylindrical coordinates. If the flows are sheared radially then they can be responsible for suppressing turbulence [138]. On the other hand sheared flows are well known to drive hydrodynamic Kelvin-Helmholtz instabilities [168] in regular fluids. In plasmas the K-H instability can be driven at high flow shear on the global plasma scale [169–171] and can also be driven locally to the plasma edge which has been suggested as a mechanism for blob production [172].

Previous measurements of the radial electric field on MAST have used the Doppler backscattering (DBS) technique [173, 174] and the charge exchange recombination spectroscopy (CXRS) technique [175, 176]. DBS measures the Doppler shift and broadening of backscattered light off of turbulent density fluctuations. The shift of the frequency peak of the backscattered light gives the local flow velocity of the density fluctuations. CXRS measures the local flow velocity by a similar method. The charge exchange process is the exchange of an electron between a neutral impurity particle and an ion in the plasma. This thermalizes the impurity species with the plasma ions so that measurements of the impurity energy spectrum are representative of the ions in the plasma and this allows CXRS to measure the flow and temperature of plasma ions. Light, emitted from the impurity species by electronic transitions, can be measured and the broadening and shift of the frequency spectrum away from the transition line provides a measurement of ion temperature and flow velocity. Assuming that the radial electric field provides the dominant mechanism producing a plasma flow, the flow velocity can be inverted to produce a measurement of the radial electric field. These techniques make

a direct measurement of the flow velocity, and indirectly measure the radial electric field. By contrast the BPP measures the plasma potential directly, from which  $E_R$  can be obtained and the flow velocity can be inferred. Previous studies have shown good agreement between  $E_R$  measurements from a BPP and a passive Doppler reflectometry system on ASDEX-Upgrade [177]. If  $T_e$  is known a correction can be made to the BPP measurement to obtain the true plasma potential. The correction is given by

$$\phi = V_{BPP} + \alpha_{BPP} T_e = (1 + \gamma) V_{BPP} - \gamma V_{fl} \quad (3.49)$$

where  $\gamma = \alpha_{BPP}/(\alpha_{LP} - \alpha_{BPP})$ . By comparison with the TS system  $\alpha_{BPP}$  has been constrained to  $0 \geq \alpha_{BPP} \leq 0.3$ , though as noted within uncertainty induced by the neglect of pitch angle in the calculation of  $\alpha_{LP}$ ,  $\alpha_{BPP} \approx 0$  can be considered appropriate. Figure 3.27 shows the corrected plasma potential using the full range of  $\alpha_{BPP}$ , and using the profiles for  $\alpha_{LP}$  shown in figure 3.22. The correction to the plasma potential

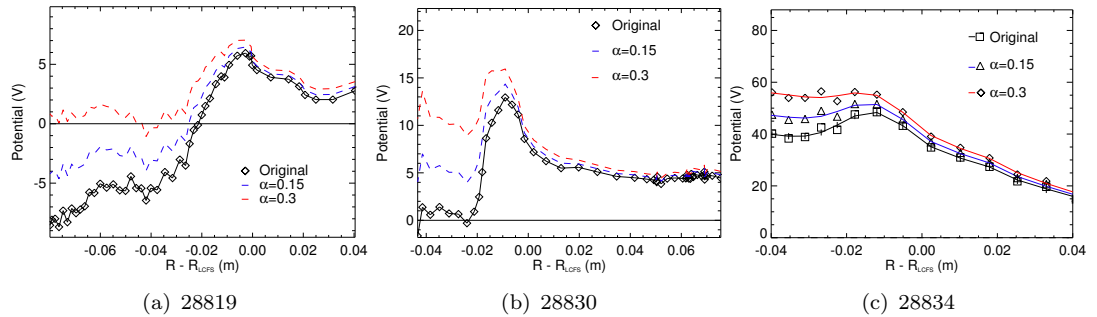


FIGURE 3.27: Corrected plasma potential measurements using the parameters  $\alpha_{BPP} = 0, 0.15$  (blue) and  $0.3$  (red).  $\alpha_{LP}$  is taken from figure 3.22. The correction to the plasma potential can be significant in the region inside the separatrix, but it small in the SOL.

measurement can be substantial on the core-side of the separatrix, where the electron temperature is highest. To calculate the radial electric field the derivative of the BPP signal must be taken with respect to the distance from the LCFS. Taking the derivative with respect to  $R - R_{LCFS}$ , rather than simply the major radius removes any time dependence of the measurement that may result from motion of the plasma edge. Taking the derivative of the raw signal directly, or of the averaged data results in discontinuities due to the discrete nature of the data, which tend to dominate the derivative. To alleviate this problem a fit of the data is performed to provide a smoothly varying representation of the profile and the derivative of this fit is taken. Predicting the structure of the radial electric field is difficult and generally depends on high order momentum transport processes [178]. As such it is overly presumptuous to pre-determine a fitting function for the potential profile. Instead a high order polynomial is used since this provides a smooth curve which captures the underlying features of the potential profile.

In this case a 17<sup>th</sup> degree polynomial is used. Figure 3.28 shows the fit to the BPP potential profile in the vicinity of the LCFS for the three analysed shots. In each case

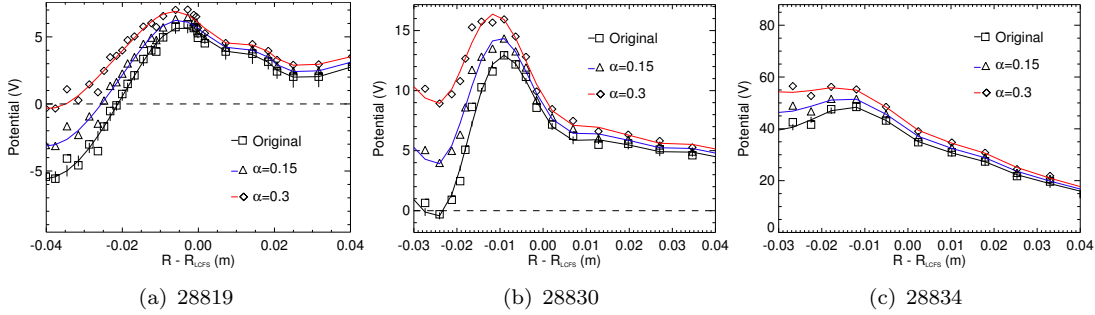


FIGURE 3.28: 17<sup>th</sup> degree polynomial fits (solid line + error bars) to the BPP potential profile (squares) in shots 28819, 28830 and 28834.

shown in figure 3.28 the polynomial fit matches the experimental profile well. The radial electric field may then be calculated by taking the derivative of these fits. Figure 3.29 shows the radial electric field calculated from the BPP potential in shots 28819, 28830 and 28834. The radial electric field is significantly less sensitive to the  $\alpha_{BPP}$  parameter

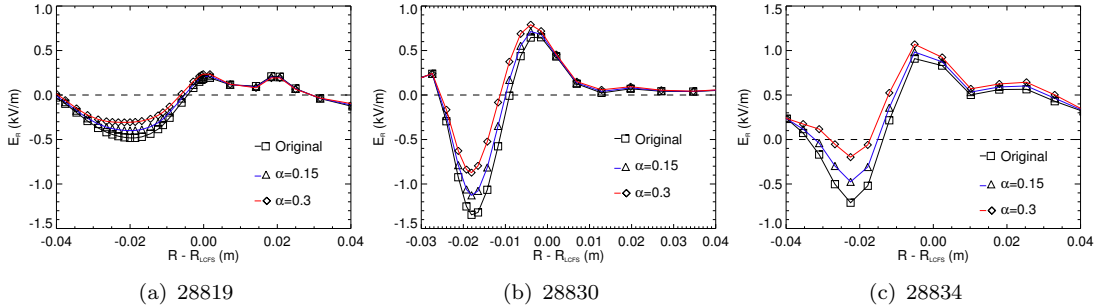


FIGURE 3.29: Radial electric field profile calculated from fitted BPP potential profiles, shown in figure 3.28, for shots 28819, 28830 and 28834.

than the potential.

The measurements obtained from the BPP agree qualitatively with previous measurements on MAST using the ECELESTE system. ECELESTE is a CXRS system and was used in [176, 179] to measure the radial electric field. Extensive studies were made of the H-mode electric field, but fewer studies were conducted in Ohmic L-mode. Nevertheless  $E_R$  was shown to exhibit a magnitude  $\sim 1kV/m$  similar to the BPP measurements. Furthermore a strong gradient region near the separatrix, which corresponds to the radial shear layer, can be identified in the BPP measurements and is in qualitative agreement with [179].

The variation of  $E_R$  between shots 28819 and 28830 (which correspond to a plasma current scan) indicates an increase in the radial electric field with plasma current whilst

$E_R$  remains relatively similar between 28830 and 28834 which represent a density scan. In each case a region of strong electric field shear is present near to the separatrix which can be identified as the radial shear layer. The length scale of the shear layer remains relatively constant between each shot, however an increase in the electric field magnitude as plasma current increases also results in increased shear of the electric field. The toroidal and poloidal magnetic field strengths can be calculated from EFIT. These are given in figure 3.30. Using the magnetic field components shown in figure 3.30 the

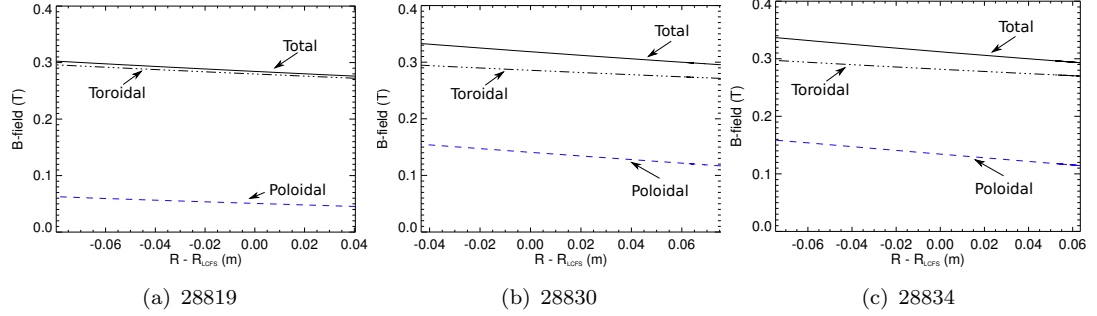


FIGURE 3.30: Poloidal magnetic field,  $B_\theta$  (blue), toroidal magnetic field,  $B_\zeta$  (dot-dash) and total magnetic field (solid) from EFIT equilibrium reconstructions of shots 28819, 28830 and 28834. Minimal variation is observed across the region of interest.

velocity components can be calculated from equations 3.47 and 3.48. These are shown in figure 3.31 for shots 28819, 28830, and 28834. The poloidal velocity is the dominant

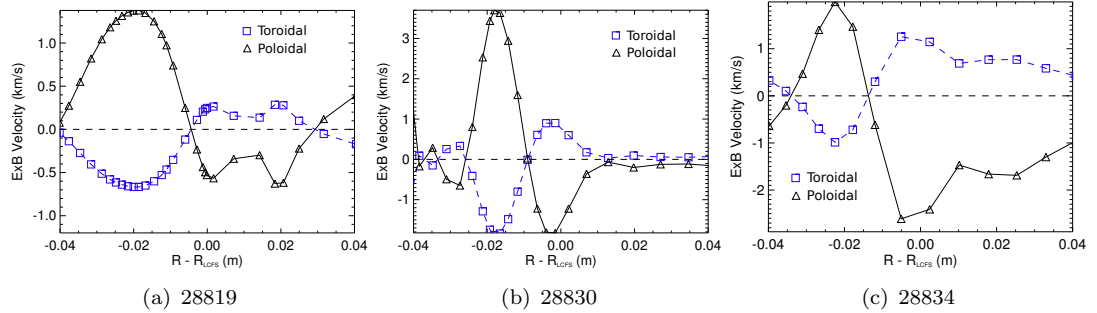


FIGURE 3.31: Toroidal (solid) and poloidal (broken)  $\mathbf{E} \times \mathbf{B}$  velocity components calculated from the BPP measurements of radial electric field for shots 28819, 28830 and 28834.

component of the  $\mathbf{E} \times \mathbf{B}$  due to the larger toroidal magnetic field. The plasma is observed to rotate toroidally and poloidally with a velocity on the order of  $\sim 1\text{km/s}$ . In each case a strong velocity shear is observed near to the separatrix in the radial shear layer. The shear has a magnitude on the order of  $5 \times 10^5\text{s}^{-1}$ .

Velocity shear in the plasma edge can have a significant effect on turbulent transport that is typical and is linked with the ejection of filaments. In the next section the impact

of the radial shear layer on statistical properties of density fluctuations in the plasma edge is analysed. The BPP offers a unique opportunity to measure this interaction locally, removing any source of uncertainty arising from the need to map measurements spatially onto one another.

### 3.5 Fluctuations in the Radial Shear Layer

Intermittency in the SOL can be inferred from the structure of the probability distribution function (PDF) of Ion saturation current ( $I_{sat}$ ) fluctuations.  $I_{sat}$ , which is given by

$$I_{sat} = AZnec_s = AZen_i \sqrt{\frac{T_e}{m_i}} \propto n_i T_e^{1/2} \quad (3.50)$$

is often used to infer fluctuations in the plasma density since low frequency (kHz range) temperature fluctuations are usually assumed to be small due to efficient parallel heat transport. The structure of the  $I_{sat}$  PDF can then be used to infer characteristics of the density fluctuations dominating transport in the SOL. If the signal is dominated by random (uncorrelated) fluctuations then the PDF of the signal reduces to a Gaussian centred on the average with a width of  $2\sigma$  where  $\sigma$  is the standard deviation of the signal. If the signal has an intermittent character, such as signals in the SOL where the ejection of filaments generates intermittency, the PDF becomes biased in the positive (or negative if the intermittent fluctuations are negative) direction. This behaviour is illustrated schematically in figure 3.32. A positively biased PDF indicates a tendency

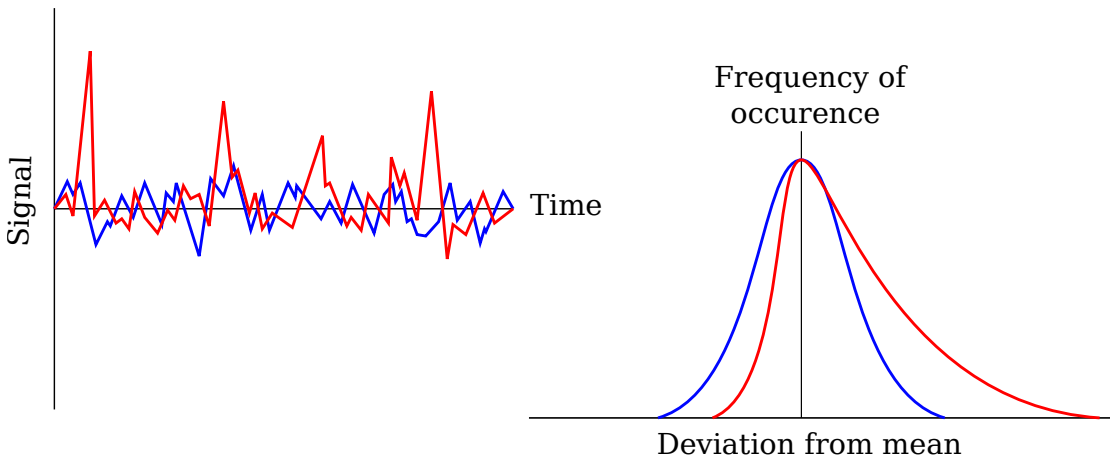


FIGURE 3.32: Schematic illustration of the biasing of a PDF by intermittent fluctuations. Random fluctuations (blue) result in a symmetric, Gaussian PDF whilst intermittent signals (red) result in a skewed PDF as large, infrequent events dominate the signal.

for the plasma to produce large intermittent fluctuations which, in the context of the

plasma edge, are filaments. On the other hand a negatively biased PDF indicates the production of negative depressions in plasma density, also known as holes. Filaments can provide a large component of density transport into the SOL in a non-diffusive manner [180], whilst holes have been cited as a possible means for enhanced impurity transport towards the tokamak core [181]. As a consequence the nature of fluctuations in the plasma edge can play a strong role in determining tokamak performance.

Probe measurements on JET [68] and ASDEX-Upgrade [76] have indicated a qualitative connection between the structure of the  $I_{sat}$  PDF and the radial shear layer. In particular both studies showed a drop in the skewness of the PDF as the shear layer was passed through, suggesting that the shear layer is a local generation region of filaments and holes. A difficulty in interpreting these measurements is an inability to accurately pinpoint the position of the radial shear layer whilst obtaining fluctuation statistics. Consequently the relationship between skewness and the radial shear layer is qualitative. Visible imaging using localized gas puffs in TEXTOR has shown that the interaction between fluctuations and the radial shear layer varies dramatically over an L-H transition [135] with eddy structures being broken into smaller structures in H-mode. A local measurement of the fluctuation characteristics in the radial shear layer would allow a quantification of these processes. The BPP offers the chance to make such a measurement by simultaneously measuring the plasma potential and  $I_{sat}$  signals local to the probe allowing the radial electric field to be measured alongside fluctuation characteristics. Since the measurements are local to the probe they can be quantitatively compared and do not rely on spatial mapping between diagnostics. Given that the shear layer width can be  $\sim 1\text{cm}$  small uncertainties introduced by such spatial mapping can strongly impact measurements in the shear layer.

MAST shot 30250 is an Ohmic L-mode CDN discharge with a plasma current of 600kA and a magnetic field of 0.585T. It is entirely equivalent to the previously analysed shot 28830. During shot 30250 the BPP pin p1 was operated in  $I_{sat}$  mode to analyse  $I_{sat}$  fluctuation characteristics in the MAST plasma edge.

The first four moments of a PDF  $\mathcal{P}(f)$  of a function  $f(t)$  are given by [182]

$$\bar{f} = \int f \mathcal{P}(f) df = \frac{1}{N} \sum_{j=0}^{N-1} f_j \quad (3.51)$$

$$\sigma^2 = V(f) = \int (f - \bar{f})^2 \mathcal{P}(f) df = \frac{1}{N-1} \sum_{j=0}^{N-1} (f_j - \bar{f})^2 \quad (3.52)$$

$$S(f) = \int \frac{(f - \bar{f})^3}{\sigma^3} \mathcal{P}(f) df = \frac{1}{N} \sum_{j=0}^{N-1} \frac{(f_j - \bar{f})^3}{\sigma^3} \quad (3.53)$$

$$K(f) = \int \frac{(f - \bar{f})^4}{\sigma^4} \mathcal{P}(f) df - 3 = \frac{1}{N} \sum_{j=0}^{N-1} \frac{(f_j - \bar{f})^4}{\sigma^4} - 3 \quad (3.54)$$

where  $V$  is the variance,  $\sigma$  is the standard deviation,  $S$  is the skewness and  $K$  is the kurtosis of the PDF of  $(f)$  with mean value  $\bar{f}$ . Also given are the expressions for the discrete series  $f_j = [f_0, f_1, \dots, f_{N-1}]$ . The mean and variance describe the most common value of the data and the spread of the series around its mean value. The skewness measures how positively or negatively the distribution is biased (the red distribution in figure 3.32 is positively skewed for example). The Kurtosis is a measure of how flat or peaked the distribution is. A Gaussian distribution (the blue PDF in figure 3.32) has  $S = K = 0$ .

The aim of this section is to compare the radial variation of the moments of the  $I_{sat}$  PDF with the radial electric field profile. To generate profiles of the statistical moments an adaptation of the box-car average method has been used. The time series is split into a set of strongly overlapping windows. Within each window the moments of the PDF are calculated and assigned a radial position corresponding to the position of the window centre. This process produces a series of values for the moments of the PDF as a function of radial position. The  $I_{sat}$  signal has been split into 200 windows with a width of 3ms. The window width is limited by the need to encompass a significant number of fluctuations allowing the statistics of the PDF to be accurately reproduced, requiring a large window width. On the other hand the width must be small enough to ensure that the low frequency component of the signal remains constant within the window, meaning that the effect of background profile variation can be neglected within each individual window. If this is not the case then a significant smoothing of the profile of the various moments occurs and the boxcar method is no longer valid. A window width of 3ms, which corresponds to a radial window of  $\sim 3\text{mm}$  was found to give adequate statistics for calculation of PDF moments, but remains small enough to minimize any radial smoothing of the underlying profiles.

The mean, variance, skewness and kurtosis of the  $I_{sat}$  signal in shot 30250 have been calculated within each window. Figure 3.33 shows these quantities as a function of distance from the LCFS during shot 30250. The skewness is positive in the SOL and drops, eventually becoming negative radially inwards. This indicates the presence of filaments in the SOL and holes in the near separatrix region. The skewness and kurtosis are strongly correlated with both showing drops as the LCFS is crossed. In previous experiments on TORPEX [183], ASDEX-Upgrade [76] and many other magnetic confinement fusion devices[184] a parabolic relationship between the skewness and kurtosis has been reported. Figure 3.34 shows that this parabolic relationship is reproduced by  $I_{sat}$  fluctuations in MAST. The data in figure 3.34 is well fitted by the generalized parabolic relationship  $K = aS^2 + bS + c$  where  $K$  is the kurtosis,  $S$  is the skewness and

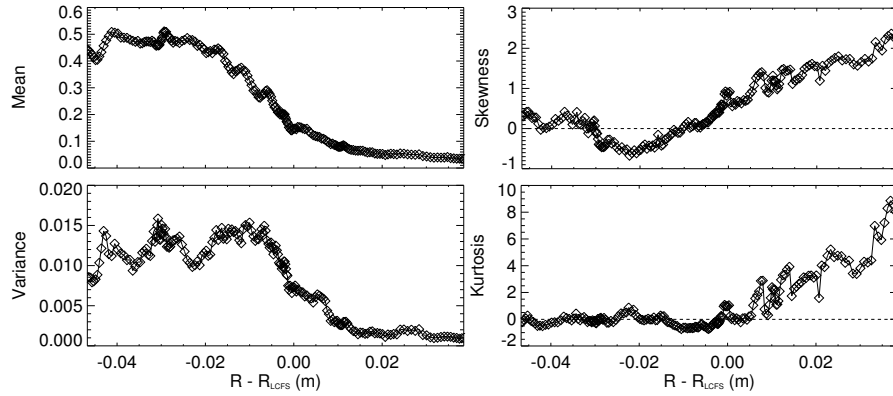


FIGURE 3.33: The mean, variance, skewness and kurtosis of  $I_{sat}$  in the time window  $[0.15, 0.27]$ s during MAST shot 30250. Notably the skewness decreases sharply as the mean increases. At this point the probe is crossing the LCFS.

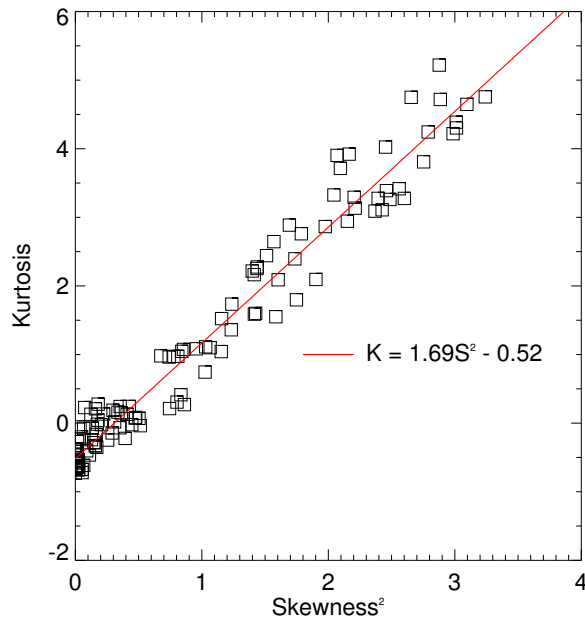


FIGURE 3.34: Kurtosis of fluctuations in  $I_{sat}$  during MAST shot 30250 as a function of the squared skewness. A clear parabolic relationship between the two is observed with a linear fit of  $K = 1.69S^2 - 0.52$  fitting the data well.

$a, b$  and  $c$  are polynomial coefficients with  $a = 1.69$ ,  $b = 0$  and  $c = -0.52$ . The fact that  $b = 0$  is in agreement with the ASDEX-upgrade and TORPEX results however here a negative value of  $c$  is observed. This arises simply because of the definition of kurtosis used here where a subtraction of  $-3$  is applied. Undoing this subtraction then gives  $c - 0.52 + 3 = 2.48$  which is in close agreement with TORPEX [183]. The universality of this relation is well established [184] and does not depend strongly on the particular system under study [185]. The particular values taken by the coefficients  $a$  and  $c$  can be dependant on local conditions of the experiment however, with the coefficient  $c$  being determined by the temporal intermittency of the signal and  $a$  being determined by the spatial intermittency [186].

To assess the accuracy of the plasma potential measurement in shot 30250 made by the BPP the electron temperature is once again compared to the TS system. This is shown in figure 3.35. The BPP measurement of electron temperature has been obtained by

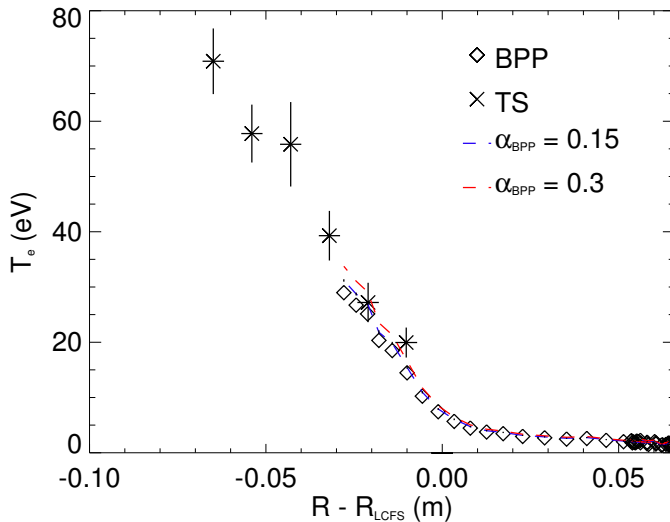


FIGURE 3.35: Comparison of  $T_e$  measured by the BPP (solid lines) and the TS system.

the method outlined in section 3.4.2 including the effects of secondary electron emission. The BPP measurement is a clear extrapolation of the TS data. Furthermore, as argued in section 3.4.2 since the effect of secondary electron emission is underestimated in figure 3.35  $\alpha_{BPP} = 0$  can be considered adequate and the BPP potential can be considered as the plasma potential.

Figure 3.36 compares the skewness of the  $I_{sat}$  PDF with the plasma potential measured by the BPP. Figure 3.36 suggests that the skewness of the  $I_{sat}$  PDF may be related to the plasma potential with a change of sign of  $S$  occurring within the region of strong potential gradient variation. This suggests that the skewness may be related to the radial electric field  $-\partial\phi/\partial R$ . To investigate this further the radial electric field is calculated using the method described in section 3.4.3. Figure 3.37 shows the radial electric field compared to the skewness of the  $I_{sat}$  PDF in the radial shear layer (the region where the

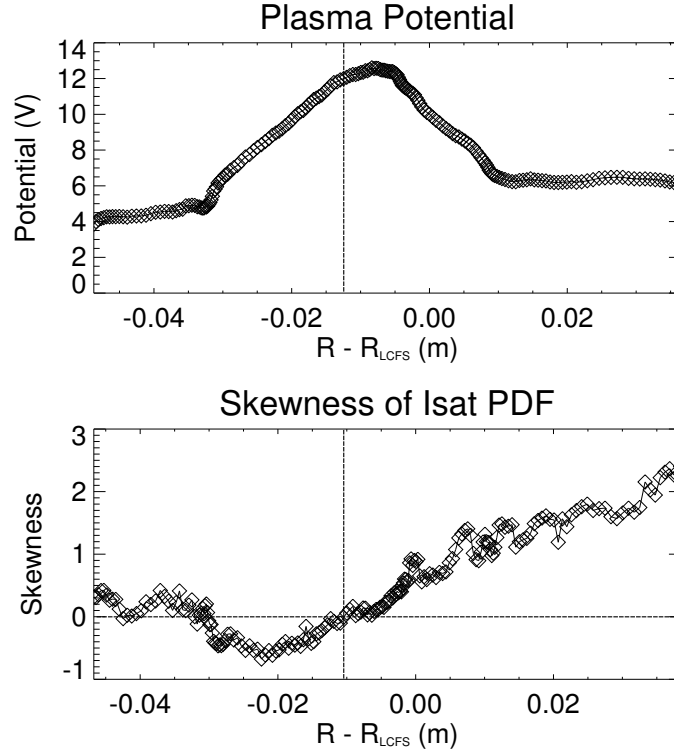


FIGURE 3.36: Skewness of the  $I_{sat}$  PDF compared to plasma potential as measured by the BPP. The skewness first becomes Gaussian in the region of high potential. As the gradient of the potential changes sign the skewness also changes sign.

radial electric field changes sign). The skewness and radial electric field appear to be strongly correlated within the radial shear layer with a strong decrease in the skewness occurring as the radial electric field changes sign. The radial shear layer produces strong levels of flow shear by  $\mathbf{E} \times \mathbf{B}$  motion. Since both the electric field and the skewness are measured locally the skewness can be plotted as a function of both  $E_R$  and  $dE_r/dR$ . This is presented in figure 3.38.

The most striking feature of figure 3.38 is the relationship between the skewness and radial electric field gradient. As the radial electric field gradient reaches a maximum the skewness tends toward 0 and as the maximum is passed through the skewness reverses sign. This suggests that the ejection of blobs outside the radial shear layer and the ejection of holes inside the shear layer and, most importantly, identifies the region around the maximum in  $dE_r/dR$  as a local generation region of intermittency and hence the birth region of filaments and holes. This trend can be clearly identified in the PDFs of  $I_{sat}$  in the filament, generation and hole regions respectively. Figure 3.39 shows the  $I_{sat}$  PDF constructed at different points during the probe reciprocation, alongside the time series used to construct the PDF. Figure 3.39 indeed confirms that the fluctuations vary from positive to negative intermittency as the radial shear layer is crossed, with the PDF tending towards a Gaussian at the peak in the generation region which corresponds to

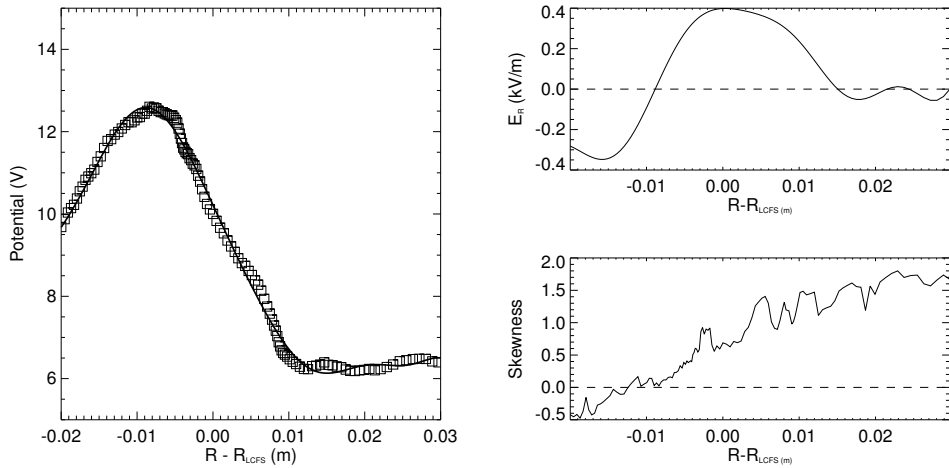


FIGURE 3.37: Comparison of the radial electric field with the skewness of the  $I_{sat}$  PDF in the vicinity of the radial shear layer during MAST shot 30250. The radial electric field is constructed by fitting the plasma potential with a smoothly varying 17<sup>th</sup> degree polynomial (left), removing small scale structure in the profile and allowing gradients to be taken.

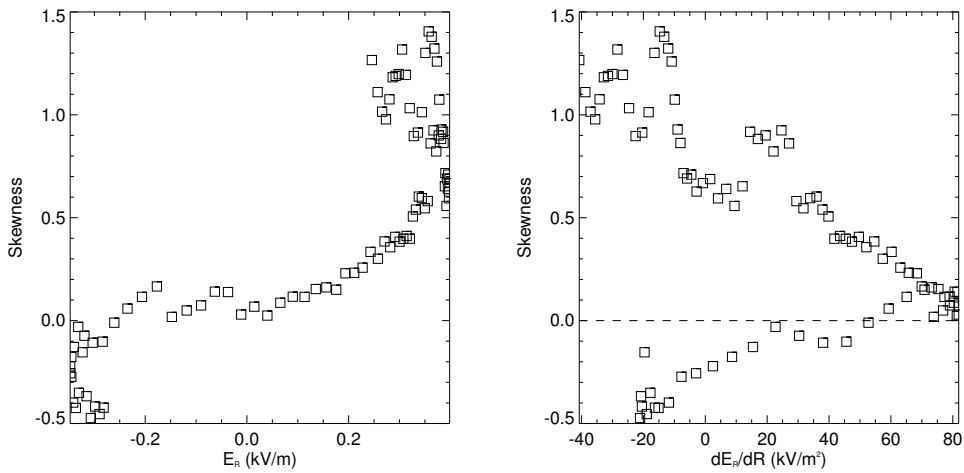


FIGURE 3.38: Skewness of the  $I_{sat}$  PDF as a function of the radial electric field (a) and the radial electric field shear (b). The skewness is at an absolute minimum when the electric field shear is a maximum, suggesting that the shear of the radial electric field is responsible for reducing the  $I_{sat}$  PDF to a Gaussian.

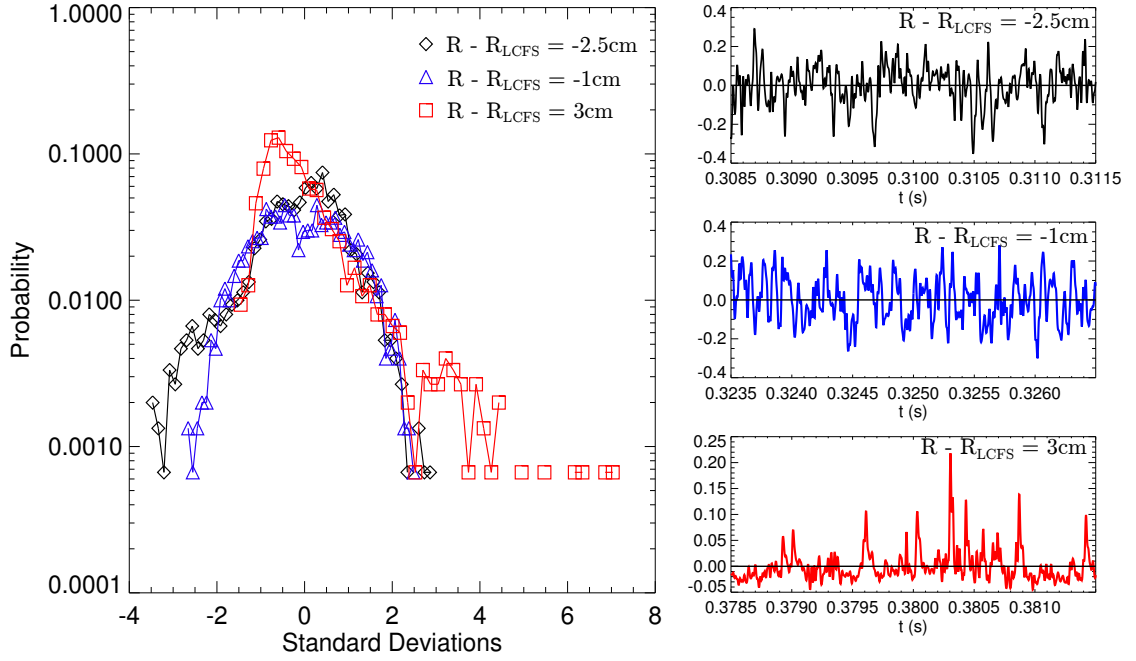


FIGURE 3.39: PDFs of the  $I_{sat}$  time series in the SOL (red) at  $R - R_{LCFS} = 3cm$ , centre of the radial shear layer (blue) at  $R - R_{LCFS} = -1cm$  and inside the radial shear layer (black) at  $R - R_{LCFS} = -2.5cm$  showing the presence of blobs in the SOL, the presence of holes in the core side and the Gaussian nature of fluctuations in the generation zone.

a maximum in the radial electric field gradient.

It should be noted that it is presently not possible to verify the causality between the observed correlation between the radial electric field gradient and the skewness of the  $I_{sat}$  PDF. This uncertainty can be highlighted by considering two cases:

1. If the sheared flow that results from the gradient in electric field is directly responsible for the generation of blobs and holes through the Kelvin-Helmholtz mechanism, as investigated in [172] for example, then the radial electric field gradient is the cause of the correlation with the skewness.
2. If blobs and holes are produced by other mechanisms, for example drift-interchange turbulence driven by pressure gradients, then net flows can develop through a Reynolds stress. The direction of this flow may then be strongly dependant on the skewness of the fluctuations (ie whether more eddys turn one way or another) and the skewness causes the observed correlation with the gradient of electric field.

It has not been possible to remove this ambiguity here, however the observation of the strong correlation between skewness and radial electric field gradient is important and it is hoped that this will lead to further study into the causality of edge turbulence and the edge radial electric field. An avenue for future work may be to apply the technique

described by Sugihara *et.al* [187] for detecting causality in correlated time-series and confirm cause and effect between the radial electric field gradient and skewness of the  $I_{sat}$  fluctuations.

### 3.6 Improvements to the MAST BPP design

The results presented in this chapter clearly demonstrate the capability of the BPP to make detailed measurements of quantities that are important in the understanding of the plasma edge. The implementation of the BPP technique is extremely simple; a BPP can be implemented on a standard reciprocating probe head simply by retracting a Langmuir probe a suitable distance ( $> \rho_i$ ) into the probe body. This can make the cost for a basic implementation of a BPP very low (the total cost for the BPP used in this study was  $< \pounds 2000$ ). As has been shown in this chapter, such an implementation can provide measurements of both the electron temperature and radial electric field profiles at the plasma edge, which are difficult to measure with a similar degree of accuracy by other means. The potential for advanced measurements by a BPP is rich, but is limited in the current design for a number of reasons. The measurement of true plasma potential fluctuations, which are not contaminated by the electron temperature as in the case of the floating potential, is a particularly appealing aspect of the BPP. This could not be achieved in the current design due to a suppression of the frequency spectrum of the BPP. Since the BPP collection relies on cross-field motion, rather than parallel motion, currents to the collector are significantly reduced. This increases the effective impedance of the BPP. If the impedance of the BPP greatly exceeds the impedance of the amplifier circuitry then a leakage current can occur across the cabling from the probe head to the amplifier. This causes the observed suppression of the BPP frequency spectra and greatly reduces the spectral window for the BPP measurement. In cases where the BPP impedance is particularly high (the BPP3 pin on the MAST design for example) the suppression can occur across the entire spectrum and an underestimate of the plasma potential profile can occur. This was also recently noted on the MIRABEL cylindrical low-temperature plasma device[155]. The solution to this problem is to replace the (relatively) low impedance electronics with a very high impedance option. In[154] and [155] an electrometer with extremely high impedance ( $> T\Omega$ ) is used as a unit gain voltage buffer which greatly increases the impedance of the measurement circuit and therefore reduces the effects of leakage current.

Of particular interest to the study of turbulent transport in the plasma edge is the interaction between fluctuations in electrostatic potential, density and electron temperature. These three quantities could be measured simultaneously by a BPP, an LP measuring  $I_{sat}$  and an LP measuring  $V_{fl}$ . The difference between  $V_{BPP}$  and  $V_{fl}$  can be used to

obtain  $T_e$ , which can then be factored into the measurement of  $I_{sat}$  to extract the electron density. The MAST BPP design can make the individual measurements required, however the spatial separation between the two LPs is 1.6cm, whilst the spatial separation between the LPs and the BPP is 2.4cm. This is a result of the inherited design of the Gundestropp probe head and could not be readily avoided. This limits any measurements to fluctuating structures with a length-scale significantly greater than 2.5cm. Unfortunately this is well within the region of interest for fluctuations on MAST [79]. An improved design would be a set of probe groupings laid out on the probe face. Each grouping would contain a BPP, an LP measuring  $I_{sat}$  and an LP measuring  $V_{fl}$  in very close proximity. The individual groupings can then be laid out in a pattern to best capture the nature of the fluctuations. A particularly enticing choice of layout would be an array spaced logarithmically away from one another. This allows an array of  $N$  groupings to measure  $\sum_{i=0}^{N-1} i = (N-1)^2/2 + (N-1)/2$  length-scales, whilst a common linear array is limited to  $N$  possible measurements. In the case of 5 groupings this provides 10 measurements in a logarithmic array compared to 5 in a linear array.

### 3.7 Conclusions and Future Work

This chapter has presented the first implementation of the ball-pen probe (BPP) technique on MAST. The specific design included three BPP pins with variable retraction depth and diameter. The two pins with a smaller diameter exhibited a significant suppression of their frequency spectra due to the inherently high impedance of the BPP pins. This high impedance is a result of the collection process in the BPP occurring across the magnetic field rather than along it. When the pin impedance is higher than the impedance of the measurement circuitry current leakage can lead to the suppression observed in the frequency spectra. Of the three BPP pin configurations a retraction of 5mm and a diameter of 4mm was optimum for measurements of the potential. A similar filtering of the frequency spectrum was observed in all BPP pins in the SOL region of the plasma, indicating that the impedance of the BPP is strongly dependant on local plasma conditions. This prevented the study of potential fluctuations in the SOL, but did not affect profile measurements.

The BPP was attached to the reciprocating probe (RP) system on MAST during the M9 campaign and was used to measure radial profiles of the plasma potential, electron temperature and radial electric field in the vicinity of the separatrix. The potential measured by the BPP was shown to differ significantly from the floating potential measured simultaneously by a Langmuir probe (LP). The BPP potential profile is always more positive than the floating potential, and exhibits polarity changes where none are observed in the floating potential. This suggests that the BPP potential is measuring

a quantity at least closely related to the plasma potential. A quantitative test of the validity of the BPP measurement of the plasma potential is achieved through a detailed comparison with the Thomson scattering (TS) system. Both the BPP and TS systems were used to measure the electron temperature. Moderate agreement between the two diagnostics was achieved by neglecting secondary electron emission however the two profiles diverged as the temperature increased. It was then argued that due to the predominantly normal angle of incidence of plasma fluxes onto the LP secondary electron emission should be included in the analysis. This was achieved by integrating an empirical formula over a Maxwellian energy distribution over a range of temperatures providing a temperature dependant parametrization of the secondary electron yield. This was then mapped to plasma radius to generate radial profiles including self-consistently the effects of secondary electron emission. This greatly improved the agreement between the two diagnostics and, within the uncertainty introduced by the neglect of pitch angle variation, showed that the BPP potential may be considered a reasonable measurement of the plasma potential. Aside from the specifics this also shows that secondary electron emission can play a significant role in midplane LP measurements and should be considered in future studies with the RP system on MAST.

By fitting a high order polynomial function to the plasma potential a smoothly varying potential profile can be extracted which retains the main features of the true profile. From these fits a derivative can be taken and an estimate for the radial electric field is produced. This showed that the BPP measurement can accurately resolve the radial shear layer in the radial electric field. From these measurements a poloidal and toroidal velocity were inferred by  $\mathbf{E} \times \mathbf{B}$  motion. Motivated by this measurement of the radial shear layer, the interaction between the statistics of  $I_{sat}$  fluctuations and the radial electric field was investigated in a single shot. Given the locality of the measurements of  $I_{sat}$  and  $E_R$  the variation in moments of the  $I_{sat}$  PDF could be compared quantitatively to aspects of the underlying profiles. In particular a strong correlation was observed between the skewness of the  $I_{sat}$  PDF and the gradient of the radial electric field,  $dE_R/dR$ . The skewness was observed to drop to 0 at the point where  $dE_R/dR$  maximises indicating that the generation region for intermittency in the plasma edge occurs at the peak in electric field gradient. The causality of this correlation could not be determined from the measurements and is an excellent topic for future investigations.

Finally improvements to the BPP design are presented which would allow for advanced measurements of fluctuations in the plasma edge. It is hoped that the work presented in this chapter acts as motivation for continued use of the BPP principle. Given its simplicity and cost to implement it is an attractive option for fluctuation measurements. The drawback of the BPP is an incomplete understanding of the collection mechanism. This was commented on and a simple model of kinetic ion filtering was derived which provided limitations on the possible collection velocities in a BPP, however a detailed

analysis was not attempted. Such an analysis requires advanced kinetic modelling using a 3D PIC code which is beyond the scope of this thesis.



## Chapter 4

# The BOUT++ Framework

BOUT++ [104, 188–190], written by B. D. Dudson of the York Plasma Institute in collaboration with Lawrence Livermore National Lab, is a framework for simulating highly non-linear problems in plasma physics. It is written predominantly in the C++ programming language with aspects of pre and post-processing written in IDL, python, mathematica and matlab. BOUT++ is an incarnation of the original **BO**U**ND**ary **T**urbulence code written by X. Q. Xu [191] of LLNL now maintained by M. V. Umansky in the form of BOUT-06 [192]. BOUT++ inherits some algorithms and ideas from BOUT, but is entirely a stand-alone code and has a number of features not present in the original BOUT. These include:

- An object oriented modular structure. This allows users to change aspects of the physics being investigated without having to alter any of the core modules. This decoupling between the numerical methods employed and the physics involved greatly speeds up the implementation of multiple physics models for use in a variety of different problems. It also gives the user access to a range of numerical methods for solving their problem with minimal alteration to the module detailing the physics under investigation.
- Generalized differential operators which can be solved in any curvilinear coordinate system with a metric tensor allowed to vary in two directions (i.e. a system with one constant direction). This allows for a large variety of geometries to be implemented in the code again with minimal alteration. Only the components of the metric tensor need to be specified.
- Syntactically simple coding of evolution equations. This speeds up the writing of the equations and greatly simplifies the task of reading them.

The strength of BOUT++ lies in its flexibility and usability. The symbolic writing of equations makes error spotting a less formidable task. An example of this style of coding in BOUT++ is given below. The Navier-Stokes equation [193] is a well known non-linear equation arising from the application of Newton's 2nd law to a fluid. This equation is

$$\frac{\partial \mathbf{u}}{\partial t} = -(\mathbf{u} \cdot \nabla) \mathbf{u} - \frac{\nabla p}{\rho} + \nu \nabla^2 \mathbf{u} \quad (4.1)$$

where  $\mathbf{u}$  is the flow velocity,  $p$  is the internal pressure of the fluid,  $\rho$  is the mass density of the fluid and  $\nu$  is the viscosity coefficient. To write this in BOUT++ a single line is required:

```
Vector3D ddt(u) = -V_dot_Grad(u,u) - Grad(p)/rho + nu*Laplacian(u)
```

This style of implementation makes it easy to add extra terms to the equations to be solved. For example in the case above one may wish to investigate the role of advection due to a background static flow,  $\mathbf{v}$ . In BOUT++ this is achieved by adding the line

```
ddt(u) += -V_dot_Grad(u,v) - V_dot_Grad(v,u) - V_dot_Grad(v,v)
```

This flexibility has prompted the use of BOUT++ for a variety of problems. In [194] BOUT++ was used to simulate the non-linear dynamics of edge localised modes (ELMs). It was shown that BOUT++ captured the ideal linear physics of ELMs by benchmarking the code against pre-existing linear MHD codes. The model was then extended to the non-linear regime and the full crash of the pedestal profiles was captured. It was also shown that the energy released by the ELM varied strongly with resistivity even in regions where the linear stability varied very little. This suggests that non-linear processes play a prominent role in energy redistribution during an ELM crash.

BOUT++ has also been used to study the complex structure of turbulence in simple linear magnetized plasmas. In [195] non-linear simulations of turbulence in the Large Plasma Device (LAPD) [196] were studied. It was shown that the driving mechanism for the turbulence was not a linear instability, as is often assumed, but a non-linear instability. In particular it was shown that an energy transfer between modes with parallel wave numbers  $k_{\parallel} = 0$  and  $k_{\parallel} \neq 0$  is required to drive turbulence which is sufficiently broadband to be compared with experiment.

As a final example BOUT++ can also be implemented in simple slab geometries to elucidate fundamental non-linear physics. In [115, 116, 197] isolated filaments were simulated in 3D. The geometry used was a simple slab with an effective gravity giving rise to interchange motion. These simulations showed that filaments of a sufficiently small cross-sectional size can become unstable to resistive drift-waves, an inherently 3D

phenomenon that cannot be accounted for in the popular 2D models of blob motion introduced in chapter 2. This effect is potentially important for intermittent transport in the edge of tokamaks since it suggests that drift-waves place a minimum possible size at which filaments can propagate a significant distance across the separatrix. This work is important in the context of this thesis where the 3D dynamics of filaments are investigated in more complex geometries.

The remainder of this chapter will describe briefly the algorithms used in BOUT++ for spatial differentiation and time integration, followed by an overview of the physics module developed to study 3D filament dynamics in complex geometries in BOUT++. See chapter 2 for a discussion of this topic.

## 4.1 Time Integration

### 4.1.1 Explicit and implicit time integration

The general evolution of a system of equations can be written in the form

$$\frac{\partial \mathbf{f}}{\partial t} = \mathbf{F}(\mathbf{f}) \quad (4.2)$$

where  $\mathbf{f} = (f_1, f_2, \dots, f_i)$  is the state vector of the system and  $\mathbf{F}(\mathbf{f})$  is a general non-linear function of time,  $\mathbf{f}$  and its spatial derivatives. To solve equations of this kind BOUT++ employs the method of lines [198] which separates the processes of time integration and spatial differentiation. The time derivative in 4.2 can be discretized by taking

$$\frac{\partial \mathbf{f}}{\partial t} \approx \frac{\mathbf{f}^{n+1} - \mathbf{f}^n}{\Delta t} = \mathbf{F}(\mathbf{f}^n) \Rightarrow \mathbf{f}^{n+1} = \mathbf{f}^n + \Delta t \mathbf{F}(\mathbf{f}^n) + \mathcal{O}(\Delta t^2) \quad (4.3)$$

where  $\mathbf{f}^n$  is the state vector at time  $t$  and  $\mathbf{f}^{n+1}$  is the state vector at time  $t + \Delta t$ . This is called the Forward Euler Method (FEM). In this approximation  $\mathbf{f}^{n+1}$  depends only on the state vector at the previous time step and is *explicit* of any variable at time  $t + \Delta t$ . Instead of making the discretization in 4.3 it is possible to substitute  $t$  for  $t - \Delta t$ . In this case the discretization formula becomes

$$\frac{\partial \mathbf{f}}{\partial t} \approx \frac{\mathbf{f}^n - \mathbf{f}^{n-1}}{\Delta t} = \mathbf{F}(\mathbf{f}^n) \Rightarrow \mathbf{f}^n = \mathbf{f}^{n-1} + \Delta t \mathbf{F}(\mathbf{f}^n) + \mathcal{O}(\Delta t^2) \quad (4.4)$$

which gives

$$\mathbf{f}^n = \mathbf{f}^{n-1} + \Delta t \mathbf{F}(\mathbf{f}^n) + \mathcal{O}(\Delta t^2) \quad (4.5)$$

which is termed the Backward Euler Method (BEM). The formula 4.5 is *implicit*; the state vector at time  $t + \Delta t$  depends implicitly on itself through the function  $\mathbf{F}(\mathbf{f}^{n+1})$ . Explicit time integration schemes are typically easier to implement than implicit schemes. The time step used in an explicit scheme is limited by the CFL condition [199] with numerical instability occurring if  $\Delta t > \Delta t_{CFL} = \Delta x/u$  where  $\Delta x$  is the spatial step and  $u$  is the fastest velocity in the system. Since the time integration in an implicit scheme already contains all required updated information the time step used can exceed  $\Delta t_{CFL}$  without incurring numerical instability. This makes implicit schemes favourable for numerically stiff problems (problems containing fast, limiting timescales), however physics occurring faster than the implicit time step may be damped in the numerical solution.

Equation 4.5 can be written in the form

$$\mathbf{G}(\mathbf{f}^n) = \mathbf{f}^n - \mathbf{f}^{n-1} - \Delta t \mathbf{F}(\mathbf{f}^n) = 0 \quad (4.6)$$

$\mathbf{G}$  can now be expanded around  $\mathbf{f}_m^n$  to first order to give

$$\mathbf{G}(\mathbf{f}^n) = \mathbf{G}(\mathbf{f}_m^n) + (\mathbf{f}^n - \mathbf{f}_m^n) \frac{\partial \mathbf{G}}{\partial \mathbf{f}^n} = 0 \quad (4.7)$$

The derivative term is given by

$$\frac{\partial \mathbf{G}}{\partial \mathbf{f}^n} = \mathbb{I} - \Delta t \mathbb{J} \quad (4.8)$$

where the Jacobian matrix,  $\mathbb{J}$  is given by

$$\mathbb{J} = \frac{\partial \mathbf{F}}{\partial \mathbf{f}} = \begin{pmatrix} \frac{\partial F_1}{\partial f_1} & \dots & \frac{\partial F_1}{\partial f_i} \\ \vdots & \ddots & \vdots \\ \frac{\partial F_i}{\partial f_1} & \dots & \frac{\partial F_i}{\partial f_i} \end{pmatrix} \quad (4.9)$$

To solve equation 4.7 a Newtonian iteration procedure is followed where a solution,  $\delta \mathbf{f}^n$ , is found to

$$(\mathbb{I} - \Delta t \mathbb{J}) \delta \mathbf{f}^n = -\mathbf{G}(\mathbf{f}^n) \quad (4.10)$$

and the state vector is then updated using

$$\mathbf{f}_{m+1}^n = \mathbf{f}_m^n + \delta \mathbf{f}^n \quad (4.11)$$

until

$$\mathbf{G}(\mathbf{f}_{m+1}^n) \approx 0 \quad (4.12)$$

is satisfied within a user defined tolerance. The inversion of equation 4.10 is often performed using a Krylov subspace method, hence this iteration procedure is often named 'Newton-Krylov iteration'.

For a typical implementation of such an implicit time integration the state vector is often very large (proportional to the number of discrete points in the spatial domain). This then leads to a Jacobian matrix which is prohibitively large and cannot be stored within the memory of the CPU. Furthermore matrix inversion methods, such as Gaussian Elimination [182], can become prone to errors in large systems. To avoid this problem the matrix-vector product  $\mathbb{J}\mathbf{v}$  can be approximated by

$$\mathbb{J}\mathbf{v} \approx \frac{\mathbf{F}(\mathbf{f} + \epsilon\mathbf{v}) - \mathbf{F}(\mathbf{f})}{\epsilon} \quad (4.13)$$

where  $\epsilon$  is a small number. This negates the need to store the large matrix  $\mathbb{J}$  and is known as a 'Jacobian-Free' implementation.

It is worth noting that higher order methods may replace the  $\Delta t$  coefficient with some other coefficient and may also depend on multiple previous time steps.

#### 4.1.2 Time integration methods in BOUT++

BOUT++ contains the option to use either explicit or implicit time integration methods. The explicit methods supported are the FEM, the Runge-Kutta 4th order (RK4) method [182], the Karniadakis method [200] and the RK3-SSP methods. No explicit methods will be used during this thesis.

For implicit time integration BOUT++ uses by default the PVIDE solver [201] which is part of the SUite of Non-linear Differential Algebraic Solvers (SUNDIALS). PVIDE is an iterative solver with a dynamically varying local time step  $h$  and method order  $q$ . Each global time step consists of a number of local PVIDE time steps. On each local time step an estimate for the local error on the state vector  $\mathbf{f}^n$ ,  $\epsilon_n$  is calculated and the inequality

$$|\epsilon_n|_{rms} < 1 \quad (4.14)$$

is tested, where  $|\epsilon_n|_{rms}$  is the weighted root-mean-square norm given by

$$|\epsilon_n|_{rms} = \left[ \sum_{i=1}^N \frac{1}{N} (w_i \epsilon_{n,i})^2 \right]^{1/2} \quad (4.15)$$

where  $i$  loops over the elements of the error vector  $\epsilon_n$ .  $w_i$  is a weight vector given by

$$w_i = \frac{1}{atol + rtol |f_i|} \quad (4.16)$$

$atol$  and  $rtol$  are the absolute and relative tolerance in the error on the state vector at each time step and combine to define the allowable error in the solution. If the inequality 4.14 is violated then the local time step,  $h$  and/or the order of the method  $q$

is dynamically altered until the inequality is once again adhered to. PVODE iterates this procedure until the user specified global time step is overtaken, at which point PVODE interpolates the solution back in time to the global time step.

## 4.2 Spatial Differentiation

The RHS function in 4.2 can be a function of the state vector and/or combinations of its spatial derivatives. To perform such derivatives computationally the continuum of the spatial domain must be represented numerically. Three common methods are used for such a representation: Finite difference, finite element and spectral methods. In finite difference schemes functions are represented at discrete locations on a spatial grid, or mesh. In finite element and spectral schemes functions are represented by a truncated set of basis functions. BOUT++ uses finite difference methods for spatial derivatives. Figure 4.1 is an example of discretization in one dimension used in typical finite difference methods. The type of the mesh used within the scheme depends on the description chosen to represent the fluid motion within the code. This can be broadly split into two categories:

- *Lagrangian mesh*: The nodes of the mesh track material properties of the fluid. This approach is advantageous for the tracking of free surfaces within the fluid, interfaces between fluid species and complex spatial domains. The drawback is its difficulty in tracking strongly sheared flows and shocks where the mesh may become severely deformed, requiring either adaptive re-meshing or other techniques for handling such deformation. This method is illustrated in figure 4.1 part b.
- *Eulerian mesh*: The nodes of the mesh are fixed in space and the variation of continuum quantities is tracked on the mesh nodes. This allows for large deformation in the continuum properties, as well a simpler computational implementation. The drawback with this method is that the resolution of flow details (eg. dissipation scales in turbulence) and of interfaces is strongly dependant on the resolution of the mesh. This method is illustrated in figure 4.1 part c.

See [202, 203] for a description of these two approaches, as well as a description of advanced methods combining qualities of each.

BOUT++ is an Eulerian code and consequently must calculate both diffusive (ie  $d/dx$ ,  $d^2/dx^2$ ) and advective ( $v \cdot d/dx$ ) derivatives. This is done through a range of possible differencing methods.

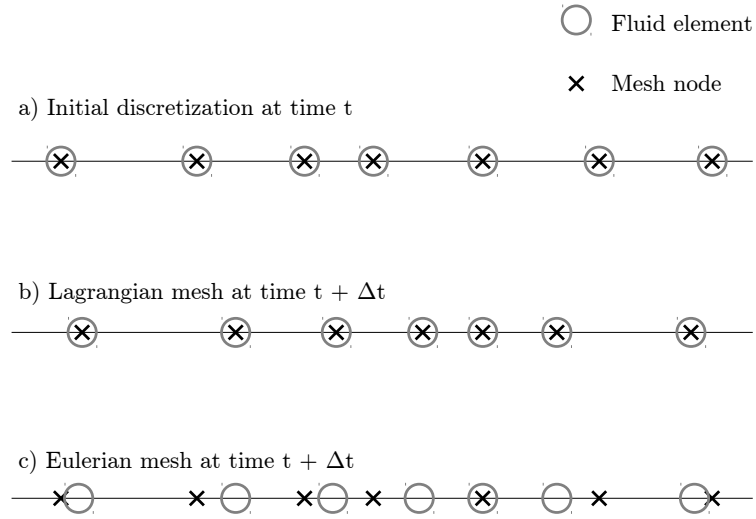


FIGURE 4.1: Mesh discretization and the difference between the Lagrangian (b) and Eulerian (c) approach.

#### 4.2.1 Finite Difference Methods in BOUT++

For diffusive operators BOUT++ employs central differencing methods of differentiation. The Taylor expansion of  $f(x+h)$  around  $f(x)$  where  $h$  is a small spatial increment (i.e. the spacing between two nodes of the mesh) is

$$f(x+h) = f(x) + hf'(x) + \frac{h^2}{2}f''(x) + \mathcal{O}(h^3) \quad (4.17)$$

whilst the Taylor expansion of  $f(x-h)$  is

$$f(x-h) = f(x) - hf'(x) + \frac{h^2}{2}f''(x) + \mathcal{O}(h^3) \quad (4.18)$$

Subtracting these two expressions and rearranging for  $f'(x)$  results in the expression

$$f'_0 = \frac{1}{2h}(f_1 - f_{-1}) \quad (4.19)$$

where  $f_0, f'_0 = f, f'(x)$  and  $f_1, f_{-1} = f(x \pm h)$ . This is an expression for the spatial first derivative of  $f$  accurate to second order in  $h$ . Higher order differencing formulas are available such as

$$f'_0 = \frac{1}{12h}(-f_{-2} + 8f_{-1} - 8f_1 + f_2) \quad (4.20)$$

which is accurate to 4th order in  $h$ . The second derivative formulas are readily calculable by adding 4.17 and 4.18 and rearranging for  $f_0''$  which gives

$$f_0'' = \frac{1}{h^2} (f_1 - 2f_0 + f_{-1}) \quad (4.21)$$

to second order in  $h$  and

$$f_0'' = \frac{1}{12h^2} (-f_{-2} + 16f_{-1} - 30f_0 + 16f_1 - f_2) \quad (4.22)$$

to fourth order. BOUT++ facilitates the use of either second order differencing with 4.19 and 4.21 or fourth order differencing with 4.20 and 4.22.

In strongly advective flows central differencing methods often produce non-physical oscillatory behaviour on the leading and/or trailing edges of advective structures [204]. To combat such spurious oscillation upwind methods can be used to calculate advective operators such as  $v \cdot d/dx$ . First developed in [204] upwind differencing accounts for the direction of information flow in advection by biasing the finite difference stencil in the direction of the incoming flow. The simplest implementation of an upwind method uses the first order difference formulae

$$v \frac{\partial f}{\partial x} \approx v \frac{(f_0 - f_{-1})}{h} \quad (4.23)$$

when the flow is in the positive  $x$  direction and

$$v \frac{\partial f}{\partial x} \approx v \frac{(f_1 - f_0)}{h} \quad (4.24)$$

when the flow is in the negative  $x$  direction. This is illustrated in figure 4.2. In BOUT++ 1st order and 4th order upwinding methods are supported. The differencing formulae for 4th order upwinding are

$$v \frac{\partial f}{\partial x} \approx v \frac{(4f_1 - 12f_{-1} + 2f_{-2} + 6f_0)}{12h} \quad (4.25)$$

for positive velocities and

$$v \frac{\partial f}{\partial x} \approx v \frac{(-4f_{-1} + 12f_1 - 2f_2 - 6f_0)}{12h} \quad (4.26)$$

for negative velocities.

BOUT++ can also use a more advanced form of upwind differencing, the **W**eighted **E**ssentially **N**on-**O**scillatory scheme [205]. The WENO scheme exploits the fact that  $f_0'$  can be approximated through a number of different stencils at the same order of accuracy. The scheme tests for discontinuities in the solution on the various stencils and adapts to generate a solution which is weighted towards the smooth stencils. This helps

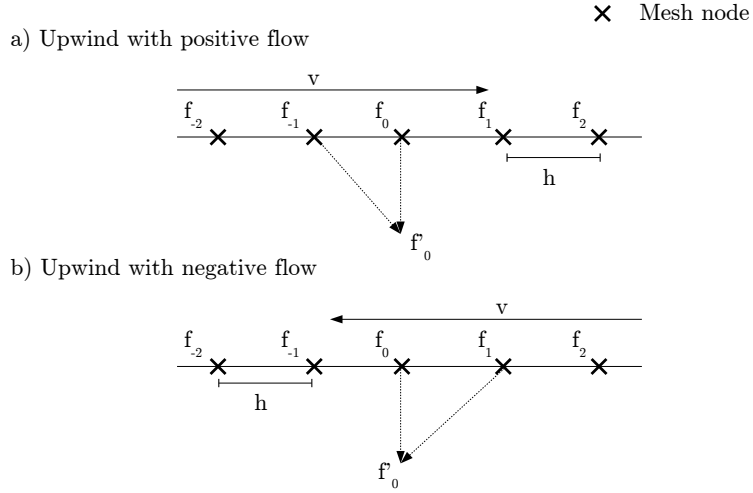


FIGURE 4.2: Schematic example of 1D upwind differencing in the presence of positive flow (a) and negative flow (b) with respect to the  $x$  direction.

to ensure monotonicity and makes the scheme exceptionally good at dealing with steep gradients and discontinuities. BOUT++ facilitates a 3rd order WENO scheme which calculates the upwind differences as

$$v \frac{\partial f}{\partial x} \approx v \frac{1}{2h} [(f_1 - f_{-1}) - w(-f_{-2} + 3f_{-1} - 3f_0 + f_1)] \quad (4.27)$$

for positive velocities (i.e. left biased upwinding) and

$$v \frac{\partial f}{\partial x} \approx v \frac{1}{2h} [(f_1 - f_{-1}) - w(-f_{-1} + 3f_0 - 3f_1 + f_2)] \quad (4.28)$$

for negative velocities (i.e. right biased upwinding). The weighting coefficient  $w$  determines the strength of upwind biasing and is given by

$$w = \frac{1}{1 + 2r^2} \quad (4.29)$$

where  $r$  is given by

$$r = \frac{\epsilon_W + (f_0 - 2f_{-1} + f_{-2})^2}{\epsilon_W + (f_1 - 2f_0 + f_{-1})^2} \quad (4.30)$$

for positive velocities/left biasing and

$$r = \frac{\epsilon_W + (f_2 - 2f_1 + f_0)^2}{\epsilon_W + (f_1 - 2f_0 + f_{-1})^2} \quad (4.31)$$

for negative velocities/right biasing.  $\epsilon_W$  is a small number included to avoid the denominator in  $r$  reducing to 0.  $r$  is used to dynamically select the most appropriate

combination of the two stencils with which to construct  $f'_0$ . For the 3rd order WENO scheme the differential is constructed from a central difference approximation (first term in 4.28, 4.27) and a left/right biased difference (second term in 4.28, 4.27). If there is a strong disparity between the second derivatives from these two schemes then it is likely that a discontinuity exists in one of the approximations. If  $|f''_0|$  from the biased difference is much larger than the central difference then  $r$  becomes very large and  $w$  becomes very small. The contribution from the biased difference to the calculation of  $f'_0$  is then strongly reduced and the smoothness of the solution is maintained. By contrast if  $|f''_0|$  from the central difference is much larger than the biased difference,  $w$  takes its maximum value of 1 and the calculation of  $f'_0$  is weighted towards the biased difference approximation. The WENO scheme in BOUT++ is a lower accuracy scheme than the 4th order upwind differencing, but it ensures monotonicity and smoothness making it a good option for simulations of advective structures.

As an alternative to finite difference methods BOUT++ also supports the use of fast Fourier transforms (FFTs) for numerical differentiation [206]. BOUT++ requires one dimension of the simulation domain to be periodic and is constrained to the use of FFTs in this direction. Internally this direction is the BOUT++  $z$  coordinate (see appendix A for a description of the BOUT++ coordinate system). BOUT++ uses the FFTW3 library [207] to perform FFTs.

These schemes for numerical differentiation are implemented in BOUT++ either directly through operators of the form

```
Field3D dfdx = DDX(f);
Field3D d2fdx2 = D2DX2(f);
Field3D vdfdx = V_dot_Grad(v,f);
```

or through more advanced differential operators which account for the metric tensor of the coordinate system.

## 4.2.2 Differential operators in BOUT++

Differential operators in BOUT++ fall into two categories: coordinate independent and coordinate dependant. The coordinate independent differential operators implemented in BOUT++ are given in table 4.1 (taken from [188]). The differential operators in table 4.1 are de-constructed internally within BOUT++ to the point at which differencing formulas using the methods outlined in section 4.2.1 can be applied. The deconstruction accounts for the metric tensor of the coordinate system. In general curvilinear coordinates with a covariant basis  $(\mathbf{e}_i, \mathbf{e}_j, \mathbf{e}_k)$  and a contravariant basis  $(\nabla u^i, \nabla u^j, \nabla u^k)$  the

Differential Operator	BOUT++ syntax
$\mathbf{v} = \nabla f$	Vector3D v = Grad(Field3D f)
$f = \nabla \cdot \mathbf{a}$	Field3D f = Div(Vector3D a)
$\mathbf{v} = \nabla \times \mathbf{a}$	Vector3D v = Curl(Vector3D a)
$f = \mathbf{v} \cdot \nabla g$	Field3D f = V_dot_Grad(Vector3D v, Field3D g)
$\mathbf{v} = \mathbf{a} \cdot \nabla \mathbf{b}$	Vector3D v = V_dot_Grad(Vector3D a, Vector3D b)
$f = \nabla^2 g$	Field3D f = Laplacian(Field3D g)

TABLE 4.1: Table of coordinate independent differential operators in BOUT++.

differential operators are given by [208]

$$\nabla f = \frac{\partial f}{\partial u^i} \nabla u^i \quad (4.32)$$

$$\nabla \cdot \mathbf{a} = \frac{1}{J} \frac{\partial}{\partial u^i} (J A^i) = \frac{1}{J} \frac{\partial}{\partial u^i} (J g^{ij} A_i) \quad (4.33)$$

$$\nabla \times \mathbf{a} = \frac{\epsilon^{ijk}}{J} \frac{\partial A_j}{\partial u^i} \mathbf{e}_k \quad (4.34)$$

$$\nabla^2 f = \nabla \cdot (\nabla f) = \frac{1}{J} \frac{\partial}{\partial u^i} \left( J g^{ij} \frac{\partial f}{\partial u^j} \right) = g^{ij} \frac{\partial^2 f}{\partial u^i \partial u^j} + \Gamma^i \frac{\partial f}{\partial u^i} \quad (4.35)$$

$$\Gamma^i = \frac{1}{J} \frac{\partial}{\partial u^i} (J g^{ij}) \quad (4.36)$$

where  $J$  is the Jacobian and  $g^{ij}$  is the contravariant metric tensor of the coordinate system,  $\epsilon^{ijk}$  is the Levi-Cevita symbol and the Einstein convention of index summation is implied. For a fuller derivation and introductory explanation to differential geometry see appendix A and/or [208].

BOUT++ is optimized for simulations at the boundary of tokamak plasmas. As a consequence it contains a suite of differential operators that depend on the equilibrium magnetic field. These operators require the magnetic field to be written in a Clebsch form [188, 208, 209],

$$\mathbf{B} = \nabla \alpha \times \nabla \beta \quad (4.37)$$

where  $\mathbf{B}$  is the equilibrium magnetic field and  $\alpha$  and  $\beta$  are stream functions of the magnetic field. In a field aligned coordinate system the stream functions define the  $x$  and  $z$  dimensions of the simulation domain such that

$$\mathbf{B} = \nabla x \times \nabla z \quad (4.38)$$

which then defines the third dimension from

$$\nabla x \times \nabla z = \frac{1}{J} \mathbf{e}_y \Rightarrow \mathbf{b} = \frac{\mathbf{B}}{B} = \frac{1}{JB} \mathbf{e}_y \quad (4.39)$$

where  $\mathbf{b}$  is the magnetic field tangency vector. The magnetic field dependant differential operators (pertinent to this thesis) included in BOUT++ are listed in table 4.2. The

Differential Operator	BOUT++ syntax
$f = \mathbf{b} \cdot \nabla g$	Field3D f = Grad_par(Field3D g)
$f = \nabla \cdot (\mathbf{b}g)$	Field3D f = Div_par(Field3D g)
$f = \mathbf{b} \times \nabla g \cdot \nabla h = \mathbf{b} \cdot \nabla g \times \nabla h$	Field3D f = bracket(Field3D h,Field3D g)
$f = \nabla_{\perp}^2 g$	Field3D f = Delp2(Field3D g)

TABLE 4.2: Differential operators implemented in BOUT++ which depend on the equilibrium magnetic field.

differential operators in table 4.2 can be written in the  $x, y, z$  coordinate system defined by 4.38, 4.39 and described in appendix A as [188]

$$\mathbf{b} \cdot \nabla f = \frac{1}{JB} \frac{\partial f}{\partial y} = \frac{1}{\sqrt{g_{yy}}} \frac{\partial f}{\partial y} \quad (4.40)$$

$$\nabla \cdot (\mathbf{b}f) = \mathbf{B} \cdot \nabla \left( \frac{f}{B} \right) = \frac{B}{\sqrt{g_{yy}}} \frac{\partial f}{\partial y} \frac{\partial}{\partial B} \quad (4.41)$$

The gradient operator perpendicular to the magnetic field is defined as

$$\begin{aligned} \nabla_{\perp} f &\equiv \nabla f - \mathbf{b} (\mathbf{b} \cdot \nabla) f = \frac{\partial f}{\partial u^i} \nabla u^i - \frac{1}{(JB)^2} g_{i,y} \frac{\partial f}{\partial y} \nabla u^i \\ &= \left( \frac{\partial f}{\partial x} - \frac{g_{xy}}{J^2 B^2} \frac{\partial f}{\partial y} \right) \nabla x + \left( \frac{\partial f}{\partial z} - \frac{g_{yz}}{J^2 B^2} \frac{\partial f}{\partial y} \right) \nabla z = A_x \nabla x + A_z \nabla z \end{aligned} \quad (4.42)$$

The perpendicular Laplacian can now be defined as

$$\nabla \cdot (\nabla_{\perp} f) = \frac{1}{J} \frac{\partial}{\partial x} (Jg^{xx} A_x + Jg^{xz} A_z) + \frac{1}{J} \frac{\partial}{\partial z} (Jg^{zz} A_z + g^{xz} A_x) \quad (4.43)$$

The flute assumption,  $k_{\parallel} \ll k_{\perp}$ , results from the field aligned nature of fluctuations in the plasma edge and allows parallel derivative terms to be neglected. Expanding the derivatives then gives

$$\nabla_{\perp}^2 f = g^{xx} \frac{\partial^2 f}{\partial x^2} + 2g^{xz} \frac{\partial^2 f}{\partial x \partial z} + g^{zz} \frac{\partial^2 f}{\partial z^2} + \Gamma_{\perp}^x \frac{\partial f}{\partial x} + \Gamma_{\perp}^z \frac{\partial f}{\partial z} \quad (4.44)$$

where

$$\begin{aligned} \Gamma_{\perp}^x &\equiv \frac{1}{J} \left( \frac{\partial}{\partial x} (Jg^{xx}) + \frac{\partial}{\partial z} (Jg^{xz}) \right) \\ \Gamma_{\perp}^z &\equiv \frac{1}{J} \left( \frac{\partial}{\partial x} (Jg^{xz}) + \frac{\partial}{\partial z} (Jg^{zz}) \right) \end{aligned} \quad (4.45)$$

are called the connection coefficients. Finally in the tokamak edge the dominant advection mechanism is  $\mathbf{E} \times \mathbf{B}$  motion perpendicular to the magnetic field. As a result the

operator

$$(\mathbf{b} \times \nabla\phi) \cdot \nabla f = \mathbf{b} \cdot (\nabla\phi \times \nabla f) \quad (4.46)$$

is commonly used in models of the edge plasma. This can be written in terms of the metric as

$$\frac{1}{JB} [g_{xy} (\nabla\phi \times \nabla f)^x + g_{yy} (\nabla\phi \times \nabla f)^y + g_{yz} (\nabla\phi \times \nabla f)^z] \quad (4.47)$$

where

$$\begin{aligned} (\nabla\phi \times \nabla f)^x &= \frac{1}{J} \left( \frac{\partial\phi}{\partial y} \frac{\partial f}{\partial z} - \frac{\partial\phi}{\partial z} \frac{\partial f}{\partial y} \right) \\ (\nabla\phi \times \nabla f)^y &= -\frac{1}{J} \left( \frac{\partial\phi}{\partial x} \frac{\partial f}{\partial z} - \frac{\partial\phi}{\partial z} \frac{\partial f}{\partial x} \right) \\ (\nabla\phi \times \nabla f)^z &= \frac{1}{J} \left( \frac{\partial\phi}{\partial x} \frac{\partial f}{\partial y} - \frac{\partial\phi}{\partial y} \frac{\partial f}{\partial x} \right) \end{aligned} \quad (4.48)$$

Using tables 4.1 and 4.2 the differential operators described in this section can be used in BOUT++.

### 4.3 BOUT++ code layout

A central aim of the BOUT++ code is to decouple the physics being investigated from the numerics used to solve the system of equations pertaining to that physics. A schematic of the layout of BOUT++ is shown in figure 4.3. The user provides an input file under the name `BOUT.inp` which contains runtime input settings for the physics module and the internal parts of BOUT++. The user also provides a physics module. The physics module contains the evolution equations to be solved as well as the initialisation of variables and parameters. The mesh, created by the user, can either be specified through the input file in the case of simple geometries or as a separate grid file containing all aspects of the mesh and metric tensor of the coordinate system.

The next section provides an overview of the physics module created to investigate filament dynamics in BOUT++.

### 4.4 Physics module for filament dynamics investigations

The aim of the physics module implemented into BOUT++ and described within this thesis is to study the dynamics of filaments. Previous studies of these phenomena have been reviewed in chapter 2. The physics model is designed to facilitate simulations in both a simple slab geometry, used to investigate basic processes in blob and filament dynamics, as well as a field aligned geometry representing a tokamak plasma edge. The

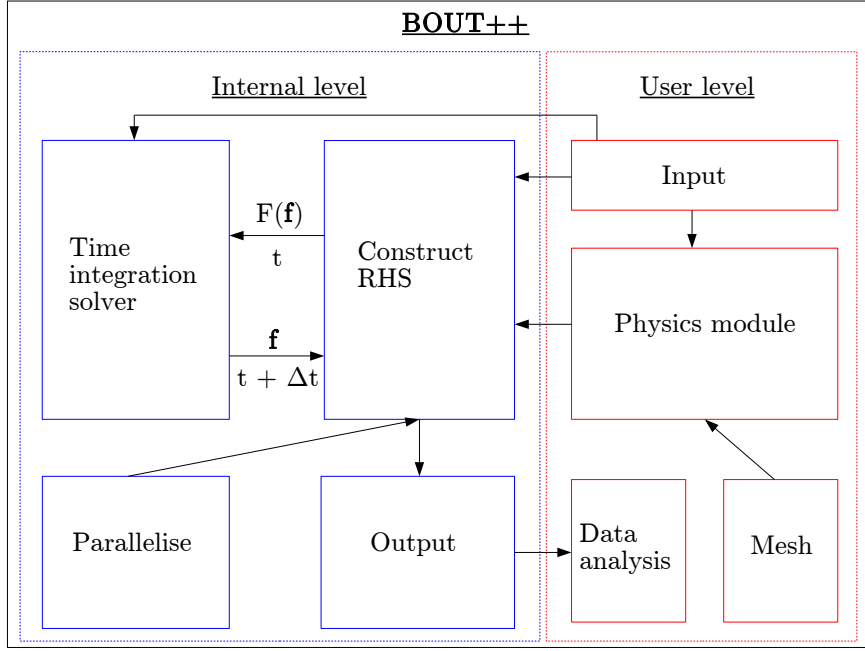


FIGURE 4.3: Schematic of the layout of the BOUT++ code showing the division between the user and the internal numerics within BOUT++.

particular tokamak simulated in this thesis is MAST in a connected double null geometry. To derive properties of the metric tensor which are required for the realistic simulations a grid generator has been developed which extracts the pertinent information from an EFIT [210] equilibrium reconstruction. This will be described subsequently. First the system of equations to be solved is introduced.

#### 4.4.1 System of Equations

The system of equations implemented in the filament dynamics physics module is derived under the drift-ordering employed in [52, 53]. The drift ordering makes the following assumptions:

- Spatial length scales can be separated between a slowly varying length scale,  $L_s$  and a quickly varying length scale,  $L_f$ . Quantities that vary on the slow time scale are assumed to have a large spatial extent, whilst quantities varying on the fast time scale are assumed to have a small spatial extent. This is effectively a splitting between the the perpendicular and parallel scales of turbulence in the SOL. The small parameter,  $\epsilon$  is characterized by

$$\epsilon \equiv \frac{L_f}{L_s} \ll 1 \quad (4.49)$$

- Other parameters assumed to be small are

$$\beta \equiv 2\mu_0 nT/B_0^2 \ll 1$$

$$\Delta \equiv \lambda/L_s \ll \lambda/L_f \ll 1 \quad (4.50)$$

$$\delta = \rho/L_f \ll 1$$

where  $\beta$  measures the ratio of thermal to magnetic pressure,  $\lambda$  is the ion-electron collisional mean free path and  $\rho$  is the gyro-radius.

- The time-scales in the system can be ordered by

$$\omega \ll \nu \ll \Omega \quad (4.51)$$

where  $\omega$  is the characteristic frequency of the physics under investigation within the system,  $\nu$  is the collision frequency between ions and electrons and  $\Omega$  is the gyro-frequency.

- The small variables can be ordered by

$$\begin{aligned} \omega &\sim \delta^2 \Omega_i \\ \delta &\sim \Delta \\ \beta &\sim \epsilon \\ v/v_{th} &\sim \epsilon/\delta \ll 1 \end{aligned} \quad (4.52)$$

Before these orderings are used to derive equations for the dynamics of filaments it is worth checking their validity using characteristic values of the ordering parameters. Four values are considered for each parameter corresponding to a typical value in the core, edge, near SOL and far SOL of the MAST tokamak. The characteristic parameters are given in table 4.3 and are based on the work in [211]. The values of  $L_f$  in table 4.3 are

	Core	Edge	Near SOL	Far SOL
$T_e(eV)$	500	50	15	5
$n_e(m^{-18})$	50	8	5	1
$B_0(T)$	0.5	0.37	0.35	0.33
$R(m)$	0.84	1.36	1.44	1.49
$q$	1.2	8	10	5
$L_s(m)$	6.3	68.2	15	8
$L_f(m)$	0.02	0.02	0.02	0.02

TABLE 4.3: Characteristic parameters in a MAST L-mode plasma to be used to assess the validity of the drift ordering.

based on typical filament length scales [79] whilst  $L_s$  is taken as  $L_s = 2\pi Rq$  for the core

and edge region and based on estimates motivated by [211] for the SOL regions. Using these parameters the drift orderings can be tested. A ratio of  $v/v_{th,i} \sim 0.05$ , as well as a characteristic frequency  $\omega \sim 20kHz$  is assumed throughout the test, motivated by the results of chapter 3.  $\Omega_i$  is given by

$$\Omega_i = \frac{eB_0}{m_i} [rad/s] \quad (4.53)$$

where  $m_i$  is the ion mass (here taken as Deuterium). The collisional mean free path is taken from the electron-ion channel and is given by

$$\lambda_{ei} = \frac{v_{th,i}}{\nu_{ei}} [m] \quad (4.54)$$

where the thermal velocity is given by (assuming  $T_i = T_e$ )

$$v_{th,i} = \sqrt{\frac{2T_e}{m_i}} [m/s] \quad (4.55)$$

and the collision frequency is given by

$$\nu_{ei} = \frac{4\sqrt{2\pi}n\Lambda e^4}{3\sqrt{m_e}T_e^{3/2}} = \frac{1}{3.44 \times 10^{11}} \frac{n\Lambda}{T_e^{3/2}} [1/s] \quad (4.56)$$

with  $T_e$  measured in eV and  $n$  measured in  $10^{19}m^{-3}$  and the Coulomb logarithm,  $\Lambda$  is taken as  $\sim 10$ . The gyro-radius is given by

$$\rho_i = \frac{v_{th,i}}{\Omega_i} [m] \quad (4.57)$$

Figure 4.4 shows the ordered terms from 4.52 calculated and compared against each other. Figure 4.4 shows that the drift ordering is valid for the near and far SOL with the exception of the ordering of  $\beta$  which is found to be  $\beta \ll \epsilon$  rather than  $\beta \sim \epsilon$ . This is not important since the system will be subsequently assumed to be electrostatic. If  $\beta$  is very low then it is very difficult for a perturbation in pressure to affect the magnetic field structure, so the electrostatic assumption is justified. It is also worth noting that this analysis shows that the fundamental assumptions of the drift ordering,  $\delta \ll 1$ ,  $\Delta \ll 1$  and  $\beta \ll 1$  are justified in the SOL regions.

The system of equations to be solved in the BOUT++ filament dynamics physics model consists of the density equation;

$$\frac{dn}{dt} = 2c_s\rho_s\xi \cdot (\nabla n - n\nabla\phi) + \frac{1}{e}\nabla_{\parallel}J_{\parallel} \quad (4.58)$$

the vorticity equation;

$$n\rho_s^2\frac{d\omega}{dt} = 2c_s\rho_s\xi \cdot \nabla n + \frac{1}{e}\nabla_{\parallel}J_{\parallel} \quad (4.59)$$

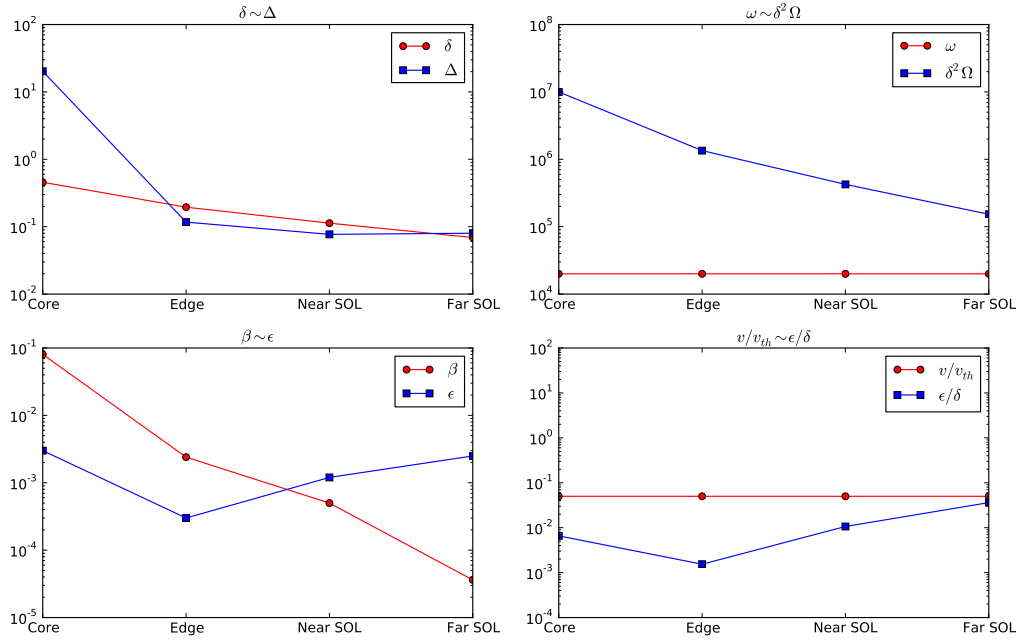


FIGURE 4.4: Test of the drift ordering given in 4.52 for MAST relevant parameters in the core, edge, near and far SOL regions.

and auxiliary equations for the parallel current

$$J_{\parallel} = \frac{\sigma_{\parallel} T_e}{e} \nabla_{\parallel} (\ln(n) - \phi) \quad (4.60)$$

and for the perpendicular vorticity

$$\omega = \nabla_{\perp}^2 \phi \quad (4.61)$$

In 4.58 and 4.59 the time derivatives are advective such that

$$\frac{d}{dt} \equiv \frac{\partial}{\partial t} + \mathbf{v}_E \cdot \nabla \quad (4.62)$$

where

$$\mathbf{v}_E \equiv c_s \rho_s \mathbf{b} \times \nabla \phi \quad (4.63)$$

is the  $\mathbf{E} \times \mathbf{B}$  velocity. A full derivation of these equations starting from the first 3 moments of the kinetic equation is given in appendix B. In the system of equations  $n$  is the electron density in  $\text{m}^{-3}$  and  $n_e = n_i$  is assumed.  $\phi$  is the electrostatic potential and is normalized to  $T_e$  in eV.  $\omega$  is the perpendicular vorticity.  $J_{\parallel}$  is the parallel current

density.  $c_s$  and  $\rho_s$  are the Bohm sound speed and Bohm gyro-radius given by

$$c_s = \sqrt{\frac{eT_e}{m_i}} \quad (4.64)$$

and

$$\rho_s = \frac{c_s}{\Omega_i} \quad (4.65)$$

with  $\Omega_i$  given by 4.53.  $\sigma_{\parallel}$  is the parallel conductivity of the system and determines the mobility of electrons flowing along the magnetic field line. It is given by [47]

$$\sigma_{\parallel} = 1.96 \frac{ne^2}{m_e \nu_{ei}} \quad (4.66)$$

with  $\nu_{ei}$  taken from 4.56. Finally the vector  $\boldsymbol{\xi}$  is here named the polarization vector since it defines the direction of charge polarization due to guiding centre drifts and is defined as

$$\boldsymbol{\xi} \equiv \mathbf{b} \times \boldsymbol{\kappa} \quad (4.67)$$

where  $\mathbf{b}$  is the magnetic field tangency vector and  $\boldsymbol{\kappa}$  is the magnetic curvature vector. In deriving these equations a number of assumptions are made, further to the assumptions of the drift-ordering. These assumptions are:

- Cold ions; Since the electrons respond to the plasma potential much faster than ions it is the electron dynamics that primarily determine the motion of the plasma, with ions following by quasineutrality. The cold ion assumption is used to neglect effects due to ionic motion.
- Isothermal; this model is used to study filaments in the far-SOL region. Thermal transport is significantly faster than particle transport [47] as such a localised excess of temperature is likely to thermalize with the background in the far SOL. This is supported by Thomson scattering measurements in MAST [61] which show that  $\delta n_e/n_e \gg \delta T_e/T_e$  in L-mode filaments.
- No parallel streaming; all advection parallel to the magnetic field line is neglected. This is valid on time-scales  $\tau < L_{\parallel}/c_s \sim 10^{-4} s$  where the parallel advection cannot move the plasma large distances and the dynamics of the filament is dominated by perpendicular motion. Figure 4.5 shows schematically the region of time under which these simulations are valid. This assumption has recently been relaxed in [212] and shown to have little effect on filament motion.
- Boussinesq approximation; this approximation assumes that  $\delta n/n$  is sufficiently small that  $\nabla \cdot (n d_t \nabla_{\perp} \phi) \sim n d_t \nabla_{\perp}^2 \phi$ . This is not strictly valid for filaments which have densities significantly above the background. The approximation was initially

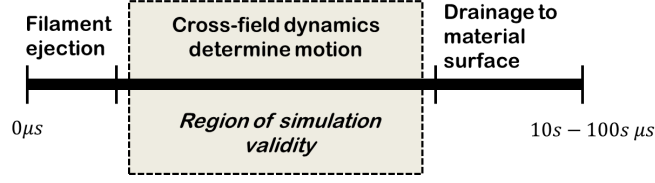


FIGURE 4.5: Schematic example of the time-history of a filament with the region under which the physics model presented in this chapter is valid. Image taken with permission from [1]

necessitated by the inability to implement the proper form numerically. In recent versions of BOUT++ this can be done using the PETSc solver suite [213] with a suitable preconditioner [190]. Unfortunately this could not be implemented during this thesis, however previous studies have shown that this approximation does not significantly affect the motion of blobs [95, 214].

- Electrostatic; This is motivated by the observation from figure 4.4 that  $\beta \ll \epsilon$  which makes electromagnetic perturbations small in comparison to thermodynamic fluctuations and validates the electrostatic approximation.
- No neutral particles. At low temperatures plasma recombination, as well as interactions with material surfaces may produce a significant source of neutral particles. This is not included here to focus on the plasma physics leading to filament motion. In [107] it is noted that a neutral wind force can produce a force perpendicular to the magnetic field and lead to enhanced blob polarization. This would be a good topic for future work.

The system is normalized as follows; density is normalized to a background value,  $n_0$ ; length scales to  $\rho_s$  ( so that  $\kappa$  is normalized to  $1/\rho_s$ ); time-scales to  $\Omega_i^{-1}$ ; the electrostatic potential to  $T_e$  in  $eV$ . The normalized system of equations is

$$\frac{\partial n}{\partial t} + \mathbf{b} \times \nabla \phi \cdot \nabla n = 2\hat{\xi} \cdot (\nabla n - n\nabla\phi) + \alpha \nabla_{\parallel} J_{\parallel} \quad (4.68)$$

$$n \left( \frac{\partial}{\partial t} + \mathbf{b} \times \nabla \phi \cdot \nabla \right) \nabla_{\perp}^2 \phi = \hat{\xi} \cdot \nabla n + \alpha \nabla_{\parallel} J_{\parallel} \quad (4.69)$$

$$J_{\parallel} = \nabla_{\parallel} \ln(n) - \nabla_{\parallel} \phi \quad (4.70)$$

The dimensionless variables are  $\alpha$  defined by

$$\alpha = \frac{\sigma_{\parallel} T_e}{n_0 c_s \rho_s e} \quad (4.71)$$

and

$$\hat{\xi} = \rho_s \xi \quad (4.72)$$

with  $T_e$  in  $eV$ .

This completes the description of the system of equations to be solved. The next section describes the boundary conditions applied to the system.

#### 4.4.2 Boundary Conditions

In either the slab geometry or the more complicated MAST SOL geometry boundary conditions are required on the two boundaries in each dimension,  $(x, y, z)$ , of the domain. The  $z$  domain, which is in the bi-normal direction in a slab, or the toroidal direction in the full magnetic geometry, is required by BOUT++ to be periodic and so has periodic boundary conditions applied to it. At the boundary of the  $x$  (radial) domain all variables have zero gradient boundary conditions. Initially the electrostatic potential was given a Dirichlet boundary condition (set to 0 on the boundary). This resulted in the potential experiencing an interaction with a reflection of itself in the boundary and was deemed non-physical. In practice the simulations are treated as void when the interaction with the radial boundary becomes strong and efforts are made to keep such interaction to a minimum.

Interaction with the  $y$  boundary along the magnetic field line cannot be readily avoided. In this direction filaments can contact material surfaces leading to the formation of a sheath. Sheath formation has been introduced in chapter 3 and results in the material surface developing a negative bias with respect to the plasma. If the angle of incidence of the magnetic field line on the material surface is oblique a magnetic pre-sheath can form. The role of the magnetic pre-sheath is to demagnetize the ions and bend their trajectories towards the surface normal. This requires electric fields forming on the gyro-radius length scale and invalidates the drift ordering [215]. Consequently the edge of the magnetic pre-sheath is the boundary for the domain of the simulations in this thesis. From [92] the parallel current at the magnetic pre-sheath entrance is

$$J_{||,sh}^{\pm} = \pm enc_s (1 - \exp(\phi_W - \phi^{\pm})) \quad (4.73)$$

where  $\pm$  corresponds to the upper and lower boundary respectively.  $\phi_W$  is the potential at the material wall and  $\phi^{\pm}$  is the potential at the magnetic pre-sheath entrance. In an isothermal plasma  $\phi_W$  can be regarded as a constant offset and so acts as a ground potential and can be set to 0. Modifications to 4.73 exist including the effect of oblique incidence to the material surface [215, 216]. For this thesis such modifications are not used. This is due to the reduced nature of the simulation geometry. A good topic for future work would be the effect of oblique field line incidence at the sheath edge on filament dynamics.

### 4.4.3 Initial Conditions

Filament simulations are initialized with a density profile of the form

$$n(t=0) = n_0 + \delta n \exp\left(\frac{(x-x_0)^2}{\delta_x^2}\right) \exp\left(\frac{(z-z_0)^2}{\delta_z^2}\right) \quad (4.74)$$

where  $x_0$  and  $z_0$  define the spatial centre of the filament in the perpendicular plane.  $\delta_x$  and  $\delta_z$  set the Gaussian widths of the filament in the  $x$  and  $z$  dimensions. Filaments are always seeded homogeneously along the magnetic field line. The vorticity,  $\omega$ , is initially 0 and grows in the initial phase of the simulation. Different initial conditions in  $\omega$  and  $\phi$  were tested but the simulations proved to be insensitive to such changes, with initial transients rapidly damped. The electrostatic potential is then set by the inversion of equation 4.61 and the parallel current set by 4.60 with the boundary conditions 4.73.

### 4.4.4 Grid Generation

BOUT++ requires a user specified grid upon which the differencing stencils used to construct spatial differential operators are applied. The physics module has been constructed for use with either simple slab geometries or complex flux-tube geometries. The results presented in this thesis all use the latter of these two options, however the former is included with a view to allowing the physics module to be used as generally as possible.

#### 4.4.4.1 Slab Grids

Whilst not used within this thesis, slab grids may be easily implemented within the input BOUT.inp file by specifying the parameters listed in table 4.4. Setting these parameters sets the grid as a Cartesian (i.e. an identity metric tensor) slab with an artificial radius of curvature set by `R_c`.

#### 4.4.4.2 SOL flux tube grids

The principal aim of the numerical studies within this thesis is to investigate the role of magnetic geometry in the dynamics of filaments. To introduce the effects of magnetic geometry a flux tube approach has been taken for the numerical grid[217]. A flux tube approach assumes that the variation of all parameters perpendicular to the magnetic field is small compared to the variation of fluctuating quantities such that, on the fluctuation length and time scales, all parameters can be considered constant. This approach is

Parameter	Function
<b>General Parameters</b>	
<code>nx</code>	Number of grid points in the $x$ dimension
<code>dx</code>	Grid resolution in $x$
<code>ny</code>	Number of grid points in the $y$ dimension
<code>dy</code>	Grid resolution in $y$
<code>MZ</code>	Number of grid points in the $z$ dimension
<code>ZMAX</code>	Limit of the $z$ domain (as a multiple of $2\pi$ )
<b>Specific Parameters</b>	
<code>Slab</code>	Boolean to optimize physics module for slab simulations
<code>R_c</code>	Radius of curvature in $m$

TABLE 4.4: Table of parameters used to set up slab grid simulations. General parameters can be specified for any BOUT++ simulation. Specific parameters are implemented for the filament dynamics physics module.

not self consistent since quantities which vary on the equilibrium scale of the tokamak are constant in the perpendicular dimensions of the flux tube, but also have constant gradients. In this sense a parameter and its spatial variation are decoupled such that for a parameter  $P(x)$  which varies in the radial  $x$  dimension the variation of  $P$  across the flux-tube is accounted for from the Taylor expansion

$$P(x) = P(x_0) + \left. \frac{dP}{dx} \right|_{x_0} (x - x_0) + \mathcal{O}\left((x - x_0)^2\right) \quad (4.75)$$

where  $x_0$  is the centre of the flux tube. The flux-tube assumption then decouples  $P \approx P(x_0)$  and its variation  $d_x P \approx d_x P|_{x_0}$  from one another. As such the flux-tube approximation is only formally valid as  $x - x_0 \rightarrow 0$ .

Flux tube geometries are popular in core turbulence simulations, including those carried out on MAST [218], where the correlation length scale of turbulence is sufficiently small that equilibrium variation can be neglected. In the SOL the validity of the flux tube approach is questionable. Both background gradients and transient events such as filaments can have a length scale of a few cm and so the fast scale dynamics can interact with equilibrium variation. In the far SOL gradients are relatively flat, however the variation of the equilibrium magnetic field may still occur within the length scales of interest. The flux tube treats the magnetic field strength and the magnetic shear as entirely independent quantities, so accounts for magnetic field variation in an approximate manner. The flux tube fully accounts for variation parallel to the magnetic field however. The effect of this parallel variation is to transform the cross-section of the flux tube. The form of this transformation will be commented on further in chapter 5, however the effect of parallel variation of the magnetic field dominates the effect of perpendicular variation [114]. In MAST the perpendicular B-field strength may vary by  $\sim 5\%$  across the magnetic field, whilst it may vary by  $\sim 70\%$  parallel to it. This

then motivates the use of the flux tube approach for a first investigation of these effects of filament motion. A good topic for future study would be to include perpendicular variation of geometric parameters, however this is outside the scope of this thesis.

The grid generator, named `sol_flux_tube.pro`<sup>1</sup>, has been written to generate flux tube grids around a single field line in the SOL. It takes as input a file containing general equilibrium properties of the plasma in either the EQDSK `g.file` format from an EFIT calculation or the `.equ` format commonly outputted from equilibrium calculation codes such as FIESTA. The user must also input the desired flux surface in the SOL by its normalized flux label,  $\psi_N = (\psi - \psi_{ax}) / (\psi_{sep} - \psi_{ax})$  where  $\psi_{sep}$  is the poloidal magnetic flux at the separatrix and  $\psi_{ax}$  is the flux at the magnetic axis. If coordinates of the first wall are included in the equilibrium file the grid generator will then select the magnetic flux surface at the desired  $\psi_N$  between its two intersections with the wall. Otherwise it selects the entire length of the flux surface. The user can optionally specify end points of the flux surface (ie an artificial wall) if no wall coordinates are present. The grid-generator then selects the desired flux surface. Figure 4.6 shows the  $\psi_N = 1.15$  surface in MAST which is the basis on which all flux tubes in this thesis are constructed.

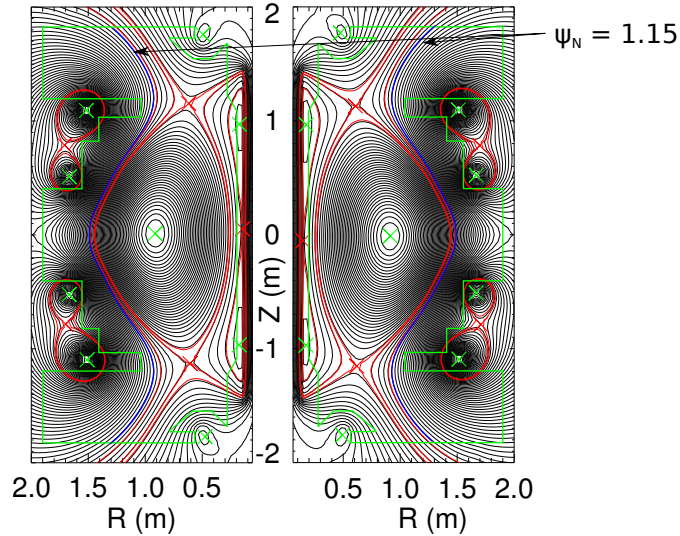


FIGURE 4.6: Visualisation of the  $\psi_N = 1.15$  flux surface in the poloidal plane of MAST, highlighted in blue. Also shown are the primary and secondary separatrices (red lines), X-points (red crosses), O-points (green crosses) and the first wall (green line).

The aim of the grid generator is to derive the parameters required for the metric tensor of the BOUT++ field aligned coordinate system given in appendix A, as well as parameters required for the physics module. These are listed in table 4.5. The grid is designed to be equally spaced along the flux surface in the poloidal plane. This means that  $h_\theta = 1/|\nabla\theta|$  is a constant in the flux tube domain. In a circular cross-section

<sup>1</sup>Available at [https://github.com/boutproject/BOUT-dev/blob/master/tools/tokamak\\_grids/gridgen/sol\\_flux\\_tube.pro](https://github.com/boutproject/BOUT-dev/blob/master/tools/tokamak_grids/gridgen/sol_flux_tube.pro)

Parameters	Function
$B(x, y)$	Total magnetic field strength
$B_p(x, y)$	Poloidal magnetic field strength
$B_T(x, y)$	Toroidal magnetic field strength
$R(x, y)$	Major radius of the field line
$h_\theta(x, y)$	Poloidal arc length
$I(x, y)$	Magnetic shear integrated in $y$
$(\mathbf{b} \times \boldsymbol{\kappa})^{x,y,z}$	Contravariant components of the polarization vector

TABLE 4.5: Parameters produced as output by the SOL flux tube grid generator required to construct the metric tensor, or required by the physics module.

$h_\theta$  can be identified with the minor radius, though in more complicated cross-sections  $h_\theta$  can be thought of as the poloidal arc length such that  $h_\theta d\theta = dL$  where  $dL$  is the elemental distance in the poloidal direction and  $d\theta$  is an elemental shift in poloidal angle. The magnetic field strength  $B$ , its components  $B_p$  and  $B_T$  and the major radius,  $R$ , are readily extracted from the equilibrium file and interpolated onto the grid. The challenging parameters to extract from the equilibrium information are the magnetic curvature vector,  $\boldsymbol{\kappa}$  and the magnetic shear,  $\partial\nu/\partial\psi$  which is then integrated in  $y$  to get  $I$ .

To derive the polarization vector  $\mathbf{b} \times \boldsymbol{\kappa}$  the grid generator uses the expression for the curvature of a general curve characterised by a tangency vector  $\hat{\mathbf{T}}$  [208]

$$\boldsymbol{\kappa} = \frac{d\hat{\mathbf{T}}}{ds} \quad (4.76)$$

where  $d/ds$  is the derivative along the curve. The relationship between the curvature and the tangency vector is illustrated in figure 4.7. On a magnetic field line the tangency vector is  $\mathbf{b} = \mathbf{B}/B$ . The tangency vector in a cylindrical coordinate system can be written as

$$\hat{\mathbf{T}} = \mathbf{b} = \frac{d\mathbf{r}}{ds} = \frac{dR}{ds}\hat{\mathbf{R}} + \frac{dZ}{ds}\hat{\mathbf{Z}} + R\frac{d\phi}{ds}\hat{\phi} \quad (4.77)$$

where  $R$ ,  $Z$  and  $\phi$  are the radial, vertical and toroidal coordinates respectively and  $s$  is the distance along the line. This then gives a curvature vector

$$\boldsymbol{\kappa} = \left( \frac{d^2R}{ds^2} - R \left( \frac{d\phi}{ds} \right)^2 \right) \hat{\mathbf{R}} + \frac{d^2Z}{ds^2} \hat{\mathbf{Z}} + \left( 2 \frac{dR}{ds} \frac{d\phi}{ds} + R \frac{d^2\phi}{ds^2} \right) \hat{\phi} \quad (4.78)$$

A derivation of equation 4.78 is given in appendix C. The grid generator calculates the derivative quantities in 4.77 and 4.78 along the selected magnetic field line and uses them to construct the vector  $\boldsymbol{\kappa}$  and subsequently  $\mathbf{b} \times \boldsymbol{\kappa}$ . The grid generator uses the relations

$$\nabla\psi = \frac{\partial\psi}{\partial R}\hat{\mathbf{R}} + \frac{\partial\psi}{\partial Z}\hat{\mathbf{Z}} \quad (4.79)$$

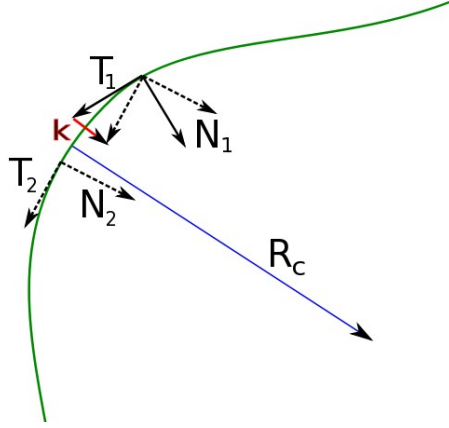


FIGURE 4.7: Schematic showing how the curvature vector ( $k$  in the figure) derives from the change of the tangency vector over a distance  $ds$  along the field line. The curvature vector is normal to the curve and its magnitude is the reciprocal of the radius of curvature,  $R_c$ .

as well as

$$\nabla\theta = \frac{1}{h_\theta B_\theta} \nabla\phi \times \nabla\psi \quad (4.80)$$

and

$$\nabla\phi = \frac{1}{R} \hat{\phi} \quad (4.81)$$

to generate the contravariant components of  $\mathbf{b} \times \kappa$  in the  $(\psi, \theta, \phi)$  coordinate system. Finally the expressions for the reciprocal vectors of the field aligned coordinate system, given in appendix A are used to generate the contravariant components of  $\mathbf{b} \times \kappa$  in the field aligned system, as required.

The grid generator must also produce the integrated magnetic shear defined as

$$\int_{y_0}^y \frac{\partial\nu}{\partial\psi} dy' \quad (4.82)$$

which requires the derivation of the magnetic shear,  $\partial\nu/\partial\psi$ . The magnetic field line pitch,  $\nu$  is

$$\nu = \frac{h_\theta B_\phi}{R B_\theta} \quad (4.83)$$

which is used to construct an expression for the magnetic shear

$$\frac{\partial\nu}{\partial\psi} = \nu \left( \frac{1}{h_\theta} \frac{\partial h_\theta}{\partial\psi} + \frac{1}{B_\phi} \frac{\partial B_\phi}{\partial\psi} - \frac{1}{B_\theta} \frac{\partial B_\theta}{\partial\psi} - \frac{1}{R} \frac{\partial R}{\partial\psi} \right) \quad (4.84)$$

The second and third terms in 4.84 can be extracted from the equilibrium file. The fourth term can be calculated by noting that

$$\frac{\partial R}{\partial \psi} = \frac{\nabla R \cdot \nabla \psi}{R^2 B_\theta^2} = \frac{1}{R^2 B_\theta^2} \frac{\partial \psi}{\partial R} \quad (4.85)$$

which can also be extracted from the equilibrium file.

The first term is the most difficult to generate from the equilibrium data. To derive an expression for  $\partial h_\theta / \partial \psi$  it is useful to first note that  $\boldsymbol{\kappa}$  can be written in the form (see reference [188])

$$\boldsymbol{\kappa} = -\frac{B_\theta}{h_\theta B} \left[ \left( \frac{\partial}{\partial x} \left( \frac{h_\theta B}{B_\theta} \right) - \frac{\partial}{\partial y} \left( \frac{B_\phi I R}{B} \right) \right) \nabla x + \frac{\partial}{\partial y} \left( \frac{B_\phi R}{B} \right) \nabla z \right] \quad (4.86)$$

Now taking  $\boldsymbol{\kappa} \cdot \nabla \psi$  and noting that

$$\nabla x \cdot \nabla \psi = R^2 B_\theta^2 \quad (4.87)$$

$$\nabla z \cdot \nabla \psi = -IR^2 B_\theta^2$$

the expression for  $\boldsymbol{\kappa} \cdot \nabla \psi$  can be written (after some algebraic manipulation)

$$\boldsymbol{\kappa} \cdot \nabla \psi = -\frac{R^2 B_\theta^3}{h_\theta B} \left( \frac{\partial}{\partial x} \left( \frac{h_\theta B}{B_\theta} \right) - \frac{B_\phi R}{B} \frac{\partial I}{\partial y} \right) \quad (4.88)$$

Exploiting

$$I = \int \frac{\partial \nu}{\partial \psi} dy \Rightarrow \frac{\partial I}{\partial y} = \frac{\partial \nu}{\partial \psi} \quad (4.89)$$

and using 4.83, again after some manipulation 4.88 can be rearranged to give an expression for  $\partial h_\theta / \partial \psi$  of

$$\frac{\partial h_\theta}{\partial \psi} = -\frac{h_\theta B^2}{B_\theta^2} \left( \frac{1}{R^2 B_\theta^2} \boldsymbol{\kappa} \cdot \nabla \psi + \frac{B_\phi^2}{RB^2} \frac{\partial R}{\partial \psi} \right) \quad (4.90)$$

This can be written in terms of derivatives along the field line by noting that  $\nabla \psi$  can be written as

$$\nabla \psi = R^2 B \mathbf{b} \times \nabla \phi \quad (4.91)$$

and since  $\nabla \phi = \hat{\phi} / R$  using 4.77 with  $\hat{\mathbf{T}} = \mathbf{b}$

$$\nabla \psi = RB \left( \frac{dR}{ds} \hat{\mathbf{Z}} - \frac{dZ}{ds} \hat{\mathbf{R}} \right) \quad (4.92)$$

Now using 4.85 and 4.78 expressions for  $\partial R/\partial\psi$  and  $\kappa \cdot \nabla\psi$  can be derived in terms of derivatives along the field line. These are

$$\frac{\partial R}{\partial\psi} = -\frac{BR}{R^2 B_\theta^2} \frac{dZ}{ds} \quad (4.93)$$

and

$$\kappa \cdot \nabla\psi = BR \left( \frac{d^2 Z}{ds^2} \frac{dR}{ds} - \frac{d^2 R}{ds^2} \frac{dZ}{ds} + \frac{dZ}{ds} R \left( \frac{d\phi}{ds} \right)^2 \right) \quad (4.94)$$

Finally since the change in toroidal angle along the magnetic field line is given by

$$\frac{d\phi}{ds} = \frac{B_\phi}{RB} \quad (4.95)$$

substituting 4.93 and 4.94 into 4.90 gives

$$\frac{\partial h_\theta}{\partial\psi} = -\frac{h_\theta B^3}{RB_\theta^4} \left( \frac{d^2 Z}{ds^2} \frac{dR}{ds} - \frac{d^2 R}{ds^2} \frac{dZ}{ds} \right) \quad (4.96)$$

The quantity  $\partial h_\theta/\partial\psi$  can now be calculated by the grid generator using only the information provided in the equilibrium file. Using 4.84 and integrating along  $y$  the quantity  $I$  can be generated.

The grid generator outputs all of the metric information required in a NetCDF grid file which is then read into the BOUT++ code and called as a `mesh` class [189]. BOUT++ also contains a pre-existing grid generation code called `Hypnotoad` [188, 190] however this is not optimized for flux-tube domains. The validity of the flux-tube grid generator can be tested by comparing the output with the profiles on the Hypnotoad grid, taken along the same magnetic field line as the flux-tube. In figure 4.8 the  $(R, Z)$  coordinates of the  $\psi_N = 1.15$  and the toroidal and poloidal magnetic field strength,  $B_\zeta$  and  $B_\theta$  are compared between the flux-tube grid and the Hypnotoad grid. The global grid output from Hypnotoad is in close agreement with results from the flux-tube grid generator. Some minor deviation is present between the two grids in the upper divertor leg where the Hypnotoad calculation predicts a slight reduction in the radial location of the field line.

Figure 4.9 shows a comparison between the Hypnotoad and flux-tube calculations of the contravariant  $x$  and  $z$  components (perpendicular components) of the polarization vector,  $(\mathbf{b} \times \kappa)^{x,z}$ , the integrated magnetic shear,  $I = \int_{y_0}^y \partial_\psi \nu dy'$ , and the component of the polarization vector lying normal to both the magnetic field line and the  $\nabla\psi$  direction,  $(\mathbf{b} \times \kappa)^z + I(\mathbf{b} \times \kappa)^x$ . The only major source of disagreement between the two calculations is in the calculation for  $(\mathbf{b} \times \kappa)^x$ . Firstly it is worth noting that whilst hypnotoad has a variety of methods used to calculate the magnetic curvature each requires derivatives of quantities perpendicular to the magnetic field[190]. The input mesh is

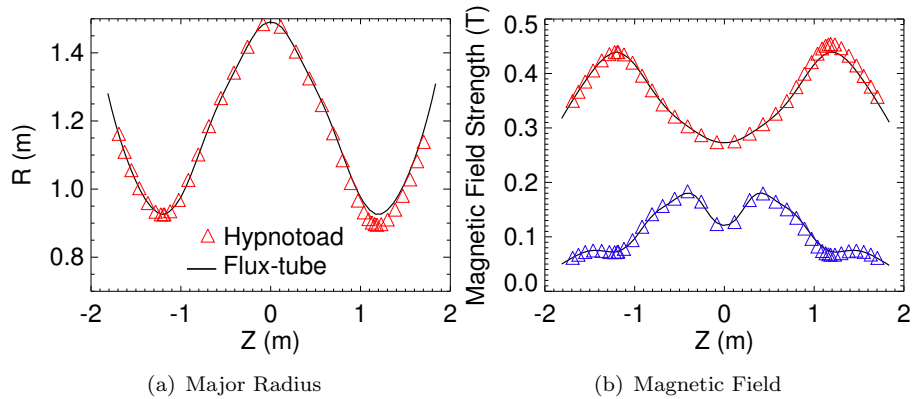


FIGURE 4.8: Comparison of flux-tube grid parameters with Hypnotoad. Left:  $R, Z$  coordinates of the magnetic field line in the poloidal plane. Right: Toroidal (red) and poloidal (blue) magnetic field strength. Note that by convention the toroidal field in MAST is negative, so data here shows  $-B_\zeta$ .

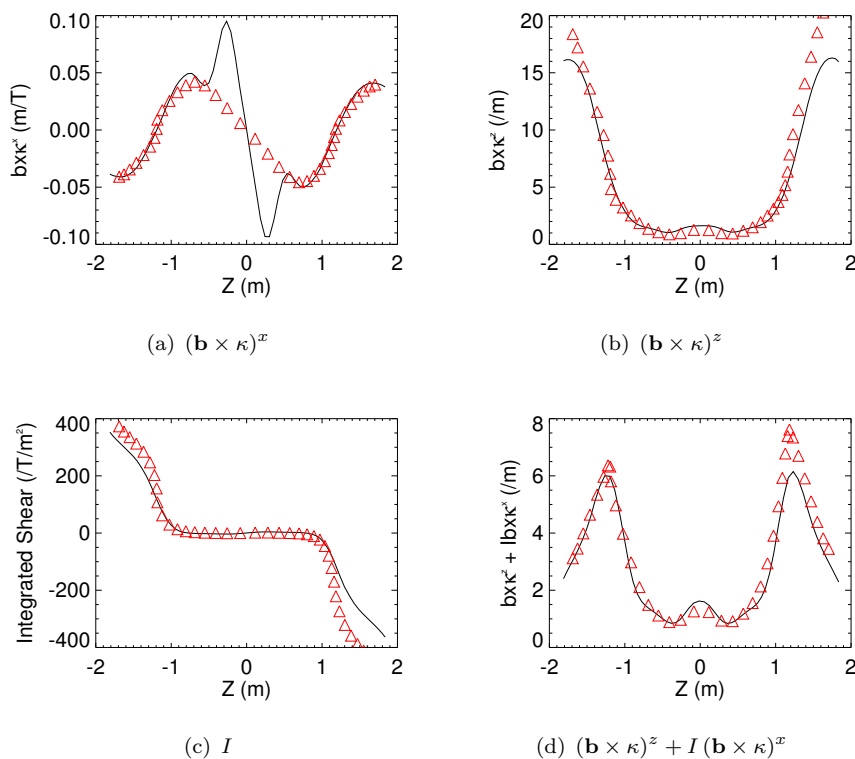
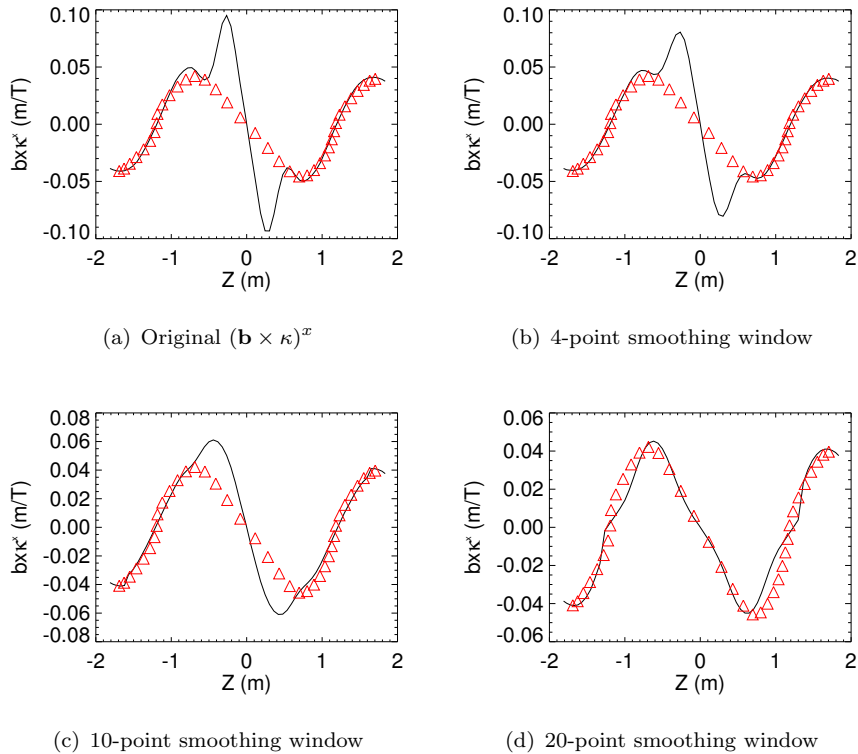


FIGURE 4.9: Comparisons of calculations of curvature quantities and integrated shear in Hypnotoad (red triangles) and in the flux-tube grid (solid black line).

often of low resolution (eg  $65 \times 65$  points in  $(R, Z)$  for a typical EFIT g. file) which can limit the resolution of derivative quantities perpendicular to the field. The flux-tube grid does not face this limitation however since it only requires derivatives along the field line curve which are typically much more well resolved in the EFIT calculations. To show the smoothed nature of the Hypnotoad calculation, the same comparison of  $(\mathbf{b} \times \boldsymbol{\kappa})^x$  has been made between the flux-tube and the hypnotoad calculation, with the flux-tube calculation smoothed by successively larger amounts. This comparison is shown in figure 4.10.




---

FIGURE 4.10: Comparison of  $(\mathbf{b} \times \boldsymbol{\kappa})^x$  calculations in Hypnotoad (red triangles) and the flux-tube generator (solid line) for successively increased levels of smoothing on the flux-tube output. Smoothing is achieved by the IDL box car average routine.

The rest of the quantities shown in figure 4.9 agree well, though once again some deviation is present in the upper divertor region ( $Z > 1\text{m}$ ). This is a result of the original deviation observed in the calculation of  $R$ . The slightly lower  $R$  in the hypnotoad calculation increases the curvature since it is proportional to  $1/R$ , and the shear by causing the field line to pass slightly closer to the X-point where magnetic shear is maximized. Nevertheless the degree of agreement between the two calculations provides reasonable confidence that the flux-tube grid is an accurate reconstruction of the true MAST case, assuming that the original EFIT file was accurate.

A final comparison between the two methods is made by comparing some of the important terms in the contravariant metric tensor of the coordinate system. In particular the terms  $g^{xx} = R^2 B_\theta^2$ ,  $g^{xz} = -IR^2 B_\theta^2$  and  $g^{zz} = I^2 R^2 B_\theta^2 + B^2/(R^2 B_\theta^2)$  which play an important role in the  $\nabla_\perp^2$  operator are compared. Full details of the metric are given in appendix A. This comparison is shown in figure 4.11. The comparison between the

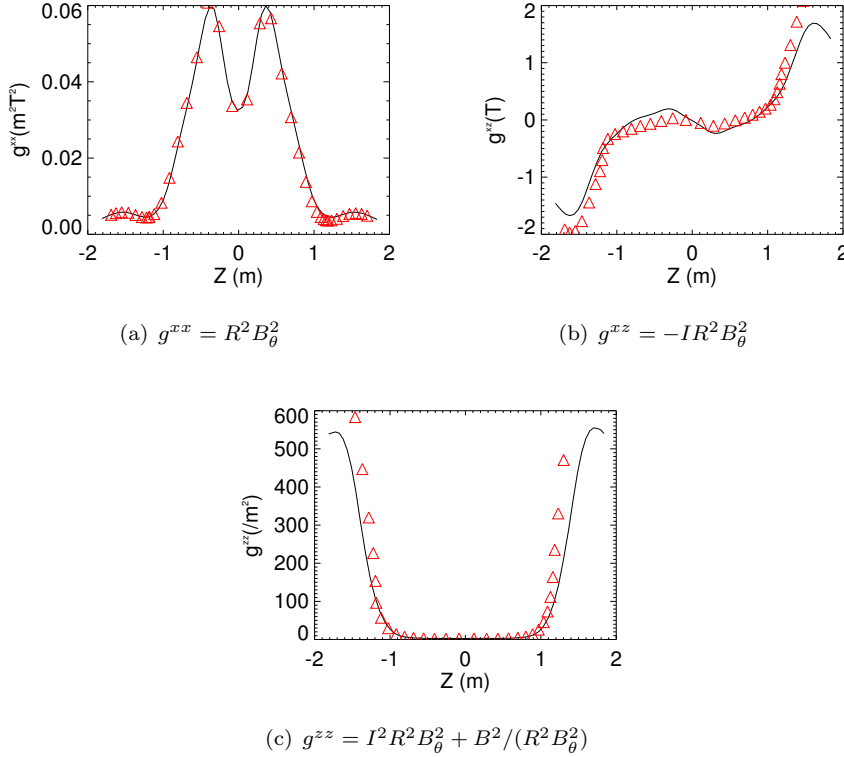


FIGURE 4.11: Contravariant metric components calculated in Hypnotoad (red triangles) and the flux-tube generator (solid black line).

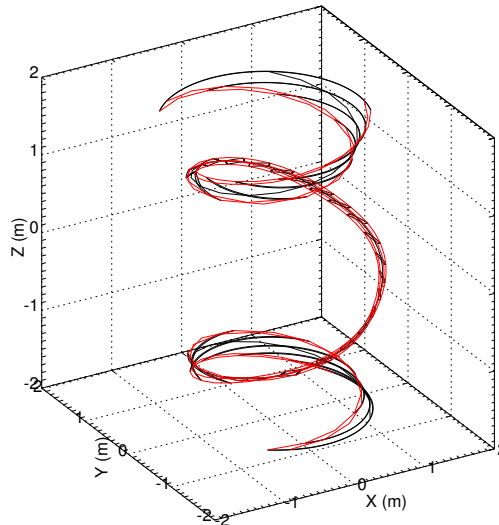
different calculations of the metric components is good and, furthermore, they are qualitatively similar to calculations in ASDEX-Upgrade [219]. There is some deviation of  $g^{xz}$  at the midplane which can once again be attributed to the averaging effect in the Hypnotoad calculation. All deviations between the Hypnotoad and flux-tube calculations are small and are unlikely to have a major effect on the simulations for which the grids are designed.

The shear of the magnetic field strongly influences the structure of the computational domain in real space. The toroidal angle at a point along the magnetic field line can be calculated from the ballooning coordinate system,  $(x, y, z)$  (see appendix A) by

$$\zeta(x, y) = \zeta(\psi, \theta) = z + \int_{\theta_0}^{\theta} \nu(\psi, \theta') d\theta' \approx z + \int_{y_0}^y \left( \nu(\psi_0, \theta') + (\psi - \psi_0) \left. \frac{\partial \nu}{\partial \psi} \right|_{\psi_0} \right) d\theta' \quad (4.97)$$

$$= z + I(\theta) \Delta\psi + \int_{\theta_0}^{\theta} \nu(\psi_0, \theta') d\theta'$$

This expression then shows that a distance  $\delta\psi$  leads to a toroidal motion as a result of the magnetic shear. This also shows that if the computational domain is orthogonal at the midplane, it will not remain so in the divertor, where  $I$  becomes very large. A typical grid spacing in  $\psi$  is  $\Delta\psi \approx 1 \times 10^{-5}$  Webers which then gives a toroidal shift between two adjacent grid cells of  $3.5 \times 10^{-3}$  radians. This can become a significant amount when many grid cells are used. Figure 4.12 shows a typical flux-tube produced by the grid-generator outlined here. As can be seen the  $(x, z)$  plane of the flux tube becomes strongly




---

FIGURE 4.12: 3D visualisation of a typical SOL flux-tube domain. Shown in black are the boundaries of the domain in the  $(x, z)$  plane, whilst red lines show the corresponding field line at the vertices of the  $(x, z)$  domain. Strong magnetic shear deforms the domain towards either termination point of the magnetic field.

sheared in the toroidal direction as the X-point is passed, towards the termination points of the magnetic field line. The effect this has on the grid is to drastically increase the spacing between grid points in the  $x$  dimension. Figures 4.13 shows the real space grid spacing between two adjacent grid points in  $x$  and  $z$ . The grid contains 516 grid points in the  $x$  direction and 256 grid points in the  $z$  dimension. Furthermore the  $x$  dimension has been scaled by a factor of 7 to ensure that the spatial extent of the grid is much larger than the cross-sectional width of a filament. The purpose of these grids is to facilitate the simulation of filament dynamics. Filaments typically occupy macroscopic length-scales (i.e. much larger than the gyro-radius, but much smaller than the equilibrium length scale) and typically have cross-sectional length scales on the cm scale. As such the macroscopic dynamics are well resolved by the grid, even in the strongly sheared region near to the X-points. The work of Angus *et.al* however has shown that smaller scale resistive drift-wave instabilities can impact filament dynamics in 3D [115, 116].

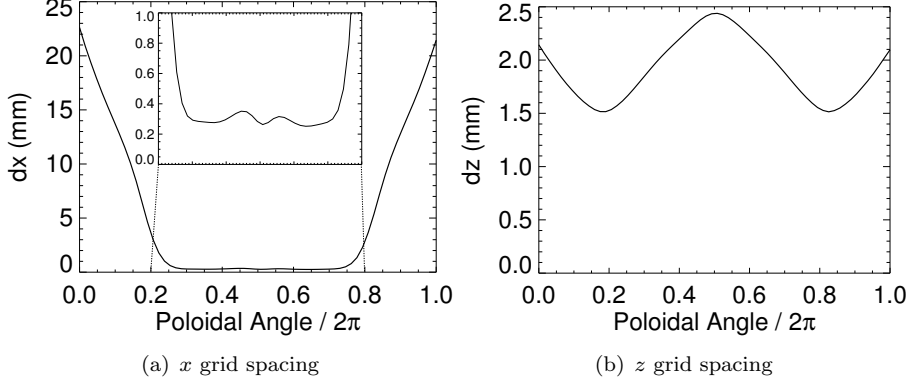


FIGURE 4.13: Spacing between adjacent grid points in the  $x$  and  $z$  dimensions of the flux-tube grid.

Angus has found numerically that the dominant resistive drift-wave instability occurs with  $k_{\perp}\rho_s \approx 0.5$  where  $\rho_s = c_s/\Omega_i$  is the Bohm gyro-radius and  $k_{\perp} = 2\pi/\lambda_{\perp}$  is the perpendicular wave-vector of the drift-wave instability with a perpendicular wavelength  $\lambda_{\perp}$ . It is important therefore to establish whether such an instability can be resolved on the resolution provided by the grid. A distance  $\Delta\zeta$  in toroidal angle results in a spatial distance  $\Delta z[m] = \Delta\zeta RB_{\theta}/B$  in the bi-normal direction of the perpendicular plane. As a result the resolution in the perpendicular plane due to the grid spacing in  $x$  and  $z$  respectively is

$$dx[m] = \Delta x \sqrt{\frac{1}{R^2 B_{\theta}^2} + \frac{I^2 R^2 B_{\theta}^2}{B^2}} \quad (4.98)$$

and

$$dz[m] = \Delta z \frac{RB_{\theta}}{B} \quad (4.99)$$

To ensure that the resistive drift-wave instability can be minimally resolved the grid resolution must exceed at least half the perpendicular wavelength of the instability. This results in the condition  $dx, dz < 2\pi\rho_s$ . In figure 4.14 the resolution in the perpendicular plane is calculated along the flux-tube and the condition on  $dx, dz$  is tested. Figure 4.14 confirms that over the majority of the flux-tube grid the resistive drift-wave instability can be resolved. This is not the case in the divertor region where the perpendicular resolution  $dx$  exceeds  $2\pi\rho_s$  at  $T_e = 1\text{eV}$ , however this will be shown to be allowable due to the presence of dissipation which stabilizes the resistive drift-wave instability in this region. As a result the flux-tube grid can be considered adequate for use within this thesis.

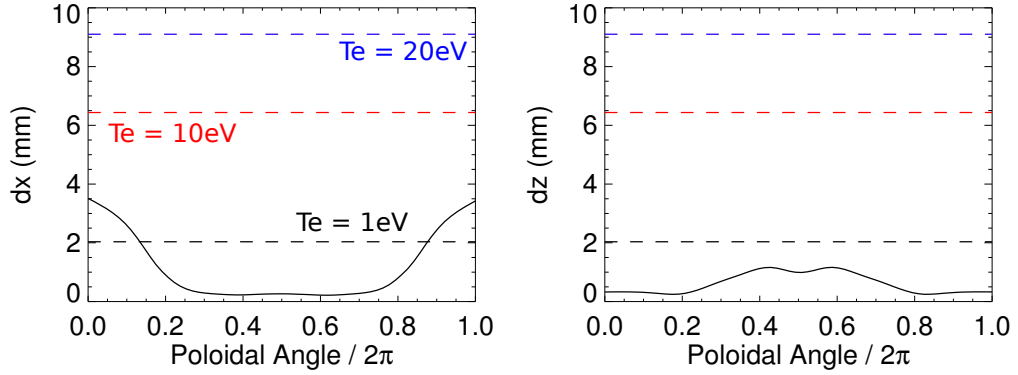


FIGURE 4.14: Resolution in the perpendicular plane due to grid spacing in  $x$  (left) and  $z$  (right) in the MAST flux-tube grid. Also shown is the quantity  $2\pi\rho_s$  calculated at 1, 10 and 20eV.

## 4.5 Summary

This chapter has provided a brief review of the BOUT++ code including time integration techniques and spatial differentiation. It has also presented an overview of the differential operators implemented in BOUT++ to facilitate the simulation of plasma dynamics in a field aligned magnetic geometry. The development of a physics module within BOUT++ has been described. The module is based on a reduction to the two-fluid equations and is ordered initially according to the drift-ordering. The ordering of parameters arising in the drift ordering has been tested for conditions representative of the core, edge, near and far SOL of MAST and the drift-ordering has been shown to apply well in the MAST SOL, with the exception of the ordering of  $\beta$ . This is not an issue however as the plasma is subsequently assumed to be electrostatic.

A grid generator has been described which produces field aligned flux-tube grids based on a selected magnetic field line in SOL. Novel techniques have been presented to derive the curvature of the magnetic field line in field aligned coordinates purely from the geometry of the magnetic flux surface. Similar techniques are also employed to calculate the magnetic shear. The grid-generator has been tested against the BOUT++ inbuilt grid generator Hypnotoad and reasonable agreement is found between the two. Finally the resolution of the grid has been investigated and found to be adequate for studies of 3D filament dynamics under the requirement that the grid needs to be able to approximately resolve wave vectors constrained by  $k_{\perp} \approx 0.5\rho_s$ .



## Chapter 5

# 3D Filament Dynamics in a MAST SOL Flux Tube Geometry

### 5.1 Introduction

The intermittent ejection of coherent, field aligned structures known as filaments is a characteristic feature of transport in the scrape-off layer of tokamak plasmas [55, 220, 221]. Statistical measurements with probe diagnostics, as performed for example in chapter 3, have been used in experiment to demonstrate the intermitency of fluctuations in the SOL whilst imaging diagnostics [79, 84, 86, 89] have highlighted the field aligned filamentary structure of these fluctuations. The presence of these filaments in L-mode [79], in inter-ELM H-mode [84] and in H-mode during ELMs [61, 111] suggests that they are universal in nature and are likely to play a prominent role in edge plasma transport. Filaments have been estimated to contribute up to 50% of the density transport within the SOL[222] however this transport is highly non-diffusive [180] due to the non-local relationship between filament motion and equilibrium plasma profiles. Filaments can travel significant distances into the SOL and can present a risk of unwanted interaction with first-wall materials, leading to a large particle source due to recycling [56] and potential damage to in-vessel components. As a means to assess these aspects of density transport due to filament motion, the non-linear dynamics of filaments may be investigated. Furthermore it is likely that analogies can be drawn between the processes involved in filament motion and non-linear theories of tokamak edge plasma turbulence, providing insight into drive and saturation mechanisms inside and outside the last closed flux surface.

The dynamics of filaments have been historically studied in the context of reduced 2D

models in the plane perpendicular to the magnetic field, where physical processes parallel to the magnetic field line are approximated by heuristic closure assumptions [95] (see chapter 2 or [55] for a discussion). Results by Angus *et.al* [115, 116, 197] have extended these studies to a full 3D slab domain and have shown that 3D effects can cause a dramatic departure from 2D predictions. More recent work by Halpern *et.al* [223] and Easy *et.al* [212] (both pieces of work being conducted after the completion of the work detailed in this chapter) have shown that 2D predictions can indeed capture some of the dynamics of 3D filaments if 3D effects can be suppressed, however that to accurately assess filament dynamics a 3D treatment is required.

Until recently the simulation of filament dynamics in 3D has been constrained to simplistic geometries. In the work of Angus *et.al*[115, 116, 197] and Easy *et.al* [212] a simple slab geometry is used whilst Helpern *et.al* [223] focussed on a simple toroidal geometry representative of the TORPEX plasma device [224]. These geometries allow for simplification of the physical processes occurring in the evolution of filaments, but do not allow for the interaction between these processes and the magnetic geometry of the tokamak SOL. An analytical treatment of the effects of magnetic geometry has been given by Myra *et.al* [54] and by Ryutov and Cohen [110, 225] which suggests that the magnetic geometry can strongly influence the motion of filaments. The work presented in this chapter represents the first dedicated numerical investigation of these processes. With advanced divertor concepts under consideration for DEMO, including the Super-X divertor [226, 227] and the snowflake divertor [228], set to complicate the magnetic geometry of the SOL further, it is increasingly important to factor in such effects into the understanding of filament dynamics.

The aim of this chapter is to investigate numerically the dynamics of 3D filaments in a magnetic geometry representative of a tokamak SOL. The particular geometry used is a flux-tube geometry based on the SOL of MAST. The geometry itself is described in chapter 4. Simulations are carried out using BOUT++ modelling framework [104] and exploit its flexible handling of complex geometries. A theoretical consideration will first be given to the effects of parallel electron dynamics on the motion of the filament, followed by a consideration of the effects of the magnetic geometry. Limiting cases are then presented where 3D effects are negligible and dominant respectively. In each case the evolution of the filament perpendicular and parallel to the magnetic field will be assessed. Finally a brief investigation into the role played by dissipation will be presented, before a discussion on the results and a summary.

Parts of this chapter are based on published work [1]. A follow up publication based on this chapter and chapter 6 is currently in preparation.

## 5.2 The role of parallel electron dynamics

The modification of the standard equations of 2D blob dynamics, outlined in chapter 2, to 3D is through the inclusion of parallel electron dynamics. As described by Angus [115, 116], this can be achieved by calculating the parallel current density through projection of Ohm's law along the magnetic field line. Under the assumptions of an isothermal, electrostatic plasma and neglecting electron inertia this is derived in appendix B as an expression for the parallel current density in Amperes as

$$J_{\parallel} = \sigma_{\parallel} T_e \nabla_{\parallel} (\ln(n) - \phi) \quad (5.1)$$

where  $\phi$  is the electrostatic potential,  $\Phi$ , normalized to the electron temperature,  $T_e$  in eV such that  $\phi = \Phi/T_e$ ,  $n$  is the electron density and  $\sigma_{\parallel}$  is the parallel conductivity, given in chapter 4 and originally derived in [229] as

$$\sigma_{\parallel} = 1.96 \frac{n e^2 \tau_{ei}}{m_e} \quad (5.2)$$

where  $\tau_{ei}$  is the electron-ion collision time given by

$$\tau_{ei} = \frac{3\sqrt{m_e} T_e^{3/2}}{4\sqrt{2\pi} n \Lambda e^4} = 3.44 \times 10^{10} \frac{T_e^{3/2}}{n} \quad (5.3)$$

with  $T_e$  in eV,  $n$  in  $m^{-3}$  and the coulomb logarithm  $\Lambda \approx 10$ . In 2D models the  $\nabla_{\parallel} \ln(n)$  term in 5.1 is neglected and the parallel current is then matched to the sheath current to provide the sheath current closure. The full form of  $J_{\parallel}$  can be calculated in 3D and input into the density and vorticity equations. These are introduced in chapter 4 and derived in appendix B as

$$\frac{dn}{dt} = \hat{\xi} \cdot \nabla n + \alpha \nabla_{\parallel} J_{\parallel} \quad (5.4)$$

$$n \frac{d}{dt} \nabla_{\perp}^2 \phi = \hat{\xi} \cdot \nabla n + \alpha \nabla_{\parallel} J_{\parallel} \quad (5.5)$$

where the dimensionless parameters are the normalized polarisation vector

$$\hat{\xi} = \rho_s \xi = \rho_s \mathbf{b} \times \boldsymbol{\kappa} \sim \rho_s / R_c \quad (5.6)$$

where  $\boldsymbol{\kappa}$  is the curvature vector of the magnetic field described in chapter 4, and

$$\alpha = \frac{\sigma_{\parallel} T_e}{n_0 c_s \rho_s e} = \frac{\sigma_{\parallel} B}{n_0 e} \quad (5.7)$$

The Bohm normalization is employed here and is summarized in table 5.1. Length scales

Description	Variable	Normalization
Density	$n$	$n_0$ ( $\text{m}^{-3}$ )
Potential	$\phi$	$T_e$ (eV)
Length scales	$\mathbf{r}$	$\rho_s$
Time-scales	$t$	$\Omega_i$

TABLE 5.1: Normalization of variables in the system of equations 5.4 and 5.5.  $n_0$  is a reference density and refers to the plasma background, whilst  $T_e$  is the isothermal background electron temperature.

in the system are normalized to the Bohm gyro-radius and time scales to the ion cyclotron frequency such that velocities are normalized to the acoustic speed  $c_s = \rho_s \Omega_i$ . In addition the potential is normalized to the electron temperature in eV and the density is normalized to the background reference density.

One method of analysing the parametric dependencies of a system is invariant scaling analysis, a technique popularised by Connor and Taylor [230] to study the tokamak energy confinement time scaling and used by Myra [54] to determine the scaling of the 2D blob velocity in the two-region model (see chapter 2 and/or [54]). The aim of the technique is to find a scale transformation that leaves the underlying system of equations invariant. This can then be used to identify combinations of parameters used to control the system, and can also elucidate the role played by different mechanisms in the equations defining the system. To perform the analysis a scale transformation is applied to all variables and parameters required to define the system of the form  $n \rightarrow \lambda^a n$ ,  $\mathbf{r} \rightarrow \lambda^b \mathbf{r}$ ,  $T_e \rightarrow \lambda^c T_e$  and so on for  $t$ ,  $B$ ,  $\phi$ ,  $\xi = |\boldsymbol{\xi}|$  and  $n_0$ . These transformed quantities are substituted into the governing equations and exponents  $a, b$  etc are found that leave the equations invariant. In the case of equations 5.1 to 5.5 a scale transformation found to leave the equations invariant is given by

$$\begin{aligned}
\phi &\rightarrow \phi & t &\rightarrow t & \mathbf{r} &\rightarrow \mathbf{r} & \delta n &\rightarrow \lambda \delta n \\
T_e &\rightarrow \lambda^\gamma T_e & B &\rightarrow \lambda^\beta B & n_0 &\rightarrow \lambda^{3\gamma/2+\beta-1} n_0 & \xi &\rightarrow \lambda^{\beta-\gamma/2} \xi
\end{aligned} \tag{5.8}$$

where  $\gamma$  and  $\beta$  are free parameters. Given that this transformation leaves the system invariant it is necessary that any solutions to the system,  $F(n, \phi; \mathbf{r}, t; B, \xi, T_e, n_0, B)$  for example, must also remain invariant under the same scale transformation. This means that it must be independent of  $\gamma$  and/or  $\beta$  since they are arbitrary. As a consequence the arguments of  $F$  can only appear in certain scale independent combinations. These combinations are:

$$\begin{aligned}
C_1 &= \frac{\xi \sqrt{T_e}}{B} \\
C_2 &= \frac{n_0 \delta n}{|\boldsymbol{\xi}| T_e^2}
\end{aligned} \tag{5.9}$$

$$C_3 = \frac{n_0 \delta n}{T_e^{3/2} B}$$

$$C_4 = \frac{n_0 \delta n |\xi|}{T_e B^2}$$

Relations  $C_1$  to  $C_4$  are related by

$$C_1 \times C_3 = C_4 \quad C_1 \times C_2 = C_3 \quad (5.10)$$

so we need to specify only two of the four parameters. In terms of system parameters  $C_1 \propto |\hat{\xi}| = \hat{\xi}$  and  $C_3 \propto n/\alpha$ . This means that the non-linear evolution of a filament is determined principally by  $\hat{\xi}$ ,  $n$  and  $\alpha$ . This is intuitive since  $\hat{\xi}$ , the normalized magnetic curvature, and  $\alpha$ , the normalized conductivity, control the right hand side (RHS) of equations 5.4 and 5.5, whilst  $n$  specifies the initial conditions of the system. Notably the parameters controlling the system consist of plasma parameters,  $n_0$ , and  $T_e$  and magnetic parameters,  $B$  and  $\xi$ . The magnetic parameters in the SOL are generally fixed during tokamak operation and to emulate this they will be held fixed in the MAST geometry investigated in this chapter. By fixing the initial conditions of the system, and keeping  $n_0$  constant, the only parameter left governing the dynamics of the system is the electron temperature,  $T_e$ .

The invariant scaling produced above differs significantly from that of the two-region model [54]. In particular in the 3D system it is no longer possible to keep the system invariant under a scale transformation of the electrostatic potential. This can be shown by re-examining the equation for parallel Ohm's law, equation 5.1. For the system to remain invariant under a scale transformation, both terms in equation 5.1 must have the same scaling exponent. Since the scale transformation of  $n$  in the term  $\nabla_{\parallel} \ln(n) = (\nabla_{\parallel} n)/n$  cancels, the only possible scale transformation to  $\phi$  that can leave the system invariant is  $\lambda^0$ . Hence the inclusion of 3D parallel electron dynamics fundamentally alters the invariant nature of the system. It should be noted that, even if a distinction in the scale transformation between perpendicular and parallel length scales is made, this result does not change and is fundamental to the 3D system.

The cause of this difference between the invariant nature of the 2D and 3D systems is the result of the inclusion of the term  $\nabla_{\parallel} \ln(n)$  in the vorticity equation via the full 3D version of Ohm's Law, equation 5.1. In 2D models the vorticity equation contains only one source, the interchange source,  $S_I = \hat{\xi} \cdot \nabla n$ , which drives interchange motion. In the 3D vorticity equation the term arising from the parallel current provides a second source,  $S_B = \alpha \nabla_{\parallel}^2 \ln(n)$ . In [115] Angus showed that this source can be responsible for inducing a spinning of a 3D blob in a slab by inducing a Boltzmann response of the potential. In the full system of equations the Boltzmann response is introduced through the  $S_B$  source term, as such this term will be called the Boltzmann source here. In 2D the entire system

can be scaled to keep the relative strength of the interchange source,  $S_I$ , constant, so that the dynamics of the blob remain invariant. If this is attempted in the 3D case, then the Boltzmann source,  $S_B$  becomes stronger or weaker relative to the interchange source,  $S_I$  and so the dynamics of the system alter. If  $S_I \gg S_B$  then the dominant source of potential arises from the magnetic curvature and the dynamics of the filament are likely to be close to 2D predictions, however if  $S_I \sim S_B$  then the Boltzmann source can play a comparable role or if  $S_I \ll S_B$  the Boltzmann source can dominate the vorticity equation and the dynamics may depart from 2D predictions. As indicated earlier, the electron temperature can be used as a primary parameter for varying the dynamics of a filament in fixed magnetic geometry, with fixed initial conditions and for fixed background density. The point at which 3D effects may become important can be estimated by weighting the two sources against one another. The two sources can be estimated by

$$S_I = 2\hat{\xi} \cdot \nabla n \approx \frac{2\rho_s^2 |\xi| \delta n}{\delta_\perp} \quad (5.11)$$

$$S_B = \alpha \nabla_\parallel^2 \ln(n) \approx \frac{\rho_s^2 \alpha}{\delta_\parallel^2} \quad (5.12)$$

where  $\delta_\perp$  and  $\delta_\parallel$  are the perpendicular and parallel filament length scales respectively, and  $\delta n$  is the peak filament density above the background. Equating these two terms against one another and rearranging for the electron temperature gives an estimate for  $T_e$  through which a transition from 2D to 3D dominated physical processes can occur in the filament. This is given by

$$T_{e,c} = \left( \frac{2n_0 \delta n m_e \delta_\parallel^2 |\xi|}{1.96 \times 3.44 \times 10^{10} \delta_\perp e B} \right)^{2/3} \quad (5.13)$$

where the denominator arises from  $\sigma_\parallel$ . To estimate this temperature typical parameters of the MAST SOL are taken. These are  $n_0 \sim 10^{19} m^{-3}$ ,  $\delta n \equiv (n - n_0)/n_0 \sim 0.5$ ,  $\delta_\perp \sim 2cm$ ,  $B \sim 0.3T$ ,  $|\xi| \sim 1/R$  with  $R \sim 1.5m$ , and  $\delta_\parallel \sim 8m$  which is representative of the connection length in the far SOL. These parameters then give an estimate for the transition electron temperature of

$$T_{e,c} \approx 4eV \quad (5.14)$$

Whilst this estimate is subject to considerable uncertainty, it suggests that 3D effects may play a role in filament dynamics at temperatures relevant to the experimental conditions. In MAST for example ball pen probe measurements in chapter 3 suggest that temperatures in the range of 5 to 20eV are appropriate for the far SOL.

### 5.2.1 Symmetry Breaking

The arguments laid out so far suggest that 3D effects may play a role in filament dynamics in a parameter range relevant to experimental conditions on MAST. To explore on a slightly deeper level the impact of these 3D effects the symmetry properties of filament dynamics can be examined. The 2D theory of blob dynamics, as outlined in chapter 2, predicts the formation of a potential dipole across a mono-polar density. Recent 3D results [115, 116] suggest that this picture changes when 3D effects are introduced. To investigate this effect the electrostatic potential can be written in terms of an even and an odd component,  $\phi^+$  and  $\phi^-$  respectively, in the bi-normal direction (perpendicular to radial and parallel directions) about the centre of the blob. The true potential is then a linear combination of these two

$$\phi = \phi^+ + \phi^- \quad (5.15)$$

The same is true for the density, however since the density is initially mono-polar in the bi-normal direction it can be approximated by  $n = n^+$  such that the density is an entirely even function about the blob centre. This decomposition of the density and potential is illustrated schematically in figure 5.1. Substituting the expression  $\phi = \phi^+ + \phi^-$  into

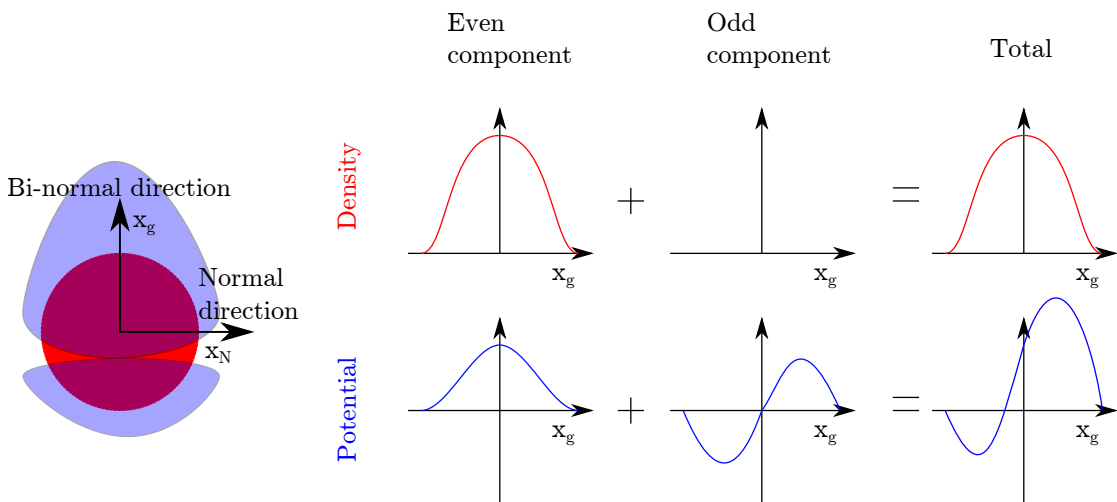


FIGURE 5.1: Schematic illustration of the decomposition of filament density and potential into even and odd components.

the vorticity equation allows the parity in the bi-normal direction of each term in the equation to be determined. In determining the parity note that even order differential operators in the bi-normal direction preserve the parity of the function they are operating on, whilst odd order operators reverse the parity. This means that  $\nabla_{\perp}\phi^+$  has an odd parity, whilst  $\nabla_{\perp}^2\phi^+$  has an even parity. The vorticity equation can then be written as

$$\begin{aligned} \frac{\partial \nabla_{\perp}^2 \phi^+}{\partial t} + \mathbf{v}_E^- \cdot \nabla \nabla_{\perp}^2 \phi^- + \mathbf{v}_E^+ \cdot \nabla \nabla_{\perp}^2 \phi^+ - \frac{\alpha}{n} \left( \nabla_{\parallel}^2 \ln(n) - \nabla_{\parallel}^2 \phi^+ \right) = & \quad (5.16) \\ - \frac{\partial \nabla_{\perp}^2 \phi^-}{\partial t} - \mathbf{v}_E^+ \cdot \nabla \nabla_{\perp}^2 \phi^- - \mathbf{v}_E^- \cdot \nabla \nabla_{\perp}^2 \phi^+ + \hat{\boldsymbol{\xi}} \cdot \nabla \ln(n) - \frac{\alpha}{n} \nabla_{\parallel}^2 \phi^- & \end{aligned}$$

where all of the even parity terms have been collected on the LHS, and the odd parity terms have been collected on the RHS. The  $\mathbf{E} \times \mathbf{B}$  advection velocity has been split into even and odd parts given by

$$\mathbf{v}_E^+ = \mathbf{b} \times \nabla \phi^- \quad (5.17)$$

$$\mathbf{v}_E^- = \mathbf{b} \times \nabla \phi^+ \quad (5.18)$$

The density  $n = n^+$  is assumed to be entirely even in parity. Note that by construction the LHS of equation 5.16 is entirely even in parity, whilst the RHS is entirely odd which can only be generally true if both sides identically equal 0. This then allows the vorticity equation to be split into two coupled equations for the odd and even components of the potential

$$\frac{\partial \nabla_{\perp}^2 \phi^+}{\partial t} + \mathbf{v}_E^- \cdot \nabla \nabla_{\perp}^2 \phi^- + \mathbf{v}_E^+ \cdot \nabla \nabla_{\perp}^2 \phi^+ = \frac{\alpha}{n} \left( \nabla_{\parallel}^2 \ln(n) - \nabla_{\parallel}^2 \phi^+ \right) \quad (5.19)$$

$$\frac{\partial \nabla_{\perp}^2 \phi^-}{\partial t} + \mathbf{v}_E^+ \cdot \nabla \nabla_{\perp}^2 \phi^- + \mathbf{v}_E^- \cdot \nabla \nabla_{\perp}^2 \phi^+ = \hat{\boldsymbol{\xi}} \cdot \nabla \ln(n) + \frac{\alpha}{n} \nabla_{\parallel}^2 \phi^- \quad (5.20)$$

If the Boltzmann source is neglected, and the initial conditions of the blob are set up such that  $\phi^+(t=0) = 0$ , as is the standard case in 2D blob theory, then the blob will maintain an odd parity of potential throughout its lifetime with no growth of the even component. By contrast when the Boltzmann source is included the initial symmetry of the blob potential can be broken by the growth of an even component alongside the odd component. This shows that 2D blob models are a rather special class of models and do not allow for a breaking of the reflective anti-symmetry imposed by the interchange source. When the symmetry is broken the non-linear operators act to mix the parities. As the blob then advects, the symmetry of the density is also broken and the assumption of  $n = n^+$  no longer applies. As such the above analysis only applies formally to the early stages of the blob motion however it serves to illustrate the role played by 3D effects. It is also worth noting that the diamagnetic contribution to the density equation also permits symmetry breaking, however this term is generally much weaker than advection by the  $\mathbf{E} \times \mathbf{B}$  velocity and is therefore negligible.

The symmetry breaking predicted here has already been observed by Angus *et.al* [115] in the form of a mono-polar potential arising across a 3D blob in a slab with a density gradient in the parallel direction. This was observed to spin the blob. The situation studied in this chapter is rather different and it will be shown that symmetry breaking can play a major role in the dynamics of 3D blobs, or filaments, despite no density

gradients being initialised. The magnetic geometry of the SOL can provide the conditions for symmetry breaking to occur as will be discussed in the next section. The odd and even components of the potential are investigated in this chapter at the post-processing level; the equations solved do not decompose the potential.

### 5.3 The role of magnetic geometry

A key feature of the work presented here is the inclusion of a realistic magnetic geometry. The principle effect of the magnetic geometry, beyond providing drive for the interchange motion through magnetic curvature, is to transform the shape of the filament in the perpendicular plane along the magnetic field line. This shaping transformation has been noted previously in [54] and [225]. The transformation of the cross-sectional shape of the filament can be derived from the ballooning coordinate system described in appendix A. For reference, the ballooning coordinate system  $(x, y, z)$  is specified by

$$\begin{aligned}x &= \psi - \psi_0 \\y &= \theta \\z &= \zeta - \int_{y_0}^y \nu dy'\end{aligned}\tag{5.21}$$

where  $\psi$  is the normalized poloidal flux and  $\psi_0$  is the poloidal flux at the separatrix,  $\theta$  is the poloidal angle and  $\zeta$  is the toroidal angle.  $\nu$  is the local field line pitch given by

$$\nu = \frac{h_\theta B_\zeta}{R B_\theta}\tag{5.22}$$

where  $R$  is the major radius of the plasma,  $B_\theta$  and  $B_\zeta$  are the poloidal and toroidal field strengths respectively and  $h_\theta = 1/|\nabla\theta|$  is related to the poloidal arc length by  $dL = h_\theta d\theta$  and can be identified with the minor radius in a circular plasma cross-section. When integrated around  $2\pi$  in the toroidal direction, this expression gives the safety factor  $q$ . The coordinate system has the contravariant basis vectors

$$\begin{aligned}\nabla x &= \nabla\psi \\ \nabla y &= \nabla\theta \\ \nabla z &= \nabla\zeta - I\nabla\psi - \nu\nabla\theta\end{aligned}\tag{5.23}$$

and covariant basis vectors

$$\mathbf{e}_x = \frac{1}{R B_\theta} \hat{\mathbf{e}}_\psi + I R \hat{\mathbf{e}}_\zeta$$

$$\mathbf{e}_y = h_\theta \hat{\mathbf{e}}_\theta + \nu R \hat{\mathbf{e}}_\zeta \quad (5.24)$$

$$\hat{\mathbf{e}}_z = R \hat{\mathbf{e}}_\zeta$$

In this coordinate system the magnetic field can be written in Clebsch form as

$$\mathbf{B} = \nabla x \times \nabla z = \frac{1}{J} (h_\theta \hat{\mathbf{e}}_\theta + \nu R \hat{\mathbf{e}}_\zeta) \quad (5.25)$$

With this description of the magnetic coordinates it is possible to identify a unit vector normal to the flux surface,

$$\hat{\mathbf{e}}_N = \hat{\mathbf{e}}_\psi = \frac{\nabla \psi}{R |B_\theta|} \quad (5.26)$$

and a unit vector normal to both the flux surface and the magnetic field line

$$\hat{\mathbf{e}}_g = \hat{\mathbf{e}}_N \times \mathbf{B}/B = \frac{RB_\theta}{B} \mathbf{e}_\zeta - \frac{h_\theta B_\zeta}{B} \mathbf{e}_\theta = \frac{RB_\theta}{B} (\nabla z + I \nabla \psi) \quad (5.27)$$

Within this chapter this direction will be referred to as the bi-normal direction. The vectors  $(\hat{\mathbf{e}}_N, \mathbf{b}, \hat{\mathbf{e}}_g)$  form a local right-handed coordinate system at any point along the magnetic field line. Returning to the ballooning coordinate system,  $(x, y, z)$ , for the system to be a valid representation the coordinates must be independent of one another. This implies that

$$\frac{dx}{dy} = \frac{dz}{dy} = 0 \quad (5.28)$$

The differential lengths  $dx$  and  $dz$  can be written in terms of the locally orthogonal vectors  $(\hat{\mathbf{e}}_N, \mathbf{b}, \hat{\mathbf{e}}_g)$  as

$$dx = \nabla x \cdot d\mathbf{r} \quad (5.29)$$

and

$$dz = \nabla z \cdot d\mathbf{r} \quad (5.30)$$

where the differential length vector is given by

$$d\mathbf{r} = dx_N \hat{\mathbf{e}}_N + dx_y \frac{\mathbf{e}_y}{JB} + dx_g \hat{\mathbf{e}}_g \quad (5.31)$$

where the equality  $\mathbf{b} = \mathbf{e}_y/JB$  has been employed. Using equation 5.23 to evaluate  $dx$  and  $dz$  then gives

$$dx = \nabla x \cdot d\mathbf{r} = R |B_\theta| dx_N \quad (5.32)$$

and

$$dz = \nabla z \cdot d\mathbf{r} = -IR |B_\theta| dx_N + \frac{B}{R |B_\theta|} dx_g \quad (5.33)$$

Since  $dx$  and  $dz$  are constant these expressions allow the elemental length scales at some point upstream on the field line,  $dx_{N,u}$  and  $dx_{g,u}$ , to be related to downstream length

scales  $dx_{N,d}$  and  $dx_{g,d}$  by

$$\begin{pmatrix} dx_{N,d} \\ dx_{g,d} \end{pmatrix} = \mathcal{T} \begin{pmatrix} dx_{N,u} \\ dx_{g,u} \end{pmatrix} \quad (5.34)$$

where the transformation matrix,  $\mathcal{T}$  is given by

$$\mathcal{T} = \begin{pmatrix} A & 0 \\ C & D \end{pmatrix} = \begin{pmatrix} \frac{R_u B_{\theta,u}}{R_d B_{\theta,d}} & 0 \\ \frac{R_u R_d B_{\theta,u} B_{\theta,d}}{B_d} (I_d - I_u) & \frac{B_u R_d B_{\theta,d}}{B_d R_u B_{\theta,u}} \end{pmatrix} \quad (5.35)$$

Here  $B_\theta$  is the poloidal magnetic field magnitude,  $R$  is the major radius and  $I$  is the integrated magnetic shear. Subscripts  $u$  indicate upstream values and  $d$  indicate downstream values. This is precisely the transformation matrix derived in [54]. To derive the corresponding transformation of perpendicular gradients the fact that  $(x_N, x_g)$  form a local coordinate system implies

$$\nabla^{d,i} x_{d,i} = \nabla^{u,i} x_{u,i} = 1 \quad (5.36)$$

where  $d$  denotes downstream and  $u$  denotes upstream quantities. The transformation matrix  $\mathcal{M}$  that transforms  $\nabla^u$  into  $\nabla^d$  is then derived from

$$\nabla^{d,i} x_{d,i} = \mathcal{M}_i^j \nabla^{u,i} \mathcal{T}_j^i x_{u,i} = \mathcal{M}_i^j \mathcal{T}_j^i = 1 \Rightarrow \mathcal{M} = \mathcal{T}^{Tr,-1} \quad (5.37)$$

which gives

$$\mathcal{M} = \begin{pmatrix} \frac{R_d B_{\theta,d}}{R_u B_{\theta,u}} & \frac{R_u R_d B_{\theta,u} B_{\theta,d}}{B_u} (I_d - I_u) \\ 0 & \frac{B_u R_u B_{\theta,u}}{B_d R_d B_{\theta,d}} \end{pmatrix} \quad (5.38)$$

Examining the transformation implied by  $\mathcal{T}$  shows two distinct transformations occurring in the flux tube as one moves along the magnetic field line. The first is a scale transformation which is a result of the requirement that the magnetic flux passing through the cross-section of the flux tube must be constant at all points along the flux tube. This transformation enlarges the flux tube in the normal direction but contracts it in the bi-normal direction. If the total magnetic field magnitude is constant along the flux tube then this transformation is area preserving. This transformation is described by the diagonal terms in  $\mathcal{T}$ . The off-diagonal term describes a shearing transformation resulting from the magnetic shear in the flux-tube. This is an area preserving transformation and acts to stretch the flux tube in the bi-normal direction. These two transformations are described schematically in figure 5.2.

In figure 5.3 the transformation elements A,C and D from equation 5.35 are calculated for

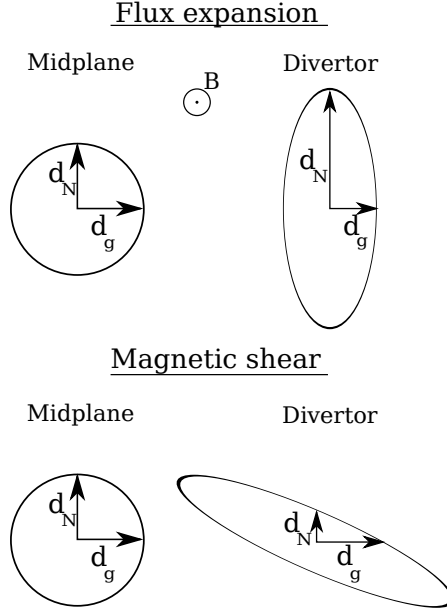


FIGURE 5.2: Schematic example of the transformation properties of a flux tube along a magnetic field line. The effects of flux expansion (upper) and magnetic shear (lower) are shown. The total transformation is a combination of the two.

the MAST SOL flux tube at  $\psi_N = 1.15$  as a function of distance along the magnetic field line,  $S$ , with the origin at the outboard midplane. The flux tube geometry is described in chapter 4. The effects of the transformation of the flux-tube (and consequently filament)

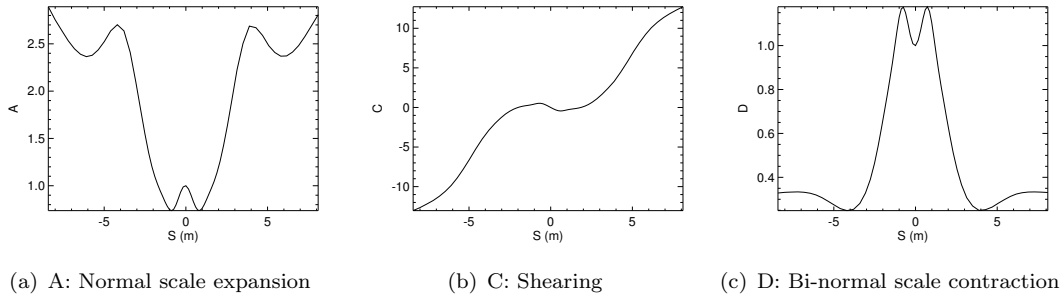


FIGURE 5.3: Components of the transformation matrix, given in equation 5.35, calculated in the MAST SOL flux-tube taken at  $\psi_N = 1.15$ . Components A and D describe a scale transformation which leads to an expansion in the normal direction and a contraction in the bi-normal direction. Component C represents a shearing transformation in the bi-normal direction.

cross-section can be rather dramatic, particularly in the divertor region, as shown in figure 5.3, where the shearing transformation begins to become large. Figure 5.4 shows an example of the transformation induced in an initially circular flux-tube cross-section at the midplane, as it appears in the divertor. The transformation properties vary with distance from the separatrix due to variation in the magnetic field. In particular the

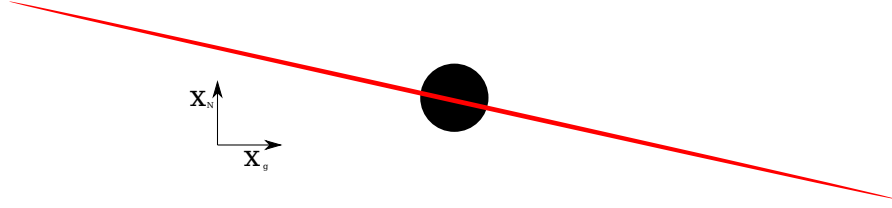


FIGURE 5.4: Transformation of a flux-tube in the divertor (red) compared to the initial circular cross-section at the midplane (black). Parameters leading to the transformation are taken from figure 5.3.

shearing transformation becomes less extreme further from the separatrix. As indicated in chapter 4 this effect cannot be captured in the flux-tube geometry since radial variation of magnetic parameters is neglected. This may affect filament dynamics if magnetic parameters vary on length scales comparable to the cross-section filament size. This is unlikely to occur at the outboard midplane in MAST as shown in figure 3.30 of chapter 3 where the magnetic field variation is weak, however close to the X-point the magnetic shear can be large due to the reduction of the poloidal field to 0 at the X-point. This will be addressed in the discussion section of this chapter. Inclusion of these effects is beyond the scope of this study, however would be a good topic for future research.

The transformation properties of the flux-tube have an important impact on the dynamics of filaments in a number of ways. Firstly and most obviously since filaments align to the magnetic field, they inherit the scale transformation of the flux-tube. Therefore the cross-sectional width of filaments vary along the magnetic field line which in turn causes a variation of the cross-field gradients in the filament. The cross-sectional width of the filament in the normal and bi-normal directions can be estimated by taking

$$\nabla \sim \begin{pmatrix} 1/\delta_N \\ 1/\delta_g \end{pmatrix}$$

where  $\delta_N$  and  $\delta_g$  are the filament half-widths (radii) in the normal and bi-normal directions respectively. This then gives the transformation

$$\begin{pmatrix} 1/\delta_{d,N} \\ 1/\delta_{d,g} \end{pmatrix} = \mathcal{M} \begin{pmatrix} 1/\delta_{u,N} \\ 1/\delta_{u,g} \end{pmatrix} \quad (5.39)$$

This expression can be rearranged to calculate  $\delta_{d,N}$  and  $\delta_{d,g}$ . Assuming a circular filament cross-section with a radius  $\delta_{\perp} = \delta_N = \delta_g = 2\text{cm}$  and taking the upstream reference position as the midplane, figure 5.5 shows the resulting width of the filament as a function of distance along the magnetic field line. The magnetic geometry can induce an extreme contraction of the filament width in the normal direction principally as a result of the shearing transformation. In the divertor region this can lead to filament widths

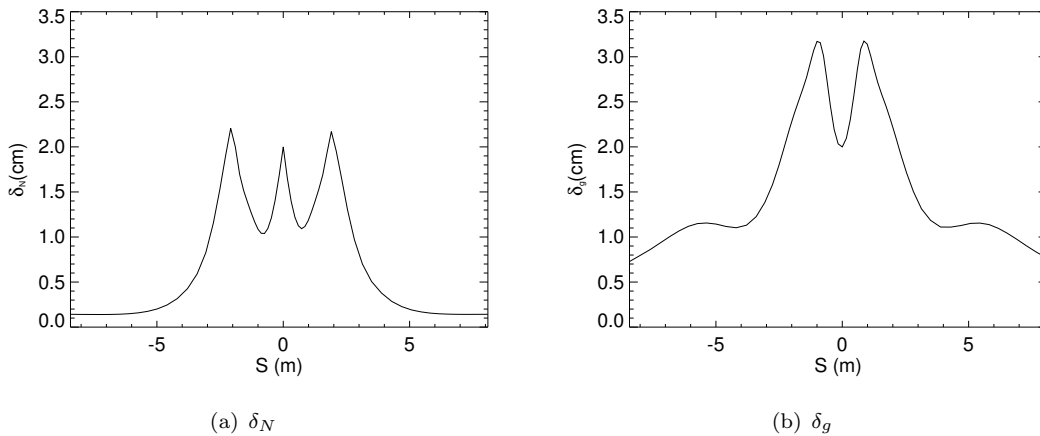


FIGURE 5.5: Filament half-width in the normal (left) and bi-normal (right) directions due to the transformation properties of the flux-tube as a function of distance along the magnetic field line. The shearing transformation leads to an extreme contraction in the normal length scale of the filament.

on the  $mm$  scale. This scale is comparable to the Bohm gyro-radius in MAST which is  $\approx 1.5mm$  at an electron temperature of 20eV. This suggests that gyro-scale effects may play a role in the physics of filaments in the divertor region. The cold-ion assumption in the model used here leads to a neglect of gyro-scale effects by assuming a vanishingly small ion gyro-radius. As such the contraction in the divertor is not inconsistent with the model used, however inclusion of gyro-scale effects may be a good topic for future work. This will be commented on further in the discussion section.

The peaks in the normal width of the filament observed in figure 5.5 occur at points where the shearing transformation,  $C$  in figure 5.3, crosses 0. At this point only the scale transformations occur. Since the shearing transformation universally reduces the normal width it is expected that the filament width maximizes when the shearing transformation is 0. In the bi-normal direction peaks in the bi-normal width correspond to peaks in the bi-normal scale transformation due to flux expansion, element  $B$  in figure 5.3. This occurs when the poloidal magnetic field maximizes along the magnetic field line. Note that this is a result of the close proximity of the plasma to the P5 poloidal magnetic field coils (see figure 1.11 from chapter 1) and as such is a feature of the tight aspect-ratio design of MAST.

The variation in the filament width can play an important role in the dynamics of the filament. The contraction of the width increases cross-field gradients which in turn increase the drive for the interchange source. The diamagnetic current produced by the interchange source is (at least partly) balanced by cross-field polarisation currents, which also increase in strength as the filament width is reduced. In the case where the diamagnetic current is dominantly balanced by polarisation currents (corresponding

to the resistive ballooning regime of the two-region model [54], described in chapter 2) the characteristic velocity of a filament is proportional to both the square root of the curvature drive,  $\boldsymbol{\xi} = \mathbf{b} \times \boldsymbol{\kappa}$ , and the filament width  $\delta_{\perp}$  as

$$v \propto \sqrt{|\boldsymbol{\xi}| \delta_{\perp}} \quad (5.40)$$

suggesting that as the filament width contracts its velocity should reduce. Before this can be commented upon further a note must be made about the magnetic curvature. In 2D studies of blob dynamics [54, 55, 94, 99] as well as 3D studies in a slab [115, 116] the magnetic curvature vector is assumed to point negatively in the normal direction. In the tokamak SOL the reality is more complicated. Generally the magnetic field is dominated by the toroidal component, as shown in chapter 4 and so the curvature vector points predominantly radially towards the centre column of the tokamak at all points along the magnetic field line. When the curvature vector is projected onto the unit vectors in the perpendicular plane it can produce a component in both the normal and bi-normal (poloidal direction if  $B \approx B_{\zeta}$ ) directions. This is illustrated schematically in figure 5.6. Also shown in figure 5.6 are the normal and bi-normal components of  $\boldsymbol{\xi} = \mathbf{b} \times \boldsymbol{\kappa}$ . These are calculated by projecting the vector  $\boldsymbol{\xi}$ , calculated in the grid generator described in chapter 4, onto the normal and bi-normal unit vectors respectively. Note that the poloidal component of curvature contributes to the normal component of  $\boldsymbol{\xi}$ , whilst the normal component of curvature contributes to the bi-normal component of  $\boldsymbol{\xi}$ . It is notable that the normal component of  $\boldsymbol{\xi}$ , which induces motion in the bi-

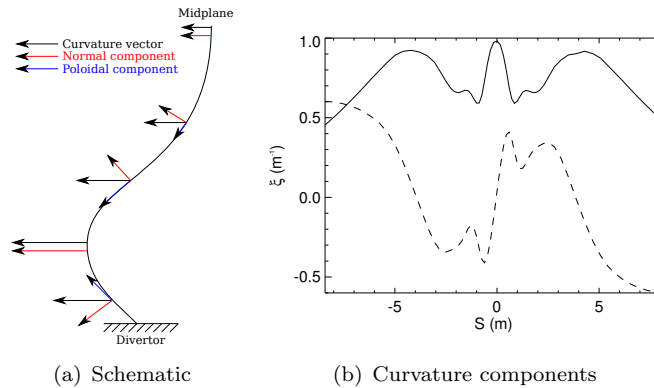
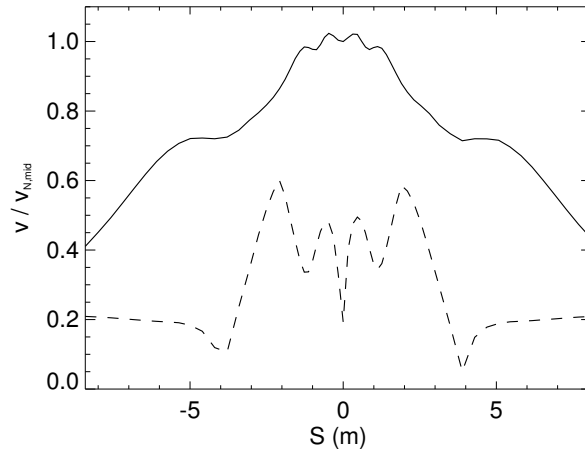


FIGURE 5.6: Left: Schematic illustration of the alignment of the curvature vector in the poloidal plane, showing that both a normal and bi-normal component of the curvature are present along the magnetic field line. Right: Bi-normal (solid line) and normal (dashed line) components of the polarisation vector  $\boldsymbol{\xi} = \mathbf{b} \times \boldsymbol{\kappa}$  in the MAST SOL flux-tube geometry. The normal component of the curvature can become comparable in magnitude to the bi-normal component in the divertor region.

normal direction, can become comparable to the bi-normal component as the field line approaches the divertor. Around the midplane the shearing transformation is weak

and the presence of the normal component of the polarisation vector indicates that the potential dipole forming across the filament may form at an angle compared to the midplane. This assumes that the dipole that forms is entirely a local process, however in reality some averaging will occur along the field line as a result of the  $\nabla_{\parallel}\phi$  term in Ohm's law. Since the normal component  $\xi$  is anti-symmetric about the midplane these effects may average to 0 if the averaging is strong enough. It is also notable that the often used approximation of  $|\xi| \sim 1/R$  where  $R$  is the major radius underestimates the strength of the magnetic curvature at the midplane. The enhancement to the curvature is a result of the poloidal magnetic field component, which can be comparable to the toroidal field at the midplane of MAST. Once again this is a feature of the spherical tokamak design of MAST and is not true in conventional aspect ratio tokamaks where  $B_{\theta}/B_{\zeta} \ll 1$ .

Having calculated the normal and bi-normal components of the polarisation vector  $\xi$ , the velocity of the filament can be estimated. The velocity in the normal direction is a result of the bi-normal component of  $\xi$  and visa versa. Figure 5.7 shows that predicted velocity of the filament normalized to the velocity in the normal direction at the midplane, as a function of distance along the field line. The filament velocity strongly peaks in




---

FIGURE 5.7: Filament velocity as a function of distance along the magnetic field line due to polarisation from the bi-normal component of  $\xi$  (solid curve) and the normal component of  $\xi$  (broken curve) predicted from the resistive ballooning scaling, normalized to the normal velocity at the midplane.

the midplane region suggesting that strong ballooning of the filament at the midplane is expected. Some fine structure is present in the velocity prediction however the averaging effect of Ohm's Law is likely to suppress this structure. The extreme contraction of the filament in the normal direction suppresses the bi-normal velocity and the predominant motion of the filament is expected to be in the normal direction.

The ballooning predicted here suggests that the magnetic geometry provides a natural

source of parallel density gradients within the filament. These density gradients can then act, through the Boltzmann source, to break the symmetry of the interchange motion and cause a departure of the filament dynamics from 2D predictions. With a view to investigating these effects, the next two sections present limiting cases of otherwise identical filaments with electron temperatures of 1eV and 20eV respectively. The former is below the critical temperature of  $\approx 4\text{eV}$  predicted earlier and is expected to be dominated by the interchange mechanism, whilst the latter is above the critical temperature and expected to display the effects of the Boltzmann source.

## 5.4 The interchange regime

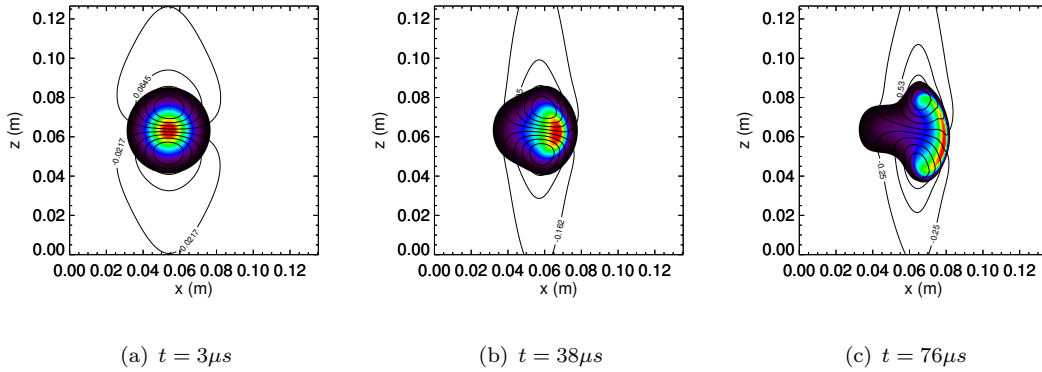
When the resistivity of the plasma is high the vorticity equation is dominated by the interchange source and the filament is governed by interchange dynamics. This is termed the interchange regime. This section will focus on filament simulations in the interchange regime and seek to characterise the resulting dynamics of the filament and investigate the role of the magnetic geometry on the filament motion. To access the interchange regime the resistivity must be large. This is achieved by taking the background density of the filament as  $n_0 = 5 \times 10^{18}\text{m}^{-3}$  and the background electron temperature as  $T_e = 1\text{eV}$ . This temperature is below temperatures that may be expected in the SOL of MAST, however it is used here to illustrate a limiting case of filament motion. At 1eV the plasma may also be subject to electron-ion recombination, which can act as a sink of plasma density and can cause detachment to occur in the divertor. These effects are not included here but would be a good topic for future study.

The filament density is initialized as a Gaussian in  $x$  and  $z$  with an initial radius of  $\delta_{\perp} \approx 2\text{cm}$  (measured as the point where the filament density is 1% above the background) at the midplane in the normal and bi-normal directions with peak density  $\delta n/n_0 = 2.06$ . Small amounts of density and momentum diffusivity are included in the simulation with coefficients of  $\hat{D} = \hat{\mu} = 0.001$  where  $\hat{D}$  is the normalized density diffusivity and  $\hat{\mu}$  is the normalized momentum diffusivity. In terms of dimensional variables these are  $\hat{D} = D/(\rho_s^2\Omega_i)$  and  $\hat{\mu} = \mu/(\rho_s^2\Omega_i)$  with  $D$  and  $\mu$  the dimensional density and momentum diffusivities in  $\text{m}^2\text{s}^{-1}$ . These values are below experimental levels and the detailed role of dissipation will be assessed in section 5.6. The filament parameters are within the ranges found experimentally on MAST [79].

### 5.4.1 Cross-field motion

The cross-field motion of filaments is well documented in the 2D limit which here corresponds to the high resistivity limit (see Chapter 2, or [55] for a review). Characteristic

aspects of the motion are the formation of a dipole potential across the filament centre, resulting in a strong electric field at the filament core which advects the filament radially. The increased advective velocity of the filament centre compared to its exterior leads to the classic 'mushroom' shape observed in simulation [94, 99] and experiment [80]. This interchange behaviour is observed in the filament simulations conducted in the MAST SOL flux tube geometry. Figure 5.8 shows the evolution of the filament cross-section in the perpendicular plane. The cross-section is taken at the midplane. Also shown in figure 5.8 is the electrostatic potential across the filament in the early stages of its motion.




---

FIGURE 5.8: Evolution of the filament cross-section at the midplane in the interchange regime. Filament density is shown in colour whilst potential is shown as contours. The filament displays the classic mushrooming motion associated with interchange motion. Here the  $x$  coordinate is the normal direction (radial at the outboard midplane) and  $z$  is the bi-normal direction.

Figure 5.8 shows the interchange characteristics of filament motion, with a strong peaking of the electric field at the filament centre leading to mushrooming motion; the evolution of the filament is similar to that observed in 2D theories. In the late stages of evolution resistive drift-waves are observed to form on the filament front. These resistive drift-waves are shown in figure 5.9.

The presence of resistive drift-waves in 3D filaments has been demonstrated by Angus *et.al* [115, 116]. In the strongly interchange driven filaments investigated here these resistive drift-waves only form towards the latter stages of the filament evolution and form with a length scale much smaller than the filament radius. The disparity in their length scale compared to the filament suggests that they are driven linearly unstable by perturbations to the filament front, as described by Angus. The delay in their onset suggests that a gradient build up is required to trigger their instability. Unlike the drift-waves found by Angus *et.al* they are not observed to significantly impact the filament motion here. This suggests that they are only marginally unstable, and require the filament to evolve and gradients on the filament front to build up before being driven unstable.

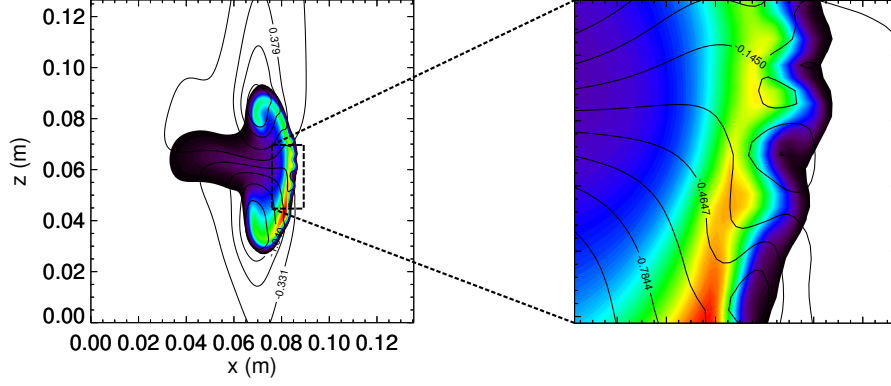


FIGURE 5.9: Resistive drift wave formation on the filament front in the late stages of its evolution at  $113\mu s$ . Colour represents density and contours represent potential. The filament front has been enlarged to show the drift-waves in detail. Here the  $x$  coordinate is the normal direction (radial at the outboard midplane) and  $z$  is the bi-normal direction.

This will be commented on further in the discussion section.

In figure 5.6 the polarisation vector,  $\xi = \mathbf{b} \times \kappa$  which determines the polarisation direction of the potential, was shown to be comparable in magnitude in the normal and bi-normal directions. At the midplane the magnetic curvature is purely in the radial direction which leads to a purely bi-normal polarisation, however moving away from the midplane the increased normal component of the polarisation vector causes the potential dipole across the filament to form at an angle. This is shown in figure 5.10 where cross-sections of the filament density are shown 2m along the magnetic field line either side of the midplane. The variation of the dipole formation about the midplane is in agreement

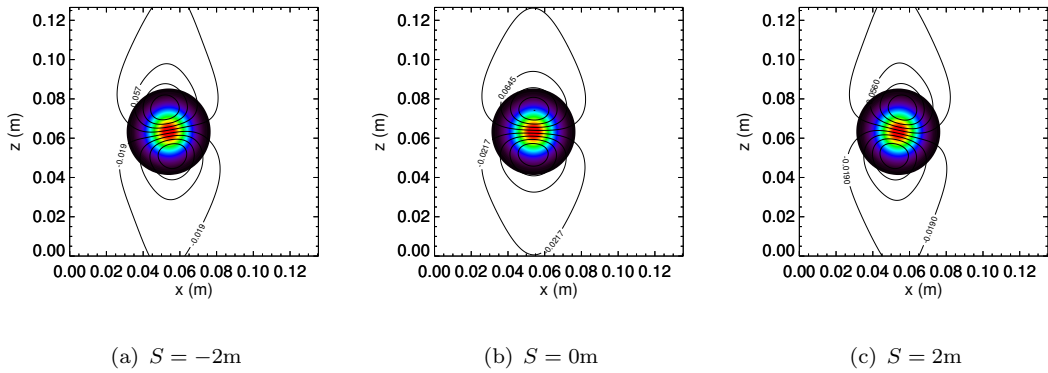


FIGURE 5.10: Filament density (colour) and potential (contours) in cross-sections taken 2m along the magnetic field line either side of the midplane. The change in the angle of the dipole is a result of the impact of a normal component of the polarisation vector  $\xi$ . Here the  $x$  coordinate is the normal direction (radial at the outboard midplane) and  $z$  is the bi-normal direction.

with the predictions made in section 5.3. Notably the angle of the dipole formation

moving away from the midplane varies weakly away from the horizontal, so the motion of the filament is still predominantly in the direction normal to the flux surface. This deviation in the motion of the filament can lead to density gradients along the magnetic field line and is the first example of the production of parallel density gradients due to the influence of the magnetic geometry.

Figure 5.11 shows the spatial structure of the electrostatic potential, vorticity and parallel current  $38\mu s$  into the filament evolution. Figure 5.11 shows that the vorticity evolves

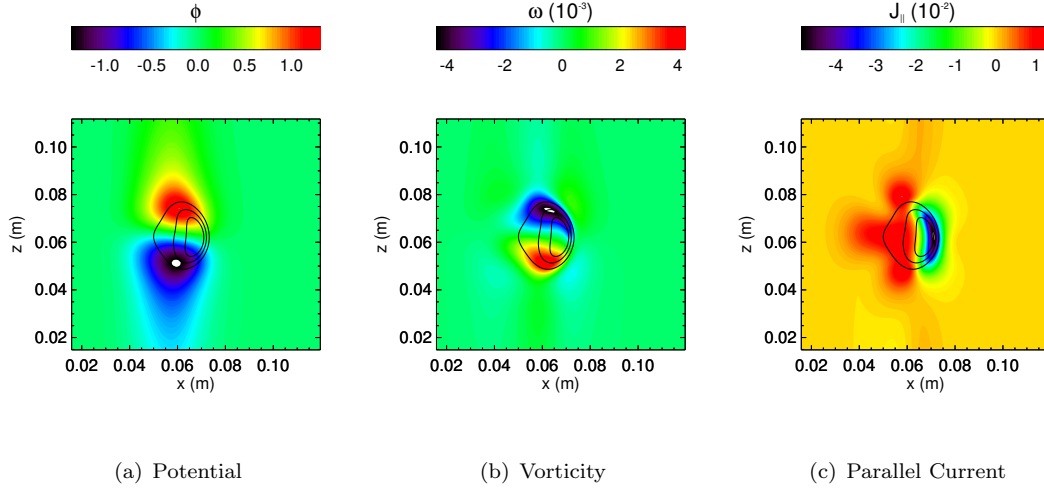


FIGURE 5.11: Electrostatic potential,  $\phi$ , vorticity,  $\omega$  and parallel current  $J_{||}$   $38\mu s$  into the filament evolution. Contours show the density of the filament for reference. Importantly, all quantities evolve on a length scale similar to the density due to the dominance of the interchange source in the vorticity equation.

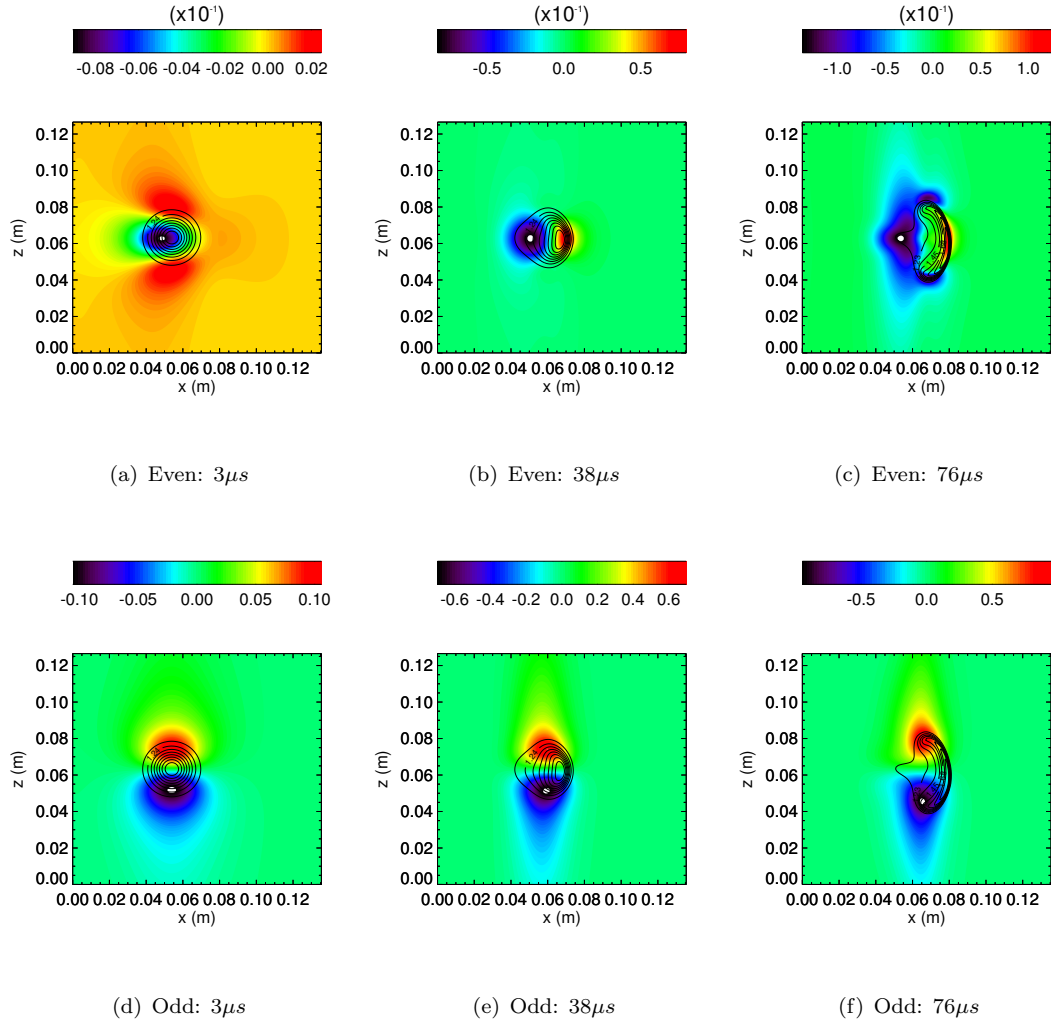
on a length scale comparable to the filament density. This indicates that the interchange source is dominant in determining the dynamics of the vorticity, and consequently the filament. As described in section 5.2 when the vorticity equation is strongly dominated by the interchange source, the electrostatic potential is expected to develop an odd structure around the filament centre. Figure 5.11 already shows that this is true, however a more detailed analysis is possible by reconstruction of the odd and even components of the potential. This is obtained by taking the original potential profile in the perpendicular plane,  $\phi(x, z)$  and constructing its reflection about the filament centre in  $z$ ,  $\phi(x, -z)$ . The odd and even components of the potential can then be obtained by

$$\phi^+ = \frac{1}{2} (\phi(x, z) + \phi(x, -z)) \quad (5.41)$$

$$\phi^- = \frac{1}{2} (\phi(x, z) - \phi(x, -z)) \quad (5.42)$$

where the even component of  $\phi$  is  $\phi^+$  and the odd component is  $\phi^-$ . In figure 5.12  $\phi^+$  and  $\phi^-$  are shown during the filament evolution at the midplane cross-section. The

potential here has been normalized to its absolute maximum in space and time before the components are extracted so that the even and odd components can be viewed comparably.




---

FIGURE 5.12: Even (upper) and odd (lower) components of the potential at the mid-plane in the interchange regime. The potential is normalized to its absolute maximum. Note the difference in scale between the even and odd components. The odd components are significantly stronger than the even components.

Figure 5.12 shows that the even component of the potential is significantly weaker than the odd component when the filament is in the interchange regime. The growth of the two components can be compared directly by taking the absolute maximum in space of each component as the filament evolves. This is shown in figure 5.13. Figure 5.13 confirms that the growth of the even component of the potential is substantially slower than the odd component. Notably though the even component does grow and this leads to the slow bi-normal motion prior to the formation of resistive drift waves.

The filament motion in the divertor region differs from the motion at the midplane as

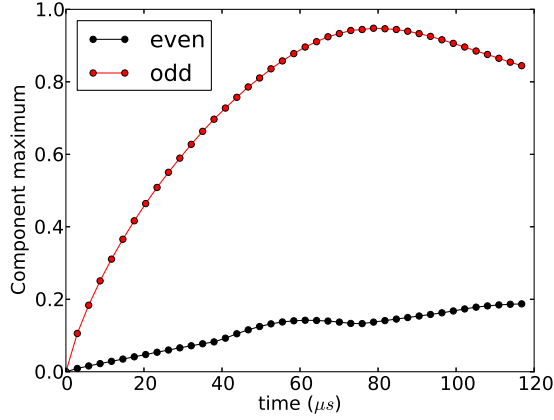


FIGURE 5.13: Growth of the even and odd components of the potential, shown by calculating the absolute maximum of each component at the midplane during the evolution of the filament.

a result of the shape transformation induced by the magnetic geometry. As discussed in section 5.3 the filament in the divertor becomes elliptical and highly sheared which greatly reduces the width of the minor axis of the filament. This has two principal effects on the filament in the divertor region:

1. Reduced electric field strength: The strength of the electric field, which results from potential polarisation across the filament arises from the balance of the diamagnetic current, the parallel current and the polarisation current in the filament. As the filament width reduces, the polarisation current increases as  $\delta_{\perp}^{-2}$  whilst the diamagnetic current, which provides the drive for the polarisation, only increases as  $\delta_{\perp}^{-1}$ . Consequently as the width reduces the polarisation current can carry away proportionally more charge and the magnitude of the potential dipole reduces. This reduces the filaments  $\mathbf{E} \times \mathbf{B}$  velocity.
2. Enhanced diffusion: As the filament width reduces, gradients increase. As such, even the small amounts of diffusion employed in these simulations (which are at least an order of magnitude below the experimental level, see section 5.6) can lead to significant dispersion of the filament density. This reduces gradients which in turn reduces the drive for the dipole potential and consequently reduces filament motion.

Both of these effects can be observed in figure 5.14 which shows the evolution of the filament in the divertor. Note that the shearing transformation of the filament cross-section has been removed in figure 5.14 to aid visual clarity. The shearing transformation *is* present during the simulation. Also note the disparity in the limits of the axes which is a result of the scale transformation due to flux expansion/contraction.

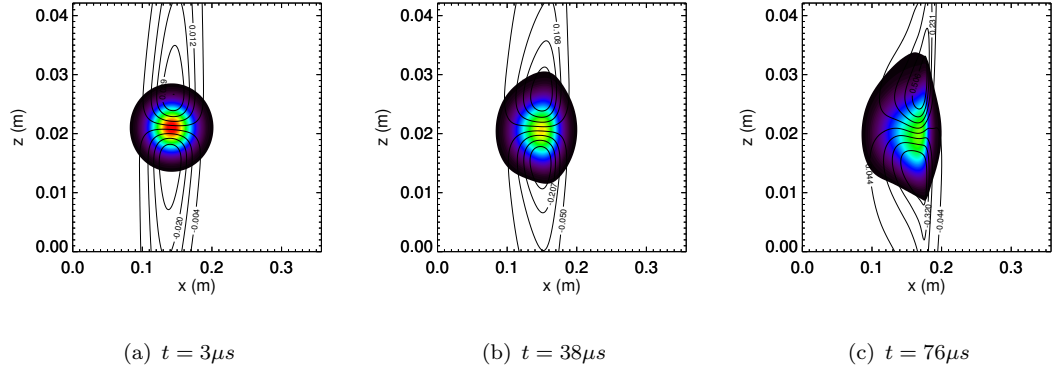


FIGURE 5.14: Evolution of the filament cross-section in the divertor region. The disparity in the scale of the axis is a result of the scale transformation due to flux expansion. Density is shown in colour and potential as contours. Note that the shearing transformation has been artificially removed in the presentation of this data to aid visual clarity, but is fully included in the calculations used to create the data.

Figure 5.14 shows that the filament remains more coherent in the divertor, with a reduced rate of outward motion as predicted in section 5.3. In figure 5.15 the spatial morphology of the potential, vorticity and parallel current in the divertor are presented.

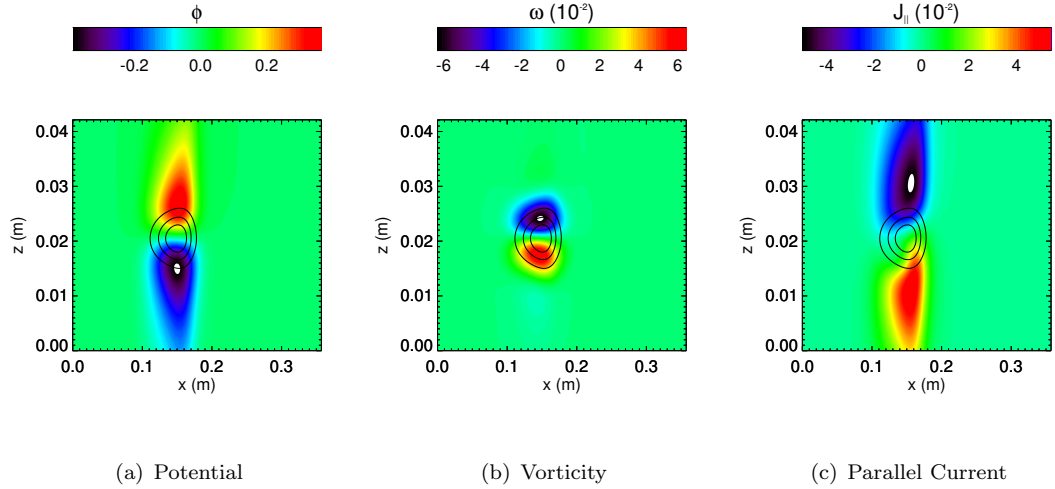


FIGURE 5.15: Electrostatic potential,  $\phi$ , vorticity,  $\omega$  and parallel current  $J_{||}$  in the divertor region  $38\mu s$  into the filament evolution.

Comparing figure 5.15 to figure 5.11 confirms that the polarisation in the divertor region is weaker than in the midplane. Also shown in figure 5.14 is a reduction in the peak density of the filament as it propagates as a result of the enhanced diffusion. In figure 5.16 the peak density of the filament in the divertor is compared to the peak density at the midplane during the evolution of the filament.

Figure 5.16 shows that the enhanced diffusion in the divertor leads to quicker reduction

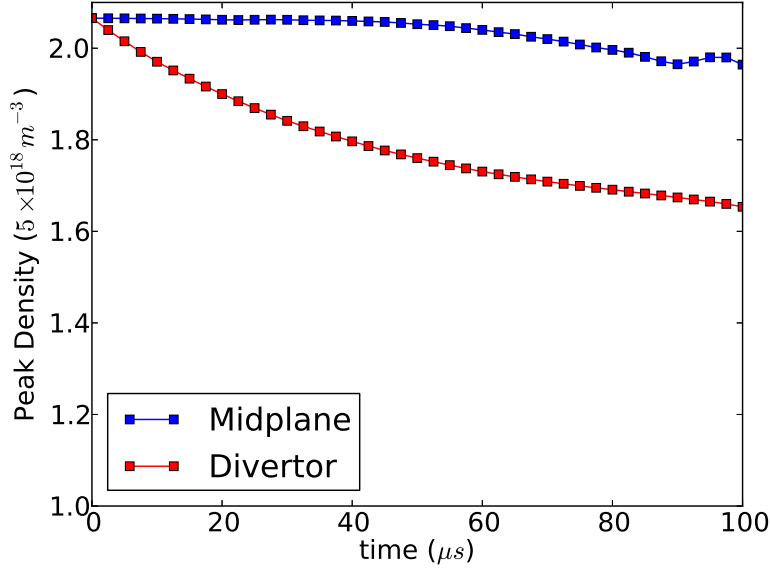


FIGURE 5.16: Evolution of the peak density of the filament cross-section at the midplane (blue) and in the divertor (red). Enhanced diffusion in the divertor leads to a reduction in the peak density compared to the midplane.

in the peak density compared to the midplane. This leads to density gradients parallel to the magnetic field which will be investigated in the next section.

#### 5.4.2 Parallel profile

A major feature of the simulations conducted in the MAST SOL flux tube geometry, compared to slab simulations such as those conducted in [115, 116, 197], is the presence of variable drive for filament motion along the length of the filament. When the resistivity is high, filaments are not tied to magnetic field lines [225] and can deviate away from field alignment. In the previous section this has already been observed in the fact that the filament dynamics in the divertor differ from the dynamics at the midplane. In figure 5.17 the evolution of the parallel profile of the filament is presented. The parallel profile is obtained by taking a cross section of the  $x, y$  plane in the field aligned coordinate system holding  $z$  constant.  $y$  can then be cast in terms of  $S$ , the distance along the field line. The effect is to lay the filament flat along the magnetic field line and take a cut through its centre showing the direction normal to the flux surface and field aligned direction.

Figure 5.17 shows that the filament does not remain aligned along the magnetic field as it evolves. Starting from a homogeneous profile along the magnetic field, the centre of the filament accelerates rapidly outwards. The region towards the divertor plates initially shows a reduction in density as a result of the enhanced diffusion in that region.

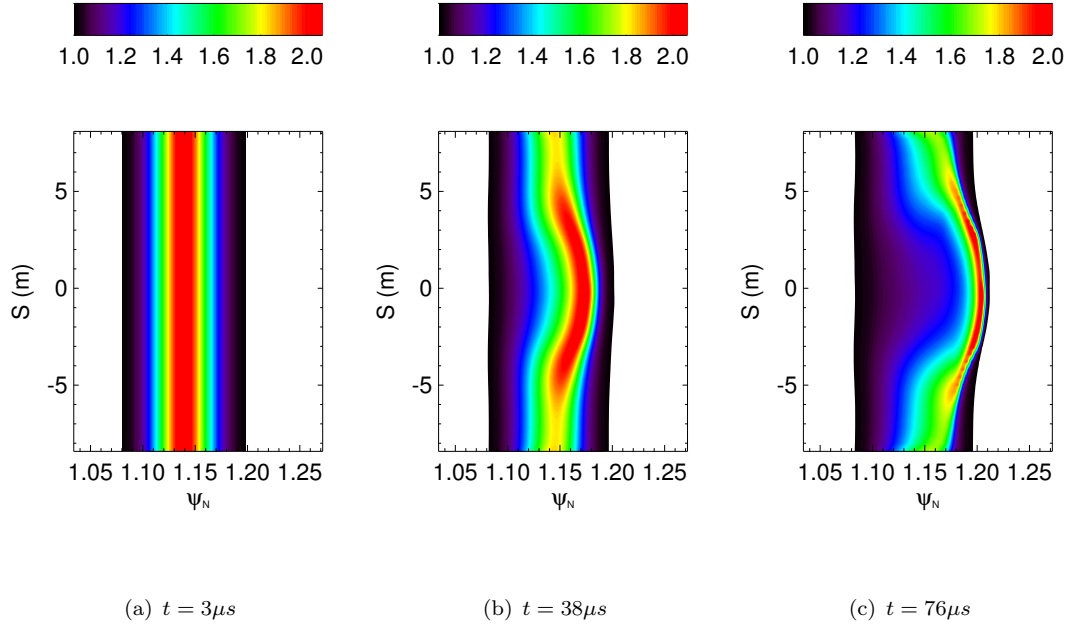


FIGURE 5.17: Evolution of the parallel profile of the filament density in the interchange regime.  $S$  is distance along the magnetic field line, whilst  $\psi_N$  is the normalized flux surface label. The divertor target is located at either boundary in  $S$ .

The propagation of the filament in the divertor regions is then slower as a result of the increased charge dissipation from the polarisation current. The net result is that the filament balloons at the midplane. The ballooning observed is a combination of three effects:

1. Curvature variation
2. Poloidal flux expansion
3. Magnetic shear

To study the role played by each of these effects in detail otherwise identical simulations have been run with two out of the three effects suppressed, thereby isolating a single effect in each case. To suppress the effects of curvature variation the curvature is artificially held constant in the flux tube at the midplane value. To suppress poloidal flux expansion,  $R$  and  $B_\theta$  are held constant, whilst to suppress the magnetic shear,  $I$  is set to 0 over the domain. In all cases the artificial dissipation is removed from the system so that only the effects of the magnetic geometry on the interchange motion is present. Figure 5.18 shows the parallel profile obtained during each simulation. These profiles are compared to the parameters which determine their shape; the curvature in the first case the filament

radius in the bi-normal direction in the second and the filament radius in the normal direction in the third. Figure 5.18 shows that that the observation of ballooning at the

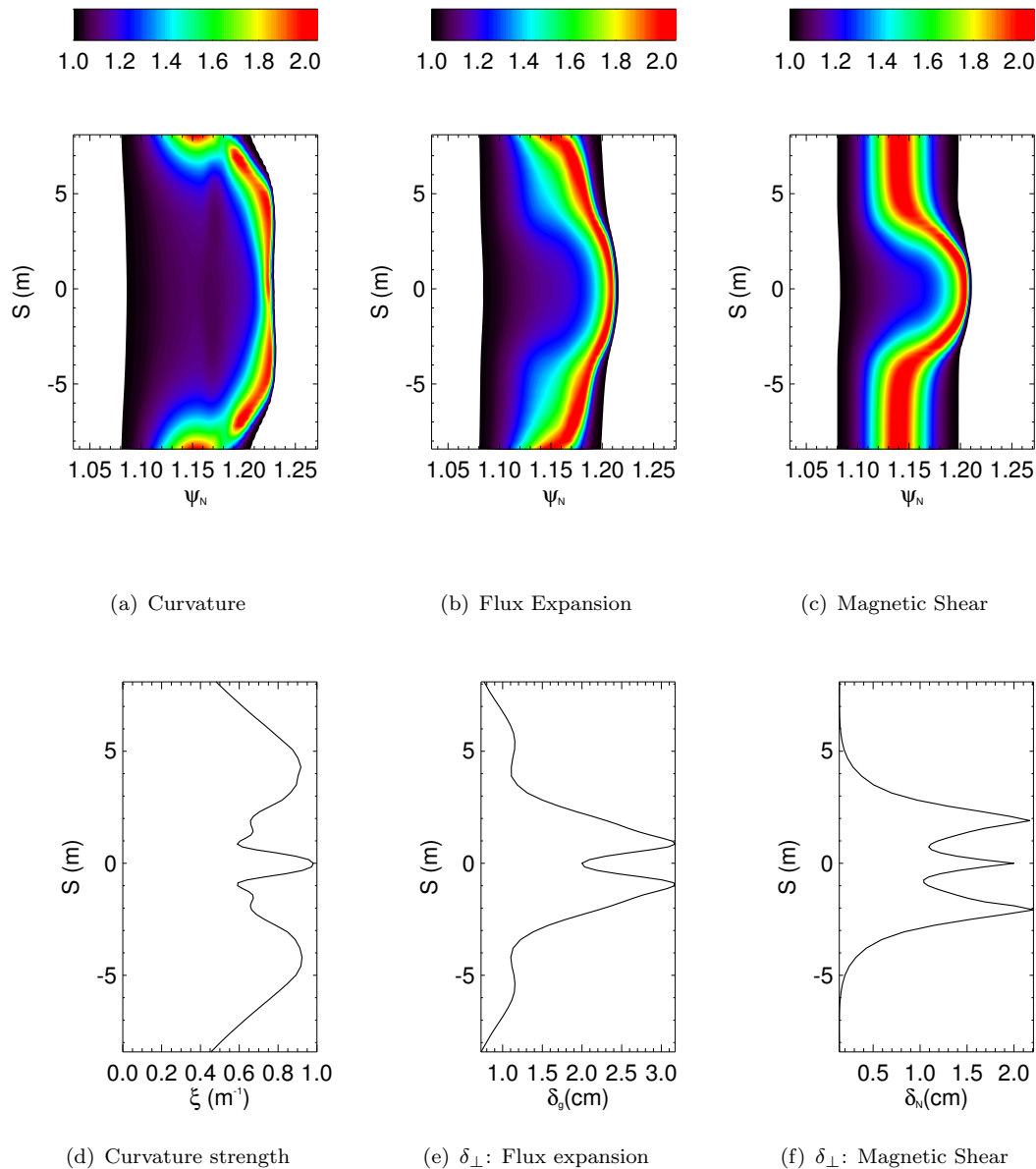


FIGURE 5.18: Comparison of mechanisms leading to resistive ballooning of the filament. Parallel profiles of filament simulations including only the effects of curvature variation (left upper), poloidal flux expansion (centre upper) and magnetic shear (right upper) are presented alongside the parameters which determine the motion. These are the curvature (left lower) and the filament width due to poloidal flux expansion (centre lower) and magnetic shear (centre right)..

midplane is a result of poloidal flux expansion and magnetic shear, and not of variable magnetic curvature. The simulations contain a degree of averaging in the parallel profiles due to the  $\nabla_{\parallel}\phi$  term in Ohm's law, which acts to couple the potential along the filament

length. Nevertheless the qualitative shape of the filament in each case is well predicted by the theoretical considerations laid out in section 5.3. The ballooning causes a departure of the filament from field alignment. The alignment of the filament can be quantified by calculating the correlation between two filament cross-sections in the field aligned coordinate system  $(x,y,z)$ . This is given in the case of the filament density at a fixed time  $t$  by

$$C_n(y) = \frac{\int dx \int dz [n(x,0,z) - \langle n(x,0,z) \rangle] [n(x,y,z) - \langle n(x,y,z) \rangle]}{\sqrt{\sigma_n(x,0,z) \sigma_n(x,y,z)}} \quad (5.43)$$

where  $y = 0$  represents the midplane,  $\langle \rangle$  indicates an average over the cross-section and the variance,  $\sigma_n$  is defined as

$$\sigma_n(x,y,z) = \int dx \int dz (n(x,y,z) - \langle n(x,y,z) \rangle)^2 \quad (5.44)$$

It is important to carry out the calculation of  $C_n$  in the field aligned coordinate system, rather than in real space since the transformation of the filament due to the magnetic geometry naturally leads to decorrelation in real space. Figure 5.19 shows the calculation of  $C_n$  and  $C_\phi$  (taken by replacing the density,  $n$ , with the potential,  $\phi$ , in equation 5.43) from the midplane to the lower divertor (though the results are symmetric about the midplane) taken  $76\mu\text{s}$  into the filament evolution. Figure 5.19 shows that the filament

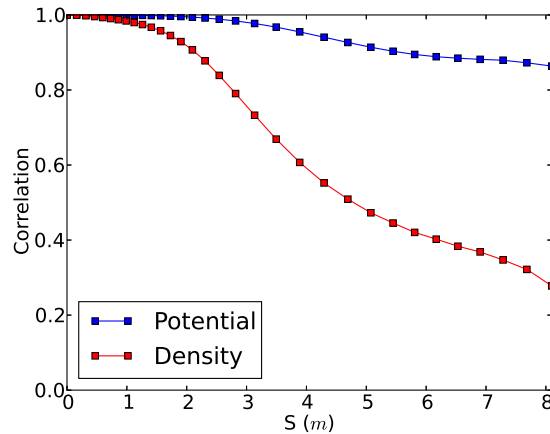


FIGURE 5.19: Correlation of filament density (red) and potential (blue) between the midplane cross-section and a cross-section displaced along the field line by a distance  $S$ , calculated from 5.43,  $78\mu\text{s}$  into the filament evolution.  $S = 0$  is the midplane position.

density remains highly correlated for the first few metres along its length. Beyond this point decorrelation is observed indicating that the filament is deviating away from field alignment. The point at which the decorrelation begins to become significant coincides with the point where the shearing transformation begins to cause a large contraction in of the filament width in the normal direction (see figure 5.18 for comparison). The

decorrelation is less severe in the case of  $\phi$  since this is unaffected by the enhanced diffusion in the divertor. The decrease in field alignment of the filament over time can also be measured with the correlation function,  $C_n, C_\phi$ , by fixing the two cross-sections in which the correlation will be calculated at the midplane and divertor (taken to be 2 grid points before the divertor surface) respectively. The correlation is then calculated at each point in time during the filament evolution. This calculation is shown in figure 5.20.

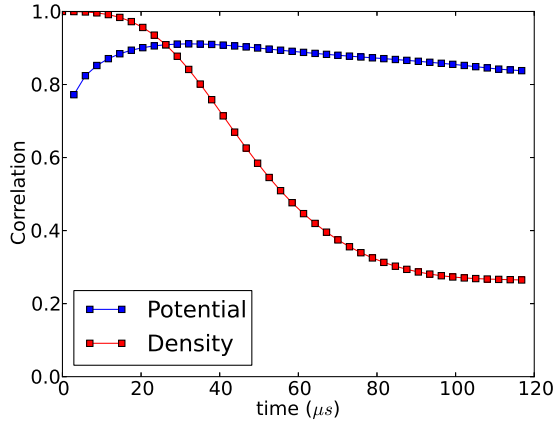


FIGURE 5.20: Evolution of the correlation between the midplane and divertor cross-sectional density (red) and potential (blue).

The filament becomes increasingly decorrelated along the field line as the midplane portion accelerates outwards relative to the divertor portion. This misalignment due to ballooning at the midplane has been predicted to be most effective at high resistivity [54, 225] which corresponds here to low temperature. As temperature is increased the field alignment of the filament may be expected to increase. From section 5.2.1 however the role of 3D effects should also become more prominent at higher temperatures and may affect the structure of the filament. This will be investigated in the next section.

## 5.5 The Boltzmann Regime

As the electron temperature is increased, and the resistivity is accordingly decreased the Boltzmann source ( $\nabla_{\parallel}^2 \ln(n)$  term) in the vorticity equation gets stronger. In this state parallel electron dynamics can play a prominent role in determining the evolution of the filament. The parallel electron dynamics are determined by parallel Ohm's law, given in dimensional form by

$$J_{\parallel} = \frac{\sigma_{\parallel} T_e}{e} (\nabla_{\parallel} \ln(n) - \nabla_{\parallel} \phi) \quad (5.45)$$

This expression neglects electron inertia and electromagnetic effects, yet retains two important terms which play different roles in determining the filament dynamics. The  $\nabla_{\parallel} \ln(n)$  term has already been shown to provide a secondary source to the vorticity equation which can break the symmetry of interchange motion, as well as drive unstable resistive drift waves [115, 116]. The  $\nabla_{\parallel} \phi$  term acts to couple the electrostatic potential along the magnetic field line and is responsible in the Two-region model [54] and the work of Ryutov [225] for aligning the filament along the magnetic field line and coupling it to the sheath. As already indicated in the previous section, when this term is not strong the filament can become decorrelated along its length and deviate away from field alignment.

In this section the role of these aspects of the parallel electron dynamics will be investigated by analysing filament simulations with a background electron temperature of 20eV. This decreases the resistivity by 90 times relative to the interchange regime simulations at  $T_e = 1\text{eV}$ , drastically increasing the strength of the Boltzmann source in the vorticity equation. At 20eV the electron temperature is above the transitional electron temperature at which 3D effects associated with the Boltzmann source may affect the filament. For this reason this regime is termed the Boltzmann regime. All other parameters of the filaments are identical to those investigated in section 5.4.

### 5.5.1 Cross-field motion

The cross-field evolution of a filament in the Boltzmann regime differs significantly from the motion found in the interchange regime. Figure 5.21 shows the evolution of the filament cross-section at the midplane making it appropriate for comparison with figure 5.8.

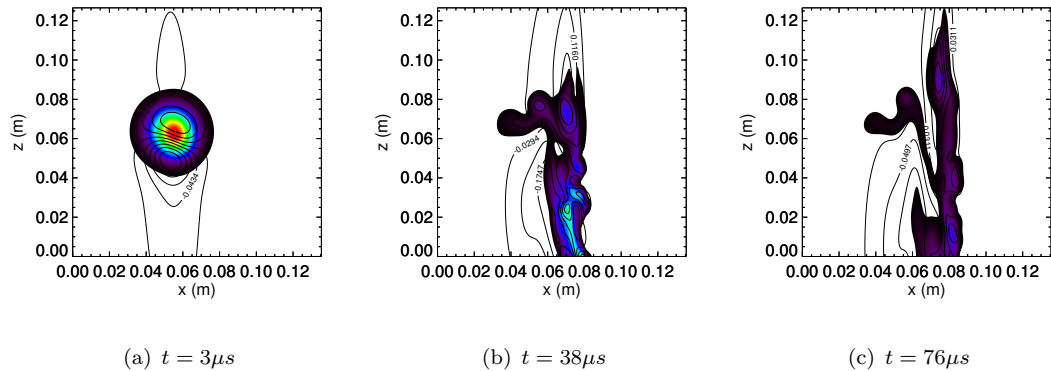


FIGURE 5.21: Evolution of the density (colour) and potential (contours) in the mid-plane filament cross-section in the Boltzmann regime. The filament becomes much less coherent than in the interchange regime.

The filament cross-section in the Boltzmann regime quickly becomes significantly less coherent than the interchange driven filament. Within the first  $30\mu\text{s}$  the filament has transitioned into a turbulent state with small scale structure starting to appear. In figure 5.22 the early evolution of the filament cross-section is presented where the filament shows a transfer of both the potential and density from larger to smaller length scales.

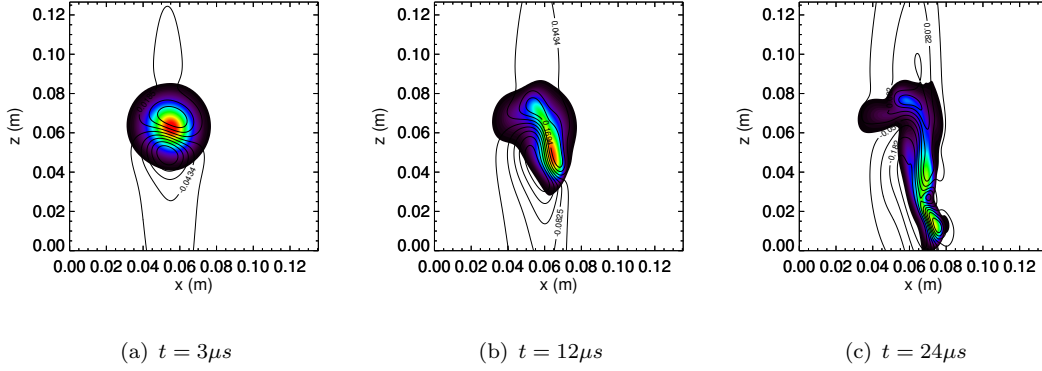


FIGURE 5.22: Evolution of filament density (colour) and potential (contours) in the early stages of the filament motion. An initial rotation of the potential dipole is followed by a gradual transition towards smaller scale turbulence leading to dispersion of the filament and propagation in the diamagnetic direction.

Figure 5.22 shows that the filament is immediately influenced by the Boltzmann source. In the initial stages a rotation of the potential dipole through nearly  $\pi/2$  radians in the bi-normal direction is observed before the filament begins to break up and a transfer to smaller length scales occurs. Notably there is no sign of the linear drift-wave instability forming on the filament front, as was observed in the interchange regime and predicted in [115, 116], but rather an indication that the turbulence is non-linearly driven. To show that the Boltzmann source is responsible for the departure of the filament from interchange dynamics a simulation has been run with the Boltzmann source omitted from the vorticity equation. This removes the drive for resistive drift-wave turbulence. Figure 5.23 shows the early stage of evolution for the case without the Boltzmann source. The data is sampled at a comparable timing to figure 5.22. Comparing figure 5.23 with figure 5.22 shows that the Boltzmann source is responsible for the departure of the filament motion from interchange dynamics. In the case with the Boltzmann source removed no rotation of the potential dipole occurs, no small length scales develop and the filament behaves in a manner similar to the interchange driven filaments studied in the previous section. An exact likeness between figure 5.23 and figure 5.8 is not present however. This arises due to additional coupling of the potential along the magnetic field line from the  $\nabla_{\parallel}\phi$  term in Ohm's Law, which becomes large when the conductivity is large. In the interchange regime the mushrooming dynamics arise predominantly locally to the filament cross-section however in the Boltzmann regime with the Boltzmann source removed, the

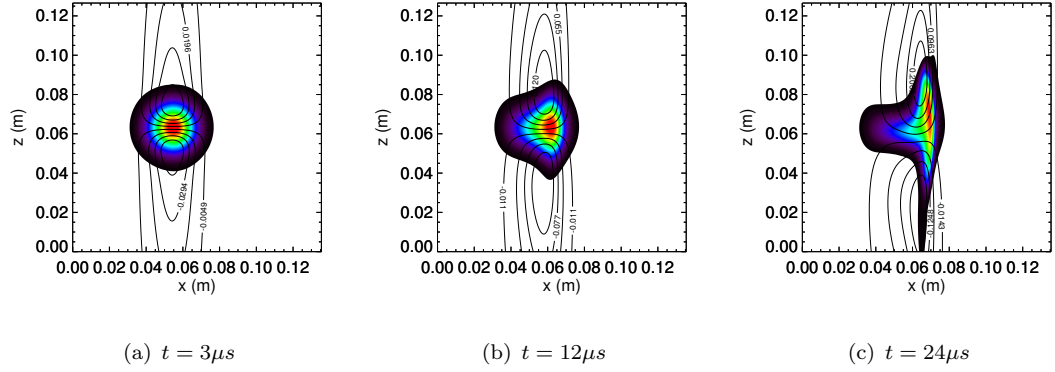


FIGURE 5.23: Evolution of the filament density (colour) and potential (contours) at the midplane cross-section with the Boltzmann source artificially removed. The simulation is otherwise identical to that presented in figure 5.22. Note that only half of the entire  $z$  domain is shown and despite appearances interaction with the  $z$  boundary is low.

dynamics are a result of strong coupling along the magnetic field line. Therefore, whilst both cases exhibit the potential dipole associated with interchange motion, the dynamics differ.

Figure 5.24 shows the spatial structure of the potential, vorticity and parallel current with and without the Boltzmann source included.

With the Boltzmann source included the vorticity now evolves on a length scale comparable to the parallel current, a smaller length scale than the density. This indicates that the parallel current (and consequently Boltzmann source) is responsible for initiating the descent down length scales. The turbulence causes dispersion of the filament and leads to significant propagation in the bi-normal direction, rather than the radial direction. When the resistivity is low parallel Ohm's law suggests that the parallel electric field must adapt to align with parallel density gradients so that  $\nabla_{\parallel}\phi \sim \nabla_{\parallel}\ln(n)$ . This is shown in figure 5.25 where  $\nabla_{\parallel}\ln(n)$  and  $\nabla_{\parallel}\phi$  are shown at the midplane cross-section in the case with and without the Boltzmann source. As expected in the case with the Boltzmann source removed the condition of  $\nabla_{\parallel}\ln(n) \sim \nabla_{\parallel}\phi$  is no longer satisfied. This shows that in a magnetic geometry relevant to the tokamak SOL the interchange model for filament motion is incompatible with the Boltzmann response, and inclusion of the Boltzmann response can cause a departure from 2D predictions.

The Boltzmann response induces strong growth of an even component of the potential which in turn leads to the observed dipole rotation. By performing a similar analysis to section 5.4 the odd and even components (about the filament centre) of the potential have been extracted and are shown in figure 5.26 prior to the transition into drift-wave turbulence.

Comparing figure 5.26 to figure 5.12 shows that the even component of potential is larger

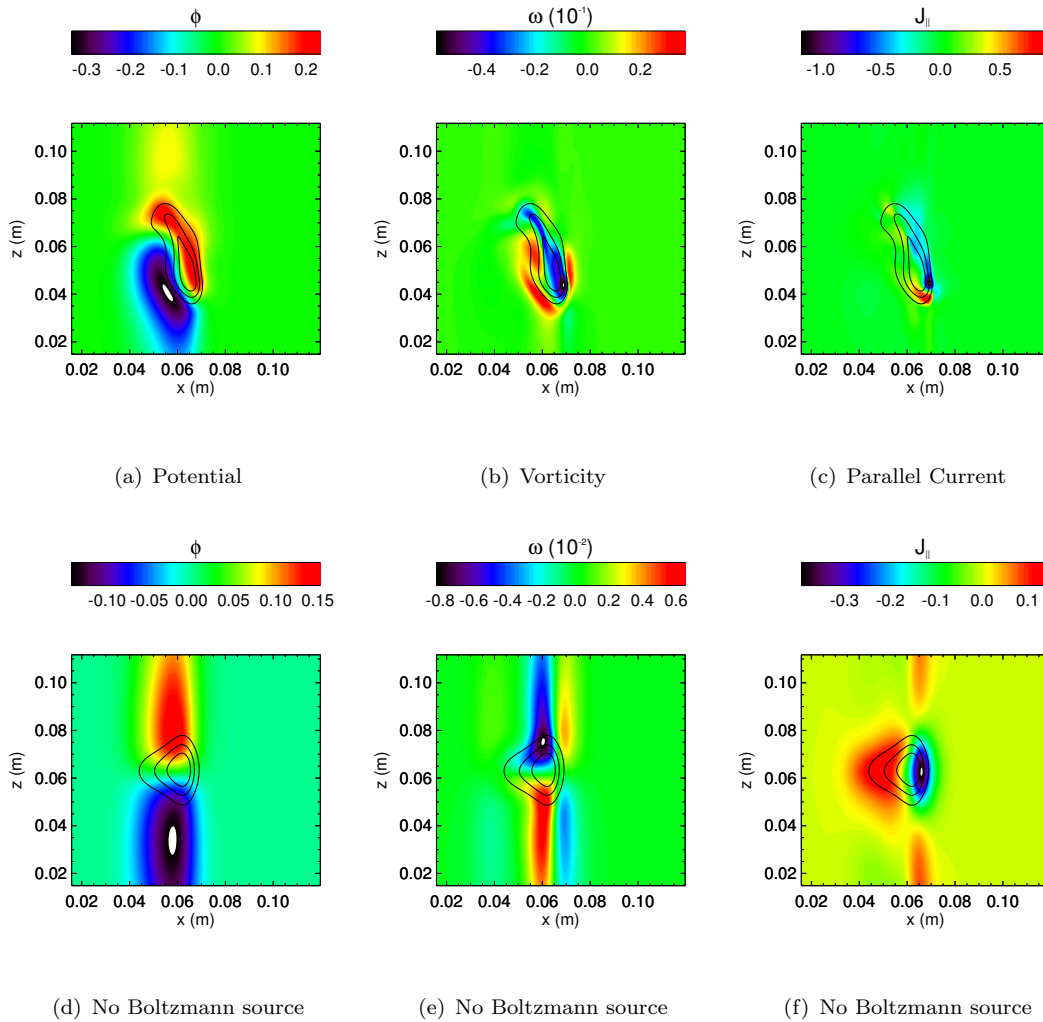


FIGURE 5.24: Electrostatic potential (left), vorticity (centre) and parallel current (right)  $33\mu\text{s}$  into the filament evolution in the Boltzmann regime with (upper row) and without (lower row) the Boltzmann source included. The vorticity and parallel current fields show small scale structure due to drift-wave turbulence when the Boltzmann source is included.

in the Boltzmann regime than in the interchange regime. As the filament propagates in the Boltzmann regime the symmetry of the density is also broken, which is not observed in the interchange regime until the late stages when linear resistive drift-waves form. The growth of the even and odd components of potential are shown in figure 5.27, which shows the absolute maximum of each component during the filament evolution. Comparing figure 5.27 with figure 5.13 shows that the initial growth-rate of the even component of the potential is substantially faster in the Boltzmann regime than in the interchange regime. The growth rate of the even component in the Boltzmann regime is comparable to the growth rate of the odd component, which leads to the initial dipole rotation observed in figure 5.22. As the filament transitions into drift-wave turbulence

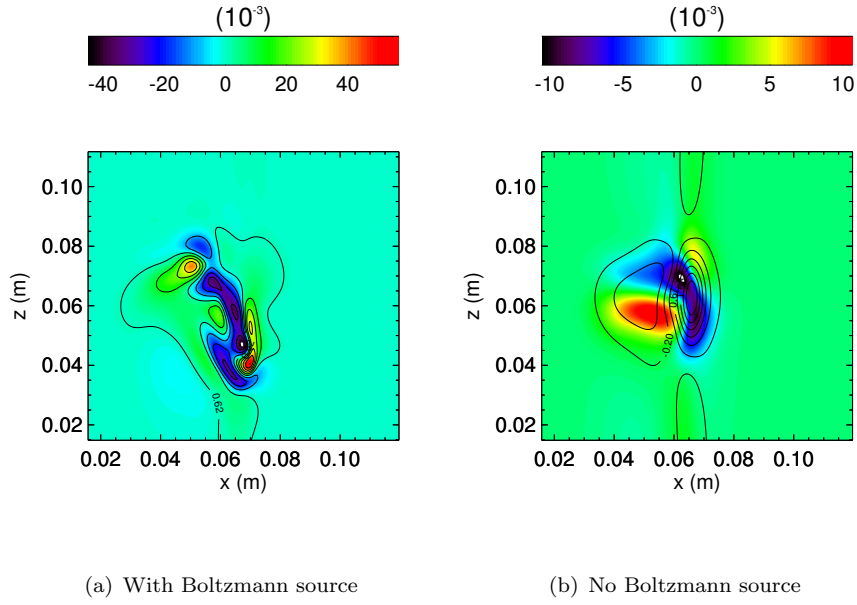


FIGURE 5.25:  $\nabla_{\parallel} \ln(n)$  (colour) and  $\nabla_{\parallel} \phi$  (contours) at the midplane cross section in the case with (left) and without (right) the Boltzmann source included. Data is sampled  $12\mu s$  after initialization. In the case with the Boltzmann source the two quantities align.

the odd and even components remain comparable. It should be noted though that at this point the assumption of  $n = n^+$  is no longer valid.

### 5.5.2 Parallel profile

In the interchange regime the filament balloons at the midplane due to the shaping transformation induced by the magnetic geometry. It was argued there, and in [225] that as the resistivity drops, or conversely as temperature increases the filament should align along the magnetic field line. Figure 5.28 shows the parallel profile of the filament in the Boltzmann regime. The profile is shown in the early stages of the filament evolution, before the onset of the drift-wave turbulence.

The parallel profile in the Boltzmann regime exhibits similar features to the interchange regime in the initial stages of evolution. In particular the effects of enhanced diffusion in the divertor leads to the strong density gradients along the length of the filament. These density gradients drive the Boltzmann source in the vorticity equation which leads to the initial dipole rotation and transition into turbulence observed in figure 5.22. As the filament evolves and begins to break down coherence along the magnetic field line is lost. This suggests that the drift-wave turbulence acting on the filament occurs fairly locally and does not lead to any significant coherent structure parallel to the magnetic field line. This is in contrast to the case of linear resistive-drift waves which were shown

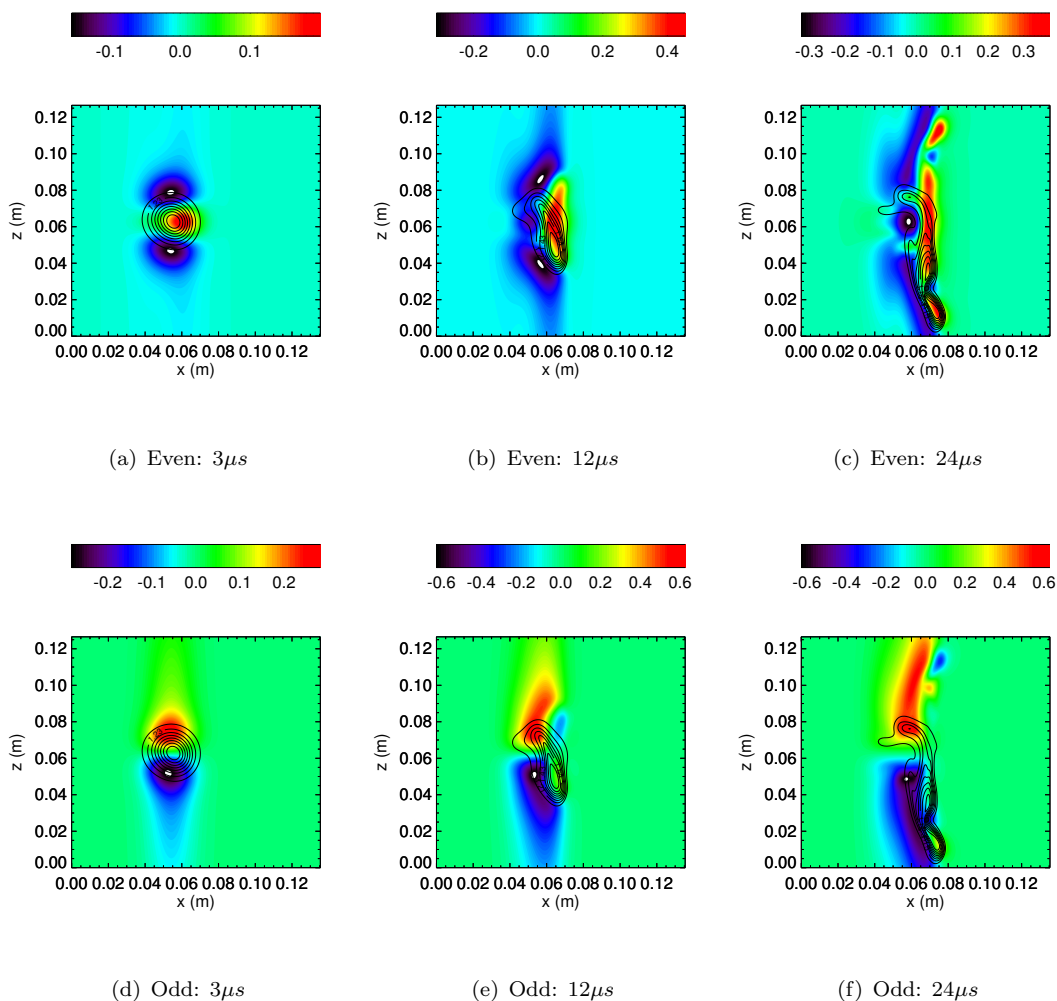


FIGURE 5.26: Even (upper) and odd (lower) components of the electrostatic potential during the early stages of evolution (prior to the transition into turbulence) of the filament in the Boltzmann regime. The components are normalized to the absolute maximum of the total potential.

by Angus [115] to produce wave-like structures along the magnetic field line in a slab geometry. To demonstrate once again that this loss in coherency along the field line is a result of the Boltzmann source, parallel profiles taken over the identical evolution time are shown in figure 5.29 with the Boltzmann source artificially removed from the vorticity equation.

Figure 5.29 shows a considerably more coherent filament along the magnetic field with the Boltzmann source removed. It also shows no signs of resistive ballooning at the mid-plane with the density strongly aligned along the field, though still showing a reduction in magnitude in the divertor due to enhanced diffusion.

In a similar manner to section 5.4 the field alignment of the filament can be assessed by calculating the correlation between cross-sections displaced along the magnetic field line

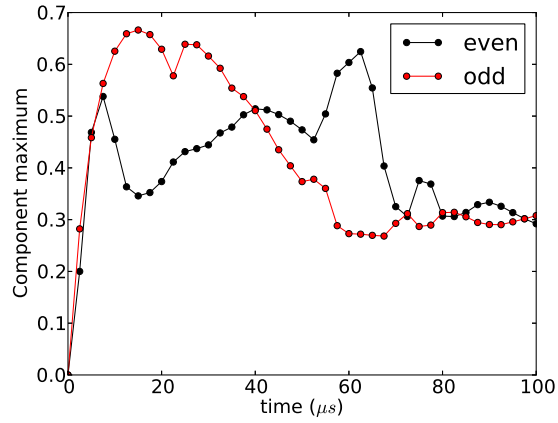


FIGURE 5.27: Growth of the absolute maximum of the even (black) and odd (red) components of potential at the midplane in the Boltzmann regime.

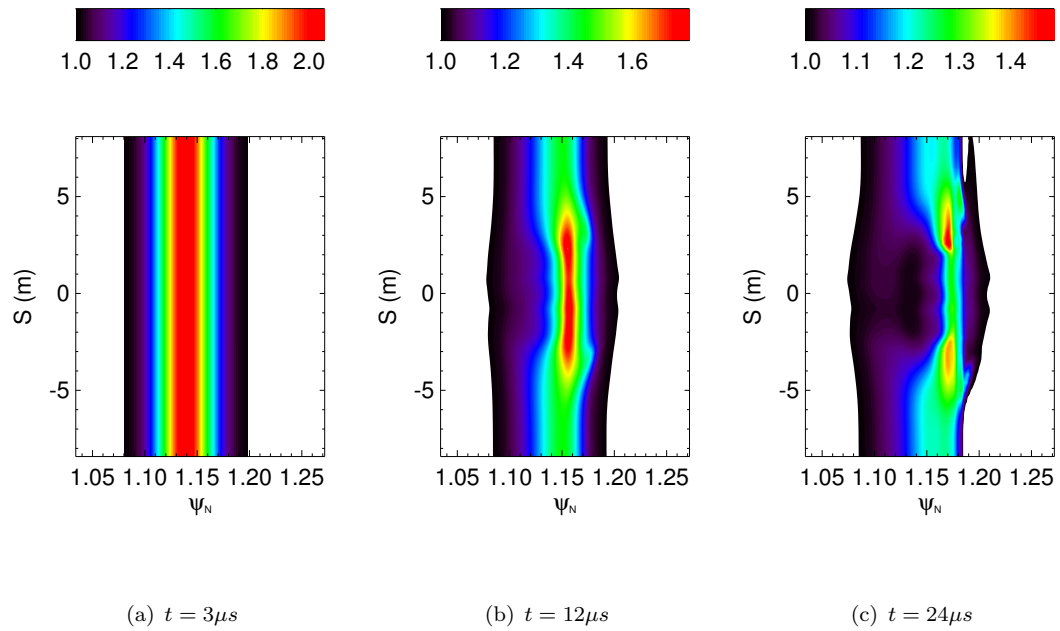


FIGURE 5.28: Evolution of the parallel profile of the filament density in the Boltzmann regime prior to the onset of the drift-wave turbulence.

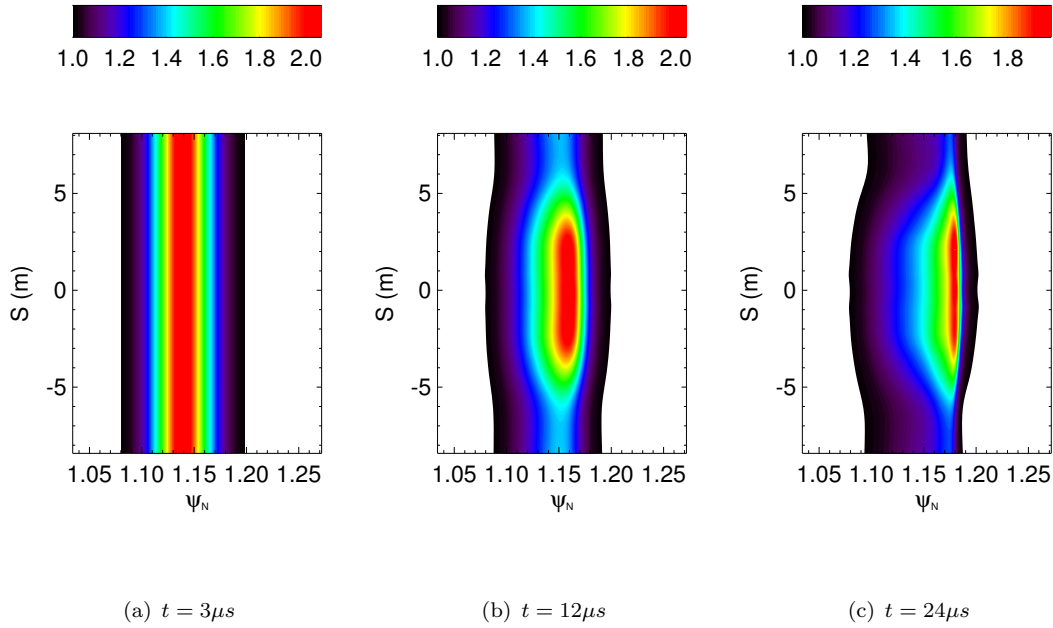


FIGURE 5.29: Parallel profile of density evolution in a filament simulation identical to figure 5.28 but with the Boltzmann source removed.

in the field aligned coordinate system. Figure 5.30 shows the correlation between the midplane cross-section and a cross-section displaced by a distance  $S$  along the magnetic field line  $24\mu s$  into the filament evolution. The cases with and without the Boltzmann source are compared.

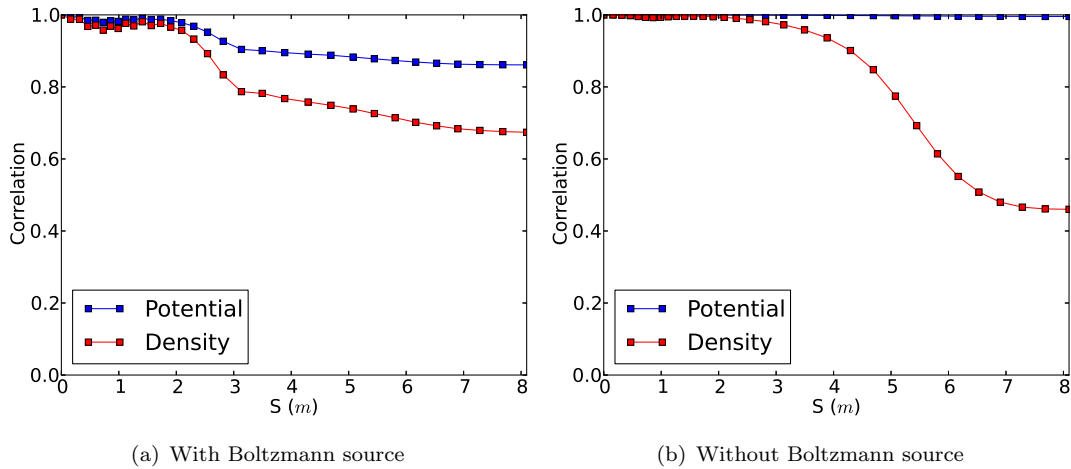


FIGURE 5.30: Correlation of the density (red) and potential (blue) between a cross-section and the midplane and a cross-section displaced by a distance  $S$  along the field line. The case with (left) and without (right) the Boltzmann source are compared  $30\mu s$  into the filament evolution, prior to the transition into drift-wave turbulence.

Comparing figure 5.30 with figure 5.19 shows that the alignment of the density along the magnetic field line is increased in the Boltzmann regime compared to the interchange regime. In particular the density remains highly correlated between the midplane and X-point. The density becomes more decorrelated in the divertor even in the Boltzmann regime as a result of the enhanced diffusion. Comparing the cases with and without the Boltzmann source shows that the correlation of the density along the field line is largely dominated by the enhanced diffusion, with both cases showing decorrelation in the divertor region. The potential, on the other hand, shows a significant difference between the two cases. With the Boltzmann source removed the potential remains entirely field aligned with a correlation of order unity over the entire filament length. With the Boltzmann source included the correlation of the potential closely resembles that of the density. In the Boltzmann regime the parallel gradients of potential and density tend to align, as shown in figure 5.25 which leads to the observed similarity in the potential and density correlation. In figure 5.31 the correlation between the midplane and divertor cross-sections is calculated over the evolution time of the filament. Once again cases with and without the Boltzmann source included are compared.

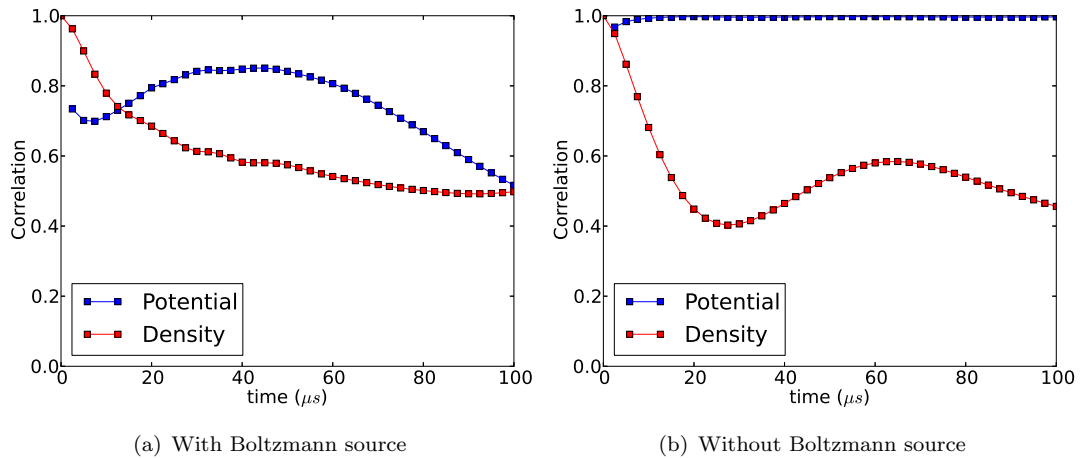


FIGURE 5.31: Correlation between the midplane and divertor cross-sections of density (red) and potential (blue) over the evolution time of the filament. Cases with (left) and without (right) the Boltzmann source are compared.

Both the potential and density become misaligned along the magnetic field as the filament evolves in the case where the Boltzmann source is included. In contrast removing the Boltzmann source leads to a strongly field aligned potential throughout the evolution of the filament.

It has become clear that as temperature increases the dynamics of 3D filaments depart significantly from conventional 2D dynamics. The departure is caused by the Boltzmann source, which becomes strongly driven as a result of the emergence of parallel gradients which occur due to the magnetic geometry of the SOL. With this departure of

the dynamics from 2D behaviour evident, it is important to assess the impact of these 3D effects on the transport due to filament motion. In particular the scaling properties of this transport may deviate from 2D predictions as a result of 3D effects. This will be assessed in the following chapter.

## 5.6 The Role of Dissipation

The simulations presented within this chapter have contained a small, constant amount of dissipation in the form of diffusion and viscosity in the density and vorticity equations respectively. In a realistic system describing a tokamak scrape off layer dissipation can be introduced from a number of sources. The principal source is ion-ion and ion-electron collisions [118] with electron-electron collisions playing a weaker role. In dimensionless form (employing the Bohm normalization used to normalize the governing equations within this thesis) the collisional diffusion and ion viscosity coefficients are given by [129]

$$D = (1 + 1.3q^2) \left(1 + \frac{T_i}{T_e}\right) \frac{\rho_e^2}{\tau_{ei}\rho_s^2\Omega_i} \quad (5.46)$$

$$\mu = (1 + 1.6q^2) \frac{\rho_i^2}{\tau_{ii}\rho_s^2\Omega_i} \quad (5.47)$$

where the terms dependant on  $q^2$  are neoclassical corrections and terms dependant on  $q^0$  are the classical calculations.  $\rho_i$  and  $\rho_e$  are the ion and electron Larmor radii respectively, whilst  $\tau_{ei}$  and  $\tau_{ii}$  are the ion-electron and ion-ion collision times. As noted in [129] there is no current theory for neoclassical transport on open magnetic field lines and therefore the above expressions must be considered approximate. Heuristic arguments laid out in [118] support the approximate use of these expressions and, for lack of an alternative, they are employed here with  $q \sim 7$  appropriate to the edge region of MAST.  $D$  and  $\mu$  are calculated below at electron temperatures of 1eV and 20eV respectively.

$$D_1 = 1.1 \quad D_{20} = 0.012 \quad (5.48)$$

$$\mu_1 = 14 \quad \mu_{20} = 0.15$$

In the calculation of  $D_1, \mu_1$  and  $D_{20}, \mu_{20}$  the ion temperature has been taken as  $T_i = 2T_e$  supported by measurements in the SOL of MAST [145]. The magnetic field has been taken as  $B = 0.3T$  appropriate to the midplane in MAST. The dissipation coefficients used previously in this chapter were  $D = \mu = 0.001$  which is at least an order of magnitude below the density diffusivity and many orders of magnitude below the momentum diffusivity.

The dissipation terms can be cast in terms of a Rayleigh number as

$$Ra = \frac{1}{\mu D} \quad (5.49)$$

The Rayleigh number is a measure of the strength of the buoyant force against the strength of dissipative forces in the system. In scans carried out in this section all aspects of the filaments are held constant, so the buoyant force is fixed (hence 1 in the numerator of  $Ra$ ). As such the scan in  $Ra$  represents a scan in the strength of dissipative forces in the system. A series of filament simulations, similar to those already presented in this chapter, have been run at two background electron temperatures of  $T_e = 1\text{eV}$  and  $20\text{eV}$  respectively and a fixed background electron density of  $n_0 = 5 \times 10^{18}\text{m}^{-3}$ . Table 5.2 details the values of  $D$  and  $\mu$  used to scan  $Ra$ . The simulations presented in the

$D$	$\mu$	$Pr$	$Ra$
$10^{-2}$	$10^{-2}$	1	$10^4$
$10^{-3}$	$10^{-3}$	1	$10^6$
$10^{-4}$	$10^{-4}$	1	$10^8$

TABLE 5.2: Parameters used to scan the Rayleigh number,  $Ra$ . The Prandtl number,  $Pr = \mu/D$  is a measure of the ratio between momentum and density diffusivity and is kept constant at unity across the  $Ra$  scan.

previous sections of this chapter were conducted with  $Ra = 10^6$  so the scans presented here centre around the level of dissipation employed to obtain the results presented so far.

The role of dissipation in non-linear fluid systems is well established [193] with increased dissipation causing a suppression of fine scale structure in the flow. In [99] similar effects were observed in the framework of blob dynamics, with increased dissipation leading to more coherent propagation of a blob with a suppression of the fine scale breakup observed in the absence of dissipation. This implies that the small scale structure induced in the interchange regime by the formation of the linear resistive drift-wave instability may be strongly affected by an increase in dissipation strength. The Boltzmann regime on the other hand displays a transfer from large length scales towards small length scales and a state of drift-wave turbulence. In this case the role of dissipation is to determine the smallest length scale of the potential, with increased dissipation leading to larger lengthscales.

Figure 5.32 shows three filament cross-sections taken at the midplane in the interchange regime (ie with  $T_e = 1\text{eV}$ ) and the Boltzmann regime (ie with  $T_e = 20\text{eV}$ ) over the 3-point scan in  $Ra$ . As expected the linear resistive drift-waves observed in the interchange regime are stabilized by a decrease in  $Ra$ , which corresponds to increased dissipation. This stabilization is observed to occur below  $Ra < 10^4$ . When  $Ra \geq 10^4$  the observed dynamics of the filament at the midplane are very similar. In the Boltzmann regime the

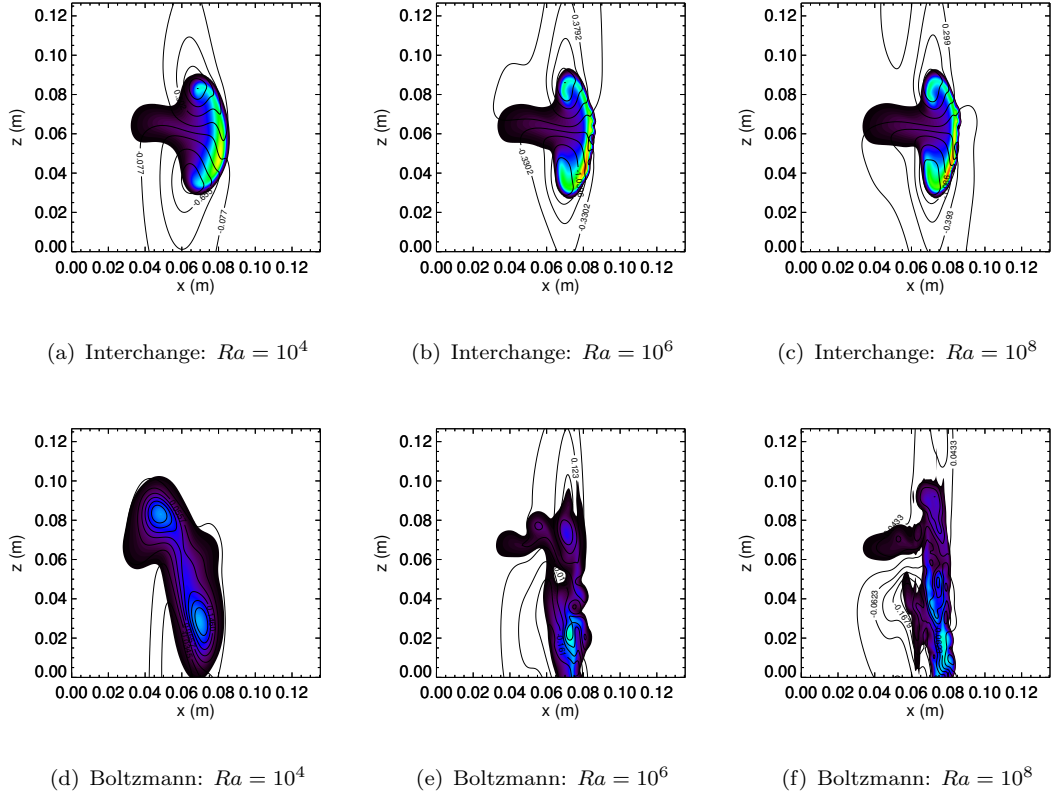


FIGURE 5.32: Cross-sections of the filament taken at the midplane across the scan in  $Ra$ . In the interchange regime simulations are sampled at  $113\mu\text{s}$ , when resistive drift-waves are unstable. In the Boltzmann regime simulations are sampled at  $41\mu\text{s}$  at the point where the transition into drift-wave turbulence occurs. Colour represents density whilst contours represent potential.

predicted suppression of small scale structure is also observed, with increasingly small scale structure in both potential and density observed as  $Ra$  increases and, correspondingly, dissipation strength decreases. The descent down length scales is halted by this suppression. In all cases the large scale structure of the filament remains similar over the scan in  $Ra$ , suggesting that the net motion of the filament is relatively unaffected by the level of dissipation employed in the simulation.

The effect of dissipation on the filament in the divertor is more drastic than the midplane. As already indicated in section 5.4 the contraction of the filament width in the divertor strongly enhances the effects of dissipation by increasing the strength of cross-field gradients. Without dissipation in the system the gradients in this region can be very large, which provides a lot of free energy to instabilities. Figure 5.33 shows cross-sections of the filament density in the divertor region over the scan in  $Ra$ . As was the case in section 5.4 the shearing transformation has been artificially removed from the images to aid visual clarity. Also note the disparity in axis scales as a result of flux expansion. At high levels of dissipation, when  $Ra = 10^4$ , the filament is observed to

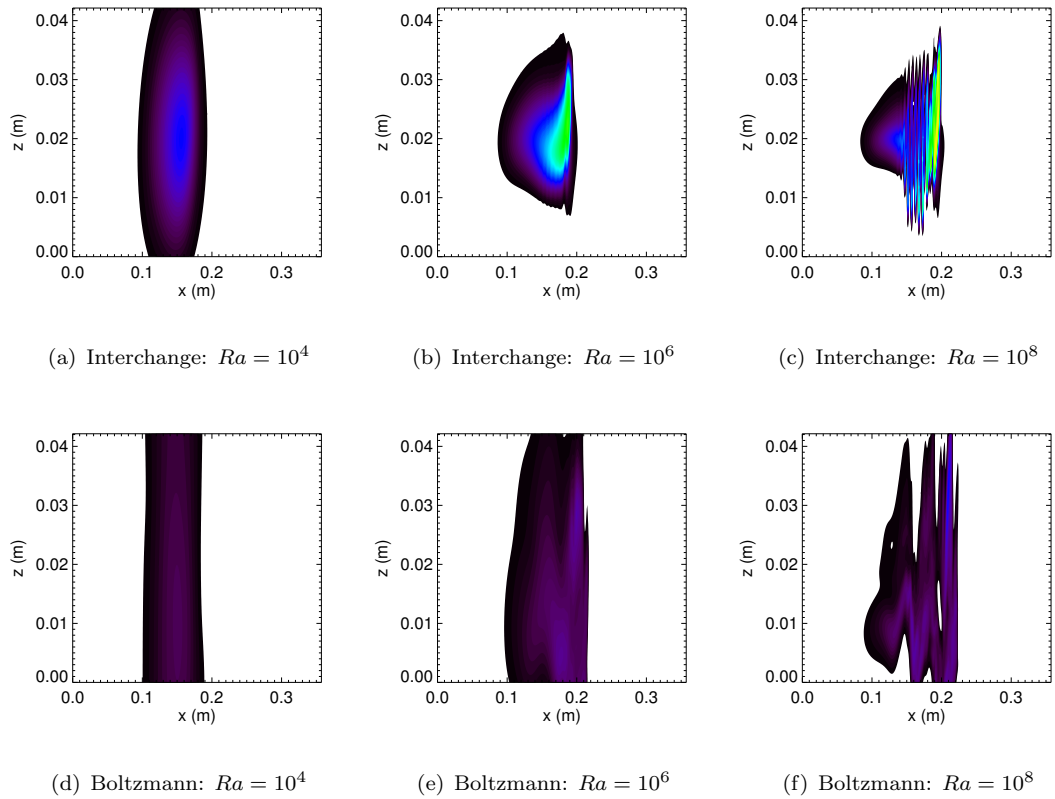


FIGURE 5.33: Cross-sections of the filament taken in the divertor across the scan in  $Ra$ . In the interchange regime simulations are sampled at  $113\mu s$  whilst in the Boltzmann regime simulations are sampled at  $57\mu s$ . Colour represents filament density. The disparity in spatial scales is a result of the flux expansion transformation. The shearing transformation has been artificially removed from the image to aid visual clarity.

disperse quickly. As the level of dissipation is reduced the filament becomes subject to a violent instability which causes it to break up. The instability has a smaller wavelength in the interchange regime than the Boltzmann regime, however the effect is the same in both; to cause the filament to disperse in the absence of dissipation. It is therefore interesting to note that with or without strong dissipation included in the system, the enhancement of gradient length scales in the divertor due to the magnetic geometry causes the filament to disperse. This either occurs via diffusive processes, or is mediated by resistive drift-wave instabilities. This suggests that density transport due to filament motion in the divertor is suppressed compared to transport at the midplane.

## 5.7 Discussion

In this chapter the combined role of magnetic geometry and 3D effects mediated by parallel electron dynamics have been investigated. This is the first dedicated numerical

study of filamentary motion in a realistic magnetic geometry. The two-region model proposed by Myra *et.al* [54, 113] (described in chapter 2 includes effects of the magnetic geometry but neglects 3D effects. In section 5.4 filaments in the interchange regime were shown to balloon at the midplane as a result of the magnetic geometry. This is consistent with the resistive ballooning regime of the two-region model. As the temperature increases the filament was shown to align strongly along the magnetic field in the case with the Boltzmann source removed, which is directly comparable with the Two-region model. The cross-field motion still displays a mushrooming characteristic and the potential develops a dipole structure with a large spatial extent, suggesting that the sheath limited regime, where large scales in the potential are preferentially damped [212] is not applicable and that the filament may be considered to be in the ideal-interchange regime. The introduction of 3D effects through the Boltzmann source causes a drastic departure of the filament dynamics from 2D behaviour when electron temperature is high. When temperature is low the impact of 3D effects is reduced. It appears therefore that the RB regime of the two-region model captures filament dynamics well, however the ideal interchange regime is subject to changes in the dynamics of filaments as a result of symmetry breaking induced by the Boltzmann source. In [84] inter-ELM filaments on MAST were shown to possess traits of the RB regime, though the results were not definitive. The results of this chapter however support the assertion that filament dynamics on MAST are ballooning by nature, with modifications resulting from 3D effects, but without a noticeable effect from the sheath.

In the work of Angus *et.al* [115, 116, 197] the effects of parallel electron dynamics were considered in a curved slab geometry. Linear resistive drift-waves were shown to grow on the filament front in the perpendicular plane. This process is also observed in the interchange regime, as shown by figure 5.9 however the observed drift-waves have a minimal impact on the evolution of the filament. The condition given by Angus for resistive drift-waves to significantly affect filament motion is

$$0.15\sqrt{\frac{1}{2|\xi|\delta_{\perp}}} \geq 1 \quad (5.50)$$

which is obtained by the requirement that resistive drift-wave instabilities grow faster than the linear interchange instability. For the MAST case considered in this chapter,  $|\xi| \approx 1\text{m}^{-1}$  at the midplane and the filament radius  $\delta_{\perp} \approx 2\text{cm}$ . This then gives  $0.15\sqrt{1/2|\xi|\delta_{\perp}} = 0.75 < 1$  which suggests that linear drift-waves may be expected to only have a marginal effect on filaments in MAST. The LHS of the inequality above gets larger as  $\delta_{\perp}$  reduces, however taking instead a filament radius of 1cm, which is well below limits observed in experiment on MAST [79, 84] only increases the LHS to 1.06,

meaning that the inequality is still marginal. This supports the observation in the interchange regime that filament dynamics are largely unaffected by resistive drift-waves. By contrast the Boltzmann regime shows a strong influence of 3D effects on the dynamics of filaments when electron temperature is increased. This was shown generally to be a result of a breaking of the interchange symmetry in the potential. The potential and density exhibit a transfer from large length scales towards smaller length scales, limited by the level of dissipation in the system. The symmetry breaking observed here is equivalent to the spinning induced by the Boltzmann response observed in [115] however an important distinction must be made. In [115] the Boltzmann response occurs due to a pre-imposed density gradient parallel to the magnetic field line. In the present work no such gradient is applied. Instead the gradients emerge in the system as a result of the magnetic geometry therefore even in an entirely homogeneous filament, symmetry breaking resulting from the Boltzmann source can still be induced. The effect of this symmetry breaking is the emergence of strong motion in the bi-normal direction, however it should be noted that the motion in the normal direction, whilst differing in nature, still produces similar levels of net displacement in the filament to the interchange regime. In experiment filaments can be tracked on fast camera imaging up to  $\approx 10\text{cm}$  from the separatrix [79], however the simulations performed here show displacements of the filament density not exceeding a few *cm*. One possibility is that the filaments simulated are not sufficiently large. Strongly coherent motion of filaments is commonly attributed to filaments in which the dissipative effects of sheath currents and polarisation currents balance one another [95], however the results of this chapter suggest that this does not occur in MAST. This suggests that the physics included in the model is not sufficient to fully describe filament motion in MAST. Two key pieces of physics have been neglected in the model used; hot ions and non-isothermal effects. Inclusion of hot ions directly into the fluid model used here requires accounting for the diamagnetic contribution to the ion polarisation current. This has the effect of adding a second, diamagnetic contribution to the vorticity [231] such that

$$\omega = \nabla_{\perp}^2 \phi + \tau \nabla_{\perp}^2 \ln(n) \quad (5.51)$$

The gyroviscous cancellation [232] prevents significant advection of the vorticity so the above modification to the vorticity can be considered as the leading order effect of the inclusion of hot ions (isothermally).  $\tau = T_i/T_e$  is the ratio of ion to electron temperatures. From the arguments of symmetry made in section 5.2.1 the role of the diamagnetic contribution to the vorticity equation is to break the symmetry of the potential. If the interchange source is strong and the vorticity obtains an odd parity about the filament centre, the potential which can be calculated by inverting the vorticity, develops an odd component from the vorticity itself, but also an even component from the density in the

diamagnetic term. In [120] this effect was observed in 2D simulations of edge turbulence which show the ejection of blobs with dipole potentials rotated with respect to the horizontal.

The results of this chapter show that the electron temperature can have a profound effect on the dynamics of filaments within experimental ranges found on MAST. The model currently assumes that the filament is thermalized to the background plasma, making it appropriate for modelling the far SOL. In the near SOL however filaments are likely to inherit the temperature of their birth region. Due to fast parallel transport the temperature of the filament is likely to fall rapidly compared to the loss of density and so the filament may exhibit a transition from the Boltzmann regime to the interchange regime on the time-scale of its perpendicular motion. This cannot be captured by an isothermal model and requires the accounting of electron temperature evolution. Both the inclusion of hot ions and non-isothermal effects would be excellent avenues of future work.

Finally a comment must be made on the magnetic geometry used here. Since the geometry is a flux-tube no radial variation of magnetic parameters is present. This approach is sufficient to demonstrate the resistive ballooning of filaments which results in a decorrelation of the upstream and downstream filament potential. In [110] such a decorrelation was observed in full turbulence simulations of a DIII-D boundary plasma. It was noted that this decorrelation, resulting from resistive ballooning induced by the magnetic geometry, may relax in the far SOL where the magnetic shear weakens and a reconnection to the sheath may occur. This cannot be captured in the flux-tube employed here, however the occurrence of this reconnection seems unlikely. The flux-tube used in this study is based on a field line approximately 4cm into the SOL already, so if the reconnection could occur it might be expected to show in the flux tube used. Nevertheless the radial variation of magnetic parameters may be an interesting avenue of future study. To achieve this the SOL grid generator outlined in chapter 4 could be extended to encompass multiple field lines in the SOL, thereby providing radial variation of magnetic parameters.

## 5.8 Summary

This chapter has studied numerically the effects of parallel electron dynamics on filament motion in a realistic magnetic geometry based on the SOL of MAST and is the first dedicated study of its kind. An invariant scaling analysis of the governing equations shows that the presence of the Boltzmann source (arising from the  $\nabla_{\parallel} \ln(n)$  term in parallel Ohm's law) can strongly influence the nature of filament dynamics in parameter ranges relevant to experimental conditions on MAST. A method of analysis based on

the symmetry properties of filament motion shows that the role of the Boltzmann source is to provide an alternative source to the vorticity equation which leads to a component of potential with an even parity in the bi-normal direction across the filament centre. This is a manifestation of the Boltzmann response. This even component can break the symmetry of the standard interchange motion of filament dynamics and led to a departure from 2D predictions. To test this hypothesis simulations of filaments were carried out at 1eV, where the effect of symmetry breaking was predicted to be negligible, and 20eV where the effect was predicted to be strong. As predicted the 1eV case shows propagation similar to 2D interchange motion. The magnetic geometry of the SOL induces a ballooning of the filament in the midplane due to the transformation of the filament cross-section. This allows the classification of filaments in MAST at low temperature as resistive ballooning filaments in terms of the Two-region model [54, 113]. The effects of parallel electron dynamics play a minimal role in this regime, however linear resistive drift-waves are observed to form on the filament front towards the end of its evolution. By contrast the high temperature case shows a strong departure from 2D physics. A breaking of the interchange symmetry of the potential is observed in the early phase of the filament motion, which is then followed by a descent down length scales as the filament becomes turbulent. The symmetry breaking induces strong motion in the bi-normal direction which is not observed with the Boltzmann source removed. The Boltzmann response causes parallel gradients in density and potential to align strongly. By comparing simulations with and without this mechanism the interchange model of filament motion is shown to be incompatible with the Boltzmann response. In both regimes of dynamics dissipation can impact the motion of the filament. In the interchange regime increased levels of dissipation suppress the linear resistive drift-wave instability, whilst in the Boltzmann regime the level of dissipation determines the size of the small length scales which are exhibited in the structure of the density and potential. This affects the finer structure of the filament dynamics, but the general motion of the filament is observed to remain qualitatively similar. In the divertor region the strong increase in gradients as a result of the shearing transformation induced by the magnetic geometry can enhance the effects of diffusion. This acts to disperse the filament. Dispersion is also observed with the strength of dissipation reduced, however this is the result of strong instabilities as opposed to diffusion. Nevertheless the net result is the same. This suggests that regardless of the level of dissipation, the dynamics of filaments at the midplane play the dominant role in determining the transport of filaments, with the strong dispersion of filaments in the divertor limiting the impact in this region.



## Chapter 6

# Scaling of the Midplane Filament Velocity in the MAST SOL geometry

### 6.1 Introduction

The contribution to density transport into the far SOL as a result of filament motion can be high [222]. Early measurements on the DIII-D tokamak indicated that up to 50% of the particle flux entering the SOL was carried by filaments [75]. As a result it is desirable to describe the properties of this transport theoretically and, in particular, how the level of transport may vary as aspects of the filaments change. Historically the scaling properties of a 'characteristic velocity' of the filament have been used to characterise the advective transport of plasma density due to filament motion. The definition of the characteristic velocity is imprecise with authors using the velocity of the filament density peak [95], the filament density front [223] and cross-sectional centre of mass [99] to investigating the velocity scaling. Although this ambiguity can lead to differences in the magnitude of the velocity measured, the scaling of the velocity should be unaffected by the choice of velocity used (so long as the choice is fixed over any individual scaling study). The filament velocity scaling is highly sensitive to the particular regime of dynamics the filament is in. In particular the scaling of the filament velocity with the cross-sectional filament radius,  $\delta_{\perp}$  and/or the electron temperature,  $T_e$  can vary dramatically between regimes. As a result quantifying the velocity scaling of the filament is a good way of identifying the filament dynamics regime.

In the simple magnetized torus device TORPEX experimental velocities of filaments are shown to agree well with theoretical scalings [82], however in the more complicated

geometry of a tokamak SOL such scalings are found to break down. In NSTX[89] the experimentally measured filament velocities were shown to be well bounded by the maximal and minimal predictions of the two-region model [54] however the detailed scaling predictions of the model could not be captured, in part due to the large statistical variation in filament properties during an experiment. In ALCATOR C-mod [90] filament velocities were shown to lie within the bounds of the theoretical predictions however statistical variation in experimental parameters once again made a detailed comparison difficult. The study did reveal a systematic increase in filament velocity with an increase in line-integrated density of the plasma from which the author inferred a breakdown of the conventional filament velocity scaling from 2D theories [95]. This phenomenon has also recently been confirmed on ASDEX-Upgrade [57–59] where a significant increase in radial transport due to filament motion is observed as the plasma density approaches half the Greenwald limit [233]. It should be noted that this increase in advective density transport was noted in 2001 [234] outside of the context of filament dynamics. In [58, 59] this increase in radial transport is attributed to a transition in the dynamics of filaments as a result of an increase in collisionality. It should be noted though that a concurrent increase in filament size is also observed during this transition. Whilst no detailed study of this kind has been carried out on MAST a similar increase in filament size with line integrated density has been observed in inter-ELM filaments [84], though the inverse was observed in L-mode filaments [79].

The role of the magnetic geometry on filament velocity scaling was investigated in the Two-region model [54, 113], however the role of 3D effects on filament velocity scaling has only very recently been investigated. In [223] 3D filaments are shown to obey well 2D scaling predictions with corrections due to an enhanced loss of density local to the sheath boundary. The geometry used was a simple magnetized torus to facilitate comparisons with the TORPEX device [224]. The authors did not report any significant effect arising from the inclusion of 3D physics, unlike the results presented in chapter 5. This may be in part due to the high collisionalities used in that study, and in part due to the simplified geometry.

In this chapter the simulations conducted in the previous chapter will be extended to encompass a scan in both electron temperature,  $T_e$ , which was shown to have a strong impact on the presence of 3D effects, and on the filament width  $\delta_\perp$  which is a common parameter used to study filament velocity scalings [95]. This chapter will begin with a brief derivation and overview of the relevant scalings of the velocity in both the normal and bi-normal directions. A scan of electron temperature at fixed  $\delta_\perp$ , followed by a scan of  $\delta_\perp$  at fixed  $T_e$  will be presented and the resulting scalings of the velocity will be analysed. A comparison with the Two-region model will be made before a discussion and summary.

## 6.2 Scaling of the Characteristic velocity

A number of methods have been used in literature to calculate the scaling of the characteristic velocity including inference from the linear stability of the system [54, 94], order of magnitude approximation of the vorticity equation [82, 223] and equilibration of drive and dissipation terms in the vorticity equation [95, 115]. In this section the latter method will be employed to derive the possible scalings of the filament velocity with electron temperature and filament width present in the model used to simulate filaments in the previous chapter and outlined in appendix B.

As indicated in section 5.2.1 in the early stages of the filament evolution (prior to the occurrence of symmetry breaking) the vorticity equation can be decoupled into an equation for the odd and even components of the potential in the bi-normal direction about the filament centre, equations 5.20 and 5.19 respectively. For reference these equations are repeated here:

$$\frac{\partial \nabla_{\perp}^2 \phi^+}{\partial t} + \mathbf{v}_E^- \cdot \nabla \nabla_{\perp}^2 \phi^- + \mathbf{v}_E^+ \cdot \nabla \nabla_{\perp}^2 \phi^+ = \frac{\alpha}{n} \left( \nabla_{\parallel}^2 \ln(n) - \nabla_{\parallel}^2 \phi^+ \right) \quad (6.1)$$

for the even component of the potential,  $\phi^+$ , and

$$\frac{\partial \nabla_{\perp}^2 \phi^-}{\partial t} + \mathbf{v}_E^+ \cdot \nabla \nabla_{\perp}^2 \phi^- + \mathbf{v}_E^- \cdot \nabla \nabla_{\perp}^2 \phi^+ = \hat{\boldsymbol{\xi}} \cdot \nabla \ln(n) + \frac{\alpha}{n} \nabla_{\parallel}^2 \phi^- \quad (6.2)$$

for the odd component of the potential,  $\phi^-$ . The 2D approximation is equivalent to neglecting the Boltzmann source in the equation for  $\phi^+$ , assuming  $\phi^+(t=0) = 0$  and using heuristic closures to represent the remaining 3D terms. This constrains the potential to  $\phi = \phi^-$  and only the odd equation needs to be considered. As such the velocity of the filament in the direction normal to the flux surface can be derived from the odd component of the vorticity equation. To derive a characteristic velocity, order of magnitude estimates are taken for each term such that  $\nabla_{\perp} \sim 1/\delta_{\perp}$  and  $\nabla_{\parallel} \sim 1/\delta_{\parallel}$  where  $\delta_{\perp}$  is the cross-field length scale and  $\delta_{\parallel}$  is the parallel length scale of the filament. The characteristic velocity can be related to a characteristic potential through the  $\mathbf{E} \times \mathbf{B}$  velocity by

$$\mathbf{v}_E = c_s \rho_s \mathbf{b} \times \nabla \phi \sim \frac{c_s \rho_s}{\delta_{\perp}} \phi \quad (6.3)$$

The hypothesis is made in this chapter that the characteristic velocity in the direction normal to the flux surface can be evaluated from the odd component of the vorticity equation, i.e. by estimating  $\phi^-$ , whilst the bi-normal velocity can be evaluated from the even component of the vorticity equation, hence by estimating  $\phi^+$ . Equilibrating the drive term (the interchange source) and the dissipation terms in the odd component of the vorticity equation, equation 5.20, arising from polarisation currents (non-linear

advective term) and parallel currents then gives (in dimensional form)

$$\frac{2c_s\rho_s|\boldsymbol{\xi}|}{\delta_\perp} \sim \frac{\rho_s^3c_s\phi^{-,2}}{\delta_\perp^4} + \frac{\sigma_\parallel T_e}{e^2\delta n\delta_\perp^2}\phi^- \quad (6.4)$$

where the LHS is the curvature drive, the first RHS term is dissipation due to polarisation currents (the square of the potential arises from the action of the  $\mathbf{E} \times \mathbf{B}$  advection on the vorticity) and the second is dissipation due to parallel currents. If the interchange drive is balanced predominantly by polarisation currents then the first term on the RHS is dominant and the characteristic velocity has the scaling

$$v_N \sim c_s\sqrt{2|\boldsymbol{\xi}|\delta_\perp} \propto T_e^{1/2}\delta_\perp^{1/2} \quad (6.5)$$

whilst if parallel currents (distinct from sheath currents) are responsible for charge dissipation then the characteristic velocity has the scaling

$$v_N \sim 2\frac{c_s\rho_s|\boldsymbol{\xi}|\delta_\parallel^2}{\sigma_\parallel B}\frac{1}{\delta_\perp^2} \propto T_e^{-1/2}\delta_\perp^{-2} \quad (6.6)$$

The former scaling is the resistive ballooning scaling of the two-region model [54] whilst the latter is the resistive X-point scaling. The Sheath-interchange and ideal interchange scalings from the two-region model can be recovered by integrating the odd component of the vorticity along the magnetic field line to the sheath boundary. The order of magnitude integrated vorticity equation is given by

$$\int_0^{L_\parallel} \left( \frac{2c_s\rho_s|\boldsymbol{\xi}|}{\delta_\perp} - \frac{\rho_s^3c_s\phi^{-,2}}{\delta_\perp^4} \right) dL \sim \left( \frac{2c_s\rho_s|\boldsymbol{\xi}|}{\delta_\perp} - \frac{\rho_s^3c_s\phi^{-,2}}{\delta_\perp^4} \right) L_\parallel \sim J_\parallel^{sh}/e \sim nc_s\phi^- \quad (6.7)$$

The integration assumes that parallel gradients in density and potential are approximately negligible. Furthermore the curvature drive is assumed constant along the magnetic field. This approximation will be discussed later in this chapter. The ideal interchange scaling, derived by balancing the curvature drive against the polarisation current dissipation, is identical to the resistive-ballooning scaling since the same balance between currents applies. The sheath-interchange scaling is derived by balancing the sheath current dissipation against the interchange drive and yields

$$v_N \sim \frac{2c_s\rho_s^2|\boldsymbol{\xi}|}{\delta_\perp^2} \propto T_e^{3/2}\delta_\perp^{-2} \quad (6.8)$$

In sections 5.4.1 and 5.5.1 3D filaments were shown to exhibit behaviour suggestive of the resistive ballooning and ideal interchange regimes. No sign of interaction with the sheath was observed, however significant breaking of the interchange symmetry was observed in the 20eV case. This led to propagation of the filament density in

the bi-normal direction. This cannot be accounted for by the odd component of the vorticity equation and requires consideration of the even component. The nature of the motion in the bi-normal direction is complex and involves a rotation of the potential dipole followed by a transition into a turbulent state mediated by resistive drift-waves. Since symmetry breaking is required for bi-normal motion the bi-normal velocity can be attributed approximately to the even component of the potential such that

$$v_g \sim \frac{c_s \rho_s}{\delta_\perp} \phi^+ \quad (6.9)$$

where  $v_g$  is the bi-normal velocity. Note that this is strictly only valid before the density develops an odd component. To estimate the scaling of  $v_g$  a similar process of equilibrating drive and dissipation terms in the even component of the vorticity equations can be applied. This leads to

$$\frac{\sigma_{\parallel} T_e}{e^2 \delta n \delta_{\parallel}^2} \ln(\delta n) \sim 2 \frac{c_s \rho_s^3}{\delta_{\perp}^4} \phi^- \phi^+ + \frac{\sigma_{\parallel} T_e}{e^2 \delta n \delta_{\parallel}^2} \phi^+ \quad (6.10)$$

The term arising from the polarisation currents now acts to mix the even and odd components of potential, whilst parallel currents again act to dissipate charge along the magnetic field line. To assess the case when dissipation by polarisation currents dominates a choice must be made for the form of  $\phi^-$ . The simulations carried out thus far indicate that the filament is subject to the resistive ballooning scaling so  $\phi^-$  is taken from the resistive ballooning calculation (i.e. from equation 6.4) as

$$\phi^- \sim \sqrt{\frac{2\delta_{\perp}^3 |\xi|}{\rho_s^2}} \quad (6.11)$$

which then gives a scaling for the bi-normal velocity of

$$v_g \sim \frac{c_s \sigma_{\parallel} B}{\delta n e \delta_{\parallel}} \sqrt{\frac{\delta_{\perp}}{8 |\xi|}} \ln(\delta n) \propto T_e^2 \delta_{\perp}^{1/2} \quad (6.12)$$

Alternatively if the drive arising from the Boltzmann source is balanced by dissipation by parallel currents the bi-normal velocity has the simple form

$$v_g \sim \frac{c_s \rho_s}{\delta_{\perp}} \ln(\delta n) \propto T_e^1 \delta_{\perp}^{-1} \quad (6.13)$$

This is the most likely scenario in MAST, since as the electron temperature increases, the resistivity decreases and parallel Ohm's law implies  $\nabla_{\parallel} \ln(n) \sim \nabla_{\parallel} \phi$ . This has already been shown in section 5.5.1 to occur when symmetry breaking is strong. In highly collisional devices such as TORPEX for example this may not be true and the closure due to parity mixing may become appropriate.

Of the various possibilities for the scaling of the filament velocity presented here, the evidence from the simulations presented thus far in this chapter suggest that the resistive ballooning scaling may be most appropriate for the radial velocity whilst the Boltzmann response scaling may be most appropriate for the bi-normal velocity. This approach does not capture the complexity of the motion, particularly when resistive drift-waves can have an impact on the system, and it remains to be seen whether the velocity scalings predicted here are indeed found in the simulations. To test this hypothesis both a temperature scan and a scan in filament width have been conducted. The results of these scans are presented in the next two sections.

### 6.3 Filament velocity in ballooning coordinates

The filament velocity is a result of  $\mathbf{E} \times \mathbf{B}$  advection of the filament density. As a result the transport of particles due to filament motion is the result of advection due to  $\mathbf{E} \times \mathbf{B}$  motion. The previous section has shown that the  $\mathbf{E} \times \mathbf{B}$  velocity can be used to analyse the scaling nature of the filament dynamics. In this section a brief derivation of the  $\mathbf{E} \times \mathbf{B}$  velocity in the normal and bi-normal directions is given in terms of the ballooning coordinates used in BOUT++ (see appendix A for details).

The  $\mathbf{E} \times \mathbf{B}$  velocity is given in terms of the potential,  $\phi$ , (normalized to the electron temperature in eV) by

$$\mathbf{v}_E = c_s \rho_s \mathbf{b} \times \nabla \phi \quad (6.14)$$

where  $c_s$  and  $\rho_s$  are the Bohm sound speed and gyro-radius respectively. The magnetic field vector can be written in the ballooning coordinate system as

$$\mathbf{B} = \frac{1}{J} \mathbf{e}_y = \frac{B_\theta}{h_\theta} \mathbf{e}_y \quad (6.15)$$

where  $B_\theta$  is the poloidal magnetic field strength,  $h_\theta$  is the poloidal arc length and  $J = h_\theta/B_\theta$  is the Jacobian of the coordinate system. The magnetic field tangency vector,  $\mathbf{b}$  can then be written as

$$\begin{aligned} \mathbf{b} &= \frac{\mathbf{B}}{B} = \frac{1}{JB} \mathbf{e}_y = \frac{1}{JB} (g_{xy} \nabla x + g_{yy} \nabla y + g_{zy} \nabla z) \\ &= b_x \nabla x + b_y \nabla y + b_z \nabla z \end{aligned} \quad (6.16)$$

Taking the metric components,  $g_{ij}$ , from appendix A the covariant components of the magnetic field tangency vector are

$$b_x = \frac{B_\zeta IR}{B}$$

$$b_y = \frac{Bh_\theta}{B_\theta} \quad (6.17)$$

$$b_z = \frac{B_\zeta R}{B}$$

$\nabla\phi$  is given in the ballooning coordinate system by

$$\nabla\phi = \frac{\partial\phi}{\partial x}\nabla x + \frac{\partial\phi}{\partial y}\nabla y + \frac{\partial\phi}{\partial z}\nabla z \quad (6.18)$$

The contravariant components of  $\mathbf{b} \times \nabla\phi$  can then be derived from

$$\mathbf{b} \times \nabla\phi = \left( b_i \frac{\partial\phi}{\partial u^j} - b_j \frac{\partial\phi}{\partial u^i} \right) \nabla u^i \times \nabla u^j = \frac{1}{J} \left( b_i \frac{\partial\phi}{\partial u^j} - b_j \frac{\partial\phi}{\partial u^i} \right) \mathbf{e}_k \quad (6.19)$$

which gives

$$\begin{aligned} (\mathbf{b} \times \nabla\phi)^x &= B \frac{\partial\phi}{\partial z} - \frac{B_\theta B_\zeta R}{h_\theta B} \frac{\partial\phi}{\partial y} \\ (\mathbf{b} \times \nabla\phi)^y &= \frac{B_\theta B_\zeta R}{h_\theta B} \frac{\partial\phi}{\partial x} - \frac{B_\theta B_\zeta IR}{h_\theta B} \frac{\partial\phi}{\partial z} \\ (\mathbf{b} \times \nabla\phi)^z &= \frac{B_\theta B_\zeta IR}{h_\theta B} \frac{\partial\phi}{\partial y} - B \frac{\partial\phi}{\partial x} \end{aligned} \quad (6.20)$$

$\partial\phi/\partial y$ , where  $y$  is the poloidal angle which follows the magnetic field line, is small in comparison to  $\partial\phi/\partial x$  and  $\partial\phi/\partial z$  which characterise perpendicular derivatives. As such the terms dependant on  $\partial\phi/\partial y$  can be neglected. This then gives contravariant components of the  $\mathbf{E} \times \mathbf{B}$  velocity

$$\begin{aligned} v_E^x &= c_s \rho_s B \frac{\partial\phi}{\partial z} \\ v_E^y &= c_s \rho_s \left( \frac{B_\theta B_\zeta R}{h_\theta B} \frac{\partial\phi}{\partial x} - \frac{B_\theta B_\zeta IR}{h_\theta B} \frac{\partial\phi}{\partial z} \right) \\ v_E^z &= -c_s \rho_s B \frac{\partial\phi}{\partial x} \end{aligned} \quad (6.21)$$

The velocities in ballooning coordinates,  $v_E^{x,y,z}$  are not necessarily the most useful for interpretive purposes. Instead the velocities in the direction normal to the flux surface,  $v_E^N$  and in the bi-normal direction,  $v_E^g$ , can be calculated from the  $\mathbf{E} \times \mathbf{B}$  velocity by

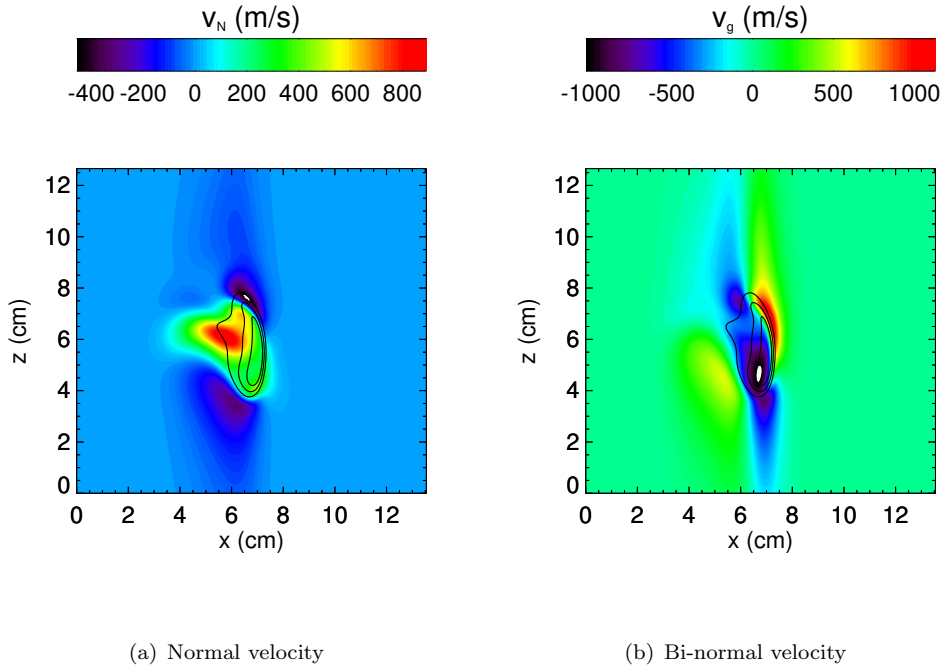
$$v_E^N = \mathbf{v}_E \cdot \hat{\mathbf{e}}_N = \frac{v_E^x}{RB_\theta} \quad (6.22)$$

and

$$v_E^g = \mathbf{v}_E \cdot \hat{\mathbf{e}}_g = \frac{RB_\theta}{B} (v_E^z + I v_E^x) \quad (6.23)$$

where  $\mathbf{e}_N$  and  $\mathbf{e}_g$  are the unit vectors in the normal and bi-normal directions respectively, derived in section 5.3 of chapter 5. Figure 6.1 shows  $v_E^N$  and  $v_E^g$  at the midplane cross-section of a filament with  $T_e = 5\text{eV}$  and  $\delta_\perp = 4\text{cm}$  (the point which straddles both the

temperature and filament width scans). Figure 6.1 shows that both the normal and bi-




---

FIGURE 6.1: Instantaneous  $\mathbf{E} \times \mathbf{B}$  velocity in the normal (left) and bi-normal (right) directions at  $T_e = 5\text{eV}$  and  $\delta_{\perp} = 4\text{cm}$ . Data is sampled at  $30\mu\text{s}$ . Velocities are shown in colour with density overlaid as contour lines.

normal velocities can be on a similar order of magnitude and in this case the bi-normal velocity can even exceed the normal velocity in magnitude, motivating the scaling study of both the normal and bi-normal velocities. It is interesting to note that experimental results on MAST have shown bi-normal filament velocities at similar magnitudes to radial velocities [79].

## 6.4 Temperature Scan

The electron temperature has already been shown in chapter 5 to play a critical role in determining the dynamics of filaments by providing drive for the Boltzmann source. To investigate the effect of electron temperature on the transport of the filament a series of simulations have been run over the range of electron temperatures  $T_e = [1, 5, 10, 15, 20]\text{eV}$ . Across the scan the geometry of the filament remains constant, as does the filament density.

In order to assess the transport of the filament in a general manner a quantity is required which can be compared between simulations. This can be provided by averaging the

$\mathbf{E} \times \mathbf{B}$  velocity over the filament cross-section at the midplane. This provides a measure of the average velocity per particle in the filament cross-section. This is explicitly calculated by

$$\langle v_E^{N,g} \rangle = \frac{\int \int v_E^{N,g} \delta n dx_N dx_g}{\int \delta n dx_N dx_g} \quad (6.24)$$

where  $\delta n$  is the filament density and  $v_E^{N,g}$  are the normal and bi-normal components of the  $\mathbf{E} \times \mathbf{B}$  velocity, with  $x_N$  and  $x_g$  the coordinates in the normal and bi-normal directions. In [99] it is noted that this quantity is equivalent to the velocity of the centre of mass when the density is assumed to be solely advected by the  $\mathbf{E} \times \mathbf{B}$  velocity, as is the case in filament dynamics. This centre of mass velocity will be calculated at the midplane cross-section of each filament within the scan and used to assess the filament velocity scaling.

Figure 6.2 shows the evolution of  $\langle v_E^N \rangle$  and  $\langle v_E^g \rangle$  at the midplane during each simulation in the  $T_e$  scan. The centre of mass velocity of the filament varies strongly in both the

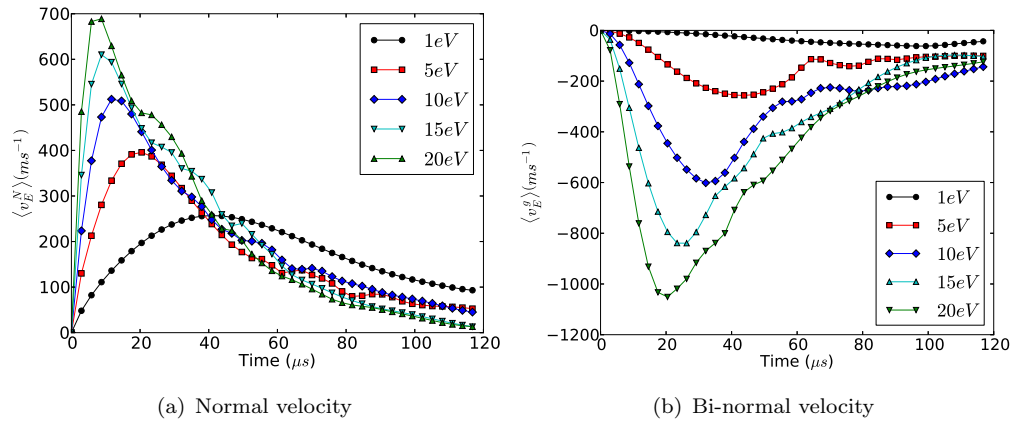


FIGURE 6.2: Filament cross-section averaged velocities in the normal (left) and bi-normal (right) directions during the evolution of the filament over the temperature scan. Variation in the velocities in both directions is observed as a result of the change in electron temperature.

normal and bi-normal directions through the scan in electron temperature. The velocity normal to the flux surface displays an initial acceleration period as the electric field across the filament grows, followed by a peak in the velocity and then deceleration as the filament propagates outwards. In a similar manner the bi-normal velocity grows initially as the dipole rotation, induced by the Boltzmann response, occurs. Again this is followed by a deceleration as the filament propagates in the bi-normal direction. Notably however the deceleration in the bi-normal direction is slower than in the normal direction.

The maximum speed of the filament in both directions increases strongly with the electron temperature. In figure 6.3 maximum speed in each direction is shown as a function

of background electron temperature. The bi-normal speed increases approximately lin-

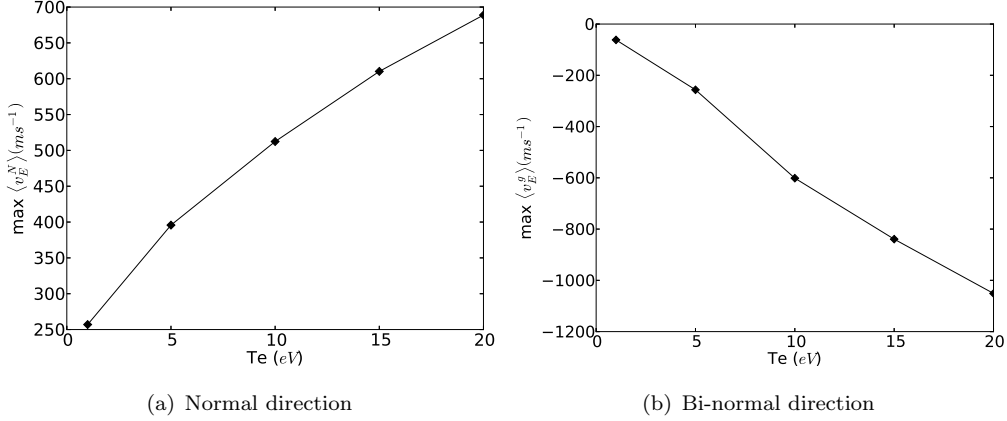


FIGURE 6.3: Peak of the averaged filament velocity in the normal (left) and bi-normal (right) directions at the midplane as a function of background electron temperature. A linear increase with temperature is observed in the bi-normal direction, whilst a weaker increase is observed in the normal direction.

early with electron temperature. This is in agreement with the scaling predictions made by balancing the Boltzmann source with dissipation by parallel currents. This scaling arises as a result of the Boltzmann response,  $\nabla_{\parallel} \ln(n) \sim \nabla_{\parallel} \phi$  and suggests that this process underlies the observed motion in the bi-normal direction. The velocity in the normal direction also shows an increase with electron temperature however this increase is weaker than that of the bi-normal speed. The scaling predictions made in section 6.2 predict a positive scaling with  $T_e$  in either the resistive ballooning/ideal interchange regimes of  $T_e^{1/2}$  or the sheath-interchange regime of  $T_e^{3/2}$ . Since the observed increase in figure 6.3 is weaker than linear suggesting the resistive ballooning scaling appears to be most appropriate in describing the normal velocity. In figure 6.4 the maximum velocity in the normal direction is shown as a function of  $T_e^{1/2}$  as a test of the RB scaling. Figure 6.4 indicates that the RB scaling of  $\langle v_E^N \rangle \propto T_e^{1/2}$  captures the increase in peak radial velocity with electron temperature. This supports the assertions made previously that the filaments simulations display the characteristics of the resistive ballooning regime and/or the ideal interchange regime. This analysis suggests that despite the complex 3D nature of the filament evolution in the Boltzmann regime, reduced 2D models may still capture the key features of the filament evolution normal to the flux surface.

In figure 6.2 the increase in the peak of the velocity in the normal directions as temperature increases is also accompanied by a quicker deceleration of the filament. The net displacement of the filament centre of mass, which can be calculated by integrating the velocity curves calculated in figure 6.2 is increased by a higher peak velocity, but also decreased by a more rapid deceleration of the filament. In figure 6.5 the displacement in the normal direction,  $\langle X^N \rangle$  and in the bi-normal direction,  $\langle X^g \rangle$  are shown over the

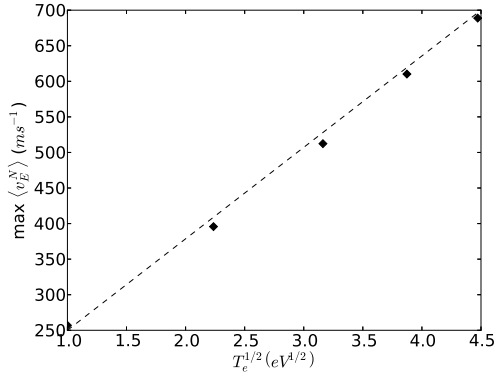


FIGURE 6.4: Peak velocity of the filament in the normal direction at the midplane as a function of  $T_e^{1/2}$ . The linear trend indicates that the temperature scaling predicted for the RB and/or  $C_I$  regimes fit the data well.

scan in electron temperature. In all cases the integration is carried out over the  $120\mu s$  of the simulation. The displacement of the filament centre of mass increases in both the

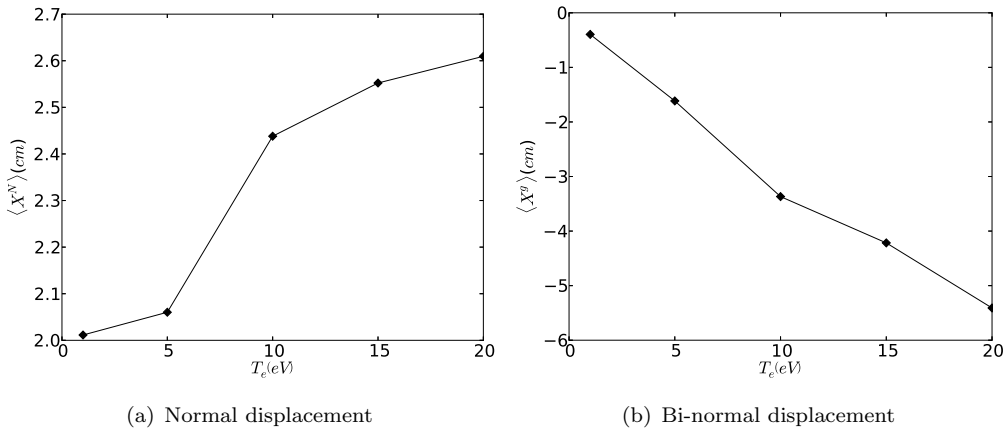


FIGURE 6.5: Displacement of the filament centre of mass in the normal (left) and bi-normal (right) directions measured by integration of the curves in figure 6.2 to  $t = 120/\mu s$ .

normal and bi-normal directions as temperatures increases. In the normal direction the increase with temperature shows that the increased maximum velocity of the filament outweighs the effect of the increased deceleration after it begins to propagate and transition into turbulence. The occurrence of this deceleration means that the increase in displacement with temperature is weaker than the  $T_e^{1/2}$  scaling observed in the velocity. The displacement in the bi-normal direction reflects the linear scaling observed in the bi-normal velocity of the filament. The propagation of the filament in the bi-normal direction can greatly exceed the radial propagation, with the  $20eV$  filament displaying a bi-normal displacement approximately twice as large as its radial displacement. It is

also clear from figure 6.5 that the relative increase in displacement across the temperature scan is far greater in the bi-normal direction than in the normal direction, with an difference of  $\approx 5\text{cm}$  in displacement in the bi-normal direction observed across the temperature scan, whilst a far more modest difference of  $\approx 0.6\text{cm}$  is observed in the normal direction. This indicates that an increase in electron temperature may result in only a modest increase in the number of particles transported into the far SOL by filaments. The bi-normal displacement of the filament can exceed a filament width and therefore may lead to interaction between filaments in the SOL. This cannot be captured in isolated filament simulations, such as those conducted here.

The transport of particles normal to the flux surface determines both the width of the density SOL, as well as the proportion of particles capable of interacting with first wall materials. With the aim of limiting interaction between the plasma and the first wall it is important to understand the detailed transport of particles in the SOL. Whilst the analysis presented so far gives useful information on the average motion of the filament, a more detailed analysis is required to assess the influence of the filament on radial particle transport. To assess the transport of the plasma density carried by the filament a series of surfaces have been constructed which lie on concentric flux surfaces and encompass the entire toroidal angle, but only extend a small distance (1cm) in the poloidal direction centred on the midplane. The small poloidal extent allows the filament properties to be considered constant parallel to the field line within the surface and focusses the study towards particle transport at the midplane. The particle flux through such a surface can then be calculated by taking

$$\Gamma^N = \int \delta n \mathbf{v}_E \cdot d\mathbf{S} = \int \delta n v_E^N dA \quad (6.25)$$

where  $\delta n$  is the filament density, and the surface element is given by  $d\mathbf{S} = \hat{\mathbf{e}}_N dA$  and  $dA \approx 2\pi R \times 1\text{cm}$  where  $R$  is the major radius. By calculating  $\Gamma^N$  at each flux-surface location within the grid (i.e. each grid point in  $x$ ) at each instant in time the instantaneous particle flux from a *single* filament can be calculated as a function of  $x$  and time,  $t$ . Note that this does not factor in the intermittency of filaments in either space or time and refers only to the flux of particles from an individual filament. Spatial intermittency can be factored in approximately by multiplying the fluxes calculated by the total number of filaments present toroidally. Note that this assumes all filaments act identically. Figure 6.6 shows a series of radial profiles of the particle flux  $\Gamma^N$  during the evolution of the filaments across the temperature scan.

In the early stages of the filament motion the hotter filaments provide a greater radial flux of particles due to their higher propagation velocities. In the latter stages this trend reverses as the velocity of the colder filaments is more sustained due to their reduced deceleration. The hottest filaments, in particular the case at  $20\text{eV}$ , shows a small but

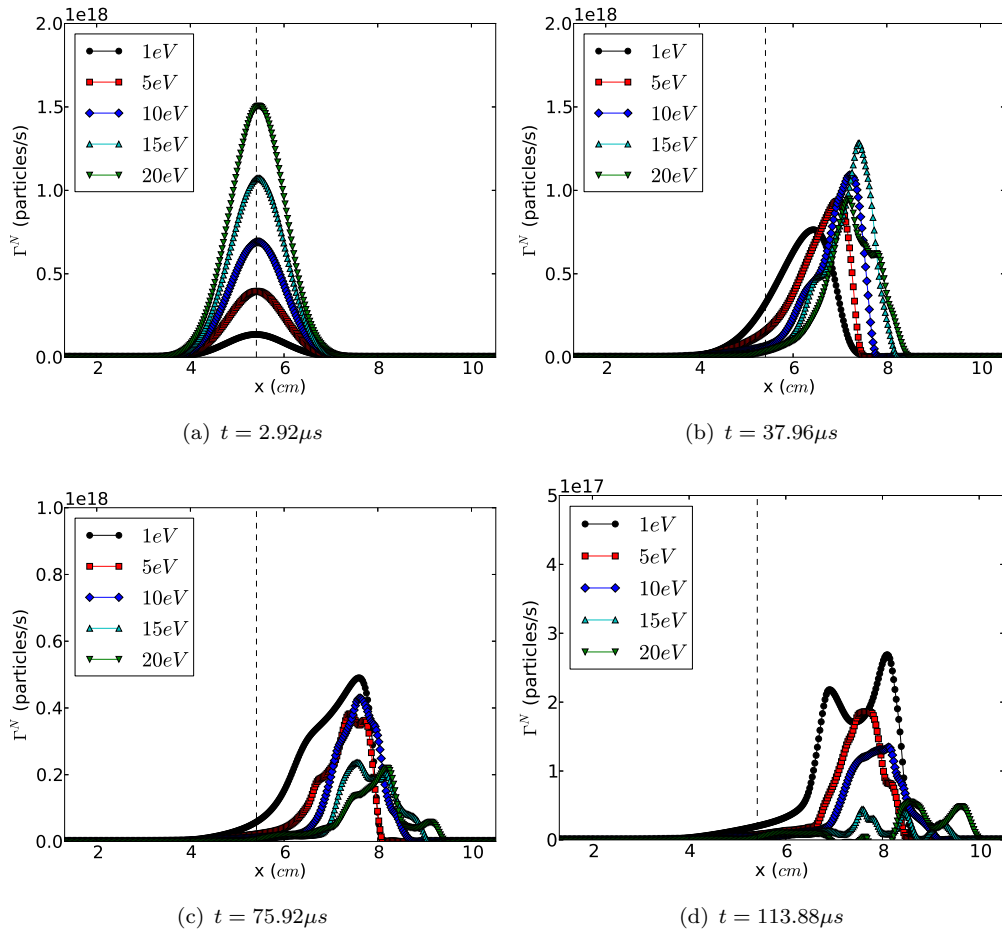


FIGURE 6.6: Radial profiles of the instantaneous particle flux,  $\Gamma^N$ , during the filament evolution across the scan in electron temperature. Note the variation in the scale of the vertical axis. The starting position of the filament is indicated by the vertical dashed line.

non-zero particle flux nearly 5cm from its starting position. At this point in its evolution the filament has become turbulent, suggesting that the drift-wave turbulence can transport particles radially after the filament has broken up and in fact enhances the transport of filament density. This can be seen clearly by integrating  $\Gamma^N$  in time at each radial location. This measures the total number of particles crossing each radial point during the simulation. Again this is for an *individual* filament. Once again the intermittency of filaments could be accounted for by multiplying the results by the total number of filaments crossing the flux surface, however this again assumes that all filaments act in exactly the same manner. This calculation is shown in figure 6.7. Figure 6.7 shows that an enhancement of particle transport into the outer regions of the domain is observed in hotter filaments. This is shown by the increase in the number of particles crossing surfaces up to nearly 5cm from the filaments initial position. To show that this enhancement is a result of resistive drift-wave turbulence, the time integrated flux of

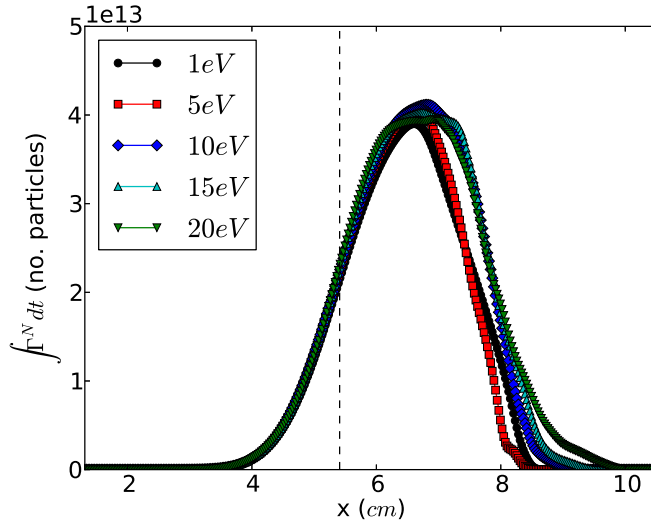


FIGURE 6.7: Time-integrated particle flux,  $\int \Gamma^N dt$ , integrated over the simulation time providing a measure of the total number of particles crossing each radial point over the simulation. This shows explicitly that simulations in which the Boltzmann source is strongly driven show an enhancement of particle transport. This is attributed to turbulent transport after the breakdown of the filament.

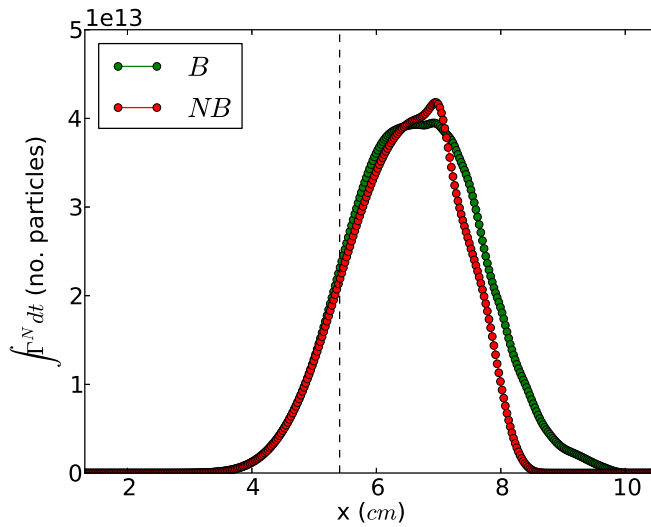


FIGURE 6.8: Time integrated particle flux profile for the  $20eV$  filament with (green) and without (red) the Boltzmann source included. A significant enhancement of the particle transport is observed with the Boltzmann source included, and is therefore associated with turbulent transport as the filament transitions into drift-wave turbulence.

particles has also been calculated in the simulation outlined in section 5.5 of chapter 5, where the Boltzmann source is omitted. This removes resistive drift-waves from the system. The comparison with and without the Boltzmann source is shown in figure 6.8.

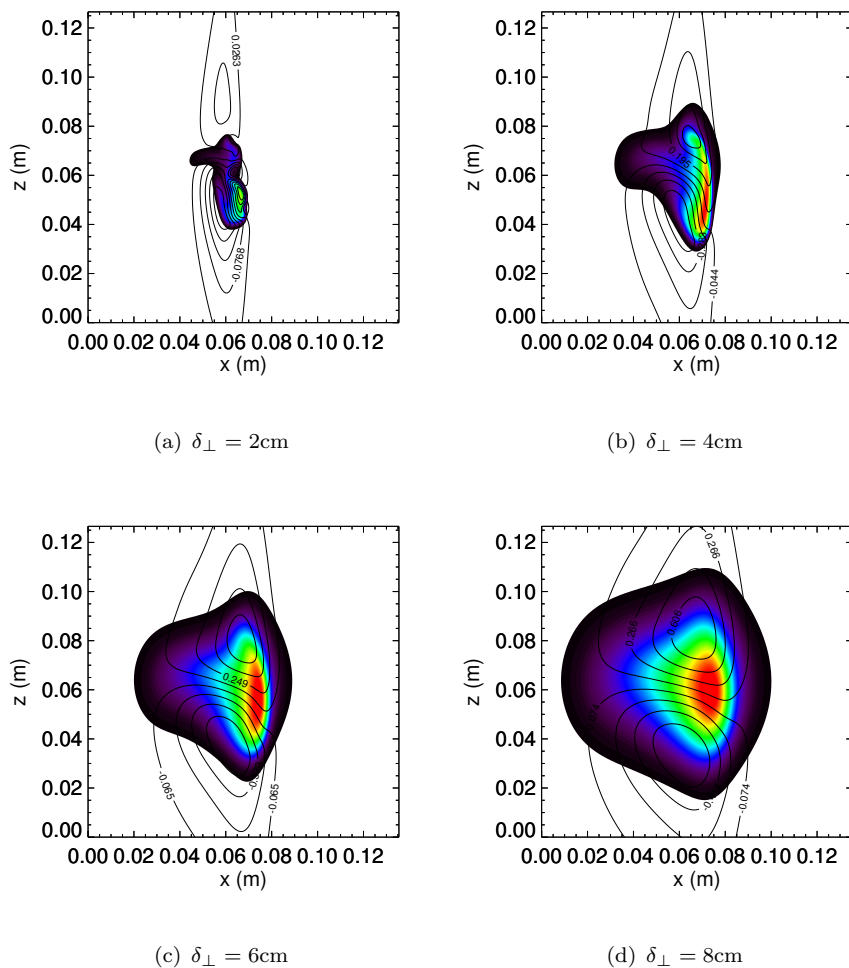
Figure 6.8 indeed confirms that the inclusion of the Boltzmann source is responsible for

the enhanced transport of particles observed in the hotter filaments. Therefore, whilst resistive drift-waves cause the filament to become more diffuse, they also provide a channel for enhanced turbulent transport of density into the outer regions of the SOL, though the enhancement is not strong. The case with no Boltzmann source under-predicts particle transport and suggests that 2D estimates may represent a lower bound on the particle transport in hot filaments.

The scan in electron temperature has shown that the radial transport of particles in an individual filament in MAST can be reasonably well approximated by reduced 2D models, though 3D effects can cause a slight enhancement of this transport. The scaling predictions made in section 6.2 also indicate the filament width,  $\delta_{\perp}$  should play an important role in the dynamics of the filaments as well. This is investigated in the next section.

## 6.5 Filament width scan

The filament width is a key scaling parameter in filament dynamics [54, 95, 99] and, as illustrated in section 6.2, its effect on the filament velocity varies depending on the dynamic regime of the filament. To test the effect of varying filament width within the MAST SOL flux tube geometry a series of simulations have been conducted at fixed  $T_e = 5\text{eV}$  and  $n_0 = 5 \times 10^{18}$  with the filament width varied in the range 2cm to 8cm. Here the filament width,  $\delta_{\perp}$ , is measured from the point where the filament density is 1% above the background density (i.e. the limit of the contours in figure 5.8). The filaments are approximately circular in the perpendicular plane, though  $\delta_{\perp}$  here is specifically taken as the bi-normal width at initialization. All other aspects of the simulations, including grid resolution, are identical to those used previously in this chapter and are held fixed over the  $\delta_{\perp}$  scan. The range of  $\delta_{\perp}$  chosen encompasses the range of observed L-mode filament widths on MAST [79], though it is worth noting that filaments on MAST have been observed with anisotropic cross-sections. This anisotropy is not considered here where filaments are taken as circular at the midplane. Figure 6.9 shows midplane cross-sections of the filament density and potential taken at  $38\mu\text{s}$  into the filament evolution with increasing  $\delta_{\perp}$ . It is immediately apparent from figure 6.9 that the symmetry breaking of the filament potential and density induced by 3D effects increases in prominence as the filament width decreases. In the  $\delta_{\perp} = 2\text{cm}$  case the filament already exhibits the initial transition into drift-wave turbulence. By contrast the  $\delta_{\perp} = 8\text{cm}$  filament shows predominantly interchange motion with only a slight component of motion in the bi-normal direction present. In figure 6.10 this is investigated further by analysing the evolution of the odd and even components of  $\phi$  over the  $\delta_{\perp}$  scan.




---

FIGURE 6.9: Midplane cross-sections of filament density (color) and potential (contours) over the range of the  $\delta_{\perp}$  scan samples at  $t = 38\mu\text{s}$ . An increase in the symmetry breaking induced by 3D effects is observed as the filament size reduces.

Both the peak and initial growth rate of the even component of potential, shown in figure 6.10, are reduced with respect to the odd component as the filament width increases. The scaling of the even component of potential arising from the Boltzmann response is independent of  $\delta_{\perp}$ , whilst the odd component of potential grows with  $\delta_{\perp}$  in the RB regime. This means that the relative strength of the even component compared to the odd component increases as filament width decreases, as shown in figure 6.10. As in the previous section, the centre of mass velocity of the filament cross-section can be used to compare the motion of the filament between simulations. Figure 6.11 shows that evolution of the normal and bi-normal velocities over the scan in filament width. Figure 6.11 shows an interesting trend with  $\delta_{\perp}$ . The maximal velocity in the normal direction reduces weakly with increasing  $\delta_{\perp}$ , in disagreement with the predicted scaling of  $\delta_{\perp}^{1/2}$  in the resistive ballooning regime though the deceleration slows in the larger

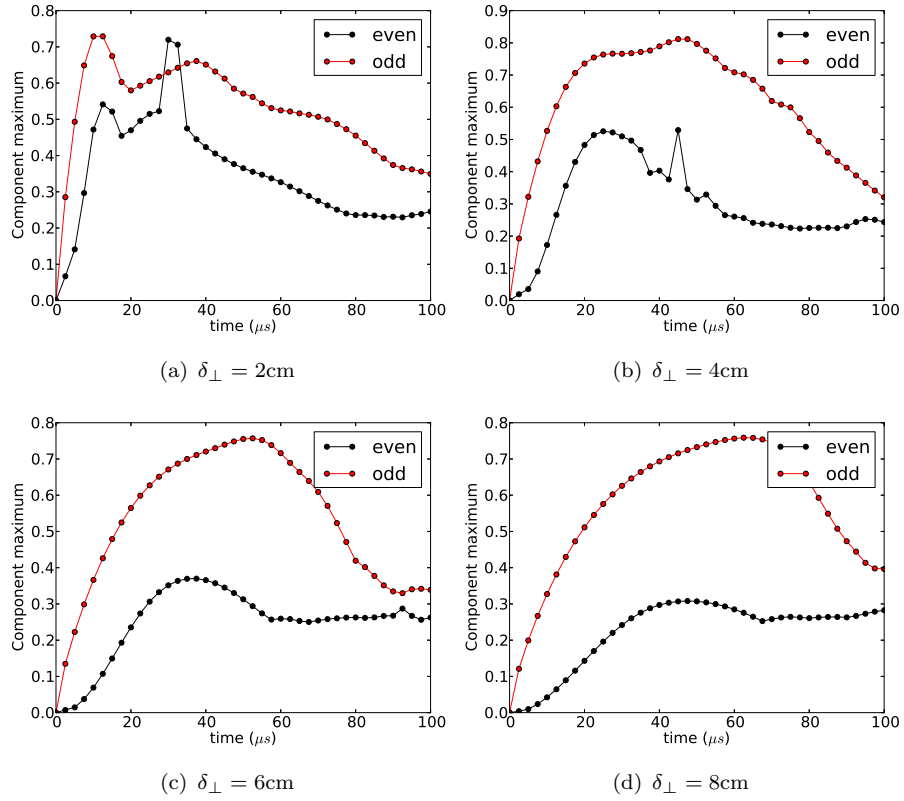


FIGURE 6.10: Evolution of the even (black) and odd (red) components of the potential compared over the  $\delta_{\perp}$  scan. The components are normalized to the absolute maximum of the total potential in each case. The relative strength of the even component is greatest as  $\delta_{\perp}$  reduces.

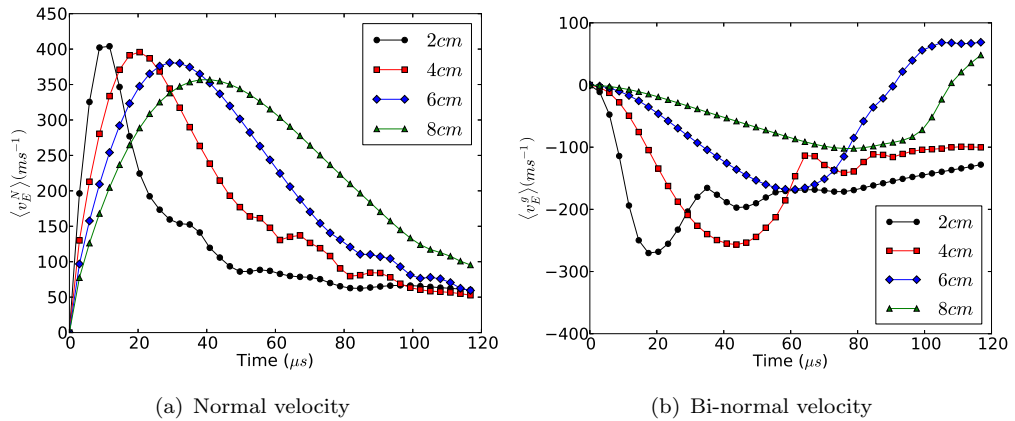


FIGURE 6.11: Evolution of the averaged filament velocity in the normal (left) and bi-normal (right) directions over the scan in the filament width,  $\delta_{\perp}$ .

filaments. Again the balance between the change in the maximum velocity and rate of deceleration affect the displacement of the filament centre of mass. Figure 6.12 shows the displacement of the filament centre of mass in the normal and bi-normal directions over the scan in  $\delta_{\perp}$ . Once again integration is carried out over the  $120\mu s$  of the simulation in each case.

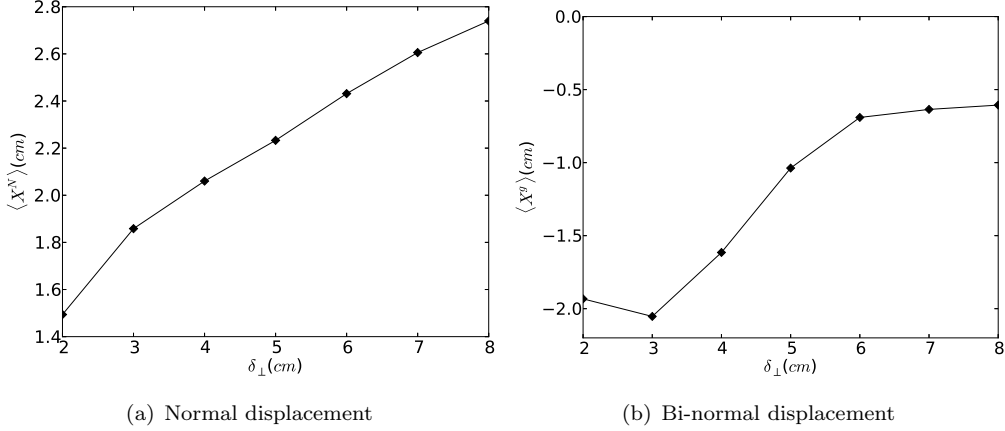


FIGURE 6.12: Average displacement in the normal (left) and bi-normal (right) directions over the scan of  $\delta_{\perp}$ .

Figure 6.12 shows that, despite the slight reduction in the maximal normal velocity of the filament, the average displacement in the normal direction still increases with  $\delta_{\perp}$  as a result of the decreasing deceleration in the larger filaments. The characteristic velocity of the filament is a loosely defined quantity and, if instead of the peak velocity, the average velocity of the filament is considered then the scaling of the velocity inherits the scaling of the centre of mass displacement. In figure 6.13 the displacement in the normal direction is shown as a function of  $\delta_{\perp}^{1/2}$ . The displacement in the normal direction is captured by the resistive ballooning scaling of  $\delta_{\perp}^{1/2}$  which re-enforces the assertion that the scaling of the perpendicular dynamics of the filament can be described by the resistive ballooning scaling in the normal direction. In the bi-normal direction the behaviour is more complicated. Both the maximum speed and the displacement of the centre of mass exhibit an inverse scaling with  $\delta_{\perp}$  as predicted by the Boltzmann response scaling, however the specific scaling of  $\delta_{\perp}^{-1}$  does not appear to capture the observed trends. This may indicate that the dynamics of filaments in the bi-normal direction as  $\delta_{\perp}$  is varied, whilst being governed strongly by the effects of the Boltzmann response, cannot be accurately captured by the scaling arguments outlined in section 6.2. This is not surprising since the dynamics in the binormal direction involve a transition into a turbulence state with complex dynamics.

As with the scan in electron temperature, the particle transport normal to the flux surface at the midplane resulting from the filament motion can be investigated in more

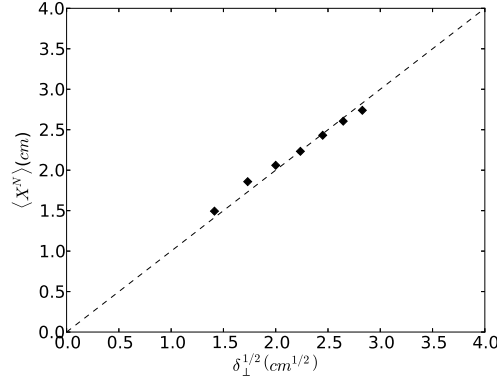


FIGURE 6.13: Average filament displacement in the normal direction as a function of  $\delta_{\perp}^{1/2}$ . The displacement shows strong agreement with the resistive ballooning scaling, suggesting that in the  $\delta_{\perp}$  scan the average velocity (calculated by dividing the displacement by the total time,  $\sim 120\mu s$ ) is a better representation of the characteristic velocity.

detail by calculating the instantaneous particle flux of an individual filament,  $\Gamma^N$ , at each radial location at the midplane. Figure 6.14 shows the radial profile of the instantaneous particle flux as the filaments evolve over the  $\delta_{\perp}$  scan. As opposed to the case of the scan in electron temperature, the largest particle fluxes are now observed when the effects of the Boltzmann source are weakest, at large  $\delta_{\perp}$ . This is a consequence of the larger filaments containing more particles and exhibiting a greater average displacement. Again in analogy to the scan in electron temperature, the instantaneous particle flux at each radial location can be integrated in time to give a measure of the total number of particles passing through each radial location during the evolution of the filament. This is shown in figure 6.15. As expected the larger filaments provide a far stronger source of particle transport than the smaller filaments. This suggests that filament size is likely to play a crucial role in determining particle transport due to filament motion in the SOL of MAST. Furthermore the relative increase in the number of particles transported a significant distance from the initial position of the filament is much larger in the  $\delta_{\perp}$  scan than in the  $T_e$  scan. This suggests that the filament width is far more critical than the electron temperature in determining the contribution of particle transport into the far SOL due to filament motion. Since the filament width is set by the mechanism producing the filament, and not by the filament itself, this suggests that to accurately predict the non-diffusive transport of particles into the SOL of MAST the distribution of filament sizes must be predicted and the underlying turbulence in the MAST plasma edge should be considered. This may show that the filament width depends on  $T_e$ . The results presented here then suggest that any change in transport is due to a change in the electron temperature indirectly, through the varying filament width, rather than directly.

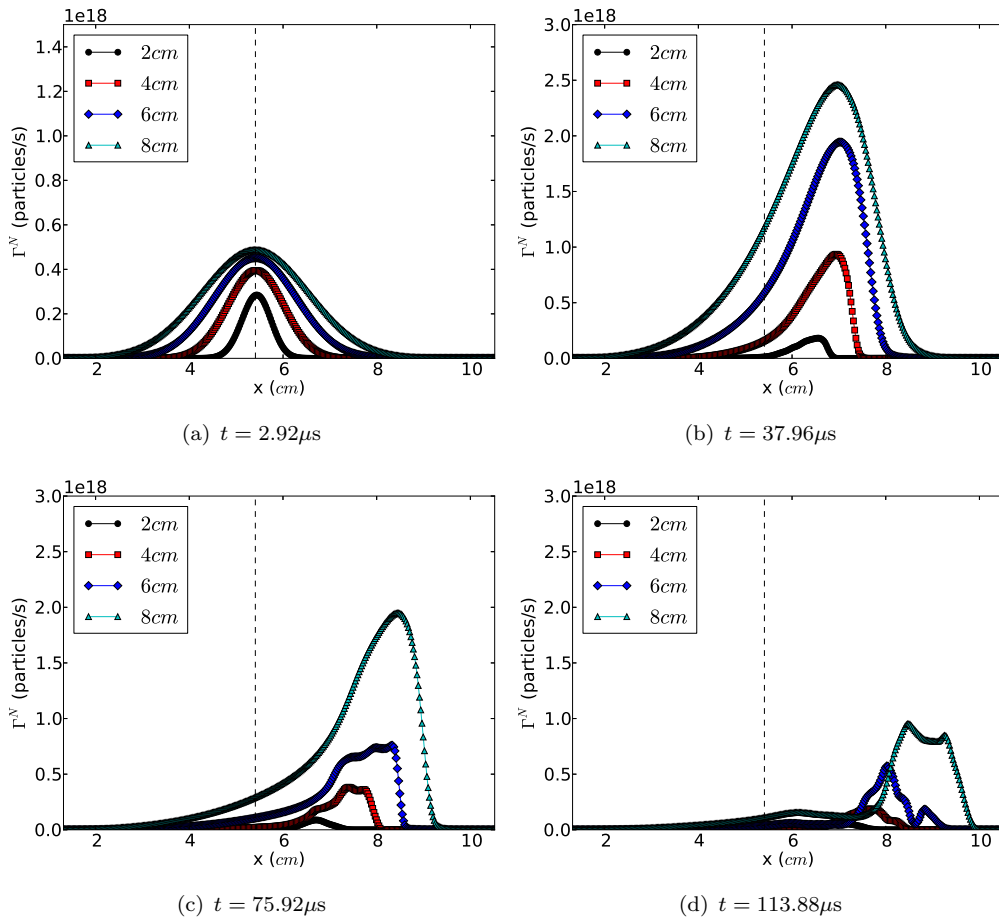


FIGURE 6.14: Instantaneous particle flux,  $\Gamma^N$  across a thin toroidal (1cm width) band at each radial location during the evolution of filaments over the  $\delta_{\perp}$  scan. Note the change in magnitude of the vertical axis. The dashed line indicates the initial position of the filament centre.

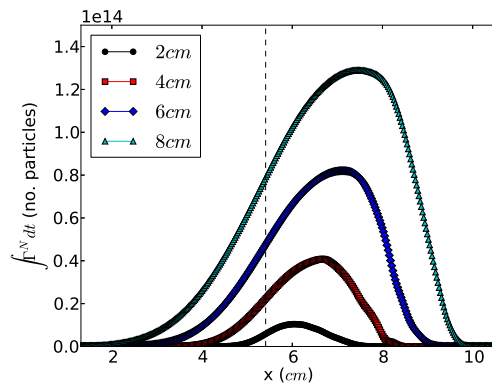


FIGURE 6.15: Integrated particle flux at each radial location over the lifetime of a filament over the  $\delta_{\perp}$  scan.

## 6.6 Discussion

The results presented in this chapter suggest that the velocity in the direction normal to the flux surface of filaments in a MAST-like geometry can be well described numerically by the resistive ballooning/ideal-interchange scaling of

$$v_N \propto T_e^{1/2} \delta_\perp^{1/2} \quad (6.26)$$

The two-region model [54] is a 2D model which attempts to capture some of the effects of magnetic geometry. As described in section 6.2 the two-region model has four possible dynamical regimes that a filament may be subject to. These can be described by two dimensionless parameters,  $\Lambda$  and  $\Omega$  where

$$\Lambda = \frac{L_\parallel}{c_s \tau_{ei}} \frac{\Omega_e}{\Omega_i} \quad (6.27)$$

and

$$\Omega = \left( \frac{\delta_\perp}{\delta^*} \right)^{5/2} \quad (6.28)$$

where  $\delta^*$  is the 'fundamental blob size' [55, 94, 95] which is the radius of a filament at which the effects of sheath dissipation and inertial dissipation are equal. This can be paraphrased as the point at which the resistive ballooning and sheath limited velocities are equal, which gives (from section 6.2)

$$c_s \sqrt{2 |\boldsymbol{\xi}| \delta^*} \sim \frac{2c_s \rho_s^2 |\boldsymbol{\xi}| L_\parallel}{\delta^{*,2}} \Rightarrow \delta^* = \left( 2\rho_s^4 L_\parallel^2 |\boldsymbol{\xi}| \right)^{1/5} \quad (6.29)$$

$\Lambda$  represents a dimensionless collisionality whilst  $\Omega$  describes the effects of increasing filament radius. Both the scan in  $T_e$  and in  $\delta_\perp$  carried out in this chapter have specific trajectories in  $\Omega, \Lambda$  space which can be readily calculated. These trajectories are shown in figure 6.16. To calculate  $\Lambda$  and  $\Omega$  the filament width cited previously in this chapter (which refers specifically to the bi-normal width between the two points across the filament where the density is 1% above the background) has been converted to the radius given by the full-width half-maximum of the filament density. The conversion is approximately a multiplication by a factor 3/8. The magnetic field is taken as 0.45T which is the maximum of  $B$  in the flux-tube. Figure 6.16 shows clear disagreement between the simulations conducted in the MAST SOL flux tube geometry and the two-region model in both the  $T_e$  and the  $\delta_\perp$  scan. Examining each scan independently, the main areas of disagreement are:

- $T_e$  scan: The two-region model predicts a trajectory in  $\Omega, \Lambda$  space that intersects all four dynamic regimes. The simulation results, particularly those presented in

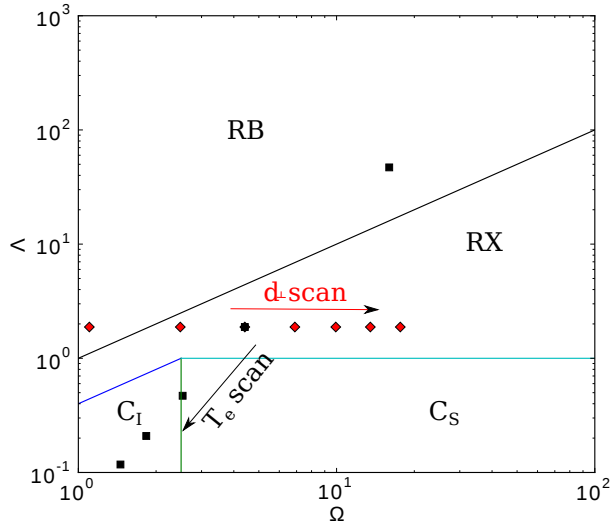


FIGURE 6.16: Trajectories of the  $T_e$  (black squares) and  $\delta_{\perp}$  (red diamonds) scan in  $\Omega, \Lambda$  space. Arrows indicate the direction of increasing  $T_e$  and  $\delta_{\perp}$  respectively. The regime boundaries of the two-region model are calculated from [54].

figures 6.3 and 6.4, show a clear scaling of  $T_e^{1/2}$  throughout the scan. This is in agreement with the RB and  $C_I$  regimes, but is a weaker scaling than predicted in the  $C_S$  regime and is opposite to the scaling expected in the RX regime. At 5eV the two-region model predicts the filament to be in the RX regime where a decrease ( $\propto T_e^{-1/2}$ ) in the filament velocity, rather than the observed increase is expected. Furthermore in the two-region model the RB velocity is the maximum attainable, therefore the 1eV filament may be expected to be faster than all others, which is in complete opposition to the observed results.

- $\delta_{\perp}$  scan: The two-region model predicts a trajectory in the  $\Omega, \Lambda$  space which is almost entirely encompassed in the RX regime. In this regime a scaling of  $\delta_{\perp}^{-2}$  is predicted for the filament velocity which should lead to a strong decrease as the filament width is increased. The results in figure 6.11 do show a reduction in peak velocity as  $\delta_{\perp}$  increases, however the reduction is very weak, and certainly much weaker than predicted by the two-region model. Furthermore the average velocity of the filament, over its evolution, shows an increase with  $\delta_{\perp}$  of approximately  $\delta_{\perp}^{1/2}$  as indicated in figure 6.13. This is suggestive of the RB or  $C_I$  regimes and is in complete disagreement with the predictions of the two-region model.

The most obvious difference between the two-region model and the simulations conducted in this chapter is the inclusion of 3D effects however this has been addressed by the separation between odd and even components of the vorticity equation suggests that 2D scalings should still apply to the motion of the filament normal to the flux surface.

A more subtle difference occurs in the way in which the effects of magnetic geometry, and in particular magnetic curvature drive are included in the two-region model. In the two-region model only magnetic curvature at the midplane is considered with author citing [54] that magnetic curvature in the divertor region is small and negligible. This can become important when the sheath-limited velocity is derived which requires an integration along the magnetic field line. The sheath-limited velocity is derived by taking

$$2c_s\rho_s \int_0^{L_{\parallel}} \boldsymbol{\xi} \cdot \nabla n dL \sim J_{\parallel}^{sh}/e \sim nc_s\phi \quad (6.30)$$

where  $J_{\parallel}^{sh} \sim nec_s\phi$  is the sheath current. In the two-region model (as well as other 2D models)  $\boldsymbol{\xi} \cdot \nabla n$  is assumed constant along the magnetic field line, fixed at the midplane value, however it has been shown in chapter 5 that both the curvature and the  $\nabla$  operator vary considerably along the magnetic field line. Furthermore when balancing the curvature drive against sheath dissipation both the normal and bi-normal components of curvature need to be considered. The transformation of the filament cross-section in the divertor region can lead to a large enhancement of the curvature drive which leads to a much larger curvature induced diamagnetic current for sheath currents to balance. To estimate this enhancement, parallel density gradients can be assumed to be weak and the gradients in the normal and bi-normal direction can be approximated as  $\nabla \sim 1/\delta_{\perp}$ . As a consequence the integrated curvature drive can be approximated by

$$\begin{aligned} 2c_s\rho_s \int_0^{L_{\parallel}} \boldsymbol{\xi} \cdot \nabla n dL &= 2c_s\rho_s \nabla^u n \cdot \int_0^{L_{\parallel}} \boldsymbol{\xi} \mathcal{M} dL \approx 2c_s\rho_s n \begin{pmatrix} 1/\delta_{\perp} \\ 1/\delta_{\perp} \end{pmatrix} \cdot \int_0^{L_{\parallel}} \mathcal{M} \boldsymbol{\xi} dL \quad (6.31) \\ &= \frac{2c_s\rho_s n}{\delta_{\perp}} L_{eff} \end{aligned}$$

where  $\mathcal{M}$  is the transformation matrix acting on the  $\nabla$  operator as a result of the magnetic geometry.  $\mathcal{M}$  is derived in section 5.3 of chapter 5. In the calculation of the sheath-limited velocity and the corresponding calculation of the fundamental blob size,  $L_{\parallel} |\boldsymbol{\xi}|$  can be replaced by  $L_{eff}$  to include the effects of enhanced curvature driven current. Making this replacement in the two-region model can then be used to produce corrected trajectories in  $\Omega, \Lambda$  space. Figure 6.17 shows the calculation of  $L_{eff}$  in the MAST SOL flux tube as a function of distance along the magnetic field line, alongside a corrected  $\Omega, \Lambda$  parameter space. Making this correction for the enhanced curvature driven current brings the predictions of the (corrected) two-region model into agreement with the simulation results. Both cases now predict that the RB scaling should be most appropriate for the filament velocity. This suggests that the two-region model can capture the salient features of the full magnetic geometry case, however to accurately predict the full 3D case requires accounting for the enhancement of the curvature driven current due to the transformation of the filament cross-section induced by the magnetic

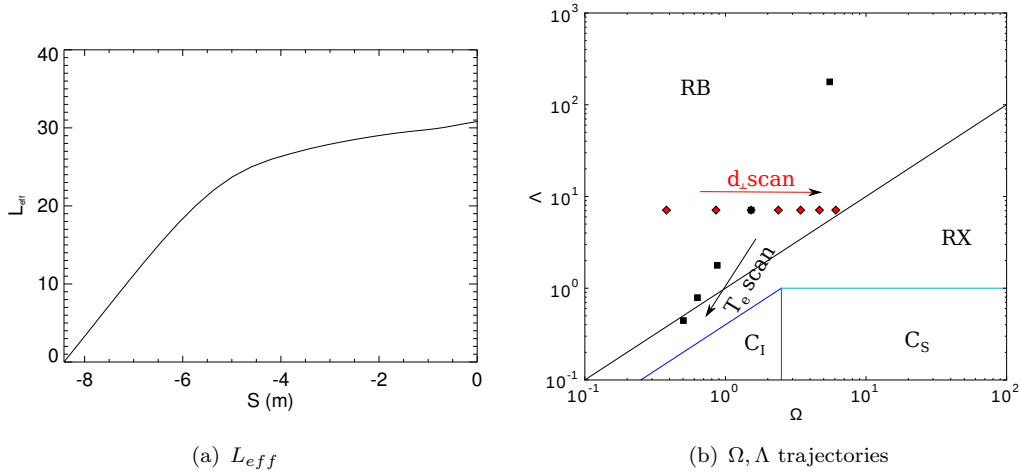


FIGURE 6.17: Left: Calculation of  $L_{eff}$  for the MAST flux tube where  $S = 0$  is the midplane and the integration is taken from the divertor plate to the midplane. Right: Corrected trajectories in  $\Omega, \Lambda$  space which includes the effects of enhanced curvature driven currents in the filament in the divertor region.

geometry.

One important consequence of these results is that no transition is predicted in the dynamics of filaments in MAST as the collisionality is increased. This is opposed to the case reported by Carallero *et.al* [58, 59] in ASDEX-Upgrade where a transition between the  $C_S$  and RX regimes is proposed as a cause for the observed sharp increase in density transport as collisionality increases. The MAST and ASDEX-Upgrade tokamaks have comparable major radii ( $\sim 1.5\text{m}$  and  $\sim 2\text{m}$  respectively), however they have very different magnetic field strengths ( $\sim 0.4\text{T}$  compared to  $\sim 2\text{T}$  in the SOL). This increase in magnetic field causes a decrease in the curvature drive and a corresponding decrease in the fundamental blob size which suggests that low collisionality filaments of comparable size will tend towards the  $C_S$  regime in ASDEX-Upgrade. A good test of the theory of filament dynamics would be the exploration of filament dynamics over a collisionality scan in MAST. This also has implications for MAST-Upgrade. The geometry of MAST and MAST-Upgrade is largely similar at the midplane with the exception of the magnetic field strength, which is roughly twice the size in MAST-Upgrade compared to MAST. This has the effect of shifting the points in figure 6.17 to the right. In larger filaments this may lead to a transition into the RX regime which may reduce the density transport into the far SOL due to filament motion and cause a narrowing of the density SOL. To accurately assess this effect requires dedicated simulations and is a good topic for future work.

## 6.7 Summary

In this chapter the scaling of the velocity of filaments at the midplane has been investigated in the MAST SOL flux tube geometry used in chapter 5 and described in chapter 4. Through the decoupling of the vorticity equation into odd and even components (in the bi-normal direction with respect to the central axis of the filament at initialization) the range of possible velocity scalings for the normal and bi-normal centre of mass velocities of the filament cross-section are derived. Simulation scans have been carried out in both electron temperature  $T_e$ , and filament cross-sectional width,  $\delta_\perp$  and the centre of mass velocity of the filament has been tested against the various possible scalings. The bi-normal velocity is well described by a velocity scaling arising from the Boltzmann response, whilst the normal velocity is well described by a resistive ballooning scaling. The displacement of the filament in the bi-normal direction can greatly exceed the displacement in the normal direction to the point where the isolated filament assumption becomes questionable. Multi-filament simulations would be a good topic for future work. The velocity scaling in the normal direction is compared to the two-region model and a correction accounting for enhanced curvature driven current in the divertor is required to obtain agreement between the simulations and the model. Nevertheless 2D models are shown to capture approximately the filament velocity normal to the flux surface, with 3D effects acting to induce bi-normal motion without strongly augmenting the radial motion of the filament.

A detailed analysis of the transport of particles within the filament shows that the breakdown into turbulence induced by 3D effects as  $T_e$  increases provides a slight enhancement to density transport normal to the flux surface, however the enhancement is weak. A much stronger increase in density transport is observed with filament size as a coupled result of an increased filament velocity and an increased number of particles within the filament. This suggests that, for MAST, the filament size is likely to have a much stronger effect on the radial transport of particles than the collisionality. This may be a good topic for experimental investigation in the future.



## Chapter 7

# Conclusions and Future Work

### 7.1 Conclusions

Transport in the periphery of magnetically confined plasmas is poorly understood. This is largely due to the highly non-linear nature of turbulence in the plasma edge and the subsequent intermittent ejection of mesoscale plasma structures known as filaments into the scrape-off layer. Filaments provide a strong non-local component of density transport into the SOL [180] and can cause anomalous interaction with first wall materials [56] which may threaten their lifetime in future high powered fusion devices [60] and can affect fuelling efficiency. Understanding the intermittent transport of density due to filaments is therefore an important step towards accurate predictions of transport in the plasma edge and next-step tokamak operation. This thesis investigates such transport both experimentally and theoretically with an emphasis on the Mega Amp Spherical Tokamak (MAST).

Probe diagnostics are commonly used to measure both profiles and fluctuations in the plasma edge. Previous probe measurements on JET [68] and ASDEX Upgrade[76] have indicated a qualitative connection between the generation of intermittency in ion saturation current time-series and the radial shear layer, a region around the last closed flux surface containing a strong radial gradient of the perpendicular plasma flow. This provided motivation for the development of a ball pen probe (see chapter 3) on MAST. The ball pen probe (BPP) [136] is capable of measuring the plasma potential by shielding the collector from plasma flux along the magnetic field line. This then requires cross-field transport to the collector which is predominantly due to  $\mathbf{E} \times \mathbf{B}$  motion, preventing the formation of a sheath and thus allowing the probe to be charged up by the plasma potential rather than the sheath formation. By combining the BPP measurement with a measurement of floating potential the probe can also measure the electron temperature

profile. This measurement was compared in detail to the Thomson scattering diagnostic and good agreement was found. In attaining this agreement the effects of secondary electron emission on the Langmuir probe (LP) measurement of the floating potential were shown to be important, which suggests that similar accounting of these effects should be taken in future LP measurements at the MAST midplane. By directly measuring the profile of the plasma potential the radial electric field could be extracted and was shown to contain the structure of the radial shear-layer. A third Langmuir probe on the probe head was used to measure fluctuations in  $I_{sat}$  from which profiles of the moments of the fluctuation PDFs were extracted. Since all of these measurements were made locally to the probe head, the profiles of the radial electric field could be directly compared to the PDF moments. In particular a strong correlation between the radial electric field gradient and the skewness of the  $I_{sat}$  PDF was observed; the skewness dropped to 0 and reversed as the electric field gradient reached a maximum. This shows quantitatively for the first time that the production of intermittency, inferred by the skewness in the PDF, is strongly coupled to the shear of the perpendicular flow, inferred through the radial electric field. It is noted that the causality of this relationship cannot be readily extracted from the data, however this observation opens an avenue for further research into the interaction between sheared flows and filament production by probe diagnostics.

As discussed in the discussion section of chapter 2 modelling the full problem of intermittent transport requires understanding a multitude of physics aspects and is generally too large a problem to tackle head on. Fortunately the problem can be approximately decoupled into the modelling of filament production and the modelling of filament motion. Whilst both of these areas are complex in their own right, they present less formidable challenges than the fully coupled problem. In chapters 5 and 6 the latter of these two modelling paradigms was adopted and the dynamics of isolated filaments in the SOL of MAST was investigated numerically using the BOUT++ framework [104]. By developing a grid generator within BOUT++ the geometry of a flux-tube centred around a magnetic field line in the SOL of MAST was used to investigate the dynamics of filaments in a realistic magnetic geometry. The inclusion of the magnetic geometry was shown to lead naturally to the formation of density gradients parallel to the magnetic field line for two reasons: 1. The local drive for potential polarisation in the filament varied along the magnetic field line leading to ballooning of the filament around the midplane and 2. Enhanced diffusion of density in the divertor region. Both of these effects are results of the transformation of the filament cross-section as a result of flux expansion and magnetic shear. This produces large cross-field gradients in the strongly sheared divertor region which suppresses polarisation due to an enhancement of the polarisation drift and naturally enhances dissipation of density and vorticity. The presence of parallel gradients necessitates the inclusion of 3D effects. At low temperatures these

3D effects have a limited role with the dynamics of the filament largely determined by mechanisms present in 2D theories. By contrast, raising the temperature of the filament and thereby decreasing the resistivity, increases the prevalence of 3D effects and can cause a drastic departure of the filament dynamics from 2D predictions. The general cause of this departure is the presence of a source driving the growth of an even (vertically about the centre of the filament cross-section) component of the potential. This source is not present in 2D models and thus 2D models are constrained to potential profiles with an odd parity. The presence of a significant even component of potential leads initially to a rotation of the potential dipole which induces filament motion in the bi-normal direction and may explain the poloidal motion of filaments often observed in experiment. The structure of the potential then exhibits a transfer from large length scales to smaller length scales towards a state of non-linear drift-wave turbulence. The extent of this cascade is limited by the level of dissipation in the system as determined by a scan in dimensionless diffusivity and viscosity. In contrast to [116] when 3D effects are strong the linear resistive drift-wave instability is not observed, instead non-linear resistive drift-wave turbulence augments the filament motion. In [116] the linear instability must grow from transient perturbations, whilst in the case of realistic geometry there is a natural source of parallel gradients which provides the non-linear drive.

In the divertor region the motion of the filament is strongly suppressed as a result of the excessive shearing due to the magnetic geometry. In this region a dissipation scan reveals that when dissipation is high the filament quickly disperses due to large cross-field gradients as a result of the shearing transformation. If dissipation is low however strong drift-wave instabilities can set in along the major axis of the filament which are otherwise stabilised, but again act to disperse the filament. It therefore appears that filaments in the divertor are naturally dispersive. These results also suggest that regardless of the level of dissipation in the system the large scale dynamics of the filament is unchanged, even if the specific details of the evolution may vary.

In order to more quantitatively compare the simulations conducted in the MAST SOL flux-tube geometry with 2D theories, in particular the two-region model [54], the scaling of the filament velocity at the midplane with electron temperature and filament cross-section was investigated. The scaling of both the peak and average (inferred through net filament displacement) radial velocity of the filaments were suggestive of the resistive ballooning or ideal interchange regimes of filament dynamics. Interestingly this suggests that 3D effects, whilst drastically altering the dynamics of the filaments, did not directly affect the net radial motion of the filament. This supports the notion that the odd and even components of the potential can be decoupled, with the odd components responsible for the radial motion and the even components responsible for the generation of poloidal motion. This is further evidenced by the scaling of the poloidal velocity, which is found to be well predicted by a simple scaling based on the Boltzmann response. This

shows that smaller, hotter filaments which are more subject to 3D effects should also exhibit faster poloidal motion. Comparisons of the observed scalings with the two-region model show disagreement, with the two region model predicting weaker and even opposed scalings to those observed numerically. Agreement is observed between the two if the parallel connection length in the two region model is artificially enhanced. This may be justified by the fact that the two-region model neglects drive for diamagnetic currents in the divertor region, where in fact the drive is rather strong due to the enhancement of cross-field density gradients by the magnetic geometry. This provides a larger current for sheath currents to close and effectively decreases the effectiveness of the sheath-current closure in the two-region model, which can be expressed as an effective increase of the parallel connection length.

Finally the transport of particles at the midplane due to the motion of a single filament was investigated across both the temperature and filament size scans. Whilst the electron temperature leads to an increase in the filament velocity the net transport of density remained relatively similar across the scan. This shows that 3D effects do not hinder the transport of density. In fact, by comparing two likewise simulations but with the 3D drive terms removed from one, it was possible to show that the presence of resistive drift-wave turbulence provided a slight increase in the net transport of density. This increase was small however and unlikely to be detectable experimentally. By contrast, the filament width was shown to strongly affect the net transport of density. This might be expected since a larger filament can hold more particles, however the increased radial motion of larger filaments acts to further enhance the transport of density. This observation suggests that filament width is the primary parameter in MAST determining the intermittent transport of density, and any changes in this transport due to variation in plasma parameters are likely to be through a change in the width distribution of emitted filaments, rather than a change in the dynamics of the filaments themselves.

## 7.2 Future Work

The ball pen probe diagnostic will be available in its current form for operation on MAST-Upgrade when it comes online in 2016 and 2017. A natural progression of the work presented in chapter 3 is to conduct systematic studies of the scaling of both  $\lambda_{T_e}$ , the electron temperature gradient scale length, and  $\partial E/\partial R$ , the radial electric field gradient, with variation of equilibrium plasma parameters. Both of these quantities are difficult to measure accurately in the plasma edge, however the BPP can make these measurements routinely. A study of  $\lambda_{T_e}$  will provide insight into the control of power deposition in the SOL which is a particularly important topic concerning future high power fusion devices. The scaling of the radial electric field and, particularly, its

gradient may provide important insight into filament generation processes (as shown in chapter 3) and the transition to higher confinement. A modified design of a BPP is presented in chapter 3 which would allow the BPP to make detailed measurements of potential, temperature, density and electric fields within individual fluctuations. This would allow for the experimental characterisation of turbulence and potentially aid in the understanding of edge plasma transport.

The work on filament dynamics could be extended in two directions: 1. Relaxation of the flux-tube approximation in the geometry of the system and 2. Inclusion of extra physics in the governing equations. The relaxation of the flux-tube geometry would allow for the investigation of effects such as sheath reconnection in the far SOL [110] where the shearing of the filament lessens and allows for easier connection to the sheath. By extending the methods employed in the flux-tube generator described in chapter 4 to work on several adjacent flux surfaces spanning the domain of interest in the SOL and interpolating between these surfaces, this approximation could be bypassed, however the non-orthogonality of the resulting mesh (in the poloidal plane) must then be accounted for in the metric tensor of the system. Such an approach is currently being investigated by Jarrod Leddy at the York Plasma Institute.

At present the model used for filament motion neglects the effects of warm ions, non-isothermal effects and electromagnetic effects. The latter of these three effects will soon be investigated by Dr Fulvio Militello of CCFE in the case of a simple slab geometry, with a view to understanding the basic physical processes involved and eventually porting the model into the more complex geometry of the SOL. The former of these two effects will be investigated during the authors fellowship at CCFE to commence in November 2014.



# Appendix A

## The BOUT++ Coordinate System

### A.1 Differential Geometry Primer

This appendix provides an overview of the ballooning coordinate system used in BOUT++ and within this thesis to simulate filaments. Before introducing this coordinate system however a brief primer on differential geometry is provided which is based largely on [208].

For a general curvilinear coordinate system given by the coordinates  $(u^1, u^2, u^3)$  a set of basis vectors can be constructed which lie tangent to the coordinate axis. These are called the *tangent* or *covariant* basis vectors and are given by

$$\mathbf{e}_i \equiv \frac{\partial \mathbf{R}}{\partial u^i} \quad (\text{A.1})$$

where  $\mathbf{R}(x, y, z)$  is the position vector in cartesian space. The covariant vectors are a triplet of linearly independent vectors with a common origin making them suitable as a basis for the coordinate system. An equally suitable basis however can be obtained by instead taking the vectors normal to the surfaces generated by the coordinate axis. These are called the *contravariant* or *reciprocal* basis vectors and are given by

$$\mathbf{e}^i \equiv \frac{\partial u^i}{\partial \mathbf{R}} = \nabla u^i \quad (\text{A.2})$$

These two basis sets are reciprocal to one another, which means that  $\mathbf{e}_i \cdot \mathbf{e}^j = \delta_i^j$  where  $\delta_i^j$  is the Kronecker delta function. This is clearly true for the covariant and contravariant basis vectors since

$$\mathbf{e}_i \cdot \mathbf{e}^j = \frac{\partial \mathbf{R}}{\partial u^i} \cdot \nabla u^j = \frac{\partial \mathbf{R}}{\partial u^i} \cdot \frac{\partial u^j}{\partial \mathbf{R}} = \frac{\partial u^j}{\partial u^i} = \delta_i^j \quad (\text{A.3})$$

which relies on the fact that the coordinates  $u^i$  and  $u^j$  must be independent of one another to form a proper coordinate system. The reciprocal nature of the two basis sets implies that (see [208] for a derivation) the vectors of one basis can be generated by the vectors from the other by

$$\mathbf{e}^i = \frac{\mathbf{e}_j \times \mathbf{e}_k}{\mathbf{e}_i \cdot (\mathbf{e}_j \times \mathbf{e}_k)}; \mathbf{e}_i = \frac{\mathbf{e}^j \times \mathbf{e}^k}{\mathbf{e}^i \cdot (\mathbf{e}^j \times \mathbf{e}^k)} \quad (\text{A.4})$$

The denominator here is called the *Jacobian*  $J$  such that  $J = \mathbf{e}_i \cdot (\mathbf{e}_j \times \mathbf{e}_k) = [\mathbf{e}^i \cdot (\mathbf{e}^j \times \mathbf{e}^k)]^{-1}$ . In cartesian coordinates the contravariant and covariant basis vectors are identical and the system is orthogonal, however this is not the general case. This is illustrated in figure A.1.

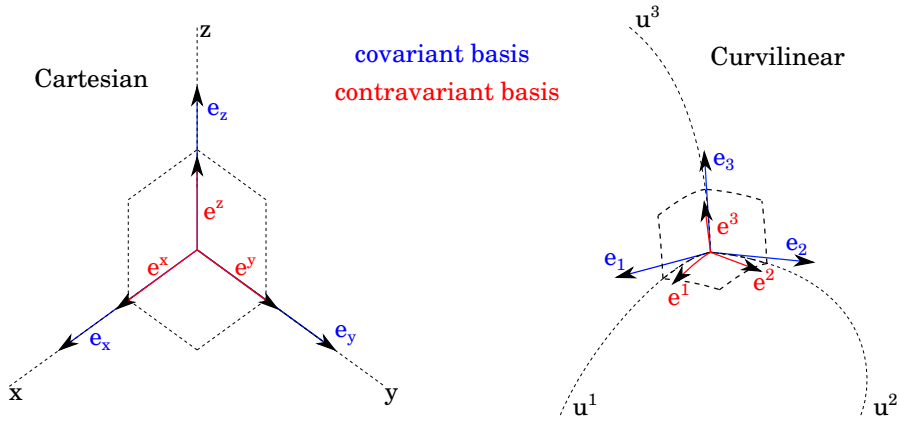


FIGURE A.1: Schematic illustration of co and contravariant basis vectors in cartesian and general curvilinear coordinates. The size of the covariant basis vectors has been exaggerated to allow the two basis sets to be distinguished in the cartesian case.

Since both the covariant and the contravariant vectors form basis sets a general vector  $\mathbf{D}$  can be written

$$\mathbf{D} = A\mathbf{e}_i + B\mathbf{e}_j + C\mathbf{e}_k = E\mathbf{e}^i + F\mathbf{e}^j + G\mathbf{e}^k \quad (\text{A.5})$$

By either dotting the above expression with  $\mathbf{e}^i$  to get  $A$  and  $\mathbf{e}_i$  to get  $E$ , the form of the coefficients can be found to be

$$\begin{aligned} A &= \mathbf{D} \cdot \mathbf{e}^i = E\mathbf{e}^i \cdot \mathbf{e}^i + F\mathbf{e}^j \cdot \mathbf{e}^i + G\mathbf{e}^k \cdot \mathbf{e}^i \\ &= (\mathbf{D} \cdot \mathbf{e}_i) \mathbf{e}^i \cdot \mathbf{e}^i + (\mathbf{D} \cdot \mathbf{e}_j) \mathbf{e}^i \cdot \mathbf{e}^j + (\mathbf{D} \cdot \mathbf{e}_k) \mathbf{e}^i \cdot \mathbf{e}^k \end{aligned} \quad (\text{A.6})$$

with the equivalent expression achieved by swapping the indices from super to sub scripts and visa versa. The terms  $\mathbf{D} \cdot \mathbf{e}^{i,j,k} \equiv D^{i,j,k}$  are the *contravariant components* of the vector  $\mathbf{D}$ , whilst the  $\mathbf{D} \cdot \mathbf{e}_{i,j,k} \equiv D_{i,j,k}$  are the *covariant components*. The two are related to each other through the *metric coefficients*. The contravariant metric components are  $\mathbf{e}^i \cdot \mathbf{e}^j \equiv g^{ij}$  whilst the covariant metric components are  $\mathbf{e}_i \cdot \mathbf{e}_j \equiv g_{ij}$ . The covariant and

contravariant components of a vector are related to each other (as can be seen from the expression above) by  $D_i = D^j g_{ij}$  and conversely  $D^i = D_j g^{ij}$  where a sum over repeated indices is implied. The same arguments can be applied to the basis vectors themselves to show that

$$\mathbf{e}_i = g_{ii} \mathbf{e}^i + g_{ij} \mathbf{e}^j + g_{ik} \mathbf{e}^k \quad (\text{A.7})$$

and

$$\mathbf{e}^i = g^{ii} \mathbf{e}_i + g^{ij} \mathbf{e}_j + g^{ik} \mathbf{e}_k \quad (\text{A.8})$$

The metric coefficients form a symmetric metric tensor which can be written

$$g^{ij} \equiv \mathbf{e}^i \cdot \mathbf{e}^j \equiv \nabla u^i \cdot \nabla u^j = \begin{pmatrix} g^{11} & g^{12} & g^{13} \\ g^{12} & g^{22} & g^{23} \\ g^{13} & g^{23} & g^{33} \end{pmatrix} \quad (\text{A.9})$$

$$g_{ij} \equiv \mathbf{e}_i \cdot \mathbf{e}_j \equiv \frac{\partial \mathbf{R}}{\partial u^i} \cdot \frac{\partial \mathbf{R}}{\partial u^j} = \begin{pmatrix} g_{11} & g_{12} & g_{13} \\ g_{12} & g_{22} & g_{23} \\ g_{13} & g_{23} & g_{33} \end{pmatrix}$$

such that the two sets of basis vectors can be related by

$$\begin{pmatrix} \mathbf{e}_1 \\ \mathbf{e}_2 \\ \mathbf{e}_3 \end{pmatrix} = g_{ij} \begin{pmatrix} \mathbf{e}^1 \\ \mathbf{e}^2 \\ \mathbf{e}^3 \end{pmatrix}; \quad \begin{pmatrix} \mathbf{e}^1 \\ \mathbf{e}^2 \\ \mathbf{e}^3 \end{pmatrix} = g^{ij} \begin{pmatrix} \mathbf{e}_1 \\ \mathbf{e}_2 \\ \mathbf{e}_3 \end{pmatrix} \quad (\text{A.10})$$

which clearly implies that

$$g^{ij} = g_{ij}^{-1} \quad (\text{A.11})$$

hence the covariant and contravariant metric tensors are inverse to one another. By substituting the above expressions for the basis vectors into the definition of the Jacobian  $J$  and after some algebraic manipulation it is possible to show that

$$J^2 = g_{11} (g_{22}g_{33} - g_{23}g_{23}) + g_{12} (g_{13}g_{23} - g_{12}g_{33}) + g_{13} (g_{12}g_{23} - g_{22}g_{23}) \quad (\text{A.12})$$

which is immediately recognisable as the determinant of the tensor  $g_{ij}$  such that the Jacobian can be given by

$$J^2 = \det(g_{ij}) \equiv g \Rightarrow J = \sqrt{g} \quad (\text{A.13})$$

Finally the  $\nabla$  operator can be defined in terms of the contravariant and covariant basis vectors. To do this note that the operation  $\nabla\Theta$  is defined by

$$d\Theta = \nabla\Theta \cdot d\mathbf{R} \quad (\text{A.14})$$

however by use of the chain rule and since  $\mathbf{e}^i \cdot \mathbf{e}_j = \delta_j^i$ ,  $d\Theta$  can equally be given by

$$d\Theta = \frac{\partial\Theta}{\partial u^i} du^i = \frac{\partial\Theta}{\partial u^i} \mathbf{e}^i \cdot \mathbf{e}_j du^j = \left( \frac{\partial\Theta}{\partial u^i} \nabla u^i \right) \cdot \left( \frac{\partial \mathbf{R}}{\partial u^j} du^j \right) \quad (\text{A.15})$$

Once again by the chain rule the second of the bracket terms can be identified as  $d\mathbf{R}$ . Thus by comparing the two equivalent statements of  $d\Theta$

$$d\Theta = \nabla\Theta \cdot d\mathbf{R} = \left( \frac{\partial\Theta}{\partial u^i} \nabla u^i \right) \cdot d\mathbf{R} \Rightarrow \nabla \equiv \nabla u^i \frac{\partial}{\partial u^i} = \mathbf{e}^i \frac{\partial}{\partial u^i} \quad (\text{A.16})$$

from which the other differential operators can be derived.

## A.2 Field Aligned Coordinates in BOUT++

As a starting point for the derivation of the field aligned coordinate system, the poloidal magnetic flux,  $\psi$  can be used to label nested magnetic surfaces with a unique label from the centre of the plasma outwards and is therefore a good coordinate for the system [209].

$$\mathbf{B} \cdot \nabla\psi = 0 \Rightarrow \mathbf{B} = \nabla\psi \times \mathbf{A} \quad (\text{A.17})$$

and the vectors  $\nabla\psi$  and  $\mathbf{A}$  lie perpendicular to the magnetic field at all points. Maxwell's law of a divergence free magnetic field then allows the magnetic field to be written in a Clebsch form [209]

$$\nabla \cdot \mathbf{B} = 0 \Rightarrow \nabla\psi \cdot \nabla \times \mathbf{A} = 0 \Rightarrow \mathbf{A} \equiv \nabla\alpha \quad (\text{A.18})$$

thus the vector  $\mathbf{A}$  can be written in terms of a scalar potential  $\alpha$  and the magnetic field is

$$\mathbf{B} = \nabla\psi \times \nabla\alpha \quad (\text{A.19})$$

This then shows that the scalar quantities  $\psi$  and  $\alpha$  can uniquely label any plane perpendicular to  $\mathbf{B}$  but do not vary along  $\mathbf{B}$ . This then naturally specifies a third coordinate,  $\beta$ , that labels the magnetic field line with the covariant vector  $\mathbf{B} = C\mathbf{e}_\beta = C\partial\mathbf{R}/\partial\beta$ . The proportionality factor  $C$  is given by dotting  $\mathbf{B}$  with the reciprocal vector in  $\beta$ ,  $\nabla\beta$

$$\mathbf{B} \cdot \nabla\beta = C = \nabla\psi \times \nabla\alpha \cdot \nabla\beta = J^{-1} \quad (\text{A.20})$$

where  $J$  is the Jacobian of the  $(\psi, \beta, \alpha)$  coordinate system. For  $(\psi, \beta, \alpha)$  to specify a set of unique coordinates the following must be true

$$\frac{d\psi}{d\beta} = \frac{d\psi}{d\alpha} = \frac{d\beta}{d\psi} = \frac{d\beta}{d\alpha} = \frac{d\alpha}{d\psi} = \frac{d\alpha}{d\beta} = 0 \quad (\text{A.21})$$

The ballooning coordinate system [217] used in BOUT++ employs the poloidal angular coordinate,  $\theta$ , to label the direction along the magnetic field line such that  $\beta = \theta$ . The above expression is then used to force the toroidal angular coordinate,  $\zeta$ , to follow the field line by making the ansatz  $\alpha = \zeta + \gamma$  which then gives

$$\frac{d\alpha}{d\theta} = \frac{d\zeta}{d\theta} + \frac{d\gamma}{d\theta} = 0 \Rightarrow \gamma(\theta) = - \int_{\theta_0}^{\theta} \frac{d\zeta}{d\theta'} d\theta' \quad (\text{A.22})$$

$\gamma$  is shown here to be a  $\theta$  dependant shift to the toroidal angle applied to ensure that the coordinate system follows the magnetic field line. The change in toroidal angle due to translation in  $\theta$  is given by

$$\frac{d\zeta}{d\theta} = \frac{\mathbf{e}_\theta \cdot \nabla \zeta}{\mathbf{e}_\theta \cdot \nabla \theta} = \frac{\mathbf{B} \cdot \nabla \zeta}{\mathbf{B} \cdot \nabla \theta} \equiv \nu(\psi, \theta) \quad (\text{A.23})$$

where the trivial fact that  $\mathbf{e}_\theta \cdot \nabla \theta = 1$  and  $\mathbf{B} = J^{-1} \mathbf{e}_\theta$  has been used.  $\nu(\psi, \theta)$  specifies the local pitch angle of the magnetic field line. The BOUT++  $(x, y, z)$  coordinate system is thus defined by

$$\begin{aligned} x &= \sigma_{B_\theta} (\psi - \psi_0) \\ y &= \theta \\ z &= \zeta - \int_{y_0}^y \nu(x, y') dy' \end{aligned} \quad (\text{A.24})$$

where  $\psi_0$  is a constant offset of the domain and  $\sigma_{B_\theta}$  is the sign of the vertical magnetic field in the  $(R, \zeta, Z)$  cylindrical coordinate system which ensures that  $x$  is always increasing from the centre of the tokamak plasma outwards. For the considerations in this theses  $\sigma_{B_\theta} = 1$ . The contravariant basis vectors of the system can now be evaluated as

$$\begin{aligned} \nabla x &= \nabla \psi \\ \nabla y &= \nabla \theta \\ \nabla z &= \nabla \zeta - \nu \nabla \theta - I \nabla \psi \end{aligned} \quad (\text{A.25})$$

where

$$I = \int_{y_0}^y \frac{\partial \nu}{\partial \psi} dy' \quad (\text{A.26})$$

is the integrated magnetic shear. The Jacobian of the system can now be evaluated from expression A.20 to give

$$J^{-1} = \nabla x \times \nabla z \cdot \nabla y = \mathbf{B} \cdot \nabla \theta = B^\theta |\nabla \theta| = \frac{B_\theta}{h_\theta} \quad (\text{A.27})$$

where  $B_\theta$  is the poloidal magnetic field strength and  $h_\theta$  is the magnitude of the poloidal basis vector. Specifically  $h_\theta$  is the proportionality factor that relates a poloidal displacement of length  $dL$  to a shift in poloidal angle of  $d\theta$  by  $dL = h_\theta d\theta$ . On closed field lines in a circular tokamak equilibrium  $h_\theta = r$  where  $r$  is the minor radius.

Using  $\mathbf{e}_i = J\mathbf{e}^j \times \mathbf{e}^k$  the covariant basis vectors of the system can be derived as

$$\begin{aligned}\mathbf{e}_x &= \mathbf{e}_\psi + I\mathbf{e}_\zeta \\ \mathbf{e}_y &= \mathbf{e}_\theta + \nu\mathbf{e}_\zeta \\ \mathbf{e}_z &= \mathbf{e}_\zeta\end{aligned}\tag{A.28}$$

In deriving these expressions the fact that the coordinates  $(\psi, \theta, \zeta)$  form a right handed coordinate system has been used. Furthermore the lengths of the basis vectors in this toroidal coordinate system are

$$\begin{aligned}h_\psi^2 &= g_{\psi\psi} = 1/g^{\psi\psi} = \mathbf{e}_\psi \cdot \mathbf{e}_\psi = \frac{1}{R^2 B_\theta^2} \\ h_\theta^2 &= g_{\theta\theta} = 1/g^{\theta\theta} = \mathbf{e}_\theta \cdot \mathbf{e}_\theta = h_\theta^2 \\ h_\zeta^2 &= g_{\zeta\zeta} = 1/g^{\zeta\zeta} = \mathbf{e}_\zeta \cdot \mathbf{e}_\zeta = R^2\end{aligned}\tag{A.29}$$

These expressions will be used to evaluate the metric coefficients of the field aligned system shortly, however first  $\nu$  is given by

$$\nu = \frac{\mathbf{B} \cdot \nabla\zeta}{\mathbf{B} \cdot \nabla\theta} = \frac{B^\zeta |\nabla\zeta|}{B^\theta |\nabla\theta|} = \frac{h_\theta B_\zeta}{R B_\theta}\tag{A.30}$$

The covariant metric coefficients are then given by

$$g_{ij} \equiv \mathbf{e}_i \cdot \mathbf{e}_j = \begin{pmatrix} I^2 R^2 + 1/(R B_\theta)^2 & B_\zeta h_\theta I R / B_\theta & I R^2 \\ B_\zeta h_\theta I R / B_\theta & B^2 h_\theta^2 / B_\theta^2 & B_\zeta h_\theta R / B_\theta \\ I R^2 & B_\zeta h_\theta R / B_\theta & R^2 \end{pmatrix}\tag{A.31}$$

and the contravariant metric coefficients by

$$g^{ij} = \nabla u^i \cdot \nabla u^j = \begin{pmatrix} (R B_\theta)^2 & 0 & -I (R B_\theta)^2 \\ 0 & 1/h_\theta^2 & -\nu/h_\theta^2 \\ -I (R B_\theta)^2 & -\nu/h_\theta^2 & I^2 (R B_\theta)^2 + B^2 / (R B_\theta)^2 \end{pmatrix}\tag{A.32}$$

Figure A.2 gives a schematic illustration of the  $(x, y, z)$  coordinate system used in BOUT++.

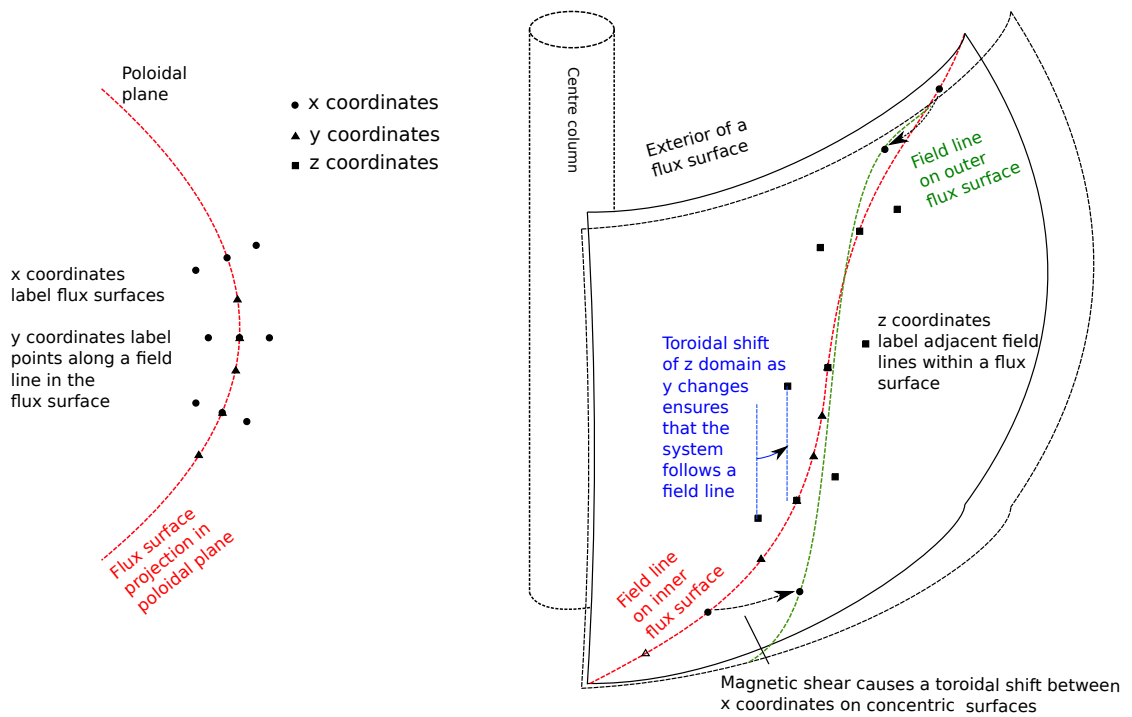


FIGURE A.2: Schematic illustration of the spatial layout of coordinates in the  $(x, y, z)$  coordinate system in the BOUT++ code. Specifically shown is the process by which a shift in the toroidal direction ensures that the coordinate system follows a magnetic field line. Note that the toroidal shift between two  $x$  coordinates on concentric flux surfaces occurs as a result of magnetic shear in order to maintain the field line following nature of the system.



## Appendix B

# Derivation of equations for filament simulations

This appendix presents a derivation of the governing equations used in this thesis to model filament dynamics. From the outset the plasma is assumed to be isothermal and the ion temperature is assumed small such that  $T_i/T_e \ll 1$ . The starting point of the derivation is the first two moments of the Vlasov-Fokker-Planck equation. For particle species  $j$  these are the equations for density conservation

$$\frac{\partial n_j}{\partial t} + \nabla \cdot (n_j \mathbf{u}_j) = S_{j,n} \quad (\text{B.1})$$

and momentum conservation

$$n_j m_j \left( \frac{\partial}{\partial t} + \mathbf{u}_j \cdot \nabla \right) \mathbf{u}_j = q_j n_j (\mathbf{E} + \mathbf{u}_j \times \mathbf{B}) - \nabla p_j - \nabla \cdot \Pi_j + \mathbf{R}_j + \mathbf{S}_{j,m} + m_j \mathbf{u}_j S_{j,n} \quad (\text{B.2})$$

where  $n_j$  is the species particle density,  $\mathbf{u}_j$  is the species fluid velocity,  $p_j = n_j T_j$  is the species scalar isotropic pressure scalar,  $\Pi_j$  is the anisotropic viscosity tensor,  $\mathbf{R}_j$  is the collisional friction,  $\mathbf{E}$  and  $\mathbf{B}$  are the electric and magnetic fields respectively,  $m_j$  is the species particle mass,  $q_j$  is the species charge and  $S_{j,n}$  and  $\mathbf{S}_{j,m}$  are external sources or sinks of density and momentum respectively.

The components of the fluid velocity perpendicular to the magnetic field can be extracted by applying the operation  $\mathbf{B} \times$  to the momentum equation. This then gives

$$\mathbf{u}_{j,\perp} = \mathbf{u}_j - (\mathbf{u}_j \cdot \mathbf{B}) \frac{\mathbf{B}}{B^2} = \mathbf{u}_E + \mathbf{u}_D + \mathbf{u}_p \quad (\text{B.3})$$

where the components of the perpendicular velocity can be identified as the  $\mathbf{E} \times \mathbf{B}$  velocity,

$$\mathbf{u}_{j,E} = \frac{\mathbf{b} \times \nabla \phi}{B} \quad (\text{B.4})$$

the diamagnetic velocity,

$$\mathbf{u}_D = \frac{\mathbf{b} \times \nabla p_j}{q_j n_j B} \quad (\text{B.5})$$

and the polarization velocity (dropping external source terms)

$$\mathbf{u}_p = \frac{1}{\Omega_j} \mathbf{b} \times \left( \frac{\partial \mathbf{u}_j}{\partial t} + \mathbf{u}_j \cdot \nabla \mathbf{u}_j + \frac{\nabla \cdot \Pi_j - \mathbf{R}_j}{m_j n_j} \right) \quad (\text{B.6})$$

Using the drift ordering described and assessed in chapter 4 the magnitude of each of the velocity components can be assessed. First the magnitude of the electrostatic potential is estimated as  $\phi \sim T_e/e$  where  $T_e$  is the electron temperature in Joules. The potential is assumed to vary on the fast length scale  $L_f$  such that

$$\mathbf{u}_E = \frac{\mathbf{b} \times \nabla \phi}{B} \sim \frac{T_e}{eB} \frac{1}{L_f} = \delta \rho_s \Omega_i \quad (\text{B.7})$$

where  $\delta = \rho_s/L_f \ll 1$  and  $\rho_s = \sqrt{T_e m_i}/eB$  is the Bohm gyroradius. The magnitude of the diamagnetic velocity can be estimated noting that  $p_j = n_j T_j$  as

$$\mathbf{u}_D = \frac{\mathbf{b} \times \nabla p_j}{q_j n_j B} \sim \frac{T_j}{eB} \frac{1}{L_f} = \frac{T_j}{T_e} \delta \rho_s \Omega_i \quad (\text{B.8})$$

This shows that the  $\mathbf{E} \times \mathbf{B}$  velocity and diamagnetic velocity are on the same order of magnitude within the drift-ordering and must both be retained. The polarization velocity can now be assessed term by term. Noting that the leading order part of the total perpendicular velocity is shown here to be  $\sim \delta \rho_s \Omega_i$  the first two terms can be estimated as

$$\frac{1}{\Omega_j} \mathbf{b} \times \frac{\partial \mathbf{u}_j}{\partial t} \sim \frac{\omega}{\Omega_j} \delta \rho_s \Omega_i \sim \delta \rho_s \Omega_i \frac{\Omega_i}{\Omega_j} \delta^2 = \frac{m_j}{m_i} \delta^2 (\delta \rho_s \Omega_i) \quad (\text{B.9})$$

$$\frac{1}{\Omega_j} \mathbf{b} \times (\mathbf{u} \cdot \nabla \mathbf{u}) \sim \frac{(\delta \rho_s \Omega_i)^2}{L_f \Omega_j} = \frac{m_j}{m_i} \delta^2 (\delta \rho_s \Omega_i)$$

The third term concerns the viscosity tensor  $\Pi_j$ . This consists of a collisional part and a non-collisional 'gyro-viscous' part [52]. As noted in [52] the collisional part is  $\nu_j/\Omega_j \ll 1$  times smaller than the gyro-viscous part, where  $\nu_j$  is the collision frequency. Consequently only the gyro-viscous part needs to be retained in  $\mathbf{u}_p$ . Under the drift-ordering and assuming an isothermal plasma the gyro-viscosity reduces to the Braginskii gyro-viscosity [47, 235], given here in the form from [52] as

$$\Pi_{j,g} = \frac{p_j}{4\Omega_j} \left[ \mathbf{b} \times \left( \nabla \mathbf{u}_j + (\nabla \mathbf{u}_j)^T \right) \cdot (\mathbb{I} + 3\mathbf{b}\mathbf{b}) - (\mathbb{I} + 3\mathbf{b}\mathbf{b}) \cdot \left( \nabla \mathbf{u}_j + (\nabla \mathbf{u}_j)^T \right) \times \mathbf{b} \right] \quad (\text{B.10})$$

Fortunately within the cold ion limit no formal evaluation of this expression will be required. Using the above expression for  $\Pi_{j,g}$  and taking order of magnitude estimates

results in

$$\frac{1}{\Omega_j} \mathbf{b} \times \frac{\nabla \cdot \Pi_{j,g}}{m_j n_j} \sim \frac{1}{\Omega_j} \frac{n_j T_j}{\Omega_j} \delta^2 \Omega_i \frac{1}{n_j m_j L_f} = \frac{m_j T_j}{m_i T_e} \delta^2 (\delta \rho_s \Omega_i) \quad (\text{B.11})$$

thus the gyro-viscous part is small compared to the rest of the polarization velocity by at least  $T_i/T_e$ . The final part of the polarization velocity to be evaluated is the collisional friction term involving  $\mathbf{R}_j$ . From [47, 52]  $\mathbf{R}_j$  is given in the case of an isothermal plasma as

$$\mathbf{R}_e = -\mathbf{R}_i = en_e (\eta_{\parallel} \mathbf{b} J_{\parallel} + \eta_{\perp} \mathbf{J}_{\perp}) \quad (\text{B.12})$$

Note that only the  $\mathbf{J}_{\perp}$  term is retained after the  $\mathbf{b} \times$  operation. The perpendicular collisional resistivity is given by [47]

$$\eta_{\perp} = \frac{m_e \nu_e}{e^2 n_e} \quad (\text{B.13})$$

where  $\nu_e$  is the electron-ion collision time. Taking the maximum possible ordering of  $\mathbf{J}_{\perp}$  as  $\mathbf{J}_{\perp} \sim n_e e u_{\perp} \sim n_e e \delta \rho_s \Omega_i$  the frictional part of the polarization velocity is estimated as (assuming  $n_e = n_i$  by quasineutrality)

$$\frac{1}{\Omega_j} \mathbf{b} \times \frac{\mathbf{R}_j}{m_j n_j} \sim \frac{1}{\Omega_j} \frac{m_e \nu_e \delta \rho_s \Omega_i}{m_j} = \frac{m_e \nu_e}{m_j \Omega_j} (\delta \rho_s \Omega_i) = \frac{\nu_e}{\Omega_e} (\delta \rho_s \Omega_i) \quad (\text{B.14})$$

There are a few key points to note about the ordering of the polarization velocity. Firstly the collisional term is the leading order part since  $\Omega_j \gg \nu_j \gg \omega \sim \delta^2 \Omega_i$  infers  $1 \gg \nu_e/\Omega_e \gg \delta^2 m_e/m_i$ . Secondly the second order terms in the electron polarization velocity are  $m_e/m_i$  times smaller than the counterpart terms in the ion polarization velocity. The leading order terms are identical in both however. Finally leading order terms of the polarization velocity are smaller than both the  $\mathbf{E} \times \mathbf{B}$  and diamagnetic velocities by  $\nu_e/\Omega_e$ , whilst second order terms are small by at least  $\delta^2$ .

The equation for density continuity can now be evaluated for electrons up to first order in  $\delta$  as (dropping subscript for brevity)

$$\frac{\partial n}{\partial t} = -\nabla \cdot (n \mathbf{u}_E) - \nabla \cdot (n \mathbf{u}_D) = -n \nabla \cdot \mathbf{u}_E - \mathbf{u}_E \cdot \nabla n - \nabla \cdot (n \mathbf{u}_D) - \nabla \cdot (\mathbf{b} u_{\parallel} n) \quad (\text{B.15})$$

The divergent terms are evaluated as

$$\nabla \cdot \mathbf{u}_E = \nabla \cdot \left( \frac{\mathbf{b}}{B} \times \nabla \phi \right) = \left( \nabla \times \frac{\mathbf{b}}{B} \right) \cdot \nabla \phi \quad (\text{B.16})$$

$$\nabla \cdot (n \mathbf{u}_D) = -c_s \rho_s \nabla \cdot \left( \frac{\mathbf{b}}{B} \times \nabla n \right) = -c_s \rho_s \left( \nabla \times \frac{\mathbf{b}}{B} \right) \cdot \nabla n \quad (\text{B.17})$$

and

$$\nabla \cdot (\mathbf{b} u_{\parallel} n) = \nabla \cdot \left( \mathbf{B} \frac{u_{\parallel} n}{B} \right) = B \mathbf{b} \cdot \nabla \left( \frac{u_{\parallel} n}{B} \right) + \frac{u_{\parallel} n}{B} \nabla \cdot \mathbf{B} = -\frac{B}{e} \nabla_{\parallel} \frac{J_{\parallel}}{B} \approx -\frac{1}{e} \nabla_{\parallel} J_{\parallel} \quad (\text{B.18})$$

where  $J_{\parallel} = ne(u_{\parallel,i} - u_{\parallel,e})$  for single charged ions, and the ion velocity contribution has been neglected. Thus the density continuity equation becomes

$$\frac{\partial n}{\partial t} + \mathbf{u}_E \cdot \nabla n = c_s \rho_s \left( \nabla \times \frac{\mathbf{b}}{B} \right) \cdot \nabla n - n \left( \nabla \times \frac{\mathbf{b}}{B} \right) \cdot \nabla \phi + \frac{1}{e} \nabla_{\parallel} J_{\parallel} \quad (\text{B.19})$$

It is worth noting that the RHS terms are  $\epsilon = L_f/L_s$  times smaller than the LHS terms and are usually neglected. Angus has shown [115] that the first and third RHS terms should be retained however to properly capture the linear stability of the resistive drift-wave.

To close the system equations for  $J_{\parallel}$  and  $\phi$  are required. The latter can be achieved by evaluating the condition for current continuity,  $\nabla \cdot \mathbf{J} = 0$  where the current density  $\mathbf{J} = \mathbf{J}_{\perp} + J_{\parallel} \mathbf{b} = ne(\mathbf{u}_{\perp,i} - \mathbf{u}_{\perp,e}) + J_{\parallel} \mathbf{b}$ . In evaluating  $\nabla \cdot \mathbf{J}_{\perp}$  it is important to retain the polarization velocity, since it is not possible to assume that the difference between two large terms will still be large enough to remain leading order. As discussed earlier though, only the collisional part of the electron polarization velocity needs to be retained. Furthermore the gyroviscous and diamagnetic parts of the ion velocity can be neglected due to  $T_i/T_e \ll 1$  and the ion and electron  $\mathbf{E} \times \mathbf{B}$  terms naturally cancel, thus

$$\nabla \cdot \mathbf{J}_{\perp} = \nabla \cdot \left[ ne \mathbf{b} \times \left( \frac{\partial}{\partial t} + \mathbf{u}_E \cdot \nabla \right) \mathbf{u}_E \right] - e \nabla \cdot (n \mathbf{u}_{D,e}) \quad (\text{B.20})$$

Note that the collisional contribution from the electron polarization cancels the corresponding contribution from the ion polarization velocity. The second term above has already been evaluated in the density continuity equation. The first term can be evaluated approximately by noting spatially derivatives of the magnetic field are small by  $L_s/L_f$  and by making the Boussinesq approximation, which is used to pull the  $n$  outside of the divergence such that

$$\nabla \cdot \left[ ne \mathbf{b} \times \left( \frac{\partial}{\partial t} + \mathbf{u}_E \cdot \nabla \right) \mathbf{u}_E \right] \approx ne \nabla \cdot \left( \frac{\partial}{\partial t} + \mathbf{u}_E \cdot \nabla \right) \mathbf{b} \times \mathbf{u}_E = -\frac{ne}{B} \left( \frac{\partial}{\partial t} + \mathbf{u}_E \cdot \nabla \right) \nabla_{\perp}^2 \phi \quad (\text{B.21})$$

where  $\mathbf{b} \times \mathbf{b} \times \nabla \phi = -\nabla_{\perp} \phi$  has been used. The full expression for  $\nabla \cdot \mathbf{J} = 0$  is now (often called the vorticity equation)

$$\frac{n}{B} \left( \frac{\partial}{\partial t} + \mathbf{u}_E \cdot \nabla \right) \nabla_{\perp}^2 \phi = c_s \rho_s \left( \nabla \times \frac{\mathbf{b}}{B} \right) \cdot \nabla n + \frac{1}{e} \nabla_{\parallel} J_{\parallel} \quad (\text{B.22})$$

Finally it remains to derive an expression for  $J_{\parallel}$ . This is achieved by dotting the electron momentum equation with  $\mathbf{b}$  and, following [52] by neglecting inertial terms as  $m_e/m_i$  times smaller than leading order and viscous terms as  $\sqrt{m_e/m_i} \epsilon \Delta / \delta$  times smaller, the

parallel momentum equations becomes

$$\mathbf{b} \cdot \mathbf{R}_e = en \nabla_{\parallel} \phi - T_e \nabla_{\parallel} n \quad (\text{B.23})$$

Evaluating  $\mathbf{R}_e$  then gives parallel Ohm's law, which is an auxiliary equation for  $J_{\parallel}$

$$\eta_{\parallel} J_{\parallel} = \frac{T_e}{e} \nabla_{\parallel} \ln(n) - \nabla_{\parallel} \phi \quad (\text{B.24})$$

This completes the derivation of the system of equations employed to simulate filament dynamics in MAST.

To summarize these are the density equation

$$\frac{\partial n}{\partial t} + \mathbf{u}_E \cdot \nabla n = c_s \rho_s \left( \nabla \times \frac{\mathbf{b}}{B} \right) \cdot \nabla n - n \left( \nabla \times \frac{\mathbf{b}}{B} \right) \cdot \nabla \phi + \frac{1}{e} \nabla_{\parallel} J_{\parallel} \quad (\text{B.25})$$

the vorticity equation

$$\frac{n}{B} \left( \frac{\partial}{\partial t} + \mathbf{u}_E \cdot \nabla \right) \nabla_{\perp}^2 \phi = c_s \rho_s \left( \nabla \times \frac{\mathbf{b}}{B} \right) \cdot \nabla n + \frac{1}{e} \nabla_{\parallel} J_{\parallel} \quad (\text{B.26})$$

and parallel Ohm's law

$$\eta_{\parallel} J_{\parallel} = \frac{T_e}{e} \nabla_{\parallel} \ln(n) - \nabla_{\parallel} \phi \quad (\text{B.27})$$

The normalization employed in this thesis is the Bohm normalization where length-scales are normalized to  $\rho_s$  and timescales to  $1/\Omega_i$  with the density normalized to the background value  $n_0$  and the potential normalized to  $T_e/e$  ( $T_e$  joules). Under these normalizations the system becomes

$$\frac{\partial n}{\partial t} + \mathbf{u}_E \cdot \nabla n = 2\hat{\xi} \cdot \nabla n - n 2\hat{\xi} \cdot \nabla \phi + \frac{1}{n_0 c_s e} \nabla_{\parallel} J_{\parallel} \quad (\text{B.28})$$

$$n \left( \frac{\partial}{\partial t} + \mathbf{u}_E \cdot \nabla \right) \nabla_{\perp}^2 \phi = 2\hat{\xi} \cdot \nabla n + \frac{1}{n_0 c_s e} \nabla_{\parallel} J_{\parallel} \quad (\text{B.29})$$

$$\eta_{\parallel} J_{\parallel} = \frac{T_e}{\rho_s e} \nabla_{\parallel} (\ln(n) - \phi) \quad (\text{B.30})$$

where  $\mathbf{u}_E = \mathbf{b} \times \nabla \phi$  and  $\hat{\xi} = \rho_s \mathbf{b} \times \kappa$  is the normalized polarization vector where the approximation [52]

$$\xi = \nabla \times \frac{\mathbf{b}}{B} = \frac{1}{2B} \mathbf{b} \times \kappa + \frac{1}{B} \mathbf{b} \times \nabla B \approx \frac{1}{2B} \mathbf{b} \times \kappa \quad (\text{B.31})$$

has been used.



## Appendix C

# Derivation of curvature vector

This appendix outlines a derivation of the curvature vector along a magnetic field line. The magnetic field line is parameterized by the cylindrical coordinates  $(R(s), \phi(s), Z(s))$  where  $s$  is the arc length along the magnetic field line. In the context of a tokamak  $R$  is the major radius,  $\phi$  is the toroidal angle and  $Z$  is the vertical dimension. The unit tangent vector, which lies tangent to the magnetic field line at all points is given by

$$\hat{\mathbf{T}} = \frac{d\mathbf{r}}{ds} = \mathbf{r}' = \frac{dR}{ds}\hat{\mathbf{R}} + R\frac{d\phi}{ds}\hat{\phi} + \frac{dZ}{ds}\hat{\mathbf{Z}} \quad (\text{C.1})$$

This expression is derived from the expression for a differential line element  $d\mathbf{r} = dR\hat{\mathbf{R}} + Rd\phi\hat{\phi} + dZ\hat{\mathbf{Z}}$ . The curvature vector is given by

$$\begin{aligned} \kappa &= \frac{d\hat{\mathbf{T}}}{ds} \\ &= \hat{\mathbf{R}}\frac{d^2R}{ds^2} + \hat{\phi}\left(\frac{dR}{ds}\frac{d\phi}{ds} + R\frac{d^2\phi}{ds^2}\right) + \hat{\mathbf{Z}}\frac{d^2Z}{ds^2} \\ &\quad + \frac{dR}{ds}\frac{d\hat{\mathbf{R}}}{ds} + R\frac{d\phi}{ds}\frac{d\hat{\phi}}{ds} + \frac{dZ}{ds}\frac{d\hat{\mathbf{Z}}}{ds} \end{aligned} \quad (\text{C.2})$$

To evaluate the derivatives of the unit vectors they are first cast into cartesian coordinates  $(x, y, z)$  such that

$$\begin{aligned} \hat{\mathbf{R}} &= \cos\phi\hat{\mathbf{x}} + \sin\phi\hat{\mathbf{y}} \\ \hat{\phi} &= -\sin\phi\hat{\mathbf{x}} + \cos\phi\hat{\mathbf{y}} \\ \hat{\mathbf{Z}} &= \hat{\mathbf{z}} \end{aligned} \quad (\text{C.3})$$

Noting that

$$\frac{d\hat{\mathbf{R}}}{ds} = \frac{\partial\hat{\mathbf{R}}}{\partial\phi}\frac{d\phi}{ds} \quad (\text{C.4})$$

and

$$\frac{d\hat{\phi}}{ds} = \frac{\partial \hat{\phi}}{\partial \phi} \frac{d\phi}{ds} \quad (\text{C.5})$$

gives

$$\frac{d\hat{\mathbf{R}}}{ds} = \frac{d\phi}{ds} (-\sin \phi \hat{\mathbf{x}} + \cos \phi \hat{\mathbf{y}}) = \phi' \hat{\phi} \quad (\text{C.6})$$

and

$$\frac{d\hat{\phi}}{ds} = \frac{d\phi}{ds} (-\cos \phi \hat{\mathbf{x}} - \sin \phi \hat{\mathbf{y}}) = -\phi' \hat{\mathbf{R}} \quad (\text{C.7})$$

Finally, substituting these into the earlier expression and noting that

$$\frac{d\hat{\mathbf{Z}}}{ds} = \frac{d\hat{\mathbf{Z}}}{d\phi} \frac{d\phi}{ds} = 0 \quad (\text{C.8})$$

gives

$$\kappa = \hat{\mathbf{R}} \left( \frac{d^2 R}{ds^2} - R \left( \frac{d\phi}{ds} \right)^2 \right) + \hat{\phi} \left( R \frac{d^2 \phi}{ds^2} + 2 \frac{dR}{ds} \frac{d\phi}{ds} \right) + \hat{\mathbf{Z}} \frac{d^2 Z}{ds^2} \quad (\text{C.9})$$

# Bibliography

- [1] N. R. Walkden, B. D. Dudson, and G. Fishpool. Characterization of 3d filament dynamics in a mast sol fluxtube geometry. *Plasma Physics and Controlled Fusion*, 55(105005), August 2013.
- [2] International Energy Authority. *Key World Energy Statistics: 2012*, 2012. URL <https://www.iaea.org>.
- [3] Exxon Mobil. *The outlook for energy: A view to 2040*, 2012. URL <https://www.exxonmobil.com>.
- [4] International Energy Authority. *World Energy Outlook 2011*, 2011. URL <https://www.iaea.org>.
- [5] A. S. Manne. Waiting for the breeder. *The Review of Economic Studies*, 41:47, 1974.
- [6] Energy from fossil fuels. Accessed June 2014. URL [https://www.wou.edu/las/physci/GS361/Energy\\_From\\_Fossil\\_Fuels.htm](https://www.wou.edu/las/physci/GS361/Energy_From_Fossil_Fuels.htm).
- [7] J. Wesson. *Tokamaks: Third Edition*. Oxford University Press, New York, 2004.
- [8] H. S. Bosch and G. M. Hale. Improved formulas for fusion cross-sections and thermal reactivities. *Nuclear Fusion*, 32(4):611, 1992.
- [9] J. Lindl. Development of the indirect drive approach to inertial confinement fusion and the target physics for ignition and gain. *Physics of Plasmas*, 2(11):3933, 1995.
- [10] J. D. Lindl, P. Amendt, R. Berger, S. G. Glendinning, et al. The physics basis for ignition using indirect-drive targets on the national ignition facility. *Physics of Plasmas*, 11(2):339, 2004.
- [11] E. I. Moses. Ignition on the national ignition facility: a path towards inertial fusion energy. *Nuclear Fusion*, 49(104002), 2009.
- [12] O. A. Hurricane, D. A. Callahan, D. T. Casey, P. M. Celliers, et al. Fuel gain exceeding unity in an inertially confined fusion implosion. *Nature*, 2014.
- [13] L. E. J. Brouwer. Uber abbildung von mannigfaltigkeiten. *Mathematische Annalen*, 71, 1912.
- [14] R. J. E. Clausius. On a mechanical theorem applicable to heat. *Philosophical Magazine, Series 4*, 40:122–127, 1870.
- [15] H. A. B. Bodin and A. A. Newton. Reversed-field-pinch research. *Nuclear Fusion*, 20(10):1255, 1980.

- [16] T. R. Jarboe. Review of spheromak research. *Plasma Physics and Controlled Fusion*, 36:945, 1994.
- [17] L. Spitzer Jr. The stellerator concept. *Physics of Fluids*, 1(4):253–264, 2004.
- [18] T. H. Stix. Heating of toroidal plasmas by neutral injection. *Plasma Physics*, 14 (367), 1972.
- [19] E. Speth. Neutral beam heating of fusion plasmas. *Reports on Progress in Physics*, 52(1):57–121, 1989.
- [20] F. W. Perkins. Heating tokamaks via the ion-cyclotron and ion-ion hybrid resonances. *Nuclear Fusion*, 17(6):1197, 1977.
- [21] V. Erckmann and U. Gasparino. Electron cyclotron resonant heating and current drive in toroidal fusion plasmas. *Plasma Physics and Controlled Fusion*, 36(12): 1689, 1994.
- [22] J. G. Cordey. A review of non-inductive current drive theory. *Plasma Physics and Controlled Fusion*, 26(1A):123 – 132, 1984.
- [23] M. Keilhacker and the ASDEX team. The asdex divertor tokamak. *Nuclear Fusion*, 25(9):1045, 1985.
- [24] M. Shimada et al. Progress on the iter physics basis, chapter 1: Overview and summary. *Nuclear Fusion*, 47:S1 – S17, 2007.
- [25] P. C. Stangeby. *The Plasma Boundary of Magnetic Fusion Devices*. IOP Publishing Ltd, London, UK, 2000.
- [26] F. Wagner et al. Regime of improved confinement and high beta in neutral-beam-heated divertor discharges on the asdex tokamak. *Physical Review Letters*, 49(19): 1408, 1982.
- [27] T. Eich, B. Sieglin, A. Scarabosio, W. Fundamenski, et al. Inter-elm power decay length for jet and asdex-upgrade: Measurement and comparison with heuristic drift-based model. *Physical Review Letters*, 107(21):215001, 2011.
- [28] C. S. Pitcher and P. C. Stangeby. Experimental divertor physics. *Plasma Physics and Controlled Fusion*, 39:779 – 930, 1997.
- [29] S. I. Krasheninnikov, A. Yu. Pigarov, T. K. Soboleva, and D. J. Sigmar. Plasma-neutral gas interaction in a tokamak divertor: Effects of hydrogen molecules and plasma recombination. *Journal of Nuclear Materials*, 241–243:283–287, 1997.
- [30] ITER physics basis editors. Iter physics basis chapter 1: Overview and summary. *Nuclear Fusion*, 39(12):2137, 1999.
- [31] Y-K. M. Peng and D. J. Strickler. Features of spherical torus plasmas. *Nuclear Fusion*, 26(6):769, 1986.
- [32] A. Sykes et al. First results from the start experiment. *Nuclear Fusion*, 32(4):694, 1992.
- [33] A. Sykes et al. The start spherical tokamak. *Plasma Physics and Controlled Fusion*, 1:719, 1994.

- [34] F. Troyon et al. Mhd limits to plasma confinement. *Plasma Physics and Controlled Fusion*, 26(1A):209, 1984.
- [35] M. Gryaznevich et al. Achievement of record  $\beta$  in the start spherical tokamak. *Physical Review Letters*, 80(18):3972, 1998.
- [36] A. Sykes et al. H-mode operation in the start spherical tokamak. *Physical Review Letters*, 84(3):495, 2000.
- [37] M. Cox and the MAST team. The mega amp spherical tokamak. *Fusion Engineering and Design*, 46:397–404, 1999.
- [38] A. Sykes et al. First physics results from the mast mega-amp spherical tokamak. *Physics of Plasmas*, 8(5):2101, 2001.
- [39] A. Sykes et al. First results from mast. *Nuclear Fusion*, 41(10):1423, 2001.
- [40] J. Harrison. *Characterization of Detached plasmas on the MAST tokamak*. PhD Thesis, University of York, 2010.
- [41] G. Voss, A. Bond, J. B. Hicks, and H. R. Wilson. Development of the spherical tokamak power plant. *Fusion Engineering and Design*, 63–64:65–71, 2002.
- [42] E. T. Cheng et al. Study of a spherical tokamak based volumetric neutron source. *Fusion Engineering and Design*, 38:219–255, 1998.
- [43] G. M. Voss et al. Conceptual design of a components test facility based on the spherical tokamak. *Fusion Engineering and Design*, 83:1648 – 1653, 2008.
- [44] P. M. Bellen. *Fundamentals of Plasma Physics*. Cambridge University Press, New York, US, 2006.
- [45] W. Fundamenski. *Power Exhaust in Fusion Plasmas*. Cambridge University Press, Cambridge, 2009.
- [46] F. F. Chen. *Introduction to plasma physics and controlled fusion: 2nd Ed*. Plenum Press, New York, US, 1984.
- [47] S. I. Braginskii. Transport processes in a plasma. *Reviews of Modern Physics; Ed. M. A. Leontovich*, 1:205, 1965.
- [48] R. D. Hazeltine and J. D. Meiss. *Plasma Confinement*. Frontiers in Physics, Addison-Wesley, Redwood City, 1992.
- [49] J. P. Friedberg. *Ideal magnetohydrodynamics*. Springer, New York, Us, 1987.
- [50] H. Grad. On the kinetic theory of rarified gasses. *Communications in Pure and Applied Mathematics*, 2(325), 1949.
- [51] A. B. Mikhailovskii and V. S. Tsypin. Transport equations of plasma in a curvilinear magnetic field. *Beitr. Plasmaphys.*, 24(4):335 – 354, 1984.
- [52] A. N. Simakov and P. J. Catto. Drift-ordered fluid equations for field aligned modes in low- $\beta$  collisional plasma with equilibrium pressure pedestal. *Physics of Plasmas*, 10(12):4744, December 2003.

- [53] A. N. Simakov and P. J. Catto. Erratum: "drift-ordered fluid equations for field aligned modes in low- $\beta$  collisional plasma with equilibrium pressure pedestal". *Physics of Plasmas*, 11(5):2326, May 2004.
- [54] J. R. Myra, D. A. Russell, and D. A. D'Ippolito. Collisionality and magnetic geometry effects on tokamak edge turbulent transport. 1. a two-region model with applications to blobs. *Physics of Plasmas*, 13(112502), 2006.
- [55] D. A. D'Ippolito, J. R. Myra, and S. J. Zweben. Convective transport of intermittent blob-filaments: Comparison of theory and experiment. *Physics of Plasmas*, 18:060501, 2011.
- [56] M. V. Umansky, S. I. Krasheninnikov, B. LaBombard, and J. L. Terry. Comments on particle and energy balance in the edge plasma of alcator c-mod. *Physics of Plasmas*, 5(9):3373–3376, 1998.
- [57] D. Carralero, G. Birkenmeier, H. W. Muller, P. Manz, P. deMarne, et al. *Influence of resistivity on filamentary transport in the SOL of ASDEX Upgrade*. 40th EPS Conference on Plasma Physics, Espoo, Finland, 2013.
- [58] D. Carralero, H. W. Muller, M. Groth, M. Komm, et al. *Implications of High Density Operation on SOL Transport: A Multimachine Comparison*. 21st International Conference on Plasma-Surface Interactions, Kanazawa, Japan, 2014.
- [59] D. Carralero, G. Birkenmeier, H. W. Muller, P. Manz, et al. An experimental investigation on the high density transition of the scrape-off layer transport in asdex upgrade. *arXiv:1407.3618*, 2014. URL <http://www.arxiv.org/abs/1407.3618>.
- [60] B. Lipschultz, X. Bonnin, G. Counsell, A. Kallenbach, et al. Plasma-surface interaction, scrape-off layer and divertor physics: implications for iter. *Nuclear Fusion*, 47:1189–1205, 2007.
- [61] A. Kirk, N. Ben Ayed, G. Counsell, B. Dudson, et al. Filament structures at the plasma edge on mast. *Plasma Physics and Controlled Fusion*, 48:B433–B441, November 2006.
- [62] R. J. Maqueda, G. A. Wurden, S. Zweben, L. Roquemore, et al. Edge turbulence measurements in nstx by gas puffing. *Review of Scientific Instruments*, 72(1):931, 2001.
- [63] J. P. Graves, J. Horacek, R. A. Pitts, and K. I. Hopcraft. Self-similar density turbulence in the tcv tokamak scrape-off layer. *Plasma Physics and Controlled Fusion*, 47:L1–L9, 2005.
- [64] B. A. Carreras, V. E. Lynch, and B. LaBombard. Structure and properties of the electrostatic fluctuations in the far scrape-off layer region of alcator c-mod. *Physics of Plasmas*, 8(8):3702, 2001.
- [65] J. A. Boedo, D. Rudakov, R. Moyer, S. I. Krasheninnikov, et al. Transport by intermittent convection in the boundary of the diii-d tokamak. *Physics of Plasmas*, 8(11):4826, 2001.
- [66] M. Endler, H. Niedermeyer, L. Giannone, E. Holzhauser, et al. Measurements and modelling of electrostatic fluctuations in the scrape-off layer of asdex. *Nuclear Fusion*, 35(11):1307, 1995.

- [67] H. Q. Liu, K. Hanada, N. Nishino, R. Ogata, et al. Study of blob-like structures in quest. *Journal of Nuclear Materials*, 415:S620–S623, 2011.
- [68] G. S. Xu, V. Naulin, W. Fundamenski, C. Hidalgo, et al. Blob/hole formation and zonal-flow generation in the edge plasma of the jet tokamak. *Nuclear Fusion*, 49 (092002), 2009.
- [69] Y. H. Xu, S. Jachmich, and R. R. Weynants. On the properties of turbulence intermittency in the boundary of the textor tokamak. *Plasma Physics and Controlled Fusion*, 47:1841–1855, 2005.
- [70] T. Happel, F. Greiner, N. Mahdizadeh, B. Nold, et al. Generation of intermittent turbulent events and the transition from closed to open magnetic field lines in a toroidal plasma. *Physical Review Letters*, 102(255001), 2009.
- [71] S. H. Muller, A. Diallo, A. Fasoli, I. Furno, et al. Plasma blobs in a basic toroidal experiment: Origin, dynamics and induced transport. *Physics of Plasmas*, 14 (110704), 2007.
- [72] G. Y. Antar, S. I. Krasheninnikov, P. Devynck, R. P. Doerner, et al. Experimental evidence of intermittent convection in the edge of magnetic confinement devices. *Physical Review Letters*, 87(6):065001, 2001.
- [73] R. E. Slusher and C. M. Surko. Study of density fluctuations in the absorption of oxygen on silicon. *Physical Review Letters*, 40(6):400–404, 1978.
- [74] G. Y. Antar, G. Counsell, Y. Yu, B. LaBombard, and P. Devynck. Universality of intermittent convective transport in the scrape-off layer of magnetically confined devices. *Physics of Plasmas*, 10(2):419, 2003.
- [75] J. A. Boedo, D. L. Rudakov, R. A. Moyer, G. R. McKee, et al. Transport by intermittency in the boundary of the dIII-d tokamak. *Physics of Plasmas*, 10(5):1670, 2003.
- [76] B. Nold, G. D. Conway, T. Happel, H. W. Muller, et al. Generation of blobs and holes in the edge of the asdex-upgrade tokamak. *Plasma Physics and Controlled Fusion*, 52(065005), 2010.
- [77] B. D. Dudson, R. O. Dendy, A. Kirk, H. Meyer, and G. F. Counsell. Comparison of l and h-mode plasma edge fluctuations in mast. *Plasma Physics and Controlled Fusion*, 47:885–901, 2005.
- [78] B. Hnat, B. D. Dudson, R. O. Dendy, G. F. Counsell, et al. Characterization of edge turbulence in relation to edge magnetic field configuration in ohmic l-mode plasmas in the mega amp spherical tokamak. *Nuclear Fusion*, 48:085009, 2008.
- [79] B. D. Dudson, N. Ben Ayed, A. Kirk, H. R. Wilson, et al. Experiments and simulation of edge turbulence and filaments in mast. *Plasma Physics and Controlled Fusion*, 50(124012), 2008.
- [80] N. Katz, J. Egedal, W. Fox, A. Lee, and M. Porkolab. Experiments on the propagation of plasma filaments. *Physical Review Letters*, 101:015003, 2008.
- [81] I. Furno, B. Labit, M. Podesta, A. Fasoli, et al. Experimental observation of the blob generation mechanism from interchange waves in a plasma. *Physical Review Letters*, 100:055004, 2008.

- [82] C. Theiler, I. Furno, A. Fasoli, P. Ricci, et al. Blob motion and control in simple magnetized plasmas. *Physics of Plasmas*, 18(055901), 2011.
- [83] S. J. Zweben, D. P. Stotler, et al. Edge turbulence imaging in the alcator c-mod tokamak. *Physics of Plasmas*, 9(5):1981, 2002.
- [84] N. Ben Ayed, A. Kirk, B. Dudson, S. Tallents, et al. Inter-elm filaments and turbulent transport in the mega-amp spherical tokamak. *Plasma Physics and Controlled Fusion*, 51(035016), 2009.
- [85] B. D. Dudson. *Edge Turbulence in the Mega Amp Spherical Tokamak*. PhD Thesis, University of Oxford, 2007.
- [86] O. Grulke, J. L. Terry, B. LaBombard, and S. J. Zweben. Radially propagating fluctuation structures in the scrape-off layer of alcator c-mod. *Physics of Plasmas*, 13(012306), 2006.
- [87] J. L. Terry, S. J. Zweben, M. V. Umankysy, I. Cziegler, et al. Spatial structure of scrape-off-layer filaments near the midplane and x-point regions of alcator c-mod. *Journal of Nuclear Materials*, 390–391:339–342, 2009.
- [88] G. Y. Antar, J. H. Yu, and G. Tynan. The origin of convective structures in the scrape-off layer of linear magnetic fusion devices investigated by fast imaging. *Physics of Plasmas*, 14:022301, 2007.
- [89] J. Myra, D. A. D’Ippolito, et al. Blob birth and transport in the tokamak edge plasma: Analysis of imaging data. *Physics of Plasmas*, 13(092509), 2006.
- [90] R. Kube, O. E. Garcia, B. LaBombard, J. L. Terry, and S. J. Zweben. Blob sizes and velocities in the alcator c-mod scrape-off layer. *Journal of Nuclear Materials*, 438:S505 – S508, 2013.
- [91] S. I. Krashenninikov. On scrape off layer plasma transport. *Physics Letters A*, 283:368–370, 2001.
- [92] A. V. Nedospasov, V. G. Petrov, and G. N. Fidel’man. Plasma convection in the poloidal limiter shadow of a tokamak. *Nuclear Fusion*, 25(1):21, 1985.
- [93] O. E. Garcia, V. Naulin, A. H. Nielsen, and J. Juul Rasmussen. Turbulence and intermittent transport at the boundary of magnetized plasmas. *Physics of Plasmas*, 12(062309), 2005.
- [94] G.Q.Yu and S.I.Krasheninnikov. Dynamics of blobs in scrape-off-layer/shadow regions of tokamaks and linear devices. *Physics of Plasmas*, 10(11):4413, 2003.
- [95] G. Q. Yu, S. I. Krasheninnikov, and P. N. Guzdar. Two-dimensional modelling of blob dynamics in tokamak edge plasmas. *Physics of Plasmas*, 13(042508), April 2006.
- [96] D. A. D’Ippolito, J. R. Myra, S. I. Krasheninnikov, G. Q. Yu, and A. Yu. Pigarov. Blob transport in the tokamak scrape-off layer. *Contributions to Plasma Physics*, 44(1–3):205–216, 2004.
- [97] N. H. Bian, S. Benkadda, J. V. Paulsen, and O. E. Garcia. Blobs and front propagation in the scrape-off layer of magnetic confinement devices. *Physics of Plasmas*, 10(3):671, 2003.

- [98] O. E. Garcia, N. H. Bian, V. Naulin, A. H. Nielsen, and J. Juul Rasmussen. Mechanism and scaling for convection of isolated structures in non-uniformly magnetized plasmas. *Physics of Plasmas*, 12:090701, 2005.
- [99] O. E. Garcia, N. H. Bian, and W. Fundamenski. Radial interchange motion of plasma filaments. *Physics of Plasmas*, 13(082309), 2006.
- [100] N. Bisai and P. K. Kaw. Role of ion temperature on scrape-off layer plasma turbulence. *Physics of Plasmas*, 20:042509, 2013.
- [101] D. A. D’Ippolito, J. R. Myra, D. A. Russell, and G. Q. Yu. Rotational stability of plasma blobs. *Physics of Plasmas*, 11(10):4603, 2004.
- [102] J. R. Myra, D. A. D’Ippolito, S. I. Krasheninnikov, and G. Q. Yu. Convective transport in the scrape-off layer by non-thermalized spinning blobs. *Physics of Plasmas*, 11(9):4267, 2004.
- [103] K. Bodi, S. I. Krasheninnikov, and A. I. Smolyakov. Blob dynamics in an inhomogeneous plasma. *Physics of Plasmas*, 15:102304, 2008.
- [104] B. D. Dudson, M. V. Umansky, X. Q. Xu, P. B. Snyder, and H. R. Wilson. Bout++: A framework for parallel plasma fluid simulations. *Computer Physics Communications*, 180:1467–1480, 2009.
- [105] S. I. Krasheninnikov, A. I. Smolyakov, and T. K. Soboleva. On anomalous cross-field edge plasma convection in fusion devices. *Physics of Plasmas*, 12:072502, 2005.
- [106] S. I. Krasheninnikov, A. I. Smolyakov, G. Q. Yu, and T. K. Soboleva. Meso-scale structures and anomalous convective transport at the edge of magnetic confinement devices. *Physica Scripta*, T124:13–17, 2006.
- [107] S. I. Krasheninnikov and A. I. Smolyakov. On neutral wind and blob motion in linear devices. *Physics of Plasmas*, 10(7):3020, July 2003.
- [108] D. D. Ryutov and R. H. Cohen. Instability driven by sheath boundary conditions and limited to divertor legs. *Contributions to Plasma Physics*, 44(1–3):168–175, 2004.
- [109] D. A. Russell, D. A. D’Ippolito, J. R. Myra, W. M. Nevins, and X. Q. Xu. Blob dynamics in 3d bout simulations of tokamak edge turbulence. *Physical Review Letters*, 93:265001, 2004.
- [110] R. H. Cohen, B. LaBombard, D. D. Ryutov, J. L. Terry, M. V. Umansky, X. Q. Xu, and S. Zweben. Theory and fluid simulations of boundary-plasma fluctuations. *Nuclear Fusion*, 47:612–625, 2007.
- [111] A. Kirk, B. Koch, R. Scannell, H. Wilson, et al. Evolution of filament structures during edge-localized modes in the mast tokamak. *Physical Review Letters*, 96(185001), 2006.
- [112] H. R. Wilson and S. C. Cowley. Theory of explosive ideal magnetohydrodynamic instabilities in plasmas. *Physical Review Letters*, 92(17):175006, 2004.

- [113] D. A. Russell, J. R. Myra, and D. A. D'Ippolito. Collisionality and magnetic geometry effects on tokamak edge turbulent transport. ii. many-blob turbulence in the two-region model. *Physics of Plasmas*, 14(102307), 2007.
- [114] D. Farina, R. Pozzoli, and D. D. Ryutov. Effect of the magnetic geometry on the flute-like perturbations near the x-point. *Nuclear Fusion*, 33(9):1315, 1993.
- [115] J. Angus, S. I. Krasheninnikov, and M. V. Umankysy. Effects of parallel electron transport on plasma blob dynamics. *Physics of Plasmas*, 19(082312), August 2012.
- [116] J. Angus, M. V. Umansky, and S. I. Krasheninnikov. Effect of drift-waves on plasma blob dynamics. *Physical Review Letters*, 108(215002), 2012.
- [117] W. Horton. *Drift waves and Transport*, volume 71. 1999.
- [118] W. Fundamenski, O. E. Garcia, V. Naulin, R. Pitts, et al. Dissipative processes in interchange driven scrape-off layer turbulence. *Nuclear Fusion*, 47:417 – 433, 2007.
- [119] O. E. Garcia, V. Naulin, A. H. Nielsen, and J. Juul Rasmussen. Computations of intermittent transport in scrape-off layer plasmas. *Physical Review Letters*, 92(16):165003, 2004.
- [120] N. Bisai, R. Singh, and P. K. Kaw. Scrape-off layer tokamak plasma turbulence. *Physics of Plasmas*, 19(052509), 2012.
- [121] J. R. Myra, D. A. Russell, and D. A. D'Ippolito. Diffusive-convective transition for scrape-off layer transport and the heat flux width. *Plasma Physics and Controlled Fusion*, 54:055008, 2012.
- [122] D. A. Russell, J. R. Myra, and D. A. D'Ippolito. Saturation mechanisms for edge turbulence. *Physics of Plasmas*, 16:122304, 2009.
- [123] Y. Sarazin and Ph. Ghendrih. Intermittent particle transport in two-dimensional edge turbulence. *Physics of Plasmas*, 5(12):4214, 1998.
- [124] Y. Sarazin, X. Garbet, Ph. Ghendrih, and S. Benkadda. Transport due to front propagation in tokamaks. *Physics of Plasmas*, 7(4):1085, 2000.
- [125] D. A. D'Ippolito, D. A. Russell, J. R. Myra, S. C. Thakur, et al. Effect of parallel currents on drift-interchange turbulence: Comparison of simulation and experiment. *Physics of Plasmas*, 19:102301, 2012.
- [126] J. R. Myra, D. A. Russell, and D. A. D'Ippolito. Transport of perpendicular edge momentum by drift-interchange turbulence and blobs. *Physics of Plasmas*, 15:032304, 2008.
- [127] A. Hasegawa and M. Wakatani. Plasma edge turbulence. *Physical Review Letters*, 50(9):682, 1983.
- [128] O. E. Garcia, J. Horacek, R. A. Pitts, A. H. Nielsen, et al. Interchange turbulence in the tcv scrape-off layer. *Plasma Physics and Controlled Fusion*, 48:L1–L10, 2006.
- [129] F. Militello, P. Tamain, W. Fundamenksi, A. Kirk, et al. Experimental and numerical characterization of the turbulence in the scrape-off layer of mast. *Plasma Physics and Controlled Fusion*, 55(025005), 2013.

- [130] J. R. Myra, W. M. Davis, D. A. D'Ippolito, B. LaBombard, et al. Edge sheared flows and the dynamics of blob-filaments. *Nuclear Fusion*, 53:073013, 2013.
- [131] S. I. Krasheninnikov and A. I. Smolyakov. Generation of mesoscale convective structures in tokamak edge turbulence. *Physics of Plasmas*, 14:102503, 2007.
- [132] S. I. Krasheninnikov and A. I. Smolyakov. Dynamics and generation mechanisms of mesoscale structures in tokamak edge plasmas. *Physics of Plasmas*, 15:055909, 2008.
- [133] K. Bodi, A. I. Smolyakov, and S. I. Krasheninnikov. On blob generation mechanisms in tokamak edge plasma. *Journal of Nuclear Materials*, 390–391:359–363, 2009.
- [134] A. I. Smolyakov and S. I. Krasheninnikov. Generation of electromagnetic structures via modulational instability of drift waves. *Physics of Plasmas*, 15:072302, 2008.
- [135] I. Shesterikov, Y. Xu, G. R. Tynan, P. H. Diamond, et al. Experimental evidence for the intimate interaction among sheared flows, eddy structures, reynolds stress and zonal flows across a transition to improved confinement. *Physical Review Letters*, 111(055006), 2013.
- [136] J. Adamek, J. Stockel, M. Hron, J. Ryszawy, et al. A novel approach to direct measurement of the plasma potential. *Czechoslovak Journal of Physics*, 54 (Supplement C):C95–C99, 2004.
- [137] J. Adamek, J. Stockel, I. Duran, M. Hron, et al. Comparative measurements of the plasma potential with the ball-pen and emissive probes on the castor tokamak. *Czechoslovak Journal of Physics*, 55(3):235–242, 2005.
- [138] K. H. Burrell. Effects of velocity shear and magnetic shear on turbulence and transport in magnetic confinement devices. *Physics of Plasmas*, 4(5):1499, 1997.
- [139] I. H. Hutchinson. *Principles of Plasma Diagnostics*. Cambridge University Press, US, 2002.
- [140] I. Langmuir. *Science*, 58(290), 1923.
- [141] H. M. Mott-Smith and I. Langmuir. The theory of collectors in gaseous discharges. *Physical Review*, 28:727, 1926.
- [142] G. Van Oost. Advanced probe edge diagnostics for fusion devices. *Transactions of Fusion Science and Technology*, 53:387, 2008.
- [143] V. I. Demidov, S. V. Ratynskaia, and K. Rypdal. Electric probes for plasmas: The link between theory and experiment. *Review of Scientific Instruments*, 73 (10):3409, 2002.
- [144] Y. Yang, G. F. Counsell, and the MAST team. Observations with a mid-plane reciprocating probe in mast. *Journal of Nuclear Materials*, 313–316:743 – 747, 2003.
- [145] S. Elmore, S. Y. Allan, A. Kirk, G. Fishpool, et al. Upstream and divertor ion temperature measurements on mast by retarding field energy analyser. *Plasma Physics and Controlled Fusion*, 54(065001), 2012.

- [146] G. Y. Antar, G. Counsell, J. W. Ahn, Y. Yang, et al. The poloidal distribution of turbulent fluctuations in the mega-amp spherical tokamak. *Physics of Plasmas*, 12(032506), 2005.
- [147] P. Tamain, A. Kirk, E. Nardon, B. Dudson, et al. Edge turbulence and flows in the presence of resonant magnetic perturbations on mast. *Plasma Physics and Controlled Fusion*, 52(075017), 2010.
- [148] S. Tallents. *Investigations of the MAST SOL using the reciprocating probe system*. Imperial College London, UK, 2009.
- [149] I. Katsumata. A review of ion sensitive probes. *Contributions to Plasma Physics*, 36(S):73–80, 1996.
- [150] J. Adamek, J. Horacek, J. Seidl, H. W. Muller, et al. Direct plasma potential measurements by ball-pen probe and self-emitting langmuir probe on compass and asdex upgrade. *Contributions to Plasma Physics*, 54(3):279–284, 2014.
- [151] J. Adamek, J. Horacek, H. W. Muller, V. Rohde, et al. Ball-pen probe measurements in l-mode and h-mode in asdex-upgrade. *Contributions to Plasma Physics*, 50(9):854–859, 2010.
- [152] J. Horacek, J. Adamek, H. W. Muller, J. Seidl, et al. Interpretation of fast measurements of plasma potential, temperature and density in sol of asdex upgrade. *Nuclear Fusion*, 50(105001), 2010.
- [153] J. Adamek, V. Rohde, H. W. Muller, A. Herrmann, et al. Direct measurements of the plasma potential in elmy h-mode plasma with ball-pen probes on asdex-upgrade. *Journal of Nuclear Materials*, 390–391:1114 – 1117, 2009.
- [154] J. Adamek, M. Paterka, T. Gyergyek, P. Kudrna, et al. Application of the ball-pen probe in two low-temperature magnetized plasma devices and in torsatron tj-k. *Contributions to Plasma Physics*, 53(1):39–44, 2013.
- [155] G. Bousselin, J. Cavalier, J. F. Pautex, S. Heuraux, et al. Design and validation of the ball-pen probe for measurements in a low-temperature magnetized plasma. *Review of Scientific Instruments*, 84(013505), 2013.
- [156] R. Schrittwisser, C. Ionita, J. Adamek, J. Stockel, et al. Direct measurements of the plasma potential by katsumata-type probes. *Czechoslovak Journal of Physics*, 56(Supplement B):145, 2006.
- [157] M. Komm, J. Adamek, Z. Pekarek, and R. Panek. Particle-in-cell simulations of the ball-pen probe. *Contributions to Plasma Physics*, 50(9):814–818, 2010.
- [158] M. Komm, J. Adamek, R. Dejarnac, J. P. Gunn, and Z. Pekarek. Transport of electrons in the tunnel of an ion-sensitive probe. *Plasma Physics and Controlled Fusion*, 53(015005), 2011.
- [159] D. Brunner, B. LaBombard, R. Ochoukov, R. Sullivan, and D. Whyte. Space-charge limits of ion sensitive probes. *Plasma Physics and Controlled Fusion*, 55(125004), 2013.
- [160] M. Komm, R. Dejarnac, J. P. Gunn, and Z. Pekarek. Three-dimensional particle-in-cell simulations of gap crossings in castellated plasma-facing components in tokamaks. *Plasma Physics and Controlled Fusion*, 55(025006), 2013.

- [161] R. M. Sullivan, R. Ochoukov, and D. G. Whyte. Internal physics of the ion-sensitive probe. *Journal of Nuclear Materials*, 438:S1253–S1256, 2013.
- [162] L. L. Lao et al. *Nuclear Fusion*, 25:1611, 1985.
- [163] R. Scannell, M. J. Walsh, P. G. Carolan, N. J. Conway, et al. Enhanced edge thomson scattering on mast. *Review of Scientific Instruments*, 77(10E510), 2006.
- [164] K. Kanaya and H. Kawakatsu. Secondary electron emission due to primary and backscattered electrons. *Journal of Physics D: Applied Physics*, 5:1727, 1972.
- [165] E. W. Thomas. Particle induced electron emission. *Nuclear Fusion Supplement: Atomic and Plasma Material Interaction Data For Fusion*, 1:79, 1992.
- [166] M. E. Woods, B. J. Hopkins, G. F. Matthews, G. M. McCracken, et al. An investigation of the secondary-electron emission of carbon samples exposed to a hydrogen plasma. *Journal of Physics D: Applied Physics*, 20:1136 – 1142, 1987.
- [167] F. Millitello, V. Naulin, and A. H. Nielson. Numerical scalings of the decay lengths in the scrape-off layer. *Plasma Physics and Controlled Fusion*, 55(074010), 2013.
- [168] Lord Kelvin. On the motion of free solids through a liquid. *Phil. Mag*, 42(281): 362–377, 1871.
- [169] I. T. Chapman, N. R. Walkden, J. P. Graves, and C. Wahlberg. The effects of sheared toroidal rotation on stability limits in tokamak plasmas. *Plasma Physics and Controlled Fusion*, 53(125002), 2011.
- [170] I. T. Chapman, S. Brown, R. Kemp, and N. R. Walkden. Toroidal velocity shear kelin-helmholtz instabilities in strongly rotating tokamak plasmas. *Nuclear Fusion*, 52(042005), 2012.
- [171] C. Wahlberg, J. P. Graves, and I. T. Chapman. Analysis of global hydromagnetic instabilities driven by strongly sheared toroidal flows in tokamak plasmas. *Plasma Physics and Controlled Fusion*, 55(105004), 2013.
- [172] P. W. Gingell, S. C. Chapman, and R. O. Dendy. Plasma blob formation by ion kinetic kelin-helmholtz and interchange instabilities. *Plasma Physics and Controlled Fusion*, 56(035012), 2014.
- [173] J. C. Hillesheim, W. A. Peebles, T. L. Rhodes, L. Schmitz, et al. A multi-channel, frequency modulated, tunable doppler backscattering and reflectometry system. *Review of Scientific Instruments*, 80(083507), 2009.
- [174] J. C. Hillesheim, N. A. Crocker, W. A. Peebles, H. Meyer, et al. Implementation of doppler backscattering on mast. *ArXiv*, 2014. URL <http://www.arxiv.org/abs/1407.2115>.
- [175] T. Morgan. *Measurement of MAST edge ion and electron temperatures and velocities*. University of York, York,UK, 2011.
- [176] H. Meyer, C. Bunting, P. G. Carolan, N. J. Conway, et al. The structure, evolution and role of the radial edge electric field in h-mode and l-mode on mast. *Journal of Physics: Conference series*, 123(012005), 2008.

- [177] H. W. Muller, J. Adamek, R. Cavazzana, G. D. Conway, et al. Latest investigations on fluctuations, elm filaments and turbulent transport in the sol of asdex-upgrade. *Nuclear Fusion*, 51(073023), 2011.
- [178] F. I. Parra and P. J. Catto. Vorticity and intrinsic ambipolarity in tokamaks. *Plasma Physics and Controlled Fusion*, 51(095008), 2009.
- [179] D. Temple. *Experiment Investigations into the Radial Electric Field in MAST*. Imperial College, London, UK, 2010.
- [180] O. E. Garcia et al. *Journal of Nuclear Materials*, 363-365(575), 2007.
- [181] V. Naulin, O. E. Garcia, M. Priego, and J. Juul Rasmussen. The application of passive tracers for investigating transport in plasma turbulence. *Physica Scripta*, T122:129–134, 2006.
- [182] W. H. Press, S. A. Teukolsky, W. T. Vetterling, and B. P. Flannery. *Numerical Recipes in C*. Cambridge University Press, Cambridge, UK, 2002.
- [183] B. Labit, I. Furno, A. Fasoli, A. Diallo, et al. Universal statistical properties of drift-interchange turbulence in torpex plasmas. *Physical Review Letters*, 98 (255002), 2007.
- [184] F. Sattin, M. Agostini, P. Scarin, N. Vianello, et al. On the statistics of edge fluctuations: Comparative study between various fusion devices. *Plasma Physics and Controlled Fusion*, 51(055013), 2009.
- [185] F. Sattin, M. Agostini, R. Cavazzana, G. Serianni, et al. About the parabolic relation existing between the skewness and kurtosis in time series of experimental data. *Physica Scripta*, 79(045006), 2009.
- [186] D. Guszejnov, N. Lazanyi, A. Bencze, and S. Zoletnik. On the effect of intermittency of turbulence on the parabolic relation between skewness and kurtosis in magnetized plasmas. *ArXiv*, 2014. URL <http://www.arxiv.org/abs/1402.4230>.
- [187] G. Sugihara, R. May, H. Ye, C h Hsieh, et al. Detecting causality in complex eco-systems. *Science*, 338(6106):496–500, 2012.
- [188] B. D. Dudson. Bout++ user manual. *University of York*, 2009. URL <https://www.github.com/boutproject/>.
- [189] B. D. Dudson. Bout++ developer manual. *University of York*, 2009. URL <https://www.github.com/boutproject/>.
- [190] B. D. Dudson et al. Bout++: Recent and current developments. *Submitted to Journal of Plasma Physics*, 2014.
- [191] X. Q. Xu, M. V. Umansky, B. D. Dudson, and P. B. Snyder. Boundary plasma turbulence simulations for tokamaks. *Communications in Computational Physics*, 4(5):949–979, November 2008.
- [192] M. V. Umansky, X. Q. Xu, B. D. Dudson, L. L. LoDestro, and J. R. Myra. Status and verification of edge plasma turbulence code bout. *Computer Physics Communications*, 180:887–903, 2009.

- [193] P. A. Davidson. *Turbulence*. Oxford University Press, UK, 2004.
- [194] B. D. Dudson, X. Q. Xu, M. V. Umansky, H. R. Wilson, and P. B. Snyder. Simulations of edge localized modes using bout++. *Plasma Physics and Controlled Fusion*, 53(054005), April 2011.
- [195] B. Friedman, T. A. Carter, M. V. Umansky, D. Schaffner, and B. D. Dudson. Energy dynamics in a simulation of lapd turbulence. *Physics of Plasmas*, 19(102307), 2012.
- [196] W. Gekelman, H. Pfister, Z. Lucky, J. Bamber, et al. Design, construction and properties of the large plasma research device - the lapd at ucla. *Review of Scientific Instruments*, 62:2875, 1991.
- [197] J. Angus, M. V. Umansky, and S. I. Krasheninnikov. Review and limitations of 3d plasma blob modelling with reduced collisional fluid equations. *Journal of Nuclear Materials*, 438:S572–S575, 2013.
- [198] S. Hamdi, W. E. Schiesser, and G. W. Griffiths. Method of lines. *Scholarpedia*, 2(7):2859, 2007.
- [199] R. Courant, K. Friedrichs, and H. Lewy. On the partial difference equations of mathematical physics. *IBM Journal*, page 215, 1967.
- [200] G. E. Karniadakis, M. Israeli, and S. Orszag. High order splitting methods for the incompressible navier-stokes equations. *Journal of Computational Physics*, 97:414–443, 1991.
- [201] G. D. Byrne and A. C. Hindmarsh. Pvode, an ode solver for parallel computers. *International Journal of High Performance Computing Applications*, 13(4):354–365, Winter 1999.
- [202] E. Stein, R. de Borst, and T. J. R. Hughes, editors. *Encyclopedia of Computational Mechanics*. John Wiley and Sons, Ltd, 2004.
- [203] J. Donea, A. Huerta, J. Ph. Ponthot, and A. Rodriguez-Ferran. *Encyclopedia of Computational Mechanics*, chapter Arbitrary Lagrangian-Eulerian Methods. In Stein et al. [202], 2004.
- [204] R. Courant, E. Isaacson, and M. Rees. On the solution of nonlinear hyperbolic differential equations by finite differences. *Communications on Pure and Applied Mathematics*, 5:243–255, 1952.
- [205] G-S. Jiang and D. Peng. Weighted eno schemes for hamilton-jacobi equations. *Journal of Scientific Computing*, 21(6):2126–2153, 2000.
- [206] M. Frigo and S. G. Johnson. The design and implementation of fftw3. *Proceedings of the IEEE*, 93(2):216–231, 2005.
- [207] M. Frigo and S. G. Johnson. *The FFTW Web page*, 2004. URL <http://www.fftw.org>.
- [208] W. D. D’haeseleer, W. N. G. Hitchon, J. D. Callen, and J. L. Shohet. *Flux Coordinates and Magnetic Field Structure*. Springer-Verlag, Berlin, 1991.

- [209] M. D. Kruskal and R. M. Kulsrad. Equilibrium of a magnetically confined plasma in a toroid. *Physics of Fluids*, 1(265), 1958.
- [210] L. L. Lao, H. St. John, R. D. Stambaugh, A. G. Kellman, and W. Pfeiffer. Reconstruction of current profile parameters and plasma shapes in tokamaks. *Nuclear Fusion*, 25(11):1611, November 1985.
- [211] F. Militello and W. Fundamenski. Multi-machine comparison of drift fluid dimensionless parameters. *Plasma Physics and Controlled Fusion*, 53(095002), July 2011.
- [212] L. Easy, B. D. Dudson, F. Militello, J. Omotani, et al. *In preparation for submission to Plasma Physics and Controlled Fusion*, 2014.
- [213] S. Balay et al. *PETSc User Manual*, 2014. URL <http://www.mcs.anl.gov/petsc/>.
- [214] J. R. Angus and M. V. Umankysy. Modelling of large amplitude plasma-blobs in three dimensions. *Physics of Plasmas*, 21:012514, 2014.
- [215] J. Loizu, P. Ricci, F. D. Halpern, and S. Jolliet. Boundary conditions for plasma simulations at the magnetic pre-sheath entrance. *Physics of Plasmas*, 19(122307), December 2012.
- [216] R. H. Cohen and D. D. Ryutov. Plasma sheath in a tilted magnetic field: Closing of the diamagnetic currents; effect on plasma convection. *Physics of Plasmas*, 2(6):2011, 1995.
- [217] M. A. Beer, S. C. Cowley, and G. W. Hammett. Field-aligned coordinates for nonlinear simulations of tokamak turbulence. *Physics of Plasmas*, 2(7):2687, 1995.
- [218] C. Roach et al. Gyrokinetic simulations of spherical tokamaks. *Plasma Physics and Controlled Fusion*, 51:124002, 2009.
- [219] A. Kendl and B. D. Scott. Flux-surface shaping effects on tokamak edge turbulence and flows. *Physics of Plasmas*, 13:012504, 2006.
- [220] S. I. Krasheninnikov, D. A. D’Ippolito, and J. R. Myra. Recent theoretical progress in understanding coherent structures in edge and sol turbulence. *Journal of Plasma Physics*, 74(679), 2008.
- [221] J. A. Boedo. Edge turbulence and sol transport in tokamaks. *Journal of Nuclear Materials*, 390-391:29 – 37, 2009.
- [222] S. I. Krasheninnikov. Multifaceted physics of edge plasma in magnetic fusion devices. *Plasma Physics and Controlled Fusion*, 53(074017), 2011.
- [223] F. D. Halpern, A. Cardellini, P. Ricci, S. Jolliet, et al. Three-dimensional simulations of blob dynamics in a simple magnetized torus. *Physics of Plasmas*, 21(022305), 2014.
- [224] A. Fasoli, B. Labit, M. McGrath, S. H. Muller, G. Plyushchev, et al. Electrostatic turbulence and transport in a simple magnetized plasma. *Physics of Plasmas*, 13(055902), 2006.

- [225] D. D. Ryutov. The dynamics of an isolated plasma filament at the edge of a toroidal device. *Physics of Plasmas*, 13(112307), 2006.
- [226] P. M. Valanju, M. Kotschenreuther, S. M. Mahajan, and J. Canik. Super-x divertors and high power density fusion devices. *Physics of Plasmas*, 16:056110, 2009.
- [227] G. Fishpool et al. Mast-upgrade divertor facility and assessing performance of long-legged divertors. *Journal of Nuclear Materials*, 438:S356–S359, 2013.
- [228] D. D. Ryutov. Geometrical properties of a "snowflake" divertor. *Physics of Plasmas*, 14:064502, 2007.
- [229] L. Spitzer Jr. and R. Harm. Transport phenomena in a completely ionized gas. *Physical Review Letters*, 89(5):977, 1953.
- [230] J. W. Connor and J. B. Taylor. Resistive fluid turbulence and energy confinement. *Physics of Fluids*, 27(11):2676 – 2681, 1984.
- [231] P. Manz, D. Carralero, G. Birkenmeier, H. W. Muller, et al. Filament velocity scaling laws for warm ions. *Physics of Plasmas*, 20(102307), 2013.
- [232] Z. Chang and J. D. Callen. Generalized gyroviscous force and its effect on the momentum balance equation. *Physics of Fluids: B*, 4(1766), 1992.
- [233] M. Greenwald, J. L. Terry, S. M. Wolfe, S. Ejima, M. G. Bell, et al. A new look at density limits in tokamaks. *Nuclear Fusion*, 28(12):2199 – 2207, 1988.
- [234] B. LaBombard, R. L. Boivin, M. Greenwald, J. Hughes, B. Lipschultz, et al. Particle transport in the scrape-off layer and its relationship to discharge density limit in alcator c-mod. *Physics of Plasmas*, 8(5):2107 – 2117, May 2001.
- [235] J. J. Ramos. General expression of the gyroviscous force. *Physics of Plasmas*, 12: 112301, 2005.